UNIVERSITY OF OKLAHOMA

GRADUATE COLLEGE

INTEGRATED GEOLOGICAL CHARACTERIZATION AT THE BED SCALE OF THE WOODFORD SHALE AT THE I-35 OUTCROP, SOUTHERN OKLAHOMA

A THESIS

SUBMITTED TO THE GRADUATE FACULTY

in partial fulfillment of the requirements for the

Degree of

MASTER OF SCIENCE

By

DANIELA MARCELA BECERRA RONDON
Norman, Oklahoma
2017

INTEGRATED GEOLOGICAL CHARACTERIZATION AT THE BED SCALE OF THE WOODFORD SHALE AT THE I-35 OUTCROP, SOUTHERN OKLAHOMA

A THESIS APPROVED FOR THE
CONOCOPHILLIPS SCHOOL OF GEOLOGY AND GEOPHYSICS

BY

Dr. Roger Slatt, Chair

Dr. Douglas Elmore

Dr. Ahmad Ghassemi

Dedicated to my grandma Zoila who was my very first teacher

ACKNOWLEDGEMENTS

First and foremost, I would like to express my sincerest gratitude to my advisor, Dr. Roger Slatt for accepting me into his research group, for his guidance, encouragement and support throughout this study, and especially for believing in me. I really want to thank him for his constant motivation and for "throwing me into the ring" since my first month in school. I sincerely acknowledge him for encouraging me to present my work at various conferences, as well as to the companies of the consortium, his classes, and field trips. I truly admire him for his commitment to research and his endless support to his students.

Secondly, I am grateful to Dr. Douglas Elmore and Dr. Ahmad Ghassemi, not only for being on my committee and providing valuable feedback for my thesis, but also for allowing me to fully use their laboratories: SEM and Rock Mechanics laboratories respectively. I also want to thank the entire staff of the School of Geology and Geophysics, especially Rebecca Fay for her help and support on solving administrative issues.

I greatly appreciate the Institute of Reservoir Characterization and the sponsors of the 'Woodford Shale Consortium Project' for their financial support. It was very helpful and gratifying for me to be able to meet many of them during field trips and presentations, I learned a lot from their questions and comments. I also want to thank my Woodford consortium peers: Richard Brito, Bryan Turner, Carlos Molinares, Sayantan Ghosh, Ifunanya Ekwunife, Benmadi Milad, Emilio Torres, Lydia Jones, and Jing Zhang.

I wish to extend my gratitude to specific persons who technically helped me in the accomplishment of this project: Dr. Andy Madden for allowing me to use the powder X-Ray Diffraction laboratory at the University of Oklahoma, but also for his excellent training in clay mineralogy. Yawei Li for kindly helping me on performing the geomechanical tests and for always being eager to answer my questions. Alex Vachaparampil for his valuable feedback on the geomechanics chapter, also for being open to discussions on generic topics of rock mechanics. Bryan Turner who gave me the first training on X-Ray Fluorescence. Gerhard Heij for training me on the Scanning Electron Microscopy technique.

I would like to extend my sincerest thanks and appreciation to my family, especially Zoila, Yalile, and Angelica for their love, warm words, and for always believing in me. Thank you for the motivation to work harder to get the best out of myself.

I am fortunate to have met so many 'latino' friends who made my time here at OU a lot more fun: David D., Alejandra, Javier, Carolina, David P., Yamile, Paula, Rafael, Laura H., Ruben, Carlos C., Emilio, Carlos M, Nestor, Laura S., Hernan, Richard, Lenon, Andreina and Gabriel. I cannot leave out my non-latino friends: Teng Fei, Sayantan, Madi, and Ashley.

Saving the most important for last, I would like to thank my wonderful husband and research-mate Henry Galvis for being my main support during this adventure, for those sunny days at the field, endless nights of studying and working in laboratories, but most importantly for his lovely company on the challenges that this journey brought to us. The graduate school definitely has been our best time together. Also, I must thank him for being the first reviewer of this document and for helping me to put my frequently-complex ideas into more simple terms. Indeed, I undoubtedly think he should be a coauthor of this thesis.

Finally, I want to leave a quote for my future self:

Sometimes the fear won't go away so you'll have to do it afraid
Unknown

TABLE OF CONTENTS

LIST OF TABLES

LIST OF FIGURES

ABSTRACT

A road-cut exposure located on the southern flank of the Arbuckle anticline along the Interstate-35 provided the opportunity to document in detail the lithological heterogeneities of the uppermost 81 feet of the Woodford Shale. This outcrop comprises portions of the middle and upper informal Woodford members. Lithologically, strata mostly consist of dark-colored, organic-rich mudrocks, which are rhythmically stacked into cm-scale cycles of 'hard' and 'soft' beds mimicking brittle-ductile couplets.

At the bed scale, based on weathering responses, the Woodford Shale is represented by two highly distinctive rock types: 'soft' and 'hard' beds. To document such typical high-frequency cyclicity, two samples were collected at every foot (one soft and one hard). In total, 157 samples were collected, from which a comprehensive multi-scale characterization was performed including several laboratory techniques: X-ray diffraction (XRD) for mineral composition, X-Ray fluorescence (XRF) for elemental composition and chemostratigraphy, total organic carbon (TOC) for organic richness, Rock-Eval pyrolysis for kerogen quality, thin sections and SEM for petrography, micro-rebound tests for rock hardness and uniaxial compressive strength tests (UCS) for mechanical properties. Laboratory results from this study corroborated the outcrop-based distinction between 'soft' and 'hard' beds, as determined by systematic contrasts in mineral/elemental composition, rock fabric and mechanical properties.

Experimentally, ‘Soft’ beds are ductile since they sustained more plastic deformation before failure; these beds are usually finely laminated, fissile, clay-rich (> 15 wt.%), and have very high TOC and organic proxies (Mo, U), low Si/Al ratios, and high detrital proxies (Ti, Zr, K, Al). Rock brittleness, UCS, Young’s modulus and hardness values are usually low for ‘soft’ beds. ‘Hard’ beds on the other hand are brittle since they sustained little to none plastic deformation before failure on lab experiments; these beds are massive, quartz-rich (> 90 wt. %), and have lower TOC contents and organic proxies (Mo, U), low detrital proxies (Ti, Zr, K, Al) and much higher UCS, Young’s modulus, brittleness and hardness values.

The high-resolution characterization results from this thesis provided insights for the prediction of rock properties for the two dominant and distinctive rock types within the Woodford Shale, ‘soft’ and ‘hard’ beds; giving rise to speculate that if proper physical distinction is made between ‘soft’ and ‘hard’ beds in cores or outcrops, few samples would work fine to upscale rock properties within larger intervals with incomplete sets of data, thus reducing costs/time related to acquiring large datasets from numerous analytical techniques.

Correlations between outcrop-based gamma-ray profiles and subsurface gamma-ray logs demonstrated good lateral and vertical continuity with systematic stacking patterns. Thus, outcrop-based rock characteristics can be projected into the subsurface to logs in un-cored wells to identify zones for optimum drilling and completion in the Woodford Shale and analog reservoirs.

1. INTRODUCTION

The Upper Devonian-Lower Mississippian Woodford shale has traditionally been regarded as the petroleum source rock for conventional reservoirs in Oklahoma. Lately, the Woodford Shale is the most attractive unconventional resource play in Oklahoma. Due to the high cost to acquire well cores along with today's low-oil-price scenarios, sizeable challenges are emerging especially for unconventional reservoir characterization. Consequently, detailed characterization of outcrops helps to overcome this limitation and additionally can provide direct evidence of the lateral and vertical shale heterogeneities which sometimes are not easily recognizable in cores and/or well-logs. Despite the significant oil/gas production from the Woodford Shale in Oklahoma, valuable information in outcrops still remains uninvestigated in terms of modern shale characterization approaches.

This thesis characterizes a road-cut exposure located along the west side of Interstate-35 that covers the uppermost 81 feet of the Woodford Shale. The I-35 Woodford outcrop is probably one of the most studied in southern Oklahoma, it has been investigated by several authors since 1985. These studies vary in scope and include stratigraphy (Ellis & Westergard, 1985; Fay, 1989), biostratigraphy (Over, 1992), organic geochemistry (Lewan 1983, 1985; Kirkland et al., 1992; Roberts & Mitterer, 1992; Nowaczewski, 2011; Jones, 2017), gamma-ray characterization (Krystyniak, 2005), analysis of phosphate nodules (Siy, 1988; Boardman, 2009), magnetic susceptibility (Aufill, 2007; Ellis, 2013), and fracture studies (Ataman, 2008; Badra, 2011).

The main purpose of this study is to demonstrate that the Woodford Shale can be simplified in rhythmically repeated soft-hard couplets which present very contrasting rock attributes as determined by organic contents, elemental compositions, mineral proportions, rock fabric and geomechanical properties.

The identification and quantification of the soft-hard couplets has a crucial implication on the reservoir and completion quality of the Woodford Shale. Although the identification of soft-hard couplets in cores may be a difficult task, this study will provide key criteria to facilitate the recognition of these couplets in cores through the use of non-destructive and hand-held techniques.

1.1.Study Area

Regionally, the study area is located in the northern termination of the Ardmore Basin or Southern flank of the Arbuckle Anticline, specifically in Carter County (**Figure 1**). Locally the I-35 section is a road-cut exposure located on the west side of Interestate-35 about 650 feet (198 m) north of milepost 44, under the geographic coordinates 34°21'06.9"N and 97°08'55.5"W.

On this location, the uppermost 81 feet and the lowermost 10 feet of the Woodford Shale are exposed (**Figure 1**); overlying strata of the Sycamore Limestone and underlying strata of the Hunton Group are also exposed on this location.

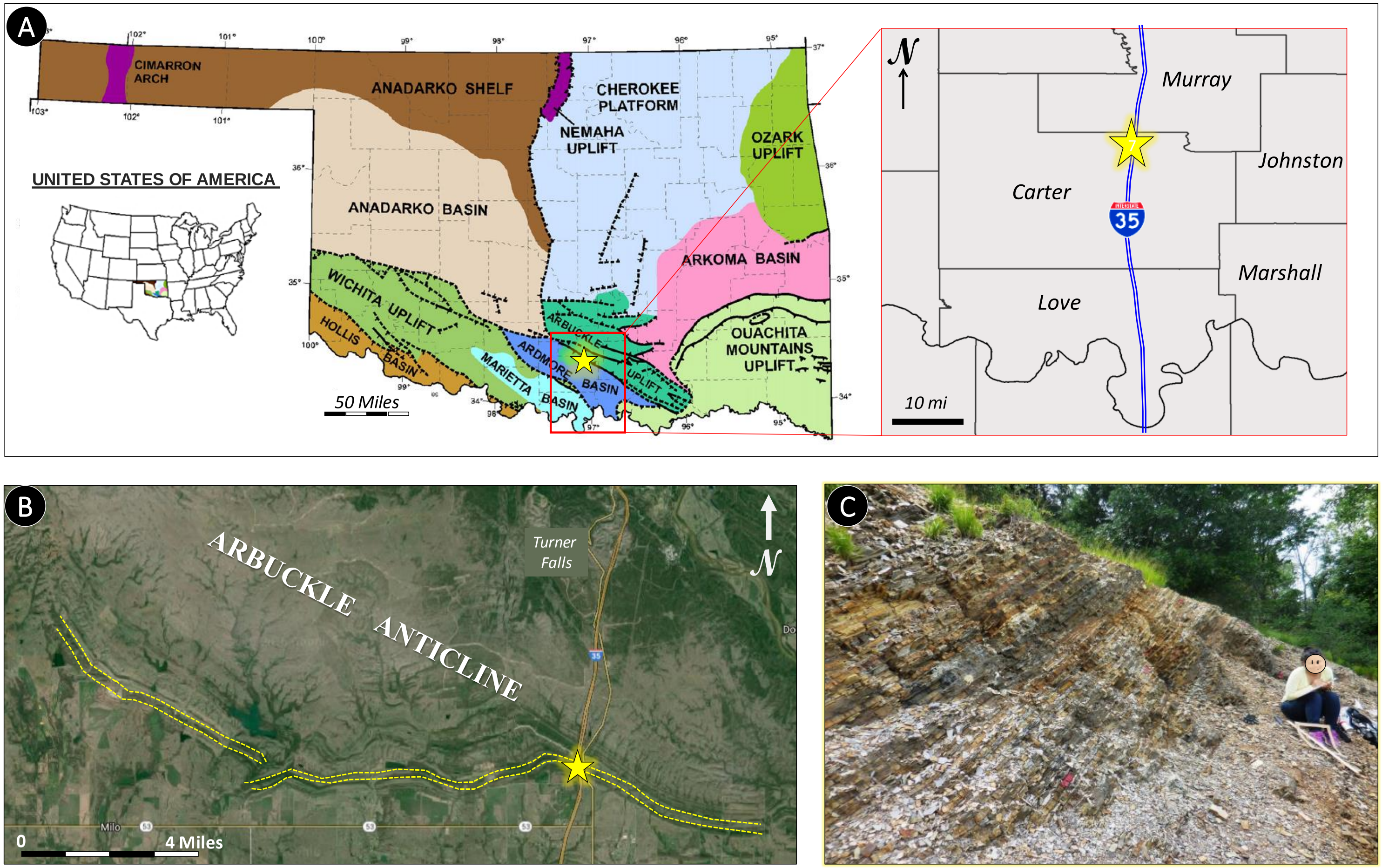

Figure 1. (**A**) Geologic provinces of Oklahoma showing the principal tectonic features surrounding the area of study; The yellow star marks the location of the I-35 outcrop. From Cardott, (2012). Originally in Northcutt & Campbell, (1995). (**B**) Aerial photograph showing the location of the I-35 outcrop (yellow star) along the Woodford Shale belt of the Arbuckle Anticline (yellow dashed lines). (**C**) Actual photograph of the Woodford Shale exposed at the I-35 section. Bedding attitude is N65°W/48°SW.

1.2.Regional Geological Setting

The Ardmore Basin is a fault-bounded basin of Pennsylvanian age in south central Oklahoma (Granath, 1989). It is nearly 100 miles long and 20 miles wide. It is elongated in a WNW-ESE direction (Suneson, 1996). The Ardmore Basin is bounded on the NE by the Arbuckle anticline (Arbuckle Mountains), on the SW by the Criner Hills uplift and the Waurika-Muenster uplift. The basin is terminated on its southeast end by the buried Ouachita Mountains (**Figure 1**).

The southern Oklahoma region was highly affected by tectonic forces from the late Precambrian to Late Pennsylvanian. The first tectonic activity occurred in the late Precambrian as a breakup of the continent to form the Proto-Atlantic Ocean, this rifting formed a series of failed-arm rifts extending into the craton (**Figure 2**).

The southern Oklahoma Aulacogen (SOA) is the most prominent North American failed-arm rift and was recognized as a classic example of an aulacogen by Shatski (1946). It is a WNW trending trough, which acted as the main depocenter of the Oklahoma basin (**Figure 3**). The aulacogen lies south of the Arbuckle Mountains and presently encompasses the Anadarko and Ardmore basins, as well as the Wichita and Amarillo uplifts. The aulacogen is truncated to the southeast by the Ouachita fold belt (Hatcher, 1989).

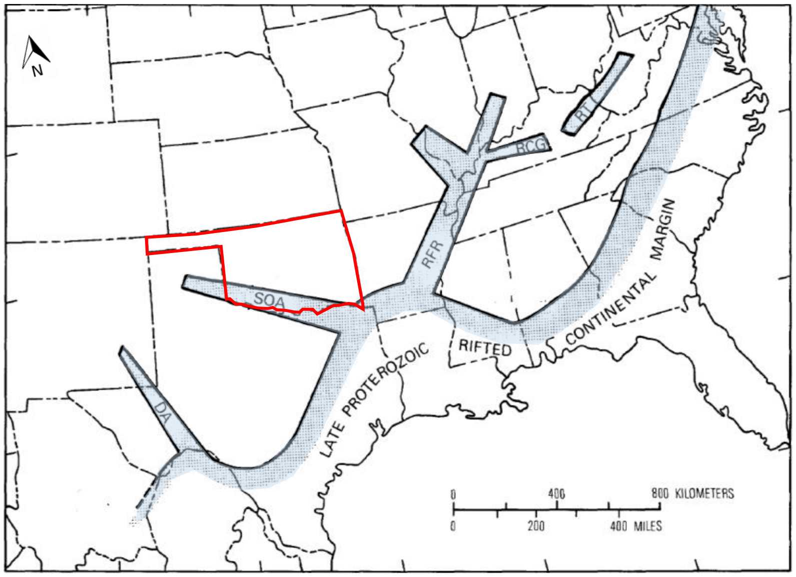

Figure 2. Generalized Late Proterozoic and early Paleozoic paleotectonic map showing the continental margin in southeastern United States and the Southern Oklahoma Aulacogen (SOA). In red the location of Oklahoma. From Perry, (1989). Originally in Keller et al., (1983).

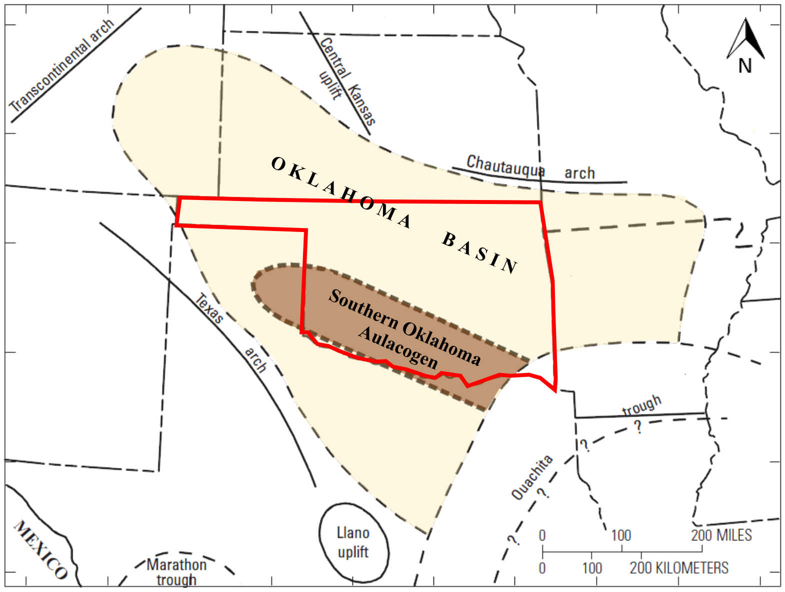

Figure 3. Schematic map of southwestern United States during early and middle Paleozoic, showing the approximate outline of the Southern Oklahoma Aulacogen (SOA) in brown, the Oklahoma state boundary is outlined in red, and the Oklahoma Basin boundary is highlighted in beige. Modified from Gaswirth and Higley, (2014). Originally in Johnson et al., (1989).

Bounding normal faults trending approximately N60°W are inferred to have existed along the northern margin of the rift (Gilbert, 1982,1987). A vast amount of volcanic rocks was intruded (gabbros and granites) and extruded (basalts and rhyolites) along the axis of the Southern Oklahoma Aulacogen (Ham et al., 1973; Gilbert, 1982). This intense igneous activity was concentrated in Southern Oklahoma because the faulting associated with the rifting had weakened the basement of the continental crust (Sunneson, 1996) (**Figure 4**).

Beginning in the late Cambrian (between about 525 and 500 my) and lasting until the late Mississippian (about 340 my), southern Oklahoma was the site of a broad, epicontinental sea that extended across most of the southern midcontinent (Suneson, 1996). Shallow-marine limestone and lesser amounts of sandstone and shale were deposited throughout this area (Suneson, 1996) (**Figure 4**). The basin rapidly subsided in the last half of the Mississippian period, generating thick sedimentary (Ham et al., 1973; Johnson, 2008) deposits (**Figure 4**). Orogenic activity in the Southern Oklahoma Aulacogen began with the Wichita Orogeny along the Wichita Mountains and Criner Hills in Late Mississippian and ended with the Arbuckle Orogeny in Early Permian (Hardie, 1990) (**Figure 4**). Evidence of these orogenies are rocks deposited in the Ardmore Basin (Suneson, 1996).

The Wichita orogeny exposed a land mass along the Wichita Mountains-Criner Hills chain. A syncline developed where the Ardmore basin and Arbuckle anticline are presently located (Cardott and Chaplin, 1993).

The Arbuckle Orogeny marks the termination of major deformation in the Arbuckle Mountain region (Cardott & Chaplin, 1993) (**Figure 5**). Extensional tectonics began shortly after maximum uplift and formed normal faults parallel to, and reactivating, major thrusts that cut many structures (Saxon, 1998).

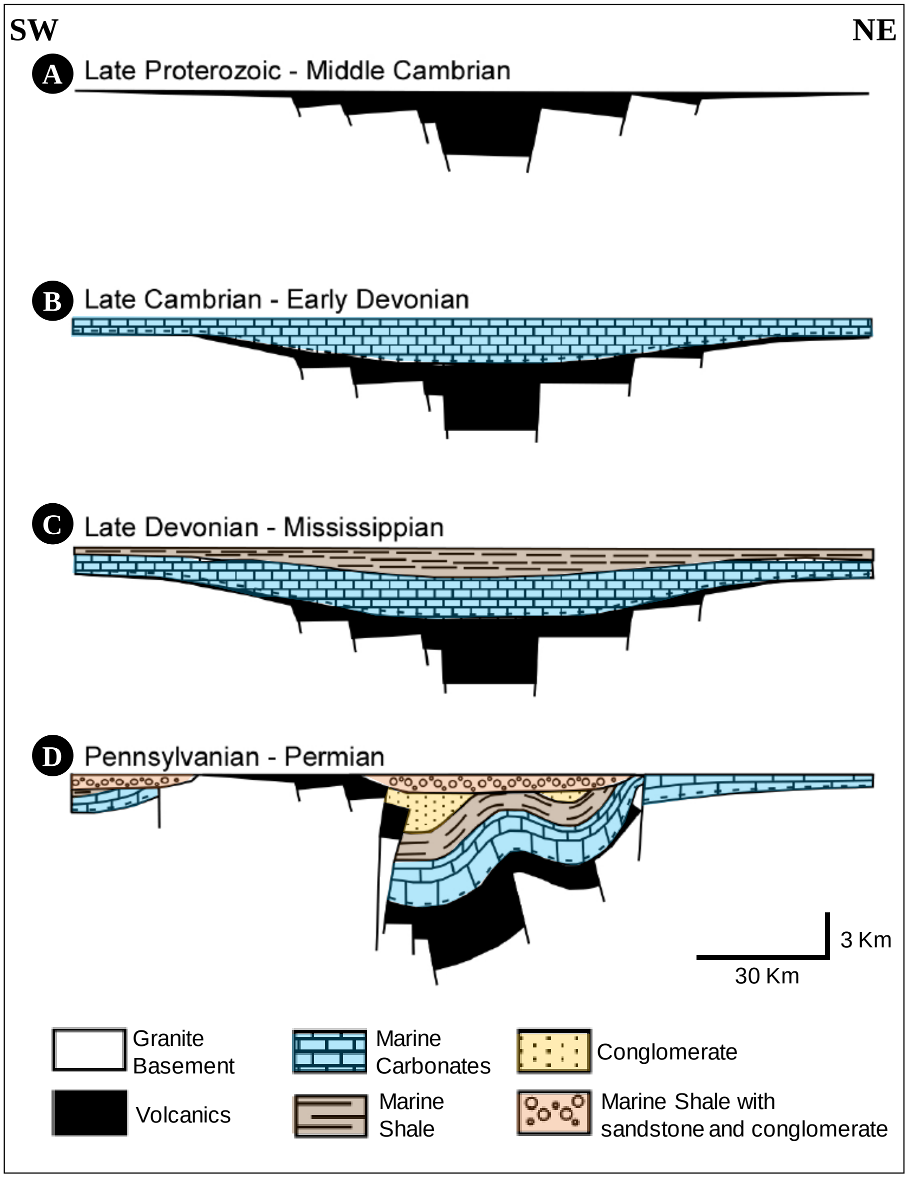

Figure 4. Schematic sections showing the evolution of Southern Oklahoma. (**A**) Graben stage, faulting and filling of rift with volcanic rocks. (**B**) Subsidence and accumulation of mostly marine carbonates. (**C**) Subsidence and deposition of marine shales. (**D**) Folding and faulting (Wichita and Arbuckle orogenies). From Hoffman et al., (1974).

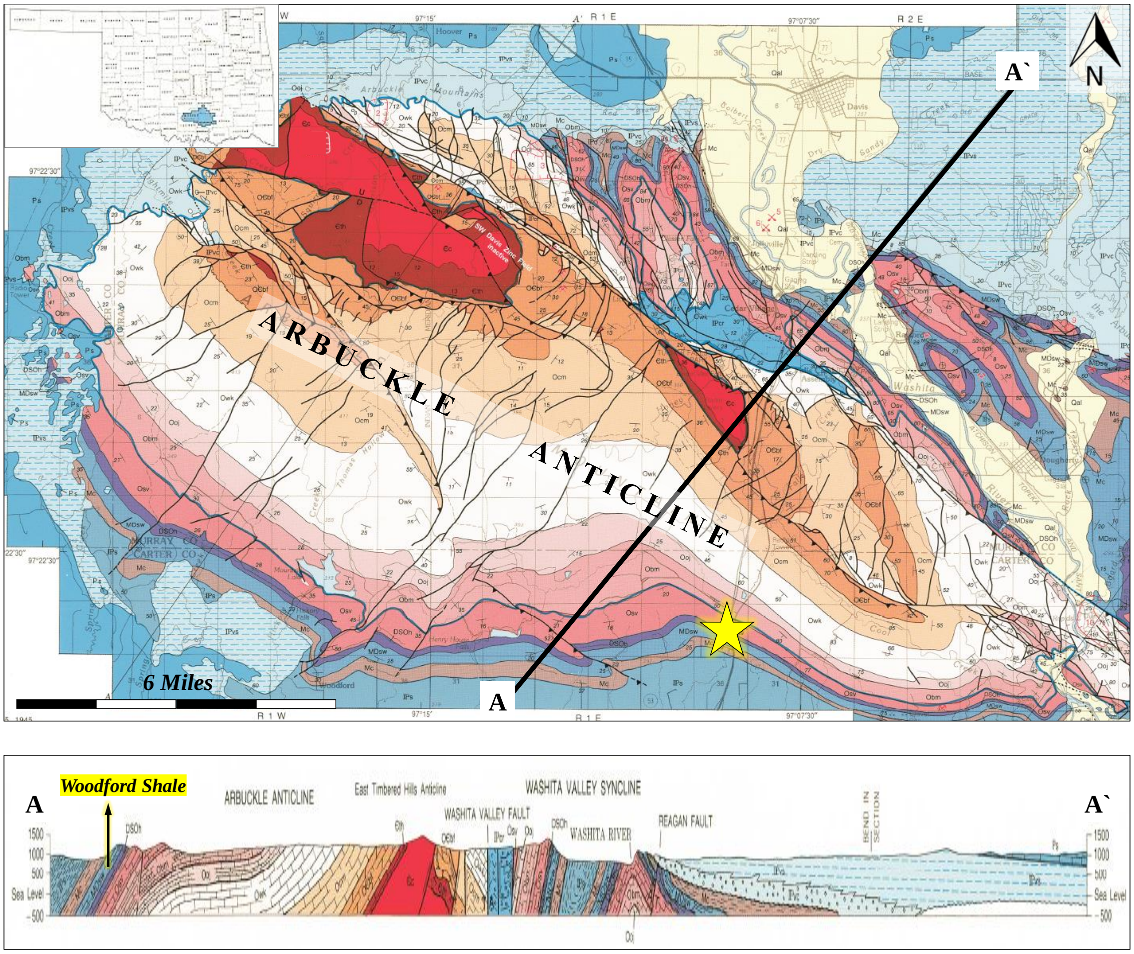

Figure 5. Geologic map of the Arbuckle anticline showing the outcrop locations. The yellow star represents the Speake Ranch shale pit and the yellow star points the I-35 exposure. Bottom figure is a regional cross-section A-A' from SW to NE running through the Arbuckle anticline. Note to the left of the cross sections the black arrow indicating the stratigraphic and structural position of the Woodford Shale. From Stanley & Chang, (2012).

1.3. Woodford Shale Stratigraphy

The Woodford Shale was deposited in equatorial or subequatorial latitudes (near 15° south latitude) in an extensive intra-cratonic sea that was generally shallow (**Figure 6**), probably less than several hundred feet deep (<500 ft) (Shaw 1964; Irwin, 1965; Hallam, 1981; Kirkland et al., 1992). Woodford strata accumulated within anoxic bottom waters and paleo-environmental settings that favored the preservation of organic material (Kirkland et al., 1992; Algeo et al., 2007). Hass and Huddle (1965) determined a Late Devonian-Early Mississippian age for the deposition of the Woodford Shale based on conodonts.

The Woodford Shale overlies carbonates of the Silurian to early Devonian Hunton Group and older units by a major erosional unconformity (**Figure 7**). It is overlaying the Mississippian Sycamore formation which consists of fine grained, silty limestone with interbedded thin dark shales (**Figure 7**).

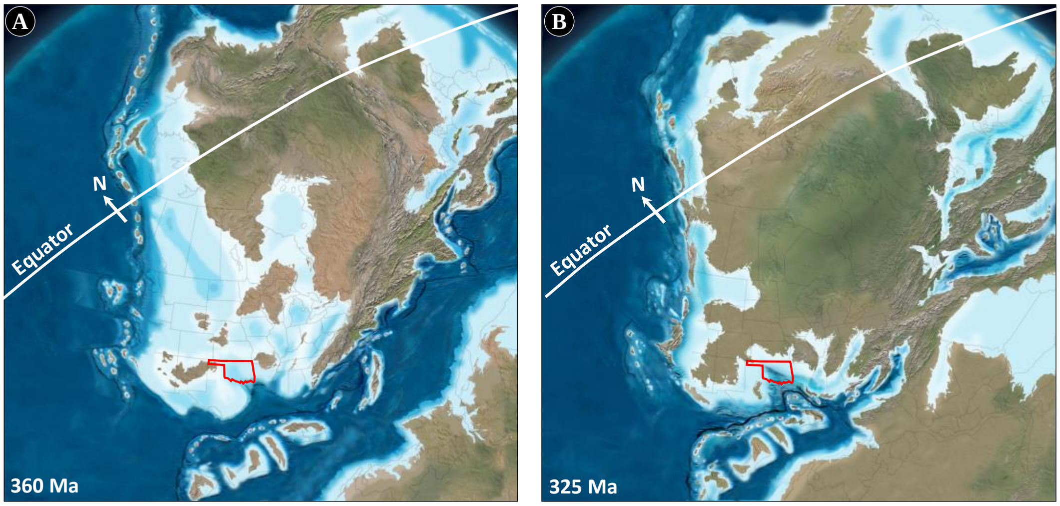

Figure 6. North American paleographic maps during times of deposition of the Woodford Shale. The Oklahoma state boundary is outlined in red. (**A**) corresponds to the Devonian time (360 ma). (**B**) corresponds to the Mississippian time (325 ma). Maps from Blakey, (2011). Paleo-equator relative position from Keith, 2014. .

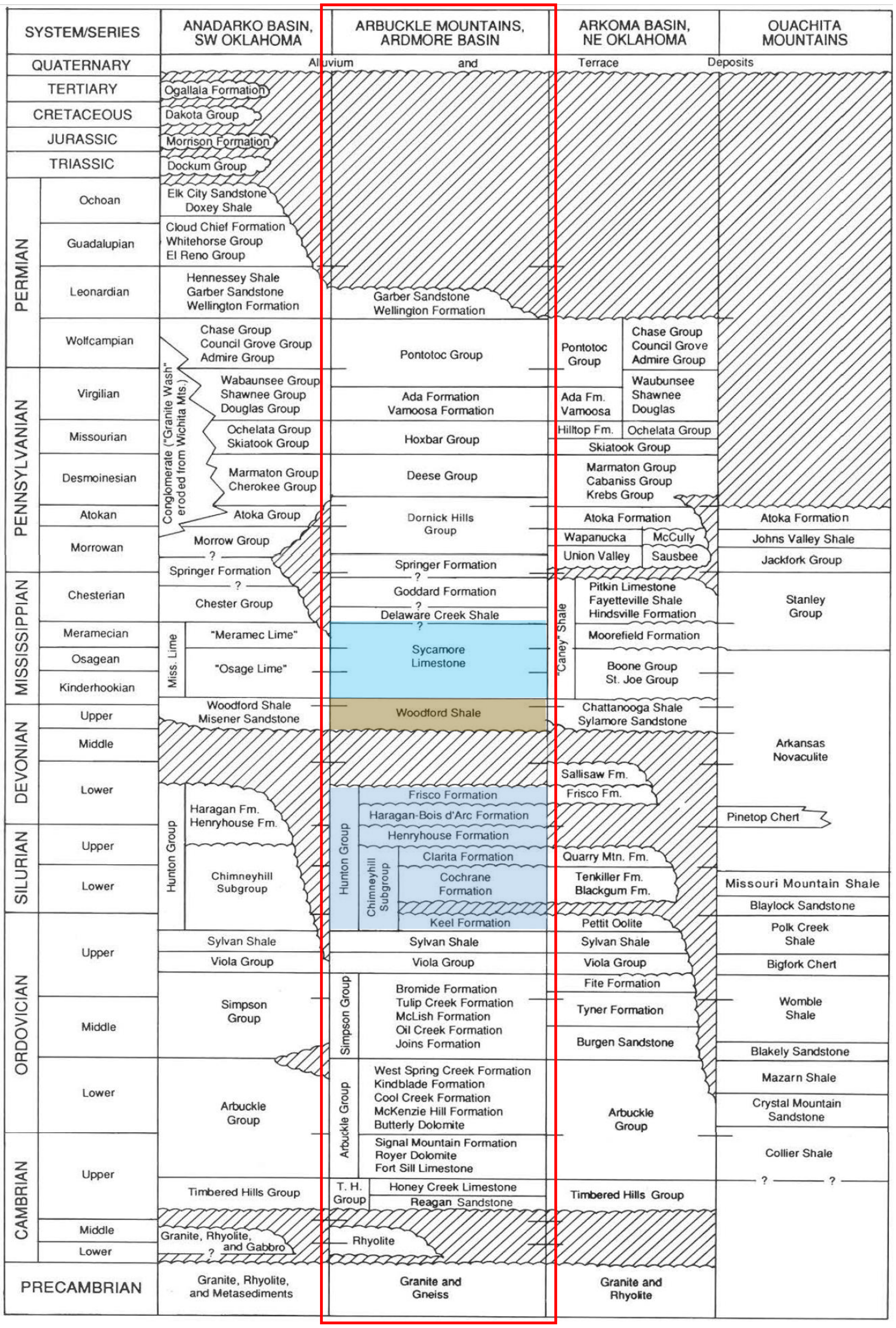

Figure 7. Generalized stratigraphic chart of south Oklahoma. In red is outlined the stratigraphy present in the study area (Arbuckle mountains). Woodford Shale and its overlying and underlying units are shaded in brown and blue respectively. From Johnson & Cardott, (1992). Originally by Hills & Kottlowski, (1983); Mankin, (1987).

The Woodford Shale is 350 to 550 feet thick in the Ardmore basin (Ham et al., 1973) and consists of organic rich, dark gray to black shale with black chert beds and phosphatic horizons (Cardott & Lambert, 1985; Sullivan, 1985; Hester et al., 1990; Lambert, 1993).

The Woodford can be easily identified on well logs by a sharp high radioactivity when compared to other formations (Cardott, 2005). **Figure 8** depicts a basic set of well logs, which have been treated as the type log for the Woodford Shale in Oklahoma. It shows the highly radioactive middle shale member and less radioactive lower and upper shale members (Hester et al., 1990).

The Woodford Shale has been informally subdivided into lower, middle and upper members. Subdivision is based on geological, paleontological, geochemical and electrical log variations (Sullivan, 1985; Hester et al., 1990; Lambert, 1993; Cardott, 2005; Slatt et al., 2012; Molinares, 2013; Puckette et al., 2013).

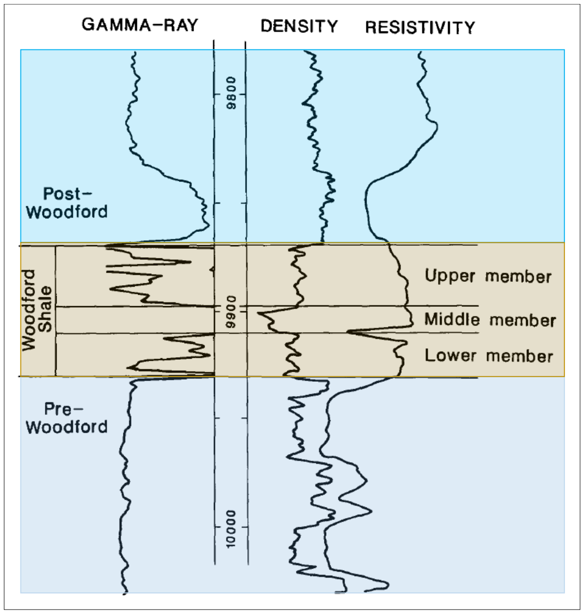

Figure 8. Woodford type log showing the characteristic log signatures of lower, middle, and upper members of Woodford Shale and its overlying and underlying units. From Hester & Smoker, (1988).

The lower Woodford was deposited in a proximal setting during a period of sea level transgression. It displays the smallest aerial extent of the three sub-units, and is composed of black siliceous shales and fissile shales (Hester et al., 1990; Lambert, 1993; Cardott, 2005; Slatt et al., 2012).

The middle Woodford was deposited in a more distal setting during continued transgression, it is finer-grained and typically displays the highest radioactivity values and contains the highest amount of total organic carbon (TOC) (Sullivan, 1985; Hester et al., 1990; Lambert, 1993; Cardott, 2005; Slatt et al., 2012).

The upper Woodford was deposited during continued progradation. It is made up of interbedded black to gray fissile shales and quartz-rich intervals, contains characteristic phosphate nodules and sporadic dolomitic beds (Sullivan, 1985; Hester et al., 1990; Lambert, 1993; Cardott, 2005; Slatt et al., 2012).

2. METHODS

Various field and laboratory methods were undertaken to characterize the Woodford Shale in the I-35 outcrop (**Figure 9**), including macroscopic rock description, outcrop gamma-ray, X-ray fluorescence (XRF), X-ray diffraction (XRD), Leeb hardness (LH), total organic carbon (TOC), thin section petrography, and scanning electron microscopy (SEM).

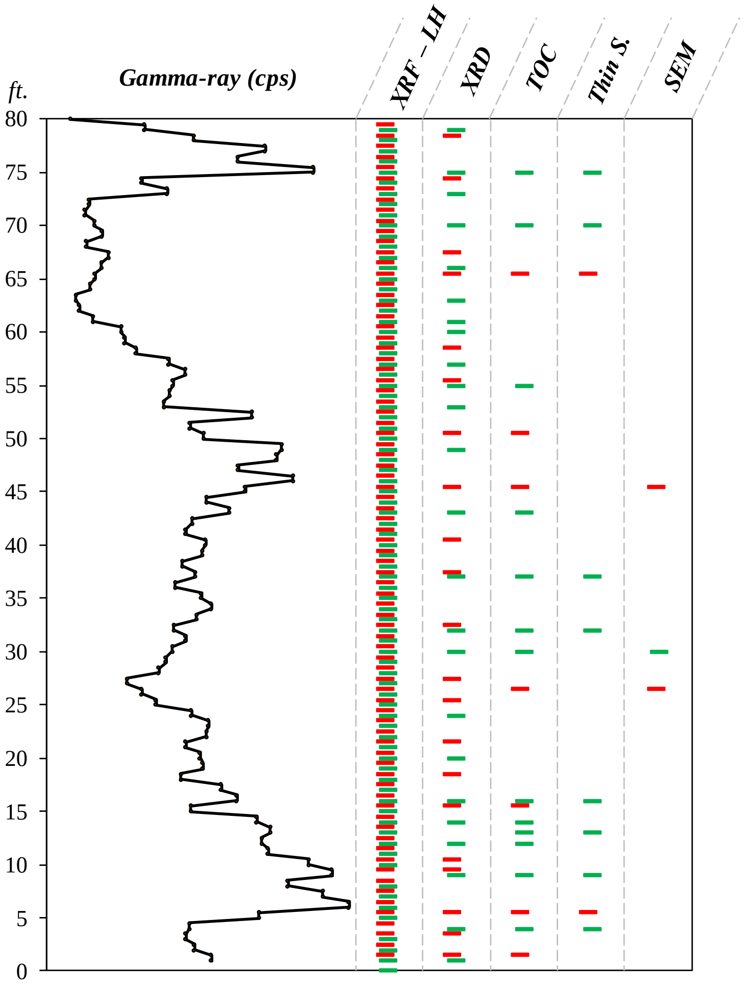

Figure 9. Gamma ray profile showing the stratigraphic distribution of laboratory analysis conducted for this study. Red bars indicate the analysis taken in soft samples, and green bars the analysis taken in hard samples. XRF n =157, rock hardness (LH) n=157, XRD n =46, TOC n=20, thin sections n = 10, SEM analysis n = 3.

2.1.Field Work

The first stage of the field work was measuring the stratigraphic section using a Jacob's staff with a brunton compass to account for bed inclination. As a supplement of the measured stratigraphic section, the natural radioactivity of the rock was obtained at every foot using a hand-held gamma ray scintillometer (Model RS-120 Super-SCINT^{TM}). As recommended by Slatt et al., (1992), five readings were recorded at every stratigraphic foot, and the highest and lowest values were discarded to average the other remaining three readings; gathered data is reported in counts per second (cps) and displayed as a standard well log curve correlatable to a conventional gamma-ray log (Ettensoiin, 1979; Slatt, et al., 1992).

Because the Woodford Shale at the I-35 outcrop consists of rhythmically interbedded 'soft' (fissile) and 'hard' (non-fissile) lithologies, a soft-to-hard ratio was measured for each stratigraphic foot using the measured bed thickness for soft and hard beds, then the soft-to-hard ratio was calculated as equation (1). **Figure 10** exemplifies the calculation of soft-to-hard ratio.

$$Soft : \ Hard\ Ratio = \%\,Soft\ beds : \%Hard\ beds \qquad (1)$$

2.1.1. Sampling

Rock sampling in this study was primarily intended to separate rock types based on the weathering response or gross lithology. Thus, at each stratigraphic foot, two samples were taken, one 'soft' and one 'hard' (**Figure 10**). This study will demonstrate the advantages of lithologically-oriented sampling over systematic sampling.

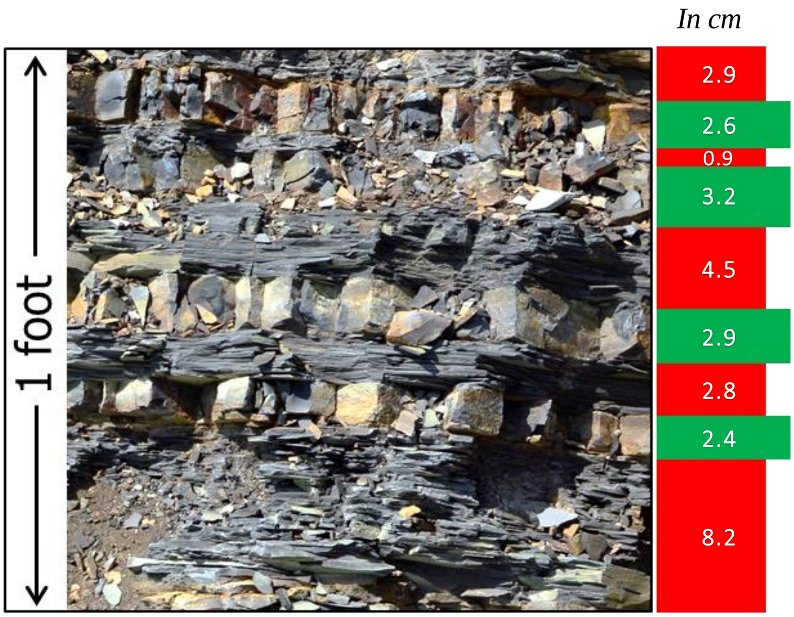

$$\boldsymbol{Soft{:}\,Hard\ Ratio} = \%\,\boldsymbol{Soft\ beds} : \%\boldsymbol{Hard\ beds}$$

$$\%\,\boldsymbol{Soft\ beds} = \frac{\sum Soft\ beds\ thicknesses}{30.48\ cm}$$

$$\sum \boldsymbol{Soft\ beds\ thick.}\ =\ 8.2 + 2.8 + 4.5 + 0.9 + 2.9\ = 19.3\ cm$$

$$\%\,\boldsymbol{Soft\ beds} = 64\%$$

$$\%\,\boldsymbol{Hard\ beds} = \frac{\sum Hard\ beds\ thicknesses}{30.48\ cm}$$

$$\sum \boldsymbol{Hard\ beds\ thick.} =\ 2.4\ + 2.9\ + 3.2\ + 2.6 = 11.1\ cm$$

$$\%\ \ \boldsymbol{Hard\ beds} = 36\%$$

$$\boldsymbol{Soft{:}Hard\ Ratio} = 64 : 36$$

Figure 10. Example of the soft to hard ratio calculation for a specific interval (1 foot) of the I-35 outcrop.

2.1.2. Natural Fractures Study

A detailed fracture-stratigraphy analysis was conducted at the I-35 outcrop in order to determine the relations among lithology, bed thickness and frequency of interbeddings on fracture density. Fracture densities were measured for every bed in the outcrop (about 600 beds) by using the scanline method, which consisted of recording the number of vertical fractures intersected by a 3 feet horizontal scanline (Priest and Hudson, 1981; Lapointe and Hudson, 1985; Priest, 1993) (**Figure 11**). In this study, only the perfect bed-bounded fractures were recorded, which are the most likely to occur for the Woodford Shale in the subsurface as reported by (Gale et al., 2014).

Figure 11. Outcrop picture showing methodology conducted for the fracture analysis. (**B**) Sketch showing the type of fractures described in this study: bed-bounded fractures (Gale et al., 2014)

2.2.Laboratory Analyses

2.2.1. X-Ray Diffraction

Forty-six samples were prepared for bulk X-Ray diffraction analyses in order to cover the I-35 section and to represent the lithofacies variability. XRD analyses were performed in the X-ray diffraction laboratory at the University of Oklahoma using a Rigaku Ultima IV diffractometer with Bragg-Brentano beam geometry and CuKα X-ray source.

The X-ray tube was set to 40 kV accelerating voltage, and 44 mA heating Amperage. Scanning conditions were from 2° to 70° 2θ for random mounts and 2° to 32° 2θ for clay oriented mounts at a step size of 0.02° and a count time of 2 seconds per step for both analyses. XRD patterns were processed and analyzed using MDI Jade 2010 software along with its associated powder diffraction database (ICDD-PDF-4+).

Specimen preparation for Bulk Powder Analysis (Random Mounts)

The sample preparation method proposed by Moore and Reynolds (1997) was followed for bulk mineralogical analysis. 1 to 2 grams of crushed rock were pulverized to micron-sized powder in a McCrone micronizing mill, dried and mounted in a glass slide (**Figure 12**).

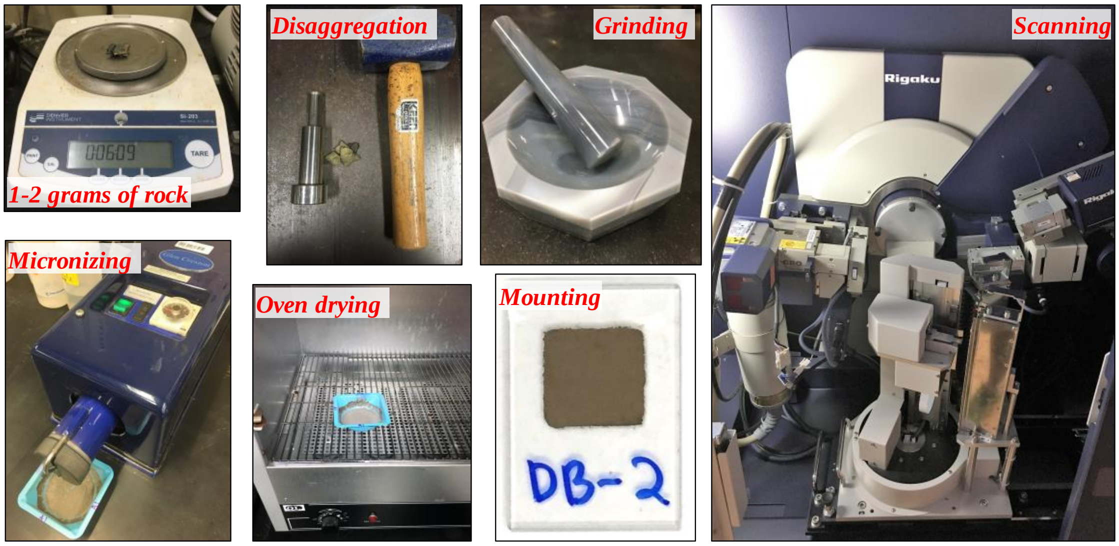

Figure 12. Mosaic of pictures of the actual procedure followed to prepare samples for bulk rock XRD analysis.

Specimen preparation for Clay Size Analysis (Clay Oriented Mounts)

Initial results of the bulk-rock analyses revealed minor amounts of clay minerals (less than 35%) and very significant quartz amounts (greater than 65%). For that reason only two samples were selected as representative for conducting clay-type analysis. Samples were prepared following standardized procedures based on Moore and Reynolds (1997), 1 to 2 grams of crushed rock were disaggregated using a sonic dismembrator, and then centrifuged to concentrate the clay fraction. Then by using a pipet the concentrated clay was dropped and smeared over a high-temperature fused-silica slide (**Figure 13**). X-ray diffraction patterns were obtained three times, for the air-dried specimen, after glycolation, and after heat treatment at 550°C.

Figure 13. Collages of pictures of the actual procedure followed to prepare samples for clay-size XRD analysis.

2.2.2. X-Ray Fluorescence

For this research, X-Ray Fluorescence (XRF) analyses were conducted on 157 samples to determine their elemental composition. A Bruker Tracer IV-SD handheld energy-dispersive XRF analyzer was used. Before scanning with the XRF, each sample was cleaned and cut to get a flat and smooth surface; then each sample was scanned twice, one for major and the other for trace elements. Major element analysis was undertaken for 90 seconds at 15 Kv, 35 mA under vacuum and with no filter. Then the same point was scanned for an additional 60 seconds at 40 Kv, 17 mA, under vacuum and with a Ti-Al filter for the trace elements. Data was collected for 30 elements: Al, As, Ba, Ca, Co, Cr, Cu, Fe, K, Mg, Mn, Mo, Na, Nb, Ni, P, Pb, Rb, S, Si, Sn, Sr, Th, Ti, U, V, Y, Zn, and Zr. Concentrations of these elements were calculated using a calibration established for mudrocks in Rowe et al., (2012).

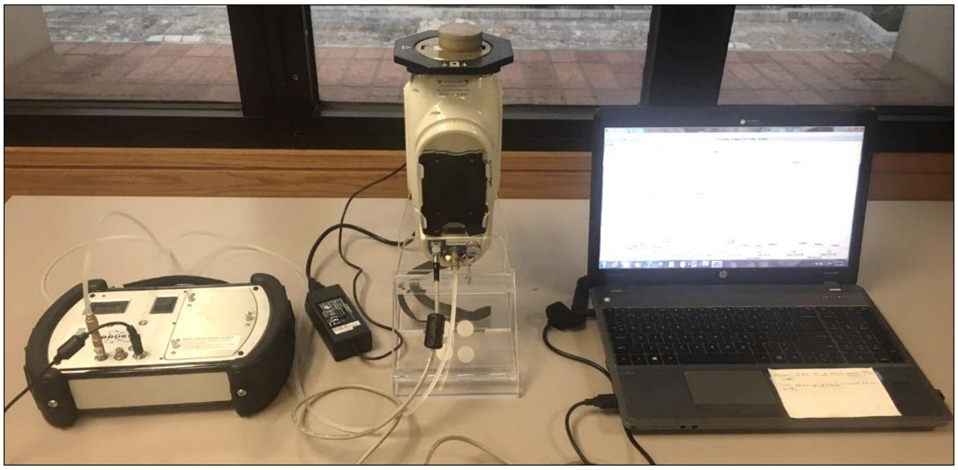

Figure 14. Overview of the actual XRF instrumentation used in this study showing samples laid directly on the nose of the instrument while data is being recorded on a computer.

2.2.3. Total Organic Carbon (TOC) and Rock-Eval Pyrolysis

To evaluate organic richness and general geochemical properties, twenty crushed samples were sent for rock-eval pyrolysis and Leco TOC to Geomark Research, LTD. **Table 1** summarizes the main geochemical parameters measured in this study.

Parameter	Definition	Units
TOC	Total Organic Carbon (kerogen + bitumen)	wt.%
S1	Free volatile hydrocarbons thermally released under 300°C (free oil/gas content)	mg HC/g rock
S2	Hydrocarbons generated during thermal cracking 300ºC to 550ºC (remaining potential)	mg HC/g rock
S3	Organic carbon dioxide generated during the S2 pyrolysis (indicator of kerogen oxidation)	mg CO2/g rock
Tmax	Temperature at peak evolution of S2 hydrocarbons (indicator of thermal maturity)	°C
HI	Hydrogen Index = S2 x 100/TOC (kerogen type indicator by Van-Krevelen plot)	mg HC/g TOC
OI	Oxygen Index = S3 x 100/TOC (kerogen type indicator by Van- Krevelen plot)	mg HC/g TOC

Table 1. Main parameters and definitions of the variables from Pyrolysis Rock-Eval and Leco-TOC. Compiled from Peters and Cassa, 1994 and Jarvie et al., 2007.

2.2.4. Thin Section Petrography

Petrographic analysis on thin sections were undertaken to analyze the fabric, texture, and composition of the mudrocks. Ten regular size thin sections (1 x 2 inches) were prepared oriented perpendicular to the bedding, impregnated with blue epoxy dye, and stained for calcite using alizarin red. Petrographic observations were made at the University of Oklahoma using a Zeiss Axiophot Microscope equipped with a Carl Zeiss Axiocam digital camera.

2.2.5. Scanning electron microscopy (SEM)

Scanning Electron Microscopy (SEM) analyses allows the study of nanometer- and micrometer-scale features of shales (O'Brien & Slatt, 1990). In this study, three rock samples were analyzed to investigate in detail the microfabric of main lithofacies identified in the I-35 outcrop.

The sample preparation procedure was followed according to O'Brien & Slatt, (1990). Firstly, samples were cut with a diamond disc until they were about 3 mm thick (**Figure 15**). A fresh broken surface was created by applying pressure from each end with a pair of vice grips (**Figure 15**). Then, samples were mounted in aluminum stubs with the freshly broken surface facing upward and finally sputter-coated with a gold-palladium alloy (**Figure 15**).

Investigations were carried out at the SEM Laboratory of the University of Oklahoma using a FEI Quantum 250 with an attached Bruker Electron Dispersive Spectrometer (EDS), images were obtained under high vacuum at 20 kV acceleration voltages using the SE, Inlens-SE, and BSE detectors.

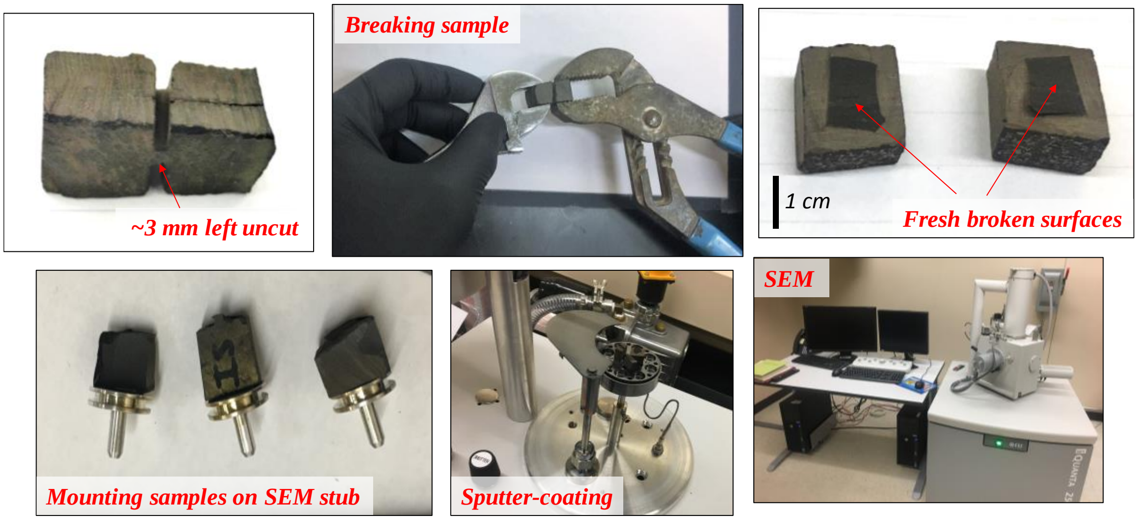

Figure 15. Collage of pictures showing a summary of the actual procedure that involves sample preparation for SEM analysis.

2.2.6. Rock Hardness Test

Hardness measurements were taken in this study using the Equotip Picolo 2 hardness tester, this is a small, inexpensive and non-destructive measuring tool. The principle of functioning consists of an impact body with a tungsten carbide ball (of 3 mm) that impacts under spring force against the surface of the sample to be measured from which it rebounds (Leeb, 1979). The ratio of rebound velocity (Vr) to the impact velocity (Vi) multiplied by the factor 1000 produces a number that translates into the Leeb hardness value (LH) (equation 2) (Leeb, 1979).

$$Hardness\ (LH) = \frac{Rebound\ velocity\ (Vr)}{Impact\ velocity\ (Vi)} * 1000 \qquad (2)$$

Before performing hardness tests, each sample was cut using a rock saw to get a flat and smooth surface. Several authors have documented the influence of the sample thickness on hardness measurements, so a minimum sample thickness of 4 to 5 cm is recommended to perform hardness test using micro-rebound hammers (e.g. Kawasaki et al., 2002; Lee et al., 2014).

Then the sample was placed onto a conventional press on a level tabletop to avoid vibrations while taking measurements (**Figure 17**); the hammer is positioned vertically so that the tip of the hammer is in contact with the rock surface and the path of the spring-loaded hammer mass can fall straight down and impact at a 90° angle to the rock surface (**Figure 17**).

Then, for each sample, ten hardness measurements were taken at about the same location where the XRF was measured. The maximum and minimum values were eliminated and the average of the remaining eight readings was expressed as the hardness number LH.

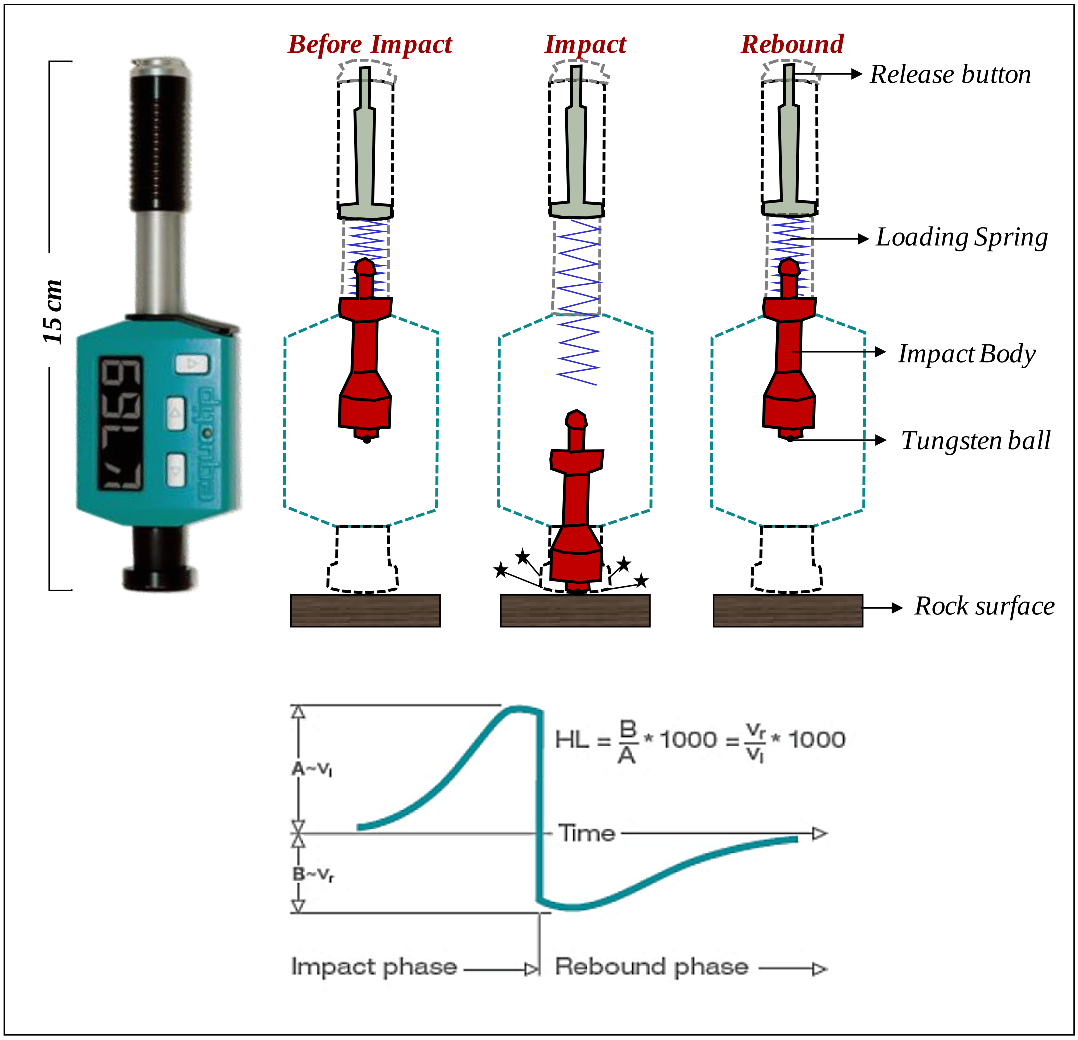

Figure 16. Schematic illustration of how the Equotip hardness tester operates. The micro-rebound hammer consists of a 3 mm diameter ball which is spring mounted in an impact body; this impacts on the test surface under spring force from which it rebounds. Hardness values are the result of the ratio between rebound and impact velocities multiplied by 1,000. The impact energy delivered by impact device type D is 11 N mm.

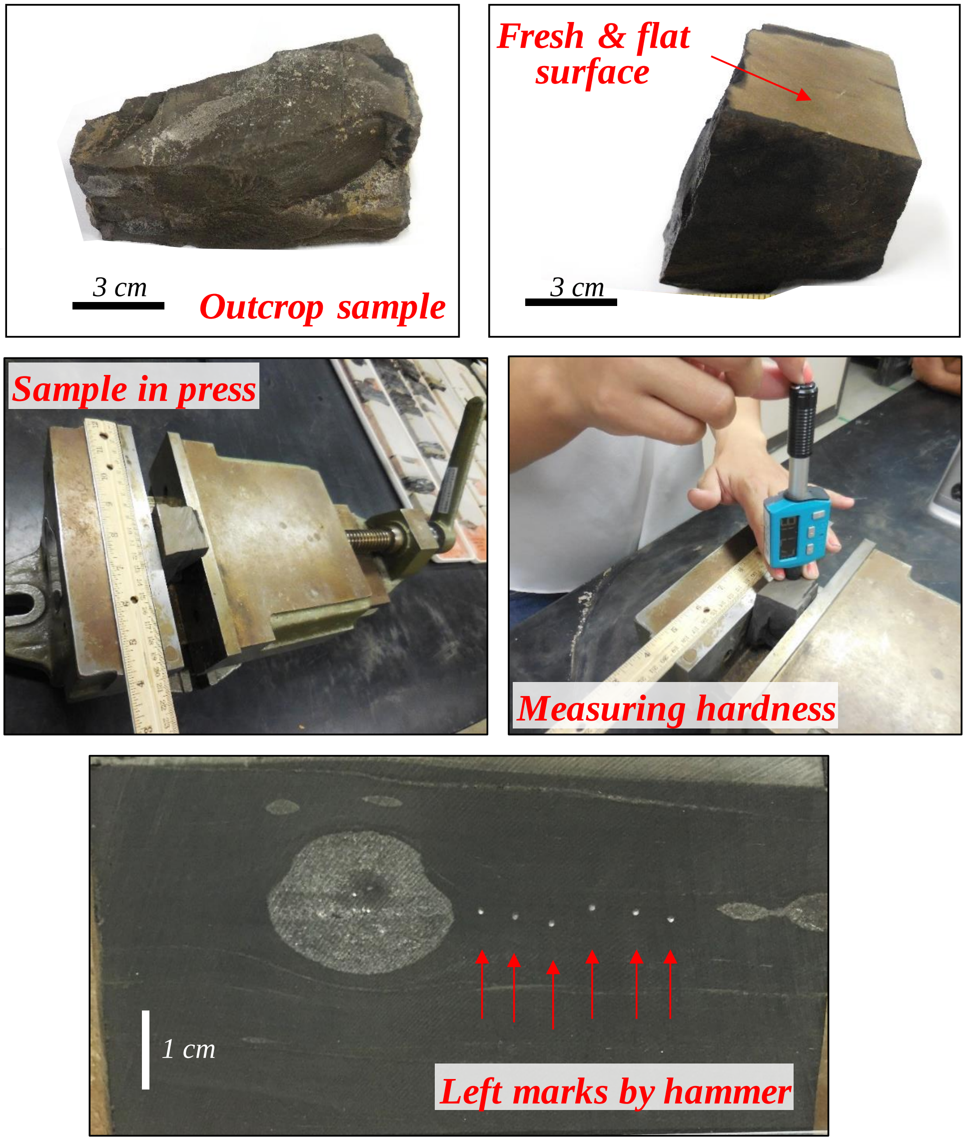

Figure 17. Photo collage showing the press assembly used to stabilize samples while taking measurements. Notice on the bottom picture the non-destructive marks left by hammer impacts (red arrows).

2.2.7. Uniaxial Compressive Strength Test (UCS)

During UCS tests, the specimen is axially loaded at a constant strain rate and its axial and lateral deformation is recorded (Hawkes & Mellor, 1970). Two main constants are obtained directly by uniaxial tests, the Young's modulus (E) referred to as the ratio of axial stress to axial strain, and the Poisson's ratio (v) referred to as the ratio of lateral strain to axial strain (Hawkes & Mellor, 1970).

For this study, five Woodford samples were tested, which comprises the 4 main lithofacies identified in the Woodford (Chert, Siliceous Shale, Siliceous-Dolomitic Shale and Dolomitic Mudstone). Because of the lack of large samples at the I-35 outcrop, the Woodford samples tested in this study came from a nearby outcrop (Speake Ranch quarry) located about 11 miles west of I-35 outcrop in Carter county (Galvis, 2017).

From the rock blocks collected (>8 cm thick), cylindrical specimens were drilled and retrieved using a core drilling machine with water as the cutting fluid (**Figure 18**). All specimens were cored normal to lamination/bedding, since mechanical properties of shales are highly dependent of core-plugs orientation (Sierra et al., 2010; Vachaparampil et al., 2016).

Specimen dimensions were 1-inch diameter (2.54 cm) by 2-inches of length. After coring, top and base surfaces of the specimens were grinded (lathe) to ensure parallel planes but also to meet the exact dimension required of 2-to-1 length-to-diameter (**Figure 18**). Finally, specimens were air-dried for one week before testing.

UCS tests were performed using an MTS 315 loading frame available at the Rock Mechanics laboratory at the University of Oklahoma (**Figure 18**), and following standard procedures (ASTM D 2938).

The applied axial displacement was constant at a rate of 0.002 mm/s. The axial strain (i.e. vertical displacement) was measured using two linear variable differential transformers (LVDT's) attached to circumferential rings (**Figure 19**). The radial strain (i.e. lateral displacement) was measured using one LVDT attached to a chain that surrounds the specimen (**Figure 19**).

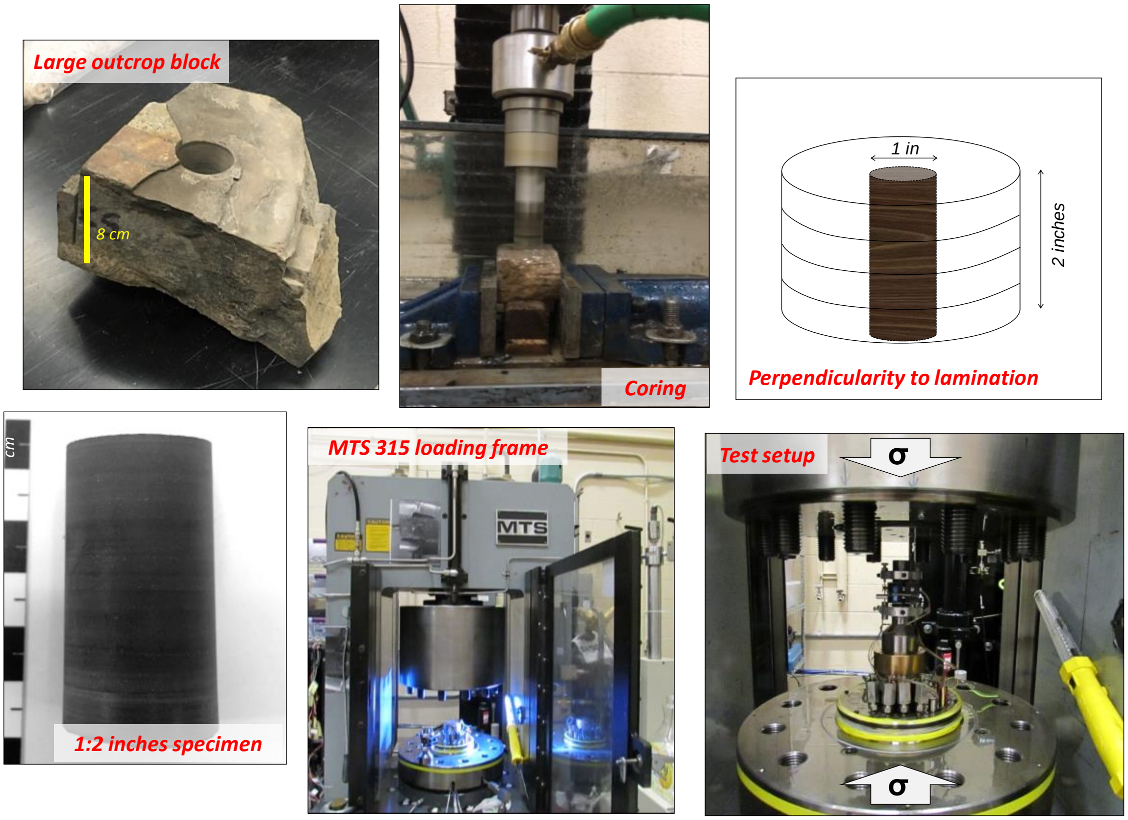

Figure 18. Methodology conducted for UCS tests. Coring of large outcrop blocks was perpendicular to lamination/bedding.

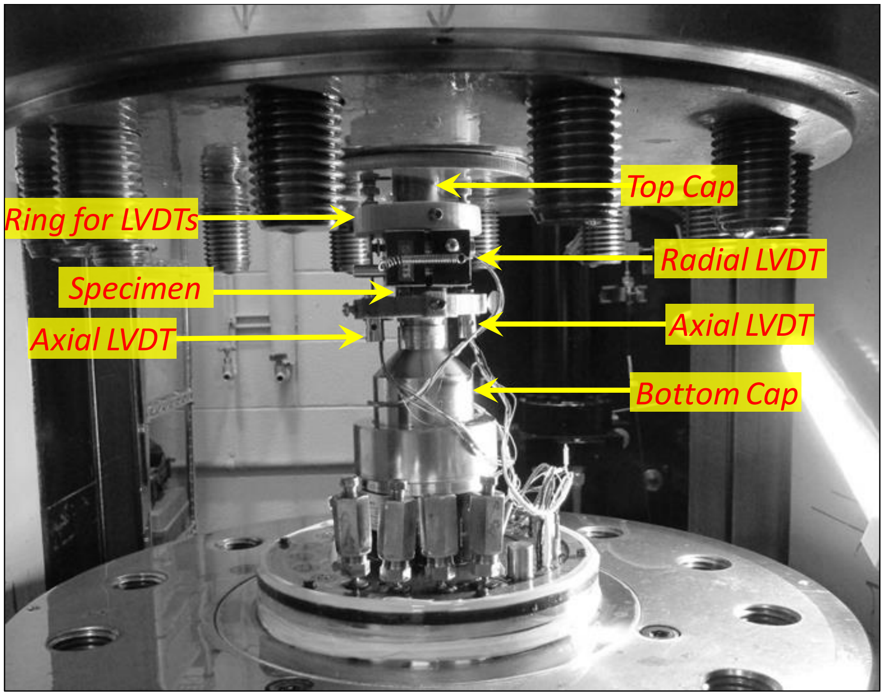

Figure 19. Assemblage used for uniaxial compressive strength tests. Axial strain was measured using two LVDTs attached to circumferential rings and radial strain was measured using one LVDT attached to a chain that surrounds the specimen.

3. OUTCROP DESCRIPTION AND STRATIGRAPHIC COLUMN

A road cut along the west side of Interstate 35, expose the uppermost 81 feet of the Woodford Shale (Figure 20); the lower and partially the middle Woodford members are eroded away possibly by a stream channel (Figure 20).

Additionally, both the upper contact with the Sycamore Limestone and the lower contact with the Hunton Group are present (**Figure 21**). If completely exposed, the total thickness of the Woodford in this location would be approximately 315 feet (**Figure 21**).

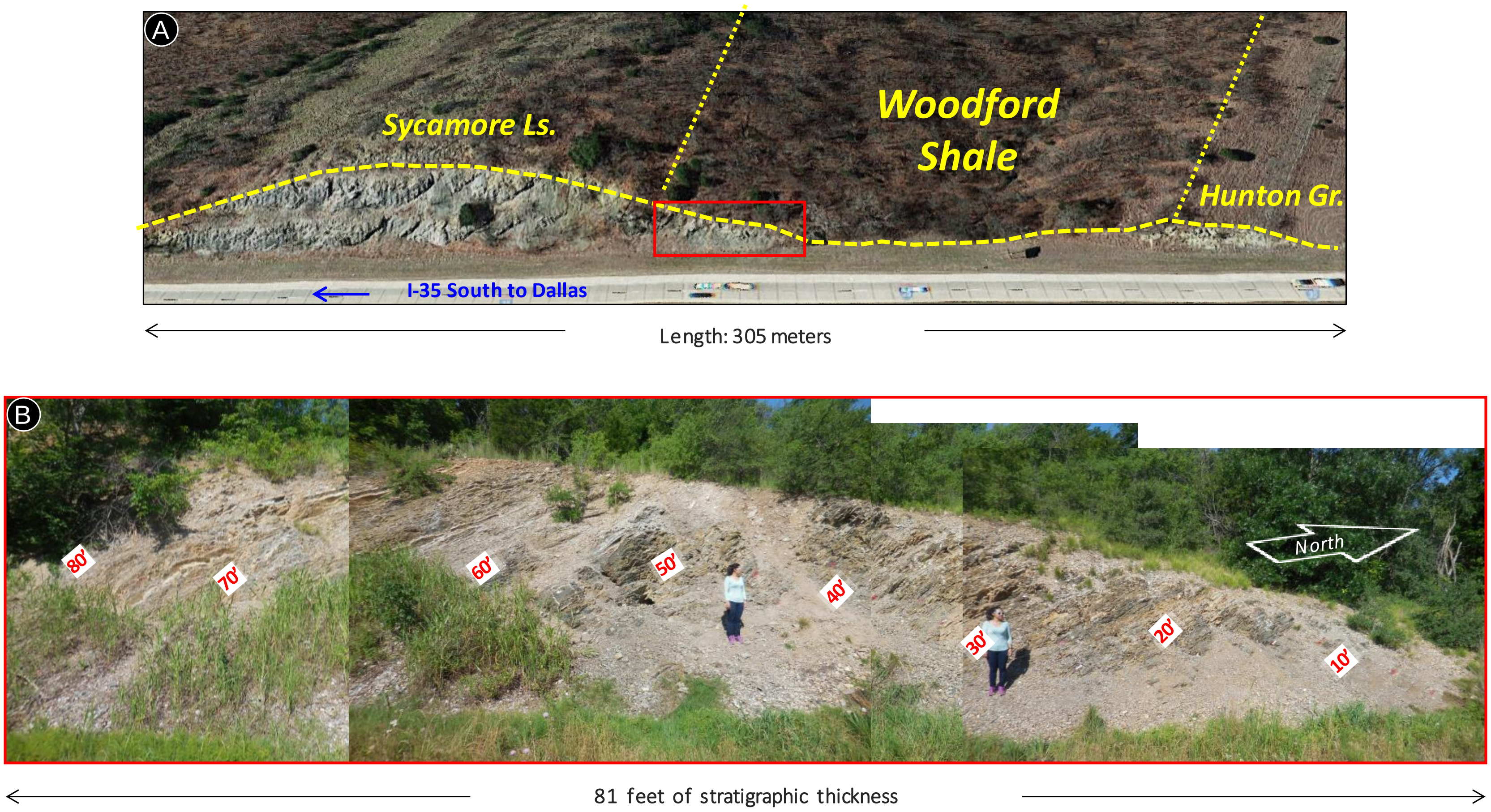

Figure 20. (**A**) Aerial photograph showing the geomorphological expression of the Woodford Shale (softer unit) and its overlying Sycamore limestone (competent unit) and Hunton group (competent unit). (**B**) Collage of pictures showing the exposure of the uppermost 81 feet of the Woodford Shale at I-35. Bedding strike is N65°W, dipping ~48° to the SW.

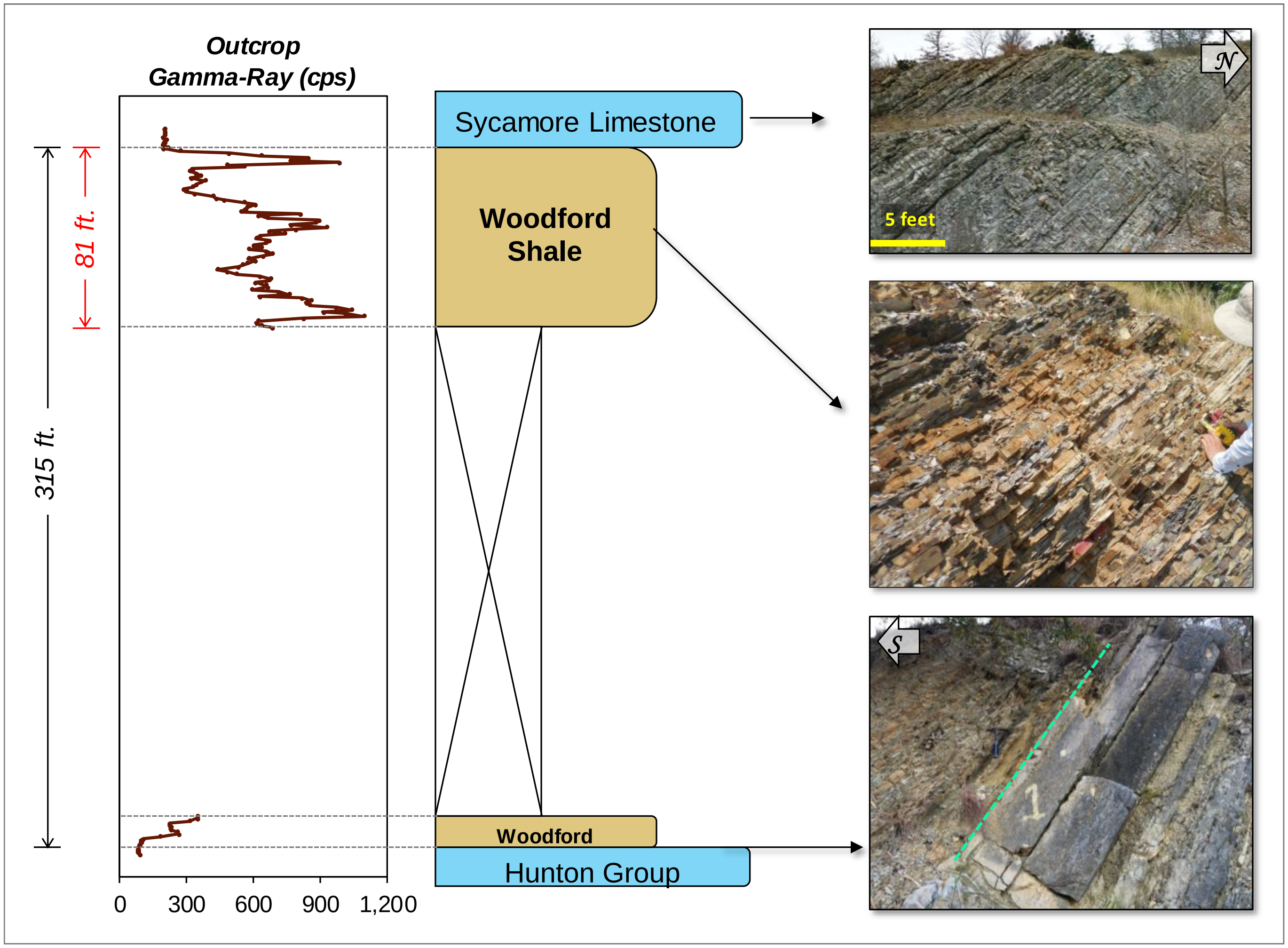

Figure 21. Gamma-ray profile and sketch of the I-35 outcrop showing the exposed Woodford intervals and its upper and lower contacts with the Sycamore Limestone and Hunton group respectively.

3.1.Basal Contact: Woodford Shale / Hunton Group

In the I-35 outcrop the base of the Woodford Shale lies unconformably above the Hunton Group, specifically the Haragan - Bois d'Arc formations as reported by Barrick & Klapper (1990). At this location, the Hunton consists of yellowish, thick-bedded limestones (marlstones) which contain well-preserved crinoids, brachiopods and trilobites (**Figure 22**); dissolution and karstification features are evident along bedding planes (**Figure 22**).

Stratigraphically above the last limestone bed of the Hunton, about one foot of poorly consolidated greenish shale is observed (**Figure 22**), which has been interpreted as lag deposits that mark the early transgressive phases of Woodford deposition (Barrick & Klapper, 1990).

Its presence within the basal Woodford – Hunton contact has been reported in well-cores as well as in other outcrops located in southern Oklahoma (Kirkland et al., 1992; Bontempi, 2015; Maynard, 2016; Galvis, 2017).

Then, above the greenish shale, approximately 10 feet of the lower Woodford Shale are exposed, consisting of intercalations between non-calcareous shales and cherts (**Figure 22**).

Gamma ray readings taken in the Hunton – Woodford contact revealed very low values of 80 (cps) for the last Hunton beds, then values increased progressively up to 350 (cps) in the Woodford Shale facies (**Figure 21**).

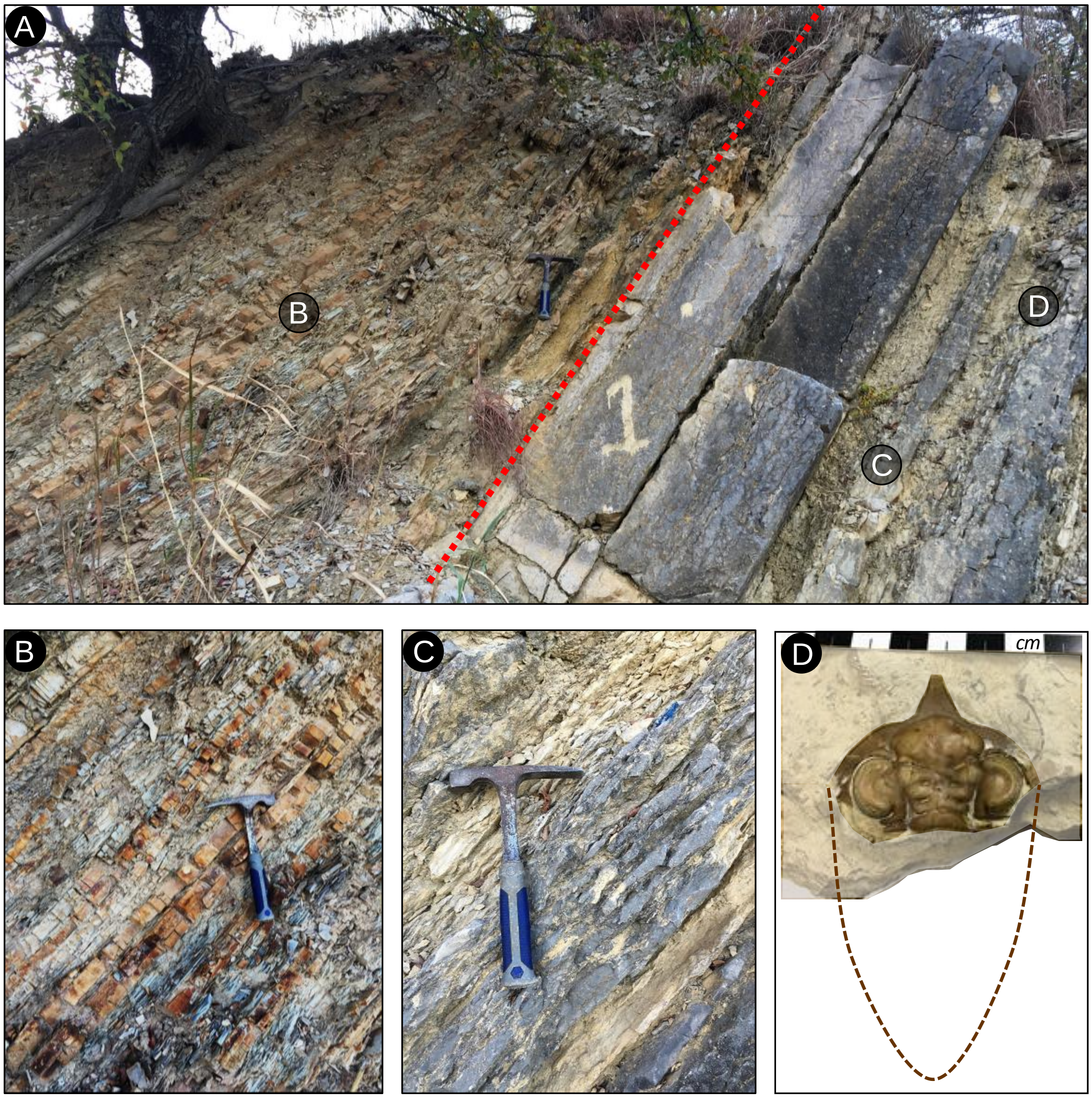

Figure 22. Outcrop characteristics of the contact between the Woodford Shale and the Hunton group at I-35. Notice the sharp contact (dashed line) marking the (**C**) uppermost beds of Hunton Limestone (Haragan - Bois d'Arc formations) overlaid by (**B**) a greenish shale and shales + cherts of the Woodford Shale on top. (**D**) Cephalon of a trilobite found during fieldwork in the Hunton at this location (Genus: Huntoniatonia).

3.2.Upper Contact: Woodford Shale / Sycamore Limestone

The contact between the Woodford Shale and the Sycamore Limestone has been interpreted as transitional in southern Oklahoma (Ham, 1969; Fay, 1989; Schwartzapfel & Holdswort, 1996; Donovan, 2001; Franklin, 2002).

In the I-35 outcrop, above the 'typical' Woodford black cherts and shales lies the "transition zone", which consists of about 60 feet of poorly indurated, calcareous greenish-gray shales interbedded with white non-calcareous cherts and yellowish limestones (**Figure 23**); this interval exhibits no evidence of phosphate nodules that are very common in the upper Woodford Shale. Overlaying the "transition zone", the first Sycamore-type limestone occurs (grey marlstones), from there, the amount of greenish-gray shale beds decreases and limestone beds increase upward to reach the thick bedded limestones of the Sycamore formation *sensu stricto* (**Figure 23**).

Gamma ray readings taken in the Woodford – Sycamore contact display an abrupt decrease from about 985 (cps) in the last Woodford facies to 200 (cps) in the base of the "transition zone" (**Figure 21**).

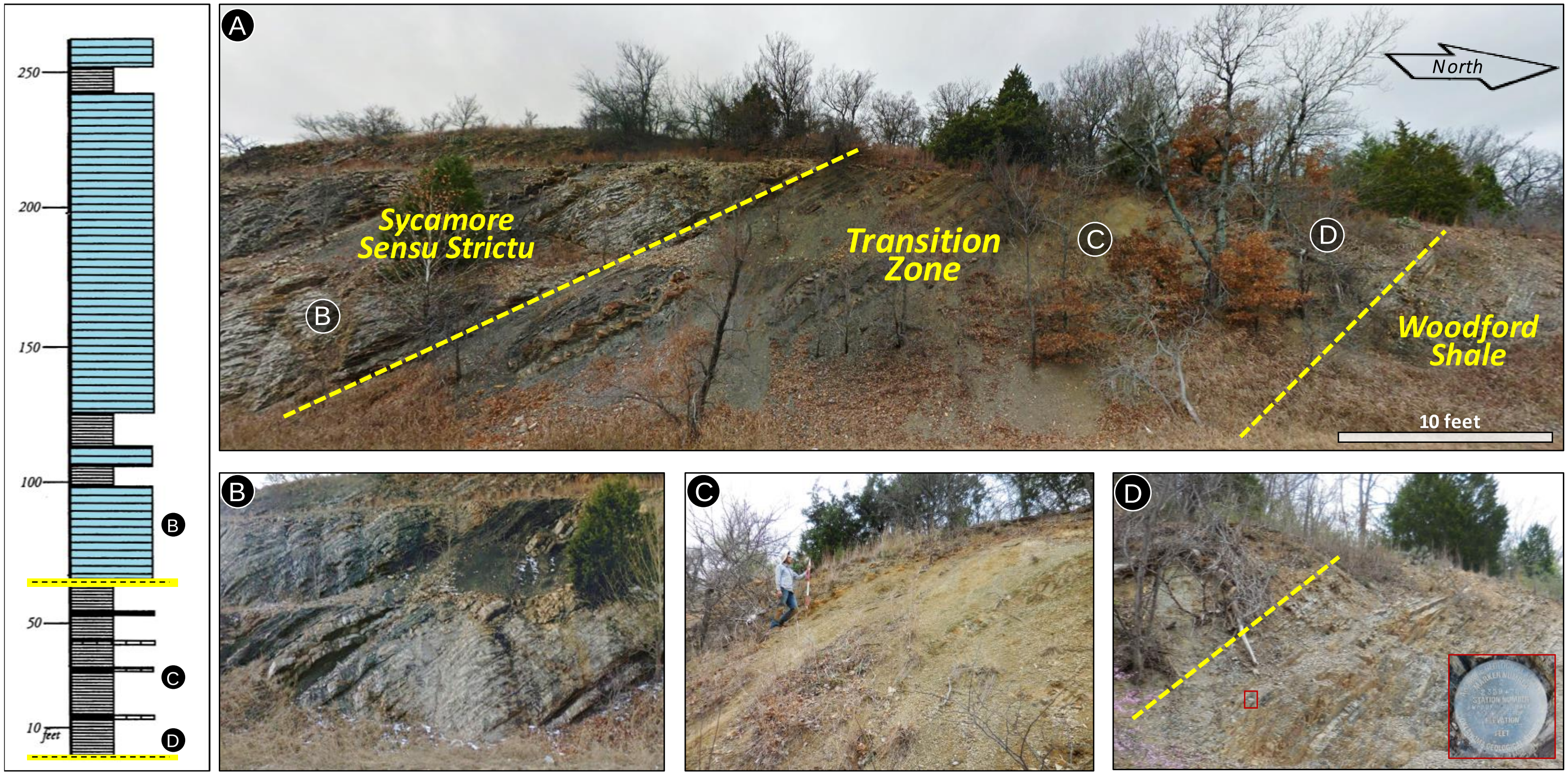

Figure 23. Characteristics of the formational contact between the Woodford Shale and the Sycamore Limestone at the I-35 outcrop. Stratigraphic column on the left side from Donovan (2001). The close up in (D) shows a brass marker left by Ardmore Geological Society (1985) indicating the top of the Woodford 9 feet above it.

3.3.The Woodford Shale measured section

Based on the outcrop-gamma ray profile, the uppermost 81 feet of the Woodford Shale exposed at I-35 were dissected into five zones or para-sequences; from the bottom to top: *(a) Decreasing Upward trend, (b) Increasing Upward trend (c) Decreasing Upward trend, (d) Blocky pattern and (e) Last high peak*. **Figure 24** illustrates the outcrop gamma ray profile tied to soft-to-hard ratios and the generalized stratigraphic column which depicts the vertical distribution of lithofacies, average bed thicknesses and main sedimentary features.

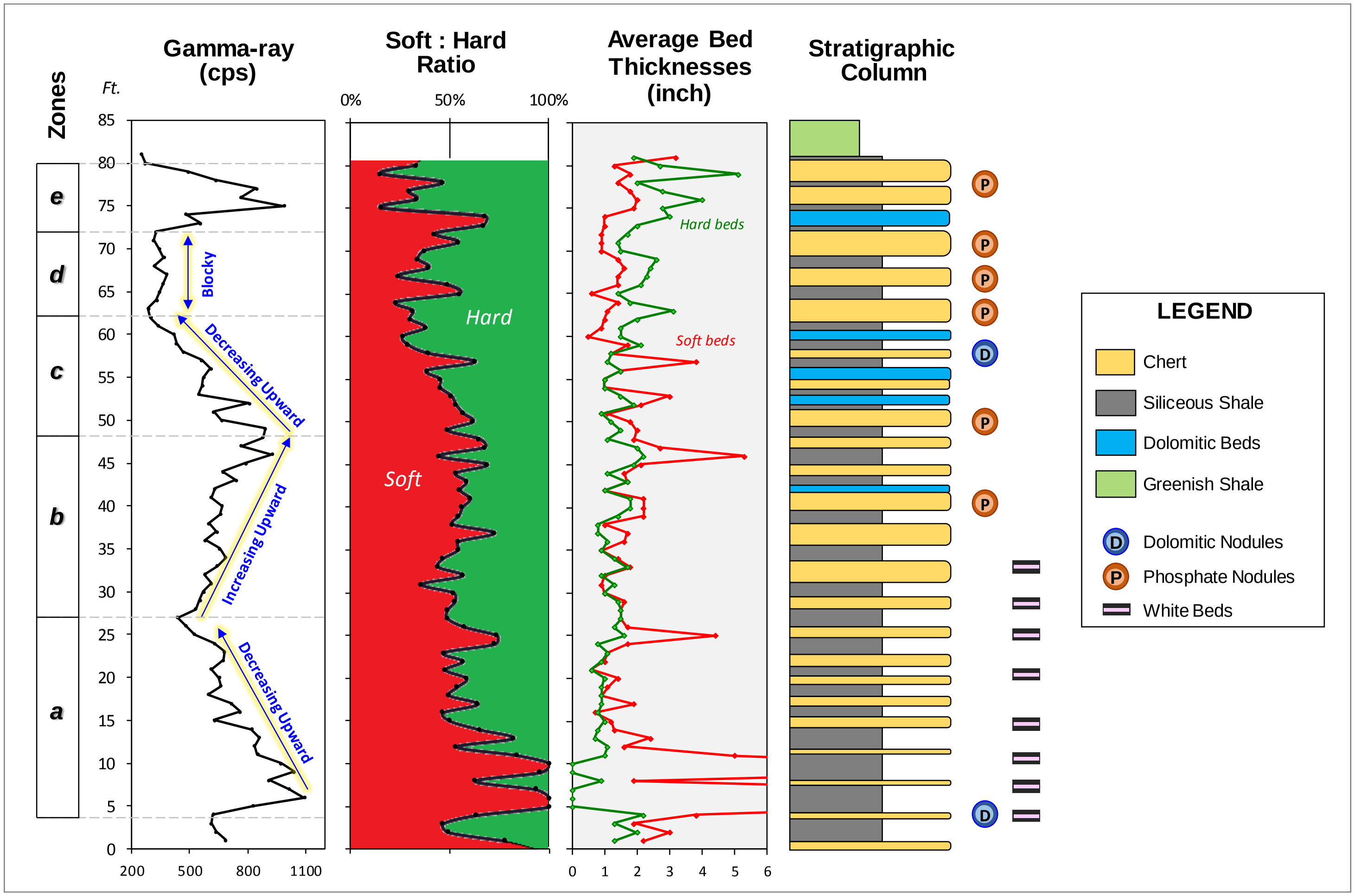

Figure 24. Outcrop gamma-ray profile, soft: hard ratio plot and generalized stratigraphic column showing the five zones identified based on gamma ray trends.

Zone a: Decreasing Upward trend (0 – 27 ft.)

This zone is defined by a progressive decrease in gamma ray readings (from 1091 to 436 cps) (**Figure 24**). Soft to hard ratios reflect a downturn representing the thinning upward of soft beds (from ~30 cm to 4 cm) and thickening upward of hard beds (from ~0.5 cm to ~3 cm) (**Figure 25**).

Lithologically, the interval consists of intercalations between Chert and Siliceous Shale beds (**Figure 24**); the presence of dolomitic beds is rare to absent. Bedding in this zone usually exhibits constant lateral thickness, which can be laterally traced over several feet (**Figure 25**).

The occurrence of porous 'white beds' is common throughout this zone, they are 4 to 6 millimeters thick and can be followed laterally up to 6 feet. These characteristic white beds are composed of 100% quartz (by XRD analysis) and are confined within the Cherts (**Figure 25**).

In this interval, nodules are scarce, indeed only one dolomitic nodule (i.e. non-phosphatic as determined by XRD) was identified hosted by a Chert bed (**Figure 25**).

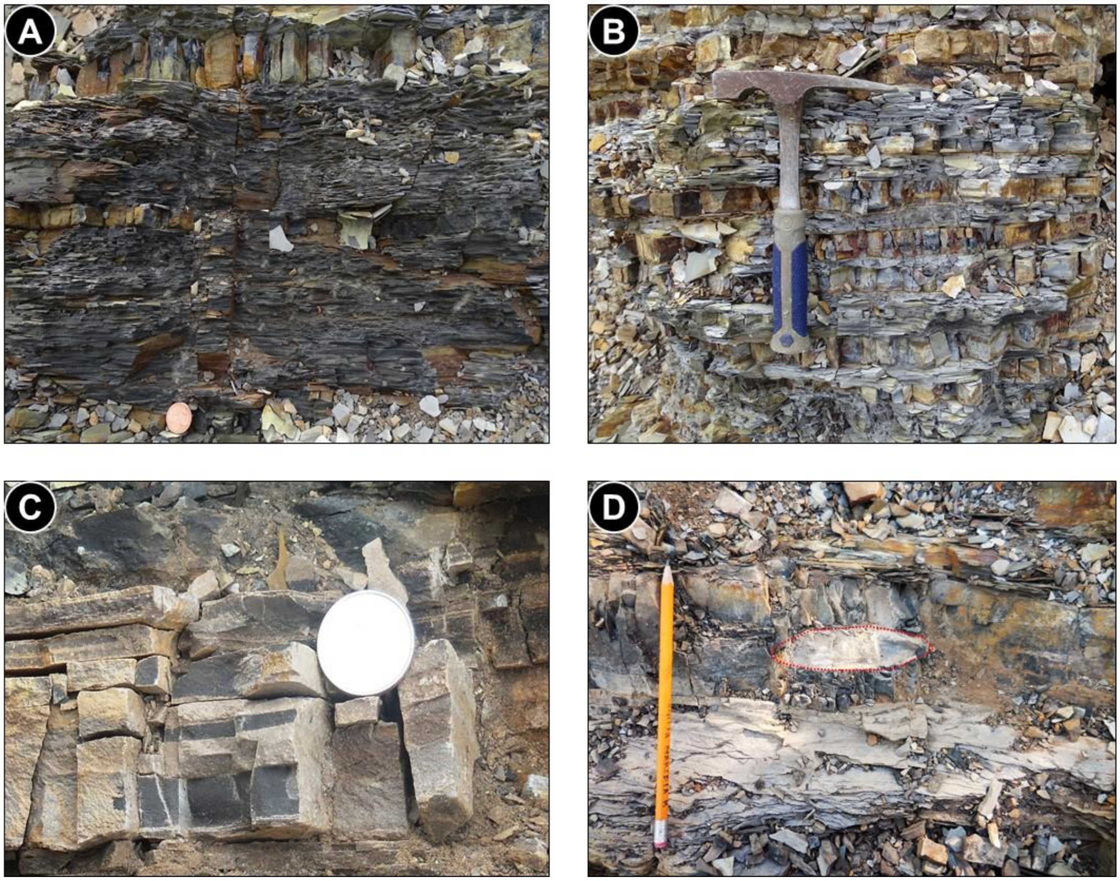

Figure 25. Remarkable outcrop features of *zone a:* (**A**) Lower portion of this zone (foot 7) showing soft to hard ratios are approximately 90: 10. (**B**) Upper portion of this zone showing soft to hard ratios of about 50:50. (**C**) Porous white beds (4 – 6 mm) contained in Chert beds. (**D**) First occurrence of a dolomitic nodule at foot 5.

Zone b: Increasing upward trend (27 – 48 ft.)

This zone is characterized by a continuous increasing of the gamma ray readings from 450 up to 800 cps (**Figure 24**). The soft to hard ratios slightly increase upward from 50:50 to 60:40 in average (**Figure 24**), and represent similar bed thicknesses of soft and hard beds (3 to 5 cm), resulting in the accommodation of a high number of beds per foot (**Figure 26**). Lithologically, this zone is made of intercalations between Chert and siliceous shales, however few dolomitic beds were found (**Figure 26**).

Scattered phosphate nodules were observed within this interval, they are elongated (5 to 10 cm in diameter) and usually hosted by Chert beds which are slightly deformed by the presence of the nodule (**Figure 26**).

The ‘white beds’ are observed in the lower half of this zone, restricted to Chert beds as in *zone a*.

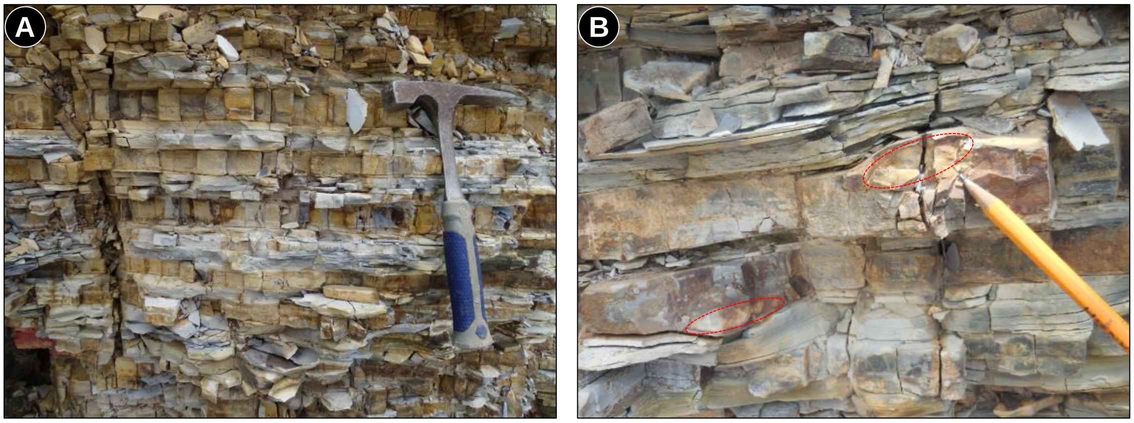

Figure 26. Remarkable outcrop features of zone b: (**A**) Similar bed thicknesses for shale and Chert beds (3 to 5 cm) resulting in soft to hard ratios of about 50:50. (**B**) Phosphate nodules slightly deforming the host Chert beds.

Zone c: Decreasing upward trend (48 – 61 ft.)

Similar to *zone a*, this zone is defined by a decreasing upward response in the gamma ray readings from 419 to 816 cps (lower values than *zone a*). The soft to hard ratios depict a decreasing upward trend, showing average ratios of 50:50 at the base of the interval and average ratios of 30:70 towards the top (**Figure 24**).

In contrary to *zone a*, thicknesses of hard beds in this interval are greater between 2 to 4 cm, whereas the soft beds range between 2 to 6 cm. Main lithofacies present on this interval are Cherts and siliceous shales; however, several dolomitic beds were described (**Figure 24** and **Figure 27**).

The presence of nodules is scarce in this interval; however some nodules were found towards the top of the zone around feet 57-61 (**Figure 27**).

A small-scale fold was found around foot 54, the orientation of the fold axis is 315°/55°; the structure is affecting about one foot of rocks, appearing slightly brecciated (**Figure 27**).

Opal veins were observed in some Chert beds in this zone (**Figure 27**), they consist of milky quartz that contrasts strongly with the dark colors of the black Cherts; some of the opal veins present inclusions of bitumen or dead oil (**Figure 27**).

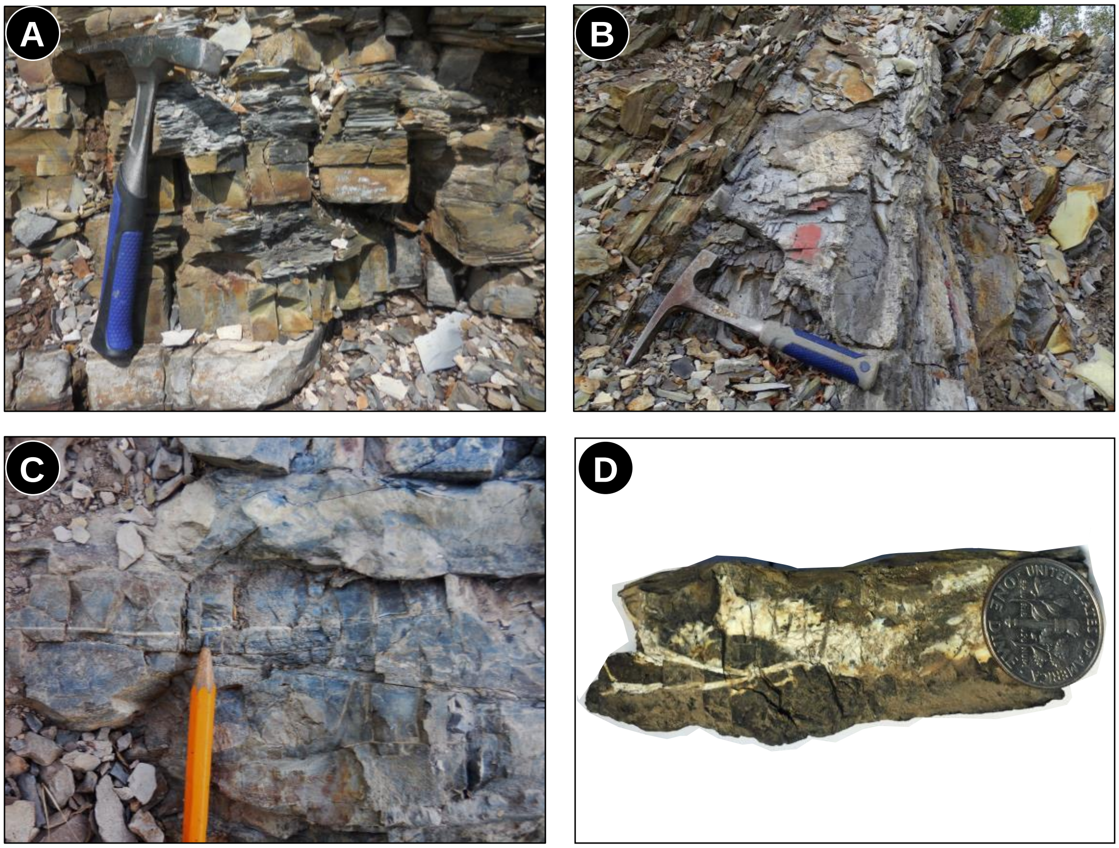

Figure 27. Remarkable outcrop features of *zone c:* (**A**) Relatively thicker shale and Chert beds (5-6 cm) in comparison to *zone a*. Notice the presence of a dolomitic bed at the base of the hammer. (**B**) Small scale fold located at 54 ft. showing a brecciated appearance of folded beds. (**C**) and (**D**) Black-Chert beds containing opal vein.

Zone d: Blocky Trend (61 – 72 ft.)

This is the most distinctive interval across the outcrop. It is named blocky trend because of the monotonous low gamma ray responses which vary from 285 to 331cps (**Figure 24**). This zone consists of intercalations of thick bedded Cherts (up to 13 cm) and relatively thin shale beds (1-4 cm), which are reflected by low soft to hard ratios of about 30:70 (**Figure 24**).

This zone contains the highest concentration of nodules in the entire section (**Figure 28**). Nodules are equally distributed within soft and hard lithologies (i.e. siliceous shales and Cherts), they are in oblate to spherical shapes, and size from 2 cm up to 4 cm in diameter (**Figure 28**). In general, beds here look highly indurated and compacted exhibiting characteristics of "pinch and swell" due to the differential compaction around nodules, so that bedding thicknesses are not easy to trace laterally even for short lateral distances as 1 foot (**Figure 28**).

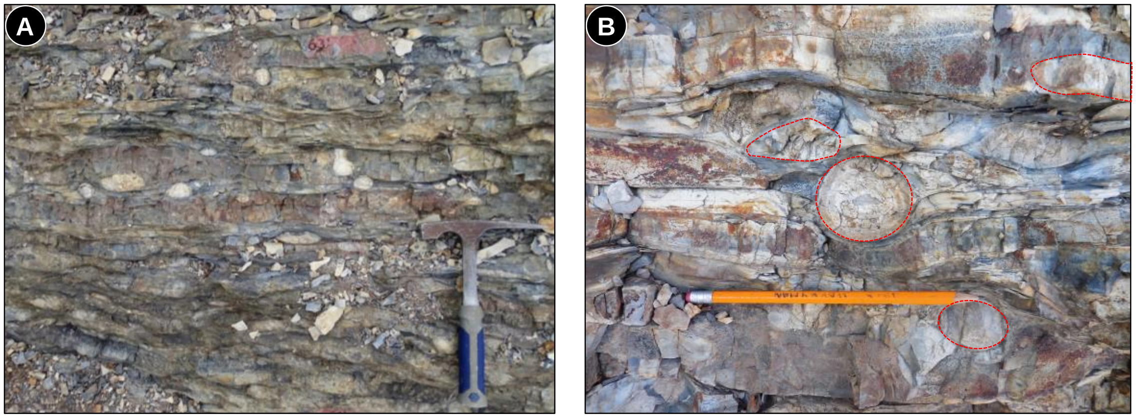

Figure 28. Remarkable outcrop features of *zone d:* (**A**) Notice the amalgamated aspect of nodular beds in this zone. (**B**) Varied sizes and shapes of phosphatic nodules which are equally distributed in shale and chert beds.

Zone e: Last High Peak (72 – 81 ft.)

This interval contains the uppermost occurrences of black Woodford shale rocks in the outcrop. Gamma ray values are low near the base of the interval (326 cps), then reaches the highest value of 985 cps towards the middle of the interval and finally decrease toward the top of the interval (268 cps) (**Figure 24**). Anomalously, the highest gamma ray reading (985 cps at 75 ft.) was measured from a dolomite bed (18 cm thick) which has a coarse crystalline appearance, and has a strong odor when hit with the hammer (**Figure 29**).

Zone e possesses the lowest hard to soft ratios (15:85) of the entire section, representing low thicknesses of shale beds (<4 cm avg.) versus high thicknesses of chert beds (up to 20 cm) (**Figure 29**). The presence of phosphate nodules is common in both, hard and soft lithologies, however the abundance of nodules is lower than the observed in the blocky pattern (*zone d*). There is also some degree of nodular bedding, however most of the beds can be traced by at least 3 feet laterally.

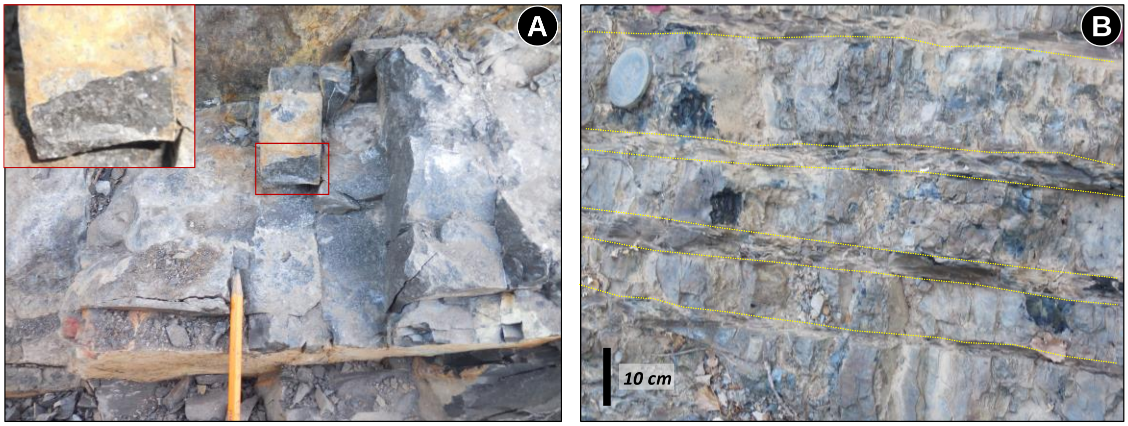

Figure 29. Remarkable outcrop features of *zone e*: (**A**) Thick dolomite bed (18 cm) at foot 75, notice the crystalline aspect. (**B**) Great thickness of chert beds (10 - 15 cm) compared to shale beds (~4 cm).

3.4.Correlation of I-35 outcrop with Nearby Outcrops and Wells

Commonly, in organic-rich shale successions gamma-ray logs provide the most useful log responses to correlate from outcrop to subsurface. In this work, the gamma-ray log of the 81 feet of the Woodford Shale at the I-35 outcrop was correlated to nearby outcrops and wells located in the Arbuckle-Ardmore area (**Figure 30**).

In the subsurface, the Woodford Shale is characterized by very high gamma-ray readings, usually >100 API. Since the outcrop-gamma ray is presented in counts per seconds (CPS) and the gamma-ray log in API units, the correlation is primarily based on gamma-ray trends, rather than magnitudes.

The maximum flooding surface (MFS) interpreted by the sequence stratigraphic model in Galvis (2017), was used as the regional datum for correlation (**Figure 31**). Generally, a good correlation of gamma-ray patterns is observed; the five stacking patterns (*zone a* to *zone e*) described at the I-35 outcrop can be traced along nearby outcrops and wells (~15 miles). From the MFS and upwards, zones interpreted were: a decreasing gamma-ray upward pattern (*zone a*) at the base of the I-35 outcrop Gamma-ray; this zone is followed upward by an increasing gamma-ray upward (*zone b*), then another decreasing upward pattern (*zone c*), the blocky pattern (*zone d*) and finally the *last high peak* (*zone e*).

According to the stratigraphic subdivision into informal Woodford members initially defined by Hester et al., (1990), and adopted by Galvis (2017) in Southern Oklahoma, the I-35 outcrop comprises the uppermost 30 feet of the middle Woodford and 50 feet of the upper Woodford member (**Figure 31**).

Overall, the correlation of detailed-characterized Woodford Shale outcrops with subsurface wells provides insights of the rock characteristics which can be projected into the subsurface, and helps to identify potential zones that may be the most optimum for drilling and completion of unconventional shale resources.

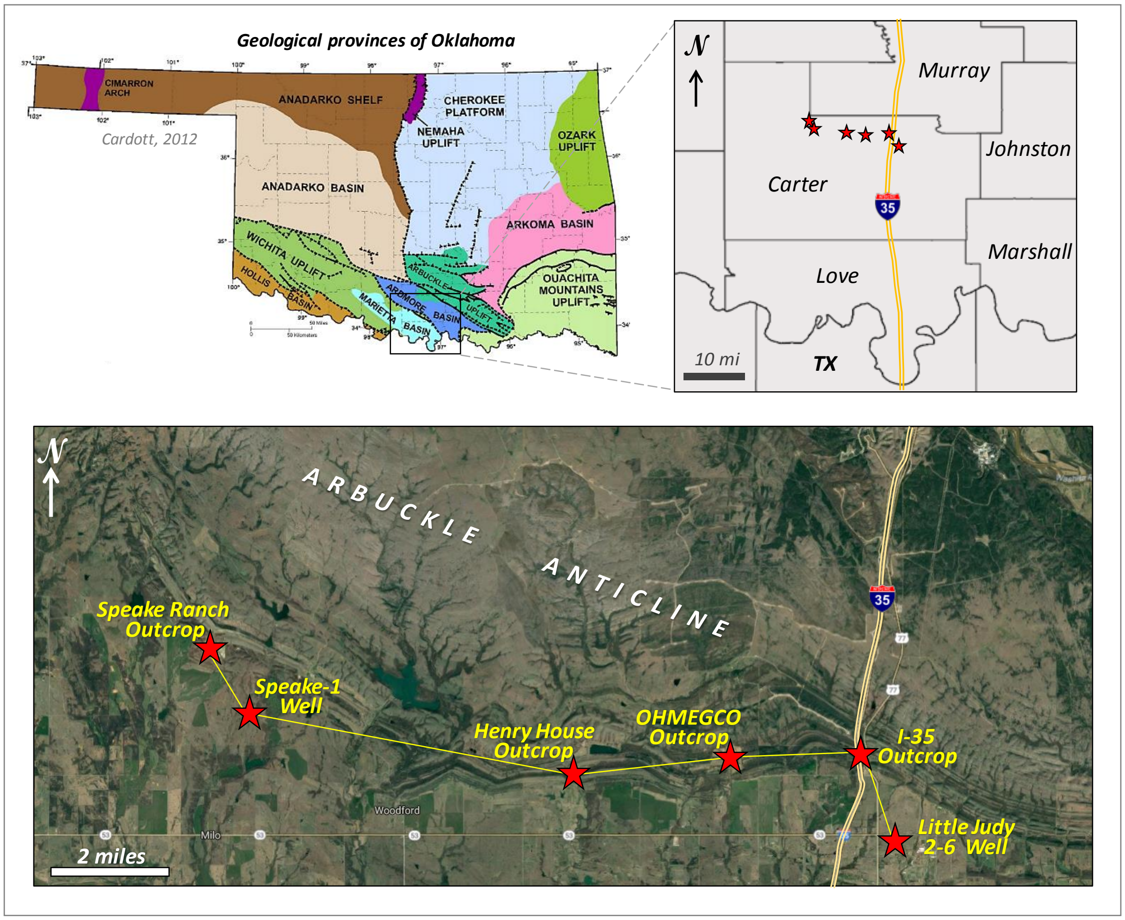

Figure 30. Location of outcrops and wells contained in the gamma-ray correlation (yellow line).

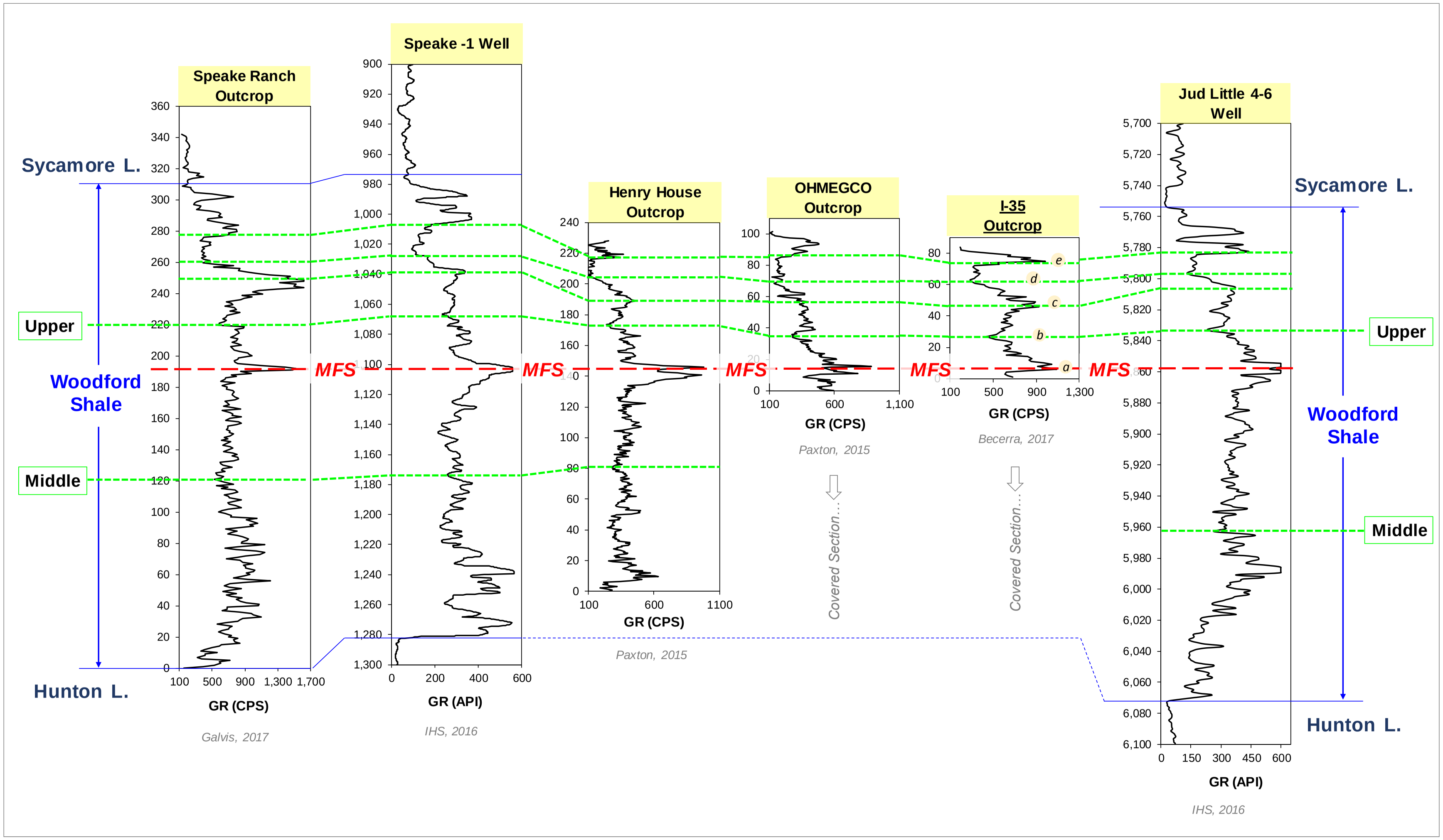

Figure 31. Gamma-ray correlation of the I-35 outcrop with nearby outcrops and wells in the Arbuckle area. The regional maximum flooding surface MFS (red line) is based on Galvis (2017). Location of outcrops and wells in Figure 30.

4. LITHOFACIES CLASSIFICATION AND DESCRIPTION

The classification of lithofacies was mostly based on field observations of hand-specimens, and included the description of weathering responses, texture (grain size), hydrochloric acid (HCL) reaction, color, and luster; this classification was later refined and supported via petrographic descriptions, mineral composition from XRD, elemental composition from XRF, organic richness (TOC) and hardness (LH).

Primary criterion in the lithofacies classification is the mean grain size. As mudrocks are sedimentary rocks in which greater than 50 percent of the constituent particles are smaller than 62 microns (Ingram, 1953; Lundegard & Samuels, 1980), all rocks described in the I-35 outcrop fall inside this mudrock category. Secondly, the weathering response was a key criterion to distinguish the two most distinctive Woodford Shale rock types, named 'Soft' and 'Hard' lithologies (**Figure 32**).

For this outcrop-based study, it is worth mentioning that the use of the soft-hard terminology was more appropriate than the brittle-ductile terminology as the former is purely descriptive (weathering response) and the latter involves a rock mechanics interpretation (of failure mode). Indeed, just at the end of this thesis and via rock mechanic experiments, we certainly proved that 'soft' beds of the Woodford shale fail in a ductile manner and 'hard' beds fail in a brittle manner.

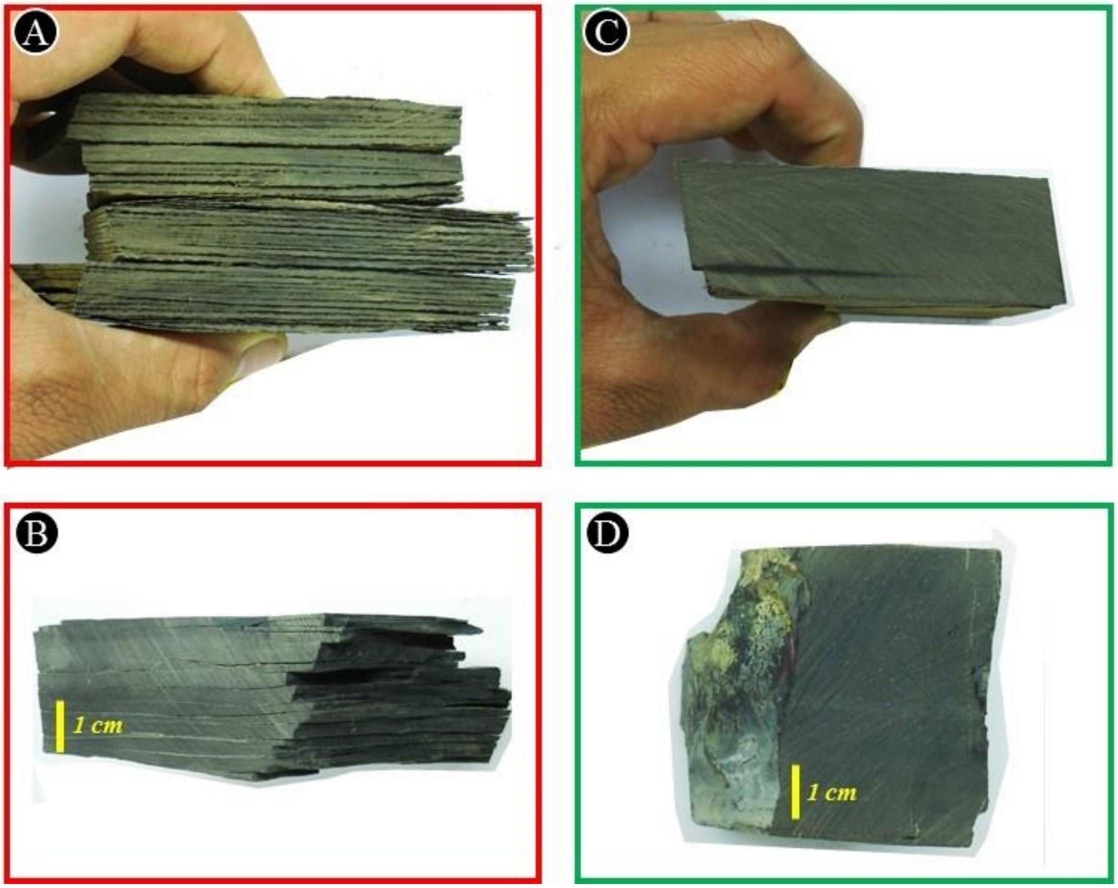

Figure 32. Hand specimens of the two most distinctive lithologies present in the Woodford Shale: (**A**) and (**B**) Soft beds display lamination enhanced by weathering. (**C**) and (**D**) Hard beds are massive and much more resistant to weathering.

'Soft' lithologies display a fissile nature represented by flaky-type broken pieces and parallel planes of weakness. Even though fissility of mudrocks is the result of weathering and might not be present in subsurface rocks, the recording of this descriptive attribute for outcrop samples provides insights of clay contents and microfabric (Ingram ,1953; Potter et al., 1980; Potter et al., 2005); this will be demonstrated afterwards with mineralogy results from XRD, in which different degrees of fissility correspond to different clay contents.

Then, by applying HCl on fresh surfaces, two lithofacies were defined from the soft category: one calcareous and the other non-calcareous, named Siliceous-dolomitic Shales and Siliceous Shales respectively (**Figure 33**). In this work, the usage of the term shale is restricted to a fine-grained sedimentary rock displaying fissility and/or lamination (Tourtelot, 1960; Lundegar & Samuels, 1980). Physically, Siliceous Shales and Siliceous-Dolomitic Shales do not show sharp differences, and in fact, a very limited amount of Siliceous-Dolomitic Shale beds was found in the section as shown by the proportion of lithofacies in **Figure 34**.

'Hard' lithologies on the other hand, are macroscopically massive (non-fissile) and much harder to break with the hammer, suggesting lesser amounts of clay minerals and more quartz and/or carbonates. Based on the effervescence to HCl on fresh surfaces, two hard lithofacies were defined: one hard calcareous lithofacies dominated by dolomite (based on slower reaction to dilute HCl), named Dolomitic Mudstone lithofacies (**Figure 33**). The second is a 'hard' non-calcareous lithofacies named Chert based on its *sensus strictus* definition (Van Hise, 1904; Bramlette, 1946; Jones and Murchey, 1986; Hesse, 1988). In the outcrop, Chert beds are dark-grey to black, massive, blocky, and exhibit typical conchoidal fracture. As for the relative abundance of hard lithofacies in the section, chert lithofacies are evidently more common than dolomitic mudstone lithofacies (**Figure 34**).

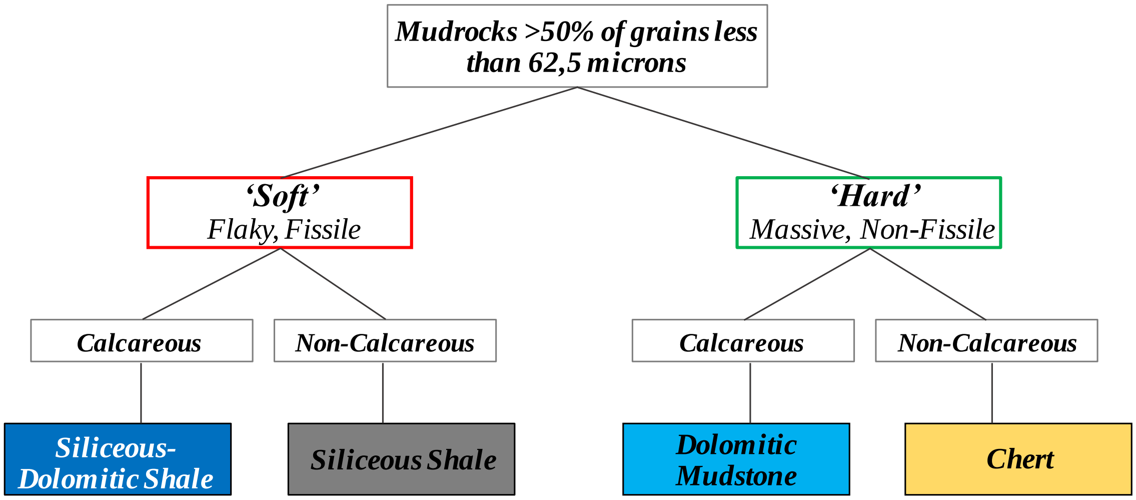

Figure 33. Field-based lithofacies classification scheme with their main criteria used to identify lithofacies.

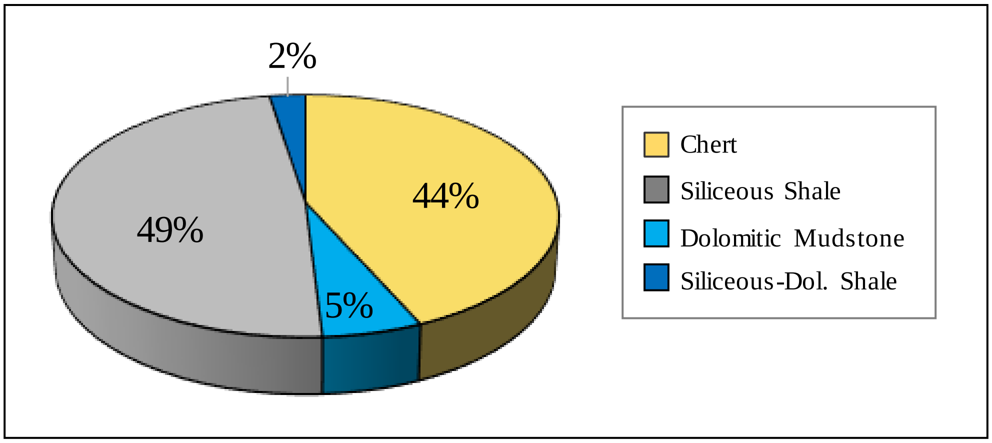

Figure 34. Pie chart showing the abundance of each lithofacies throughout the section. This diagram is based on lithofacies of 157 samples that covers the upper most 81 feet of the Woodford section of this study.

Here, it is worth mentioning that the lithofacies terminology of this study uses the same classification criteria in Galvis (2017), who described an entire Woodford outcrop section (i.e. lower, middle and upper informal members) in southern Oklahoma. Thus, for consistency in future correlations lithofacies reported in this work are completely correlatable to his identified lithofacies.

5. MINERALOGICAL COMPOSITION

5.1.Bulk-Rock composition

In total, 46 bulk rock analyses were carried out in order to determine the mineralogical composition of the Woodford Shale present at I-35 outcrop. To better understand mineralogical contrasts between hard and soft beds, out of the total 46 analyzed samples, 22 correspond to soft lithologies and 24 were hard lithologies (**Table 2**).

The interpretation of X-ray diffractograms was achieved based on the premise that each mineral produces a unique set of reflections or peaks located at a set of specific angles (2Θ) with a characteristic *d*-spacing (**Figure 35**) (Moore & Reynolds, 1997). Thus, the mineral identification consisted of comparing peaks from the experimentally obtained patterns with standard reference patterns (**Figure 35**).

Visual analysis of the interpreted diffraction patterns (**Figure 35**) revealed very high intensities of quartz at 3.34 Å. Feldspar contents appear to be very low based on the small peaks around 3.25 Å. Illite was identified by reflections at 10.06 Å, 4.49 Å and 4.27 Å. Kaolinite has very subtle peaks at 7.20 Å. Jarosite was interpreted at 5.12Å and 3.09 Å. Pyrite was interpreted by small peaks at 2.71 Å. Dolomite is almost restricted to the dolomitic mudstone lithofacies; it was identified as large peaks at 2.89 Å, 2.19Å and 1.78 Å. Then, by using the software package JADE, quantitative bulk-rock mineralogy was estimated for each sample, and their results are reported in **Table 2**.

Main minerals occurring in most of the samples were quartz and illite/mica, whereas minerals occurring in minor amounts (<10 wt.%) included feldspars, kaolinite, pyrite, jarosite and gypsum; the last two are most likely related to modern weathering and filling fractures respectively. No detectable smectitic phases were identified in the samples of this study.

Figure 36 presents a summary of the average mineral composition for each lithofacies (i.e. siliceous shale, Chert and Dolomitic Mudstone), from which a quartz cut-off of approximately 85% was a useful boundary to distinguish hard (quartz>85%) and soft rocks (quartz<85%). This was also confirmed when XRD results were plotted on a ternary diagram (**Figure 37**).

The stratigraphic distribution of the mineral composition of the 46 samples is graphically presented in **Figure 38B**, where it can be noticed, that almost regardless of the stratigraphic position, siliceous shale lithofacies (soft samples) show significantly higher clay contents (10 to 30 wt.%) than Chert lithofacies. Either in the lower or upper part of the section Chert beds maintain elevated quartz contents (85 to 98 wt.%) along with very low clay contents (avg. clay 4 wt.%) (**Figure 38C**); additionally, looking at the results of the hard samples (**Figure 38C**), there are 6 carbonate rich samples with dolomite contents between 80 to 90 wt.% where the summation of quartz and clay content is not higher than 20 wt.%.

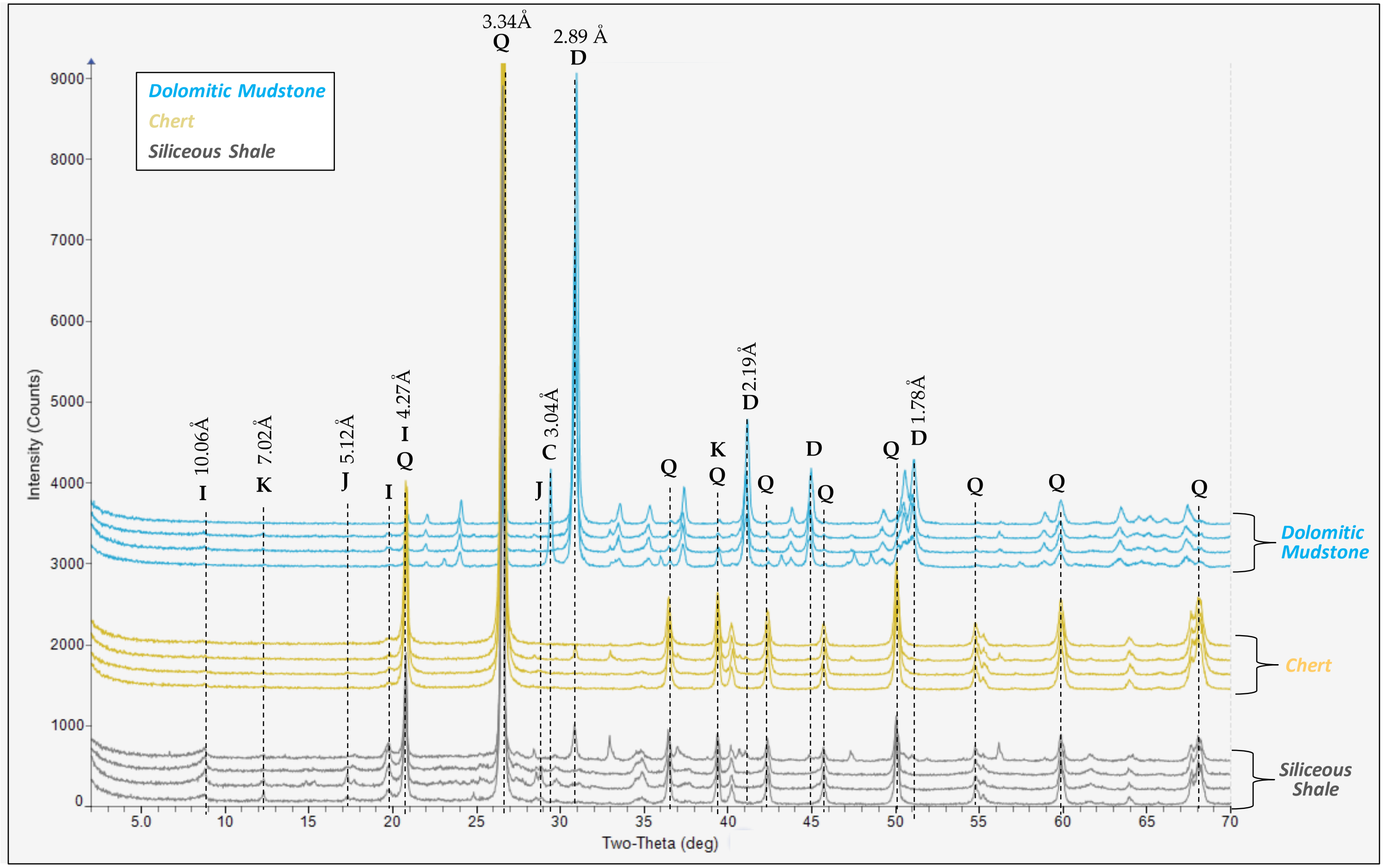

Figure 35. Stacked XRD patterns for some selected samples displaying the bulk-rock mineralogy of Siliceous Shales, Cherts and Dolomitic Mudstones. Dashed vertical lines indicate the peak position (2Θ) and their mineral interpretation based on d-spacing values in Å. The most dominant signal is quartz (Q). Next abundant mineral in Dolomitic mudstone lithofacies is Dolomite (D). The principal clay minerals present are illite (I) and kaolinite (K). Traces of jarosite (J) are also identified.

Sample Number	Stratig. Foot	Weathering Response	Lithofacies	Quartz (wt%)	K-spar (wt%)	Calcite (wt%)	Dolomite (wt%)	Illite (wt%)	Kaolinite (wt%)	Pyrite (wt%)	Gypsum (wt%)	Jarosite (wt%)
2	1.5	Soft	Siliceous Shale	74				21	1			4
6*	3.5	Soft	Siliceous Shale	55				40	2	3		
9	5.5	Soft	Siliceous Shale	59	5			30	6			
16	9.5	Soft	Siliceous Shale	72	5			22	2			
17	10.5	Soft	Siliceous Shale	69				31				
27*	15.5	Soft	Siliceous Shale	54	7			39				
33	18.5	Soft	Siliceous Shale	68	6			25				1
38	21.5	Soft	Siliceous Shale	82	6			13				
46	25.5	Soft	Siliceous Shale	57			7	26			4	
50	27.5	Soft	Siliceous Shale	58	7			33				2
60	32.5	Soft	Siliceous Shale	72				25	1		1	
70	37.5	Soft	Siliceous Shale	70				28				2
76	40.5	Soft	Siliceous Shale	89				10	1			
86	45.5	Soft	Siliceous Shale	76				21	1		3	
96	50.5	Soft	Siliceous Shale	62				36	2			
106	55.5	Soft	Siliceous Shale	60	5			31	1			3
112	58.5	Soft	Siliceous Shale	64	5			30	1			
126	65.5	Soft	Siliceous Shale	81				17	2			
130	67.5	Soft	Siliceous Shale	64				34		2		
144	74.5	Soft	Siliceous Shale	71				26			3	
152	78.5	Soft	Siliceous Shale	78				23				
156	80.5	Soft	Siliceous Shale	72				28				
1	1.0	Hard	Chert	97				2	1			
7	4.0	Hard	Chert	95			2	2			1	
15	9.0	Hard	Chert	87				12	1		1	
20	12.0	Hard	Chert	94				6				
24	14.0	Hard	Chert	98				3				
28	16.0	Hard	Chert	97				3				
35	20.0	Hard	Chert	96				4				
43	24.0	Hard	Chert	96				3			1	
55	30.0	Hard	Chert	95				5				
59	32.0	Hard	Chert	97				3			1	
93	49.0	Hard	Chert	95				5				
109	57.0	Hard	Chert	98			2					
115	60.0	Hard	Chert	97				3				
121	63.0	Hard	Chert	96				4				
127	66.0	Hard	Chert	91				9				
135	70.0	Hard	Chert	99				1				
141	73.0	Hard	Chert	94				6			1	
153	79.0	Hard	Chert	96				4			1	
69	37.0	Hard	Dolomitic Mudstone	5			91	3				
81	43.0	Hard	Dolomitic Mudstone	1			98					
101	53.0	Hard	Dolomitic Mudstone	5			94				1	
105	55.0	Hard	Dolomitic Mudstone	4			94	1			1	
117	61.0	Hard	Dolomitic Mudstone	6			90	4				
145	75.0	Hard	Dolomitic Mudstone	6		15	78				1	

Table 2. Results of quantitative bulk-mineralogy from 46 Woodford samples grouped by weathering response (soft and hard) and by lithofacies. Asterisks (*) next to sample number denotes clay-fraction analysis.

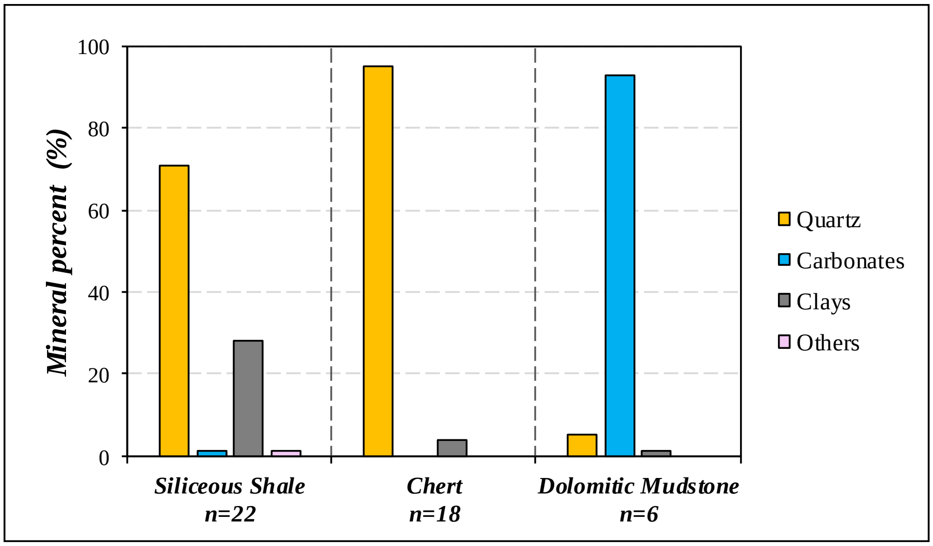

Figure 36. Average mineral composition of quartz, clays and carbonates by lithofacies. Siliceous shales of the Woodford are very quartz-rich, and usually do not exceed clay contents of 50%. *n* indicates the number of samples analyzed per lithofacies.

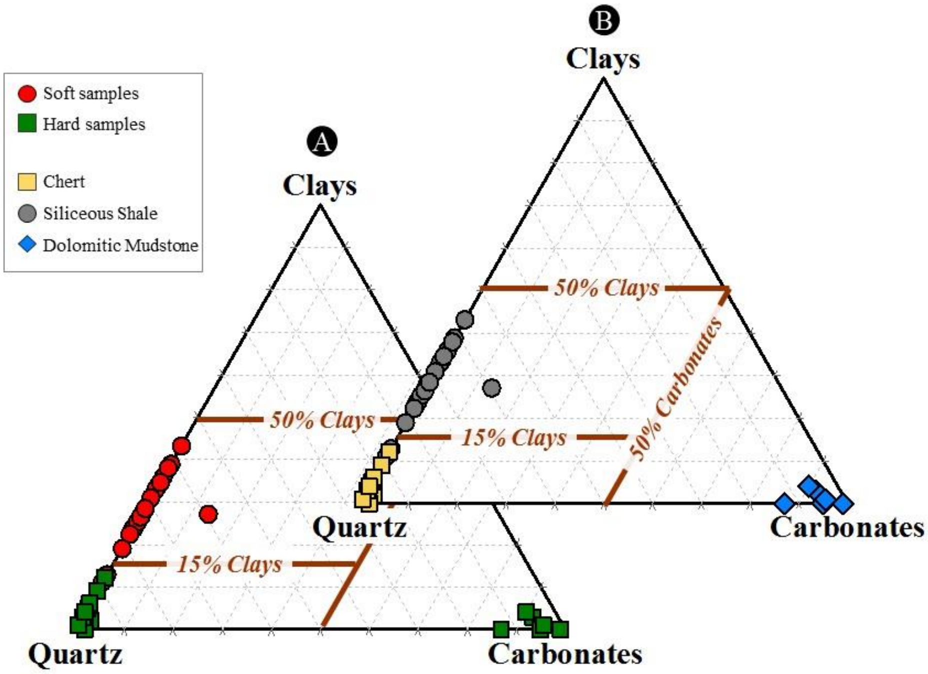

Figure 37. Ternary plots of mineral composition differentiated by (A) hard/soft weathering response and by (B) lithofacies. Three groups can be easily distinguished: a quartz dominated (Cherts), quartz + clays (Siliceous Shales) and carbonate dominated (Dolomitic Mudstones). Graphically these plots confirm the distinctive mineralogy of soft and hard beds.

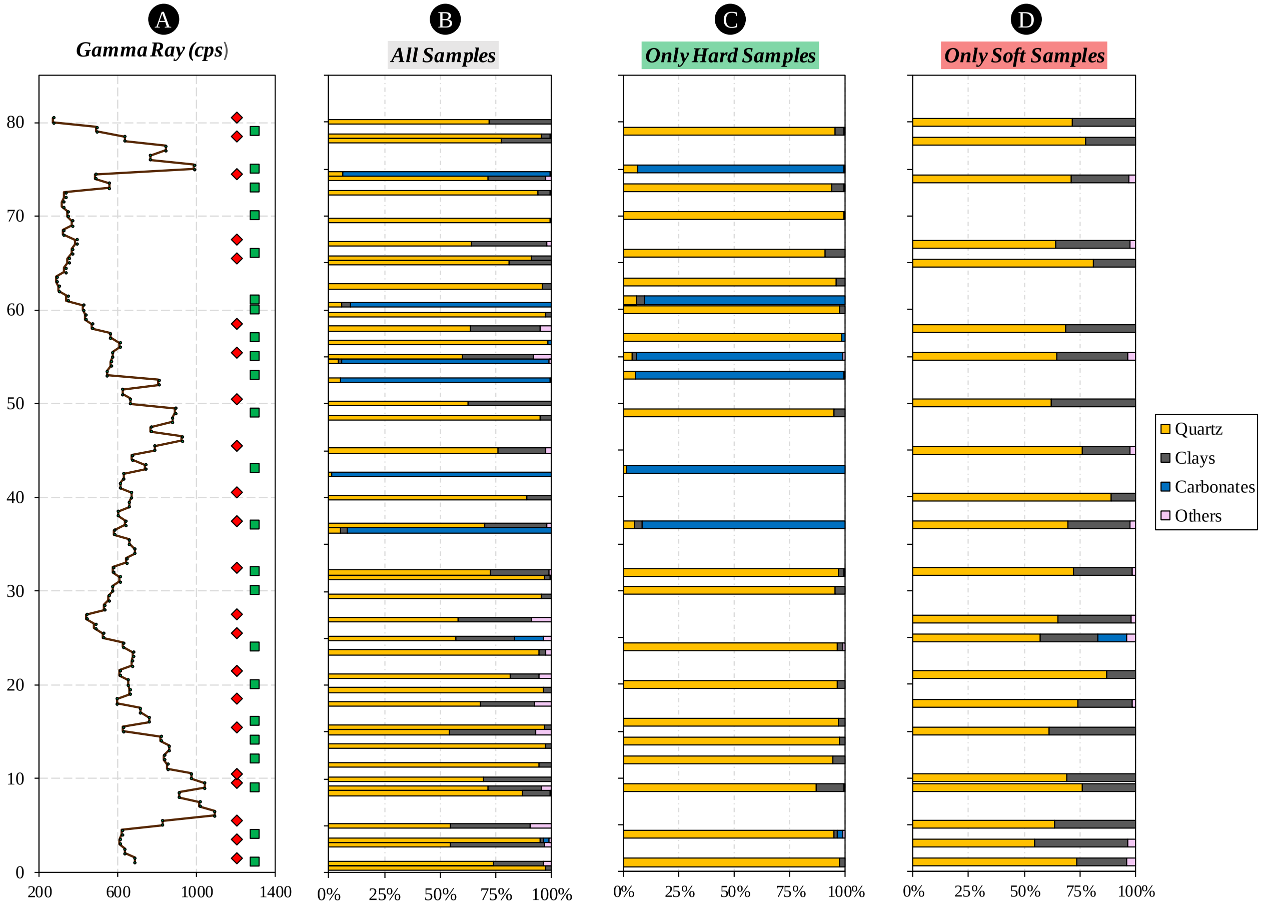

Figure 38. A) Gamma-ray profile of the measured section showing the vertical distribution of 46 XRD samples separated by hard (green squares) and soft (red diamonds) lithologies. B) Stacked percentages of mineral composition of all samples. C) and D) present the stacked percentages of mineral composition separated by hard and soft respectively. Note the distinctive clay/quartz contents for hard and soft lithologies and the low percentages of (clay+quartz) for the carbonate rich beds. Minerals are by weight percent (wt.%).

5.2.Clay-Fraction Mineral Composition

The purpose of conducting clay-fraction analyses was to identify clay types rather than quantify the amount of them in the rock. Based on their high bulk clay contents (>40wt.%), only two samples were selected for clay-fraction analysis.

X-ray diffraction patterns from the clay-sized fraction for both samples revealed quartz as the most dominant clay-sized mineral, identified at 4.26Å and 3.34Å (**Figure 39**). Following in declining order of abundance, illite and kaolinite occur as the main phyllosilicate minerals. Illite was clearly identified by its 10Å sharp peak being almost unaffected after glycolation and heat treatments (**Figure 39**). Kaolinite was recognized from its 7.23Å peak in the air-dried and glycolated patterns (**Figure 39**), and then confirmed by its disappearance in the heat-treatment pattern (**Figure 39**). There were no indicators of smectite or illite/smectite mixed layers in the samples.

Jarosite was detected in the air-dried and glycolated patterns by a sharp peak at 5.12Å and a doubled peak at 3.12 and 3.09Å (**Figure 39**), and confirmed by disappearing in the heated pattern (**Figure 39**). Though jarosite was detected in both bulk and clay-fraction analyses, this study considers this mineral as a product of modern weathering; the presence of jarosite within the Woodford Shale was previously reported by Kirkland et al., (1992) who associated this mineral to the weathering of pyrite.

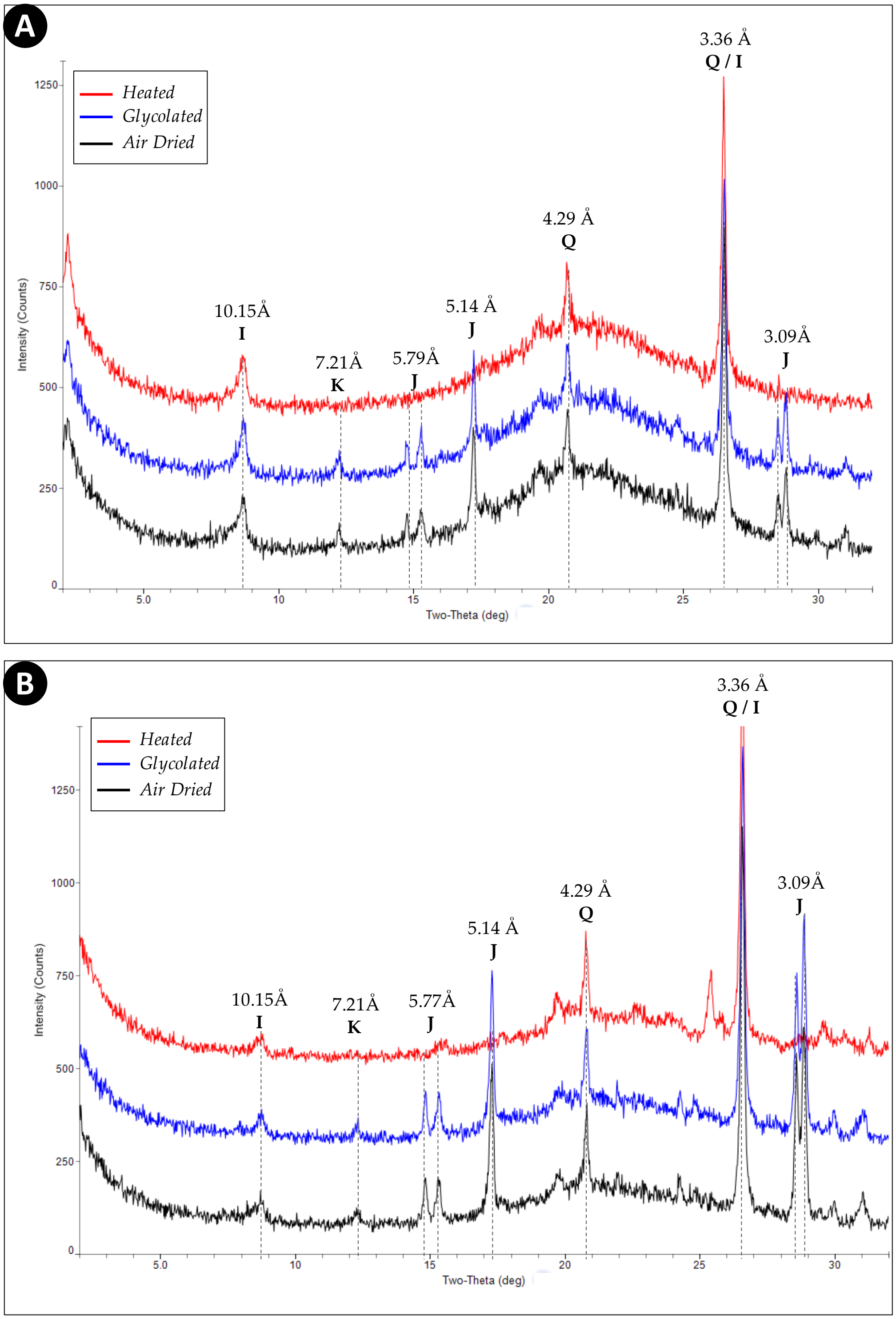

Figure 39. XRD patterns for two clay-sized analysis after treatments: Air-dried, Ethylene Glycol and Heated 550°. (**A**) Sample 6 in Table 2. (**B**) Sample 27 in Table 2. Dashed vertical lines mark the peak position (2Θ) and their mineral interpretation based on standard d-spacing values. Identified minerals in the clay fraction include quartz (Q), Illite (I), kaolinite (K) and jarosite (J). .

6. PETROGRAPHIC DESCRIPTION

Thin section petrography and scanning electron microscopy on fresh broken surfaces were conducted to characterize microfabric, mineral assemblages, and fossil-related features of the different lithofacies described in this Woodford outcrop.

6.1.Cherts

As observed in hand specimens, lamination in Chert beds is almost absent to very subtle (**Figure 40A** and **36B**). The microfabric of Cherts is largely made of microcrystalline quartz groundmasses and with little evidence of clay flakes (less than 10wt.%) (**Figure 40E** and **36F**). Dark brown organic material is common, and occurs as parallel strings dispersed within the matrix (**Figure 40C** and **36D**).

Numerous well-preserved radiolarians are observed within Cherts, which sometimes can be seen by naked-eye (**Figure 40A**). The presence of *Tasmanites* is also common but in much lower proportions; most *Tasmanites* observed in Cherts retained their original spherical shape, and are usually filled by quartz, dolomite and/or pyrite (**Figure 41**). Radiolarians can be differentiated from *Tasmanites* cyst because *Tasmanites* usually preserve the organic wall (**Figure 42A**).

The main accessory mineral is pyrite, which occurs as framboid aggregates embedded in the matrix. No visible evidence of detrital quartz is within Chert beds. Vertical to sub-vertical microfractures are common, these are filled with quartz, bitumen and/or calcite (**Figure 40C**).

Additionally, the presence of ‘white beds’ in some Chert beds was described in *zones a and b* of the section (**Figure 24**). In hand-size samples as in thin sections white beds look porous; they are composed by radiolarian tests embedded in a matrix made up authigenic/biogenic quartz (**Figure 43**); XRD analysis of white beds yielded 100% quartz.

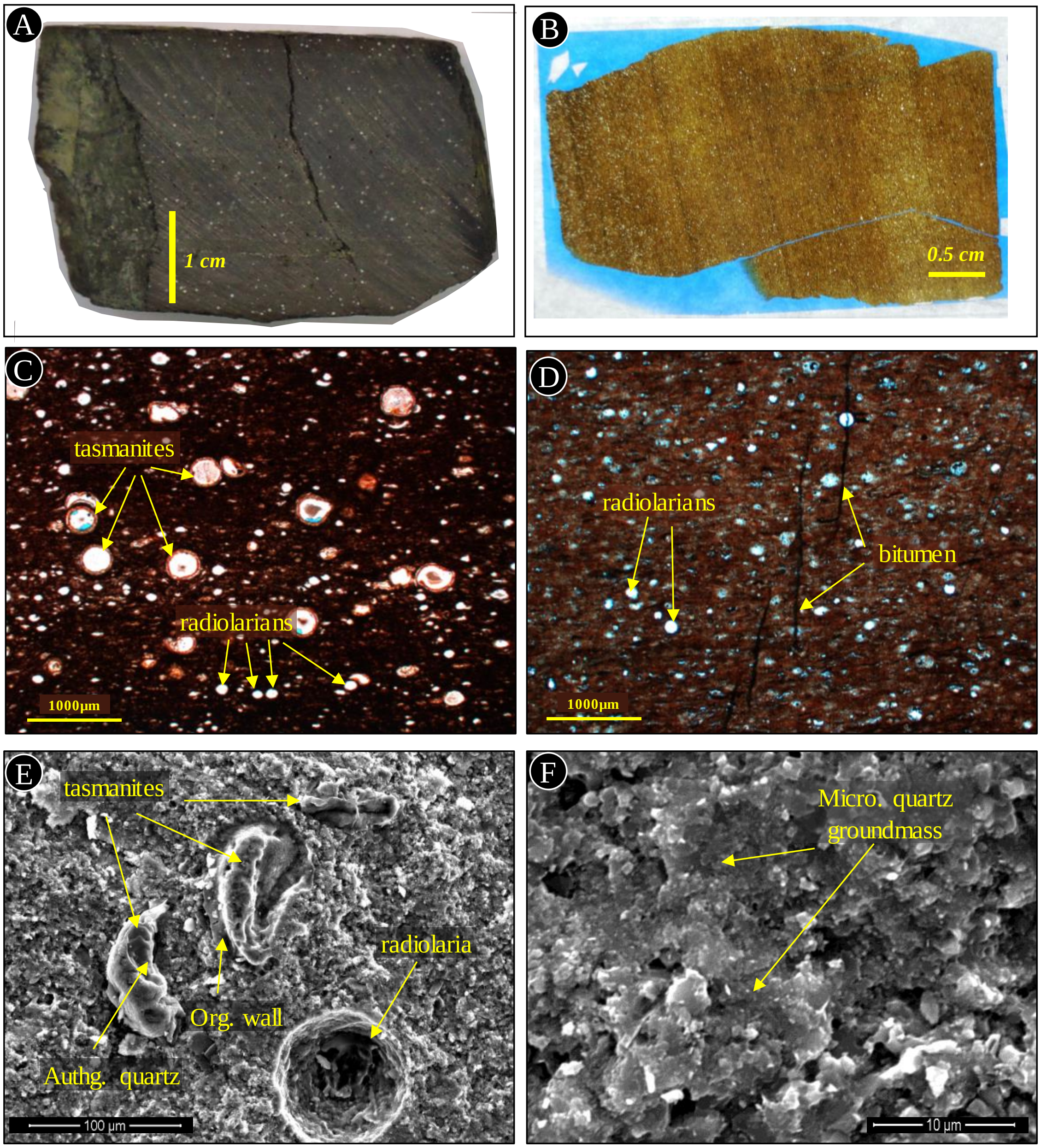

Figure 40. Petrographic characteristics of typical Chert lithofacies. (**A**) Freshly-cut surface image where visible white dots correspond to silicified radiolarian and/or *Tasmanites* tests. (**B**) Thin section photograph. (**C**) Photomicrograph showing well-preserved radiolarians and *Tasmanites* replaced by quartz; photo taken in plane-polarized light. (**D**) Photomicrograph showing vertical to sub-vertical microfractures filled with bitumen; photo taken in plane-polarized light. (**E**) SEM image showing *Tasmanites* and radiolarian tests filled by authigenic quartz. (**F**) High magnification SEM image evidencing a tight aspect of chert matrix. SEM images taken on fresh broken surfaces. Average composition for chert beds is 95% quartz and 5% clay; TOC is 3 wt%.

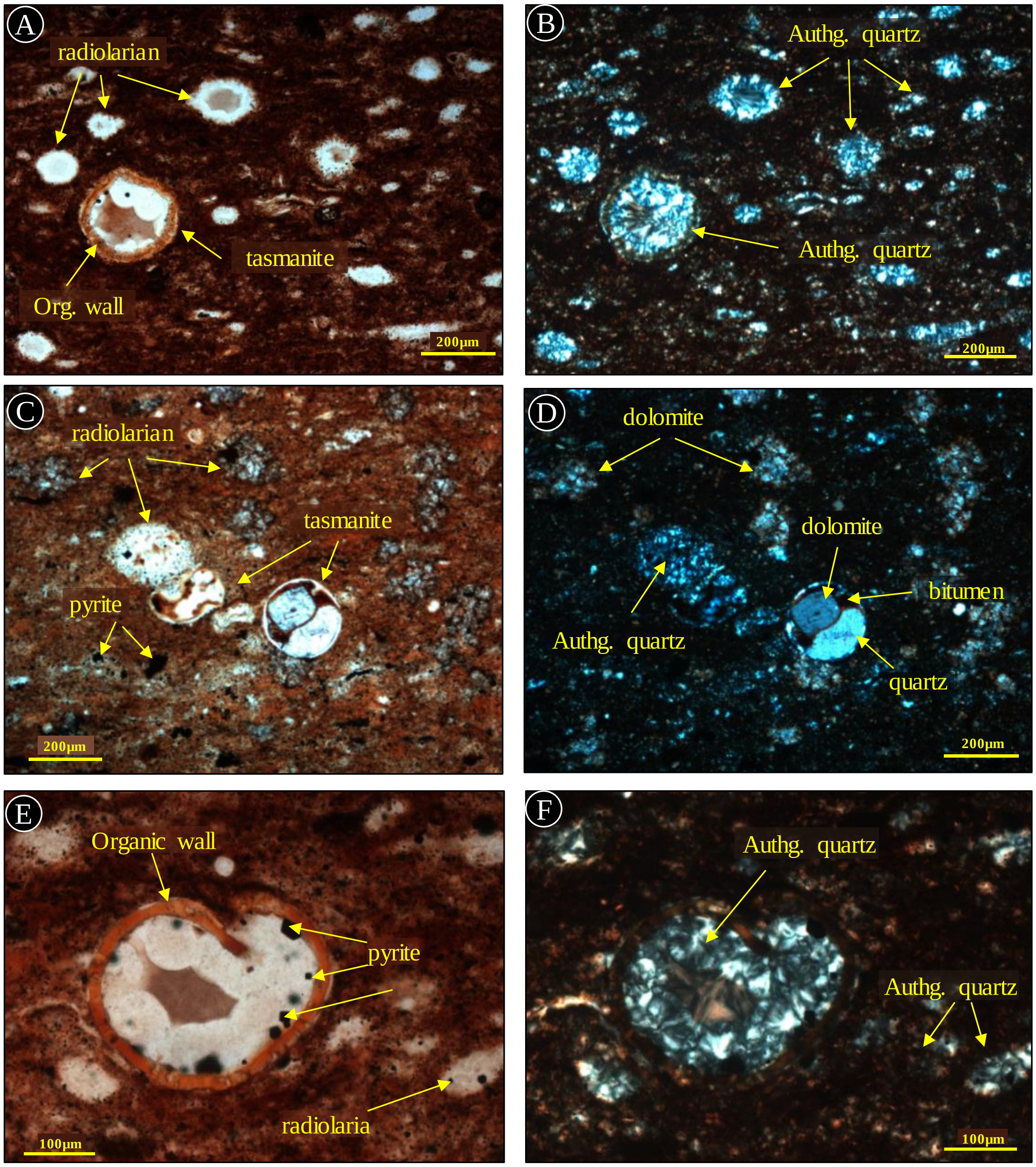

Figure 41. Petrographic characteristics of radiolarians and *Tasmanites* present in Chert lithofacies. (**A**), (**C**) and (**E**) are thin section photomicrographs taken in plane-polarized light showing quartz, dolomite, pyrite and organic material filling radiolarians and *Tasmanites*. (**B**), (**D**) and (**F**) are photomicrographs taken in cross-polarized light, evidencing chalcedonic quartz as the main material infilling radiolaria and *Tasmanites*.

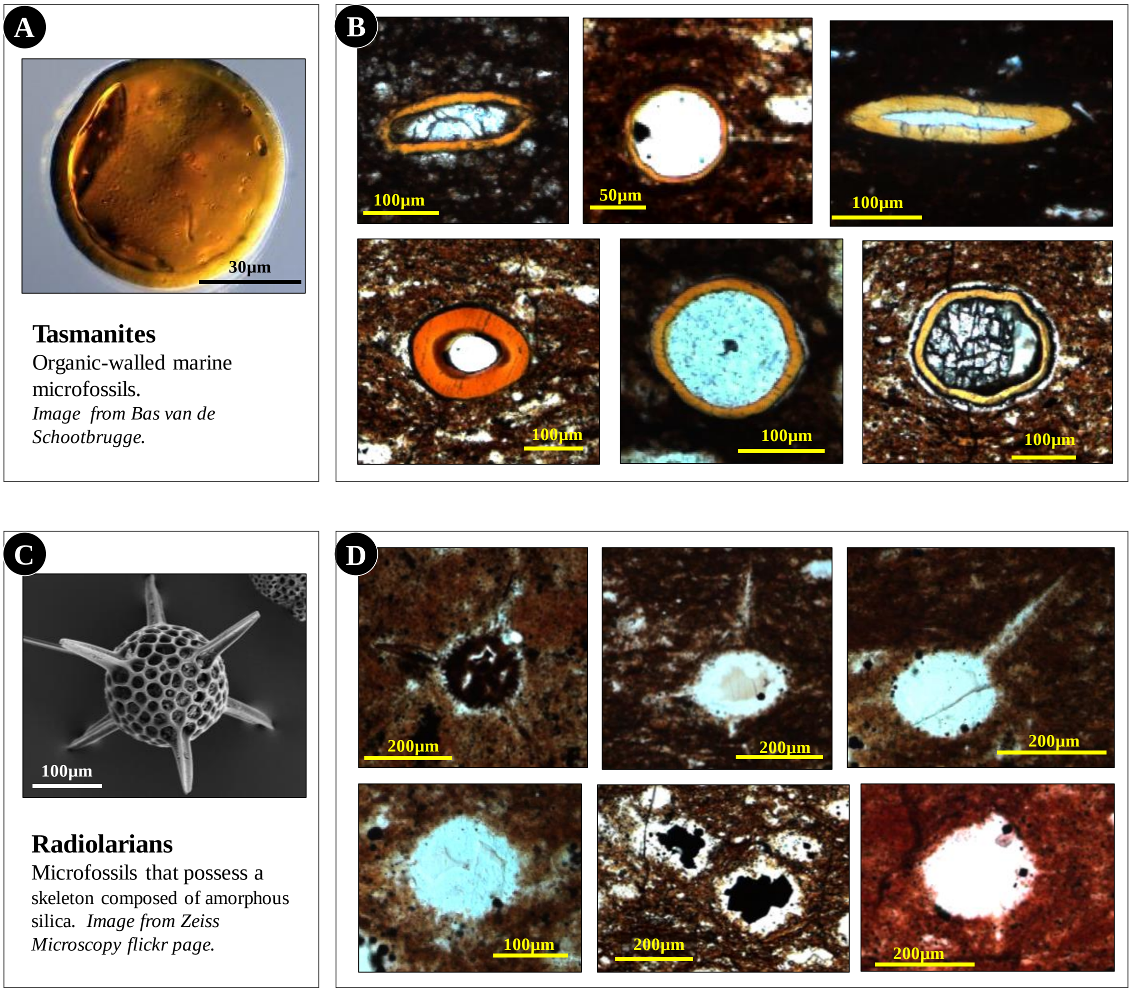

Tasmanites
Organic-walled marine microfossils.
Image from Bas van de Schootbrugge.

Radiolarians
Microfossils that possess a skeleton composed of amorphous silica. *Image from Zeiss Microscopy flickr page.*

Figure 42. (**A**) Isolated *Tasmanite* used for reference (from literature). (**B**) Photomicrographs of typical *Tasmanites* present in the Woodford Shale evidencing the organic walls as a key feature to identify them in petrographic analysis. (**C**) Isolated radiolarian used for reference (from literature). (**D**) Photomicrographs of typical radiolarian present in the Woodford Shale showing the lack of organic walls (diffusive borders) and presence of spines as key features to identify them in petrographic analysis. All thin section photomicrographs were taken in plane-polarized light.

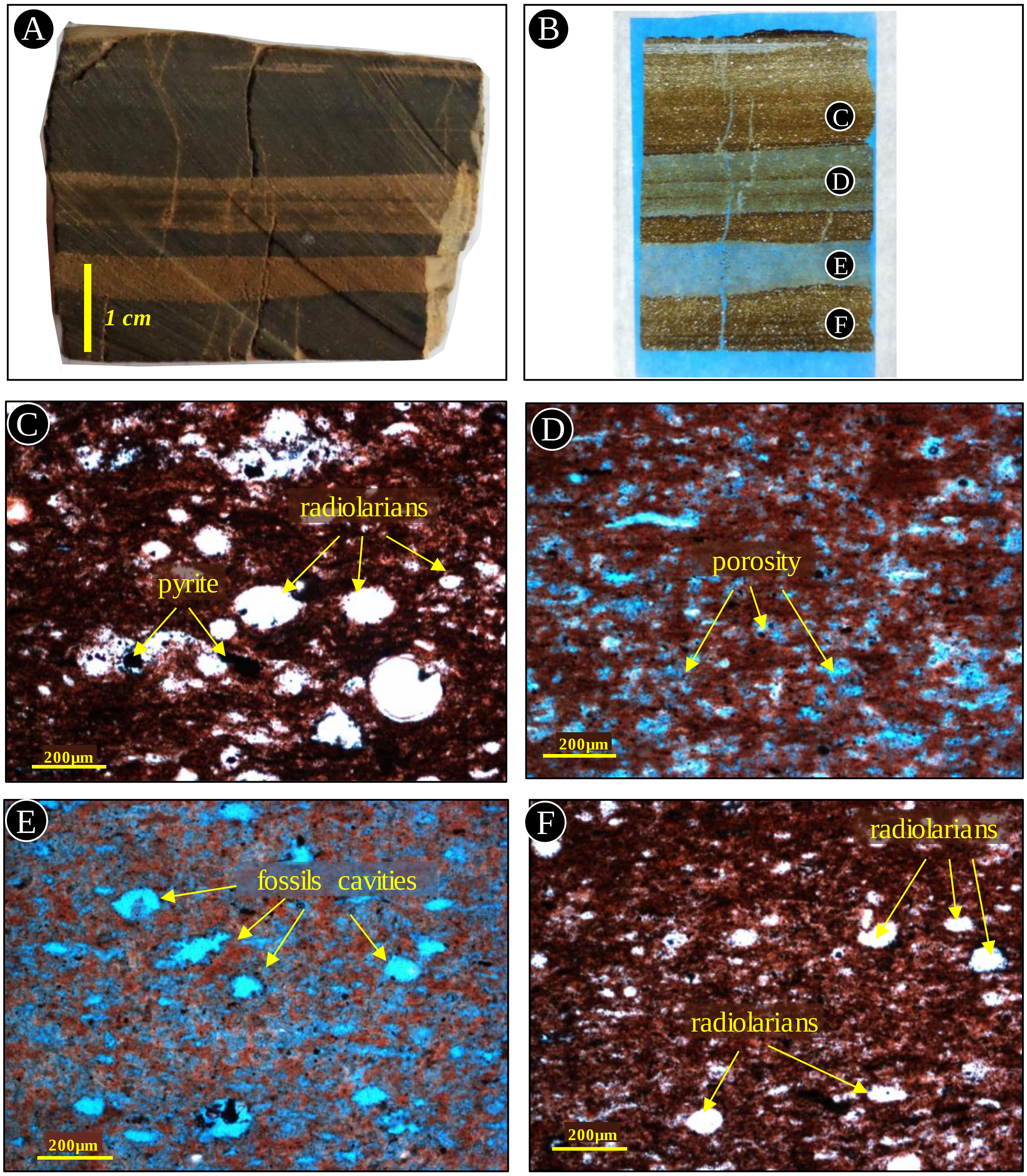

Figure 43. Petrographic characteristics of white beds present within Chert lithofacies. (**A**) Fresh-cut surface image of a Chert sample that contains two white beds. (**B**) Thin section photograph of same sample in A displaying location of C, D, E and F photomicrographs. (**C**) and (**F**) shows the typical chert matrix with abundant radiolarian tests. (**D**) and (**E**) corresponds to the actual white beds showing a porous matrix (dissolution?) and empty cavities more likely left by radiolarians. All thin sections photomicrographs were taken in plane-polarized light. XRD results for white bed E yielded 100% quartz.

6.2.Siliceous Shale

Typically, this lithofacies presents a dark brown laminated matrix predominantly composed by microcrystalline quartz admixed with clay minerals (mainly illite), organic matter, and pyrite (**Figure 44**). Visible coarser particles include palynomorphs (*Tasmanites*), characterized by thick organic yellow-orange walls (**Figure 44**). Within this lithofacies most of these *Tasmanites* are highly compacted and are aligned with shale lamination (**Figure 44**). Authigenic quartz fills cavities of some *Tasmanites*. Detrital quartz grains are scattered. Pyrite is commonly observed as individual crystals but also aggregated in bands. Radiolarian tests are rare to absent.

Generally, SEM images of fresh-broken surfaces revealed the preferred orientation of clay minerals in siliceous shale beds (**Figure 44**). *Tasmanites* cysts are commonly flattened and display thick organic walls of approximately 7µm (**Figure 44**). Some cavities of *Tasmanites* are observed as open spaces (porosity?) (**Figure 45**). Pyrite framboids are observed in elongated aggregates following lamination (**Figure 44**). Organic matter and porosity were not easily discriminated as they both appear as dark/black areas in SEM images, also some of the black spots can be cavities left by silt grains pulled off during sample preparation.

A particular variation of the siliceous shale lithofacies was found in the uppermost part of the section (*zones d and e* in **Figure 24**). During field work, those beds were described as ‘indurated siliceous shales’ because shale parting responses (flakes) were much thicker than a regular siliceous shale (**Figure 45**). Then, when analyzing these indurated shales under the microscope, *Tasmanites* were found more silicified than in a typical siliceous shale (**Figure 45**). Radiolarians are rare to absent.

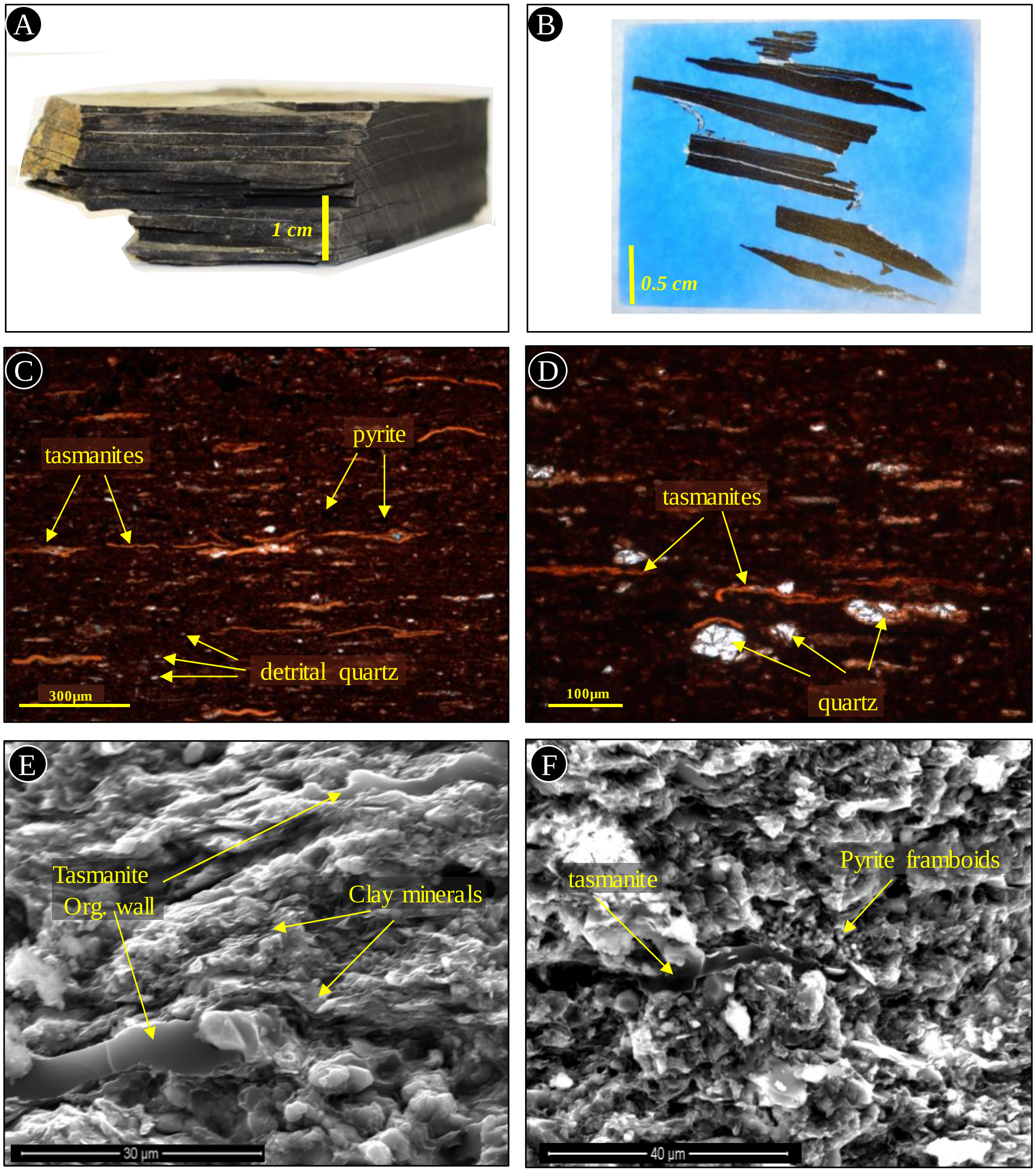

Figure 44. Petrographic characteristics of siliceous shales lithofacies. (**A**) Freshly fractured image of a siliceous shale bed showing typical lamination of shales. (**B**) Thin section photograph displaying thin flakes. (**C**) and (**D**) photomicrographs taken in plane-polarized light showing the dark brown shale matrix made of microcrystalline quartz and clays; embedded coarser particles include flattened *Tasmanites* and silt-sized detrital quartz. (**E**) and (**F**) are SEM images taken on fresh broken surfaces showing preferred orientation of clay minerals, organic wall of flattened *Tasmanites* and aggregates of pyrite framboids. Sample is 64% quartz and 36% clay; TOC is 16 wt.%.

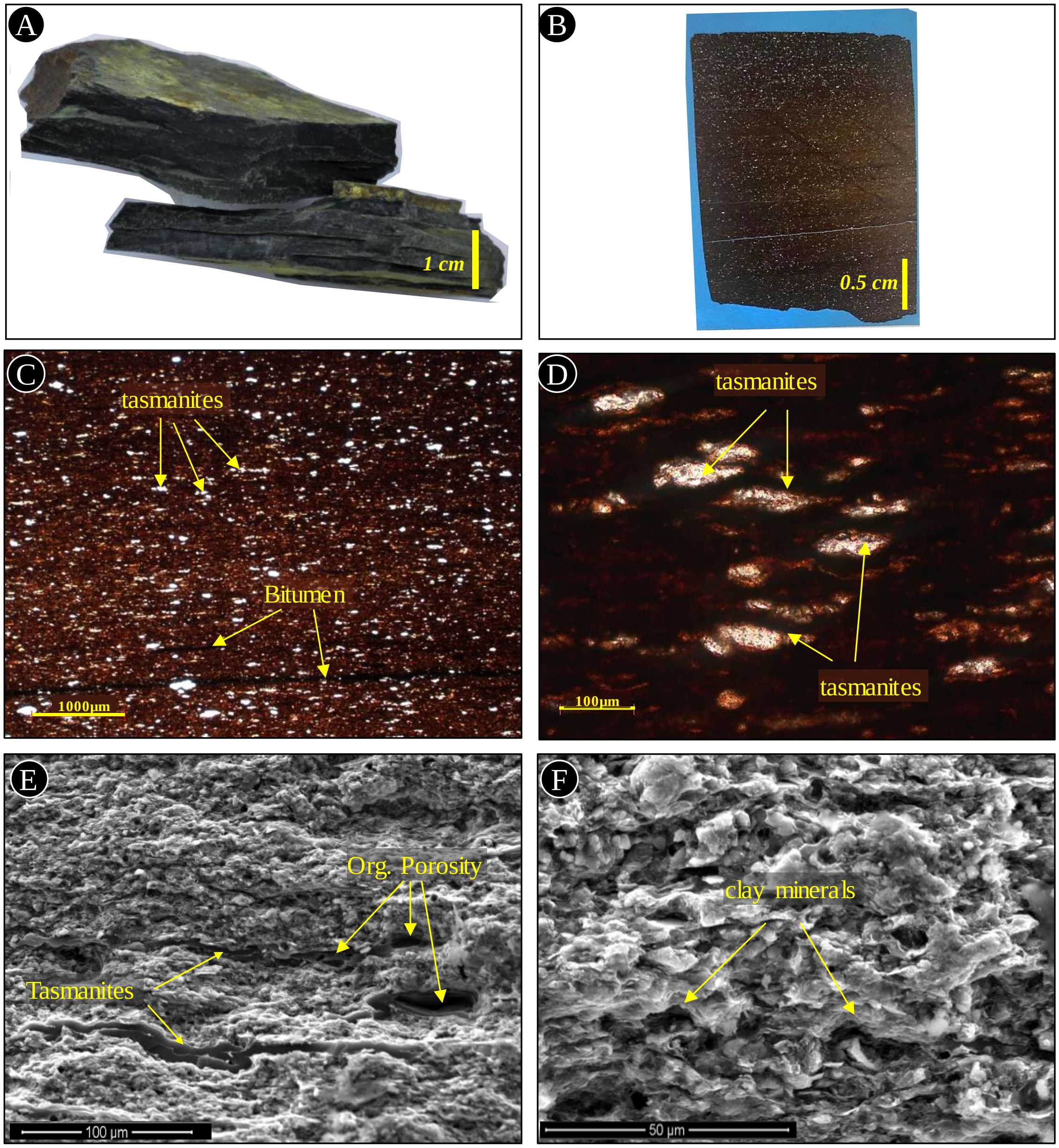

Figure 45. Petrographic characteristics of an indurated siliceous shale sample. (**A**) Freshly fractured surface image evidencing 'thick flakes' (less laminated than a typical siliceous shale). (**B**) Thin section photograph displaying a massive-aspect (less laminated). (**C**) and (**D**) Photomicrograph taken in plane-polarized light showing a high amount of silicified *Tasmanites*. (**E**) and (**F**) corresponds to SEM images taken in fresh surfaces, note organic porosity in *Tasmanites* cysts. Sample is 81% quartz and 19% clay; TOC is 13 wt.%.

6.3.Dolomitic Mudstone

Even though this lithofacies generally appears hard (non-fissile) in the outcrop as in hand-specimen, in thin sections it displays a microfabric similar in appearance to a dolomitized shale, and in some cases, they preserve the former shale fabric where lamination has not been completely removed or destroyed (**Figure 46**).

The matrix of dolomitic mudstones is composed of microcrystalline dolomite (i.e. crystal size less than 50 microns), microcrystalline quartz, and visible disseminated organic material. *Tasmanites* and radiolarians are rare, but when found they are replaced either by dolomite or authigenic quartz (**Figure 46**).

On the other hand, towards the uppermost part of the section (foot 75) a very particular dolomitic bed 18 centimeters thick was described as remarkably dissimilar to the typical dolomitic mudstones beds in the section. In hand specimen, the sample is coarsely crystalline, which was then confirmed by thin sections (**Figure 47**). Microscopically, the matrix is composed by a mosaic of zoned subhedral dolomite crystals which can reach up to 3 millimeters in diameter (**Figure 47**). Sporadically, dolomite crystals present bladed-like inclusions of other carbonate minerals, most likely ankerite (ferroan dolomite) and sulfate minerals (anhydrite, gypsum) (**Figure 47**). Branched microfractures are filled with calcite and bitumen (**Figure 47**).

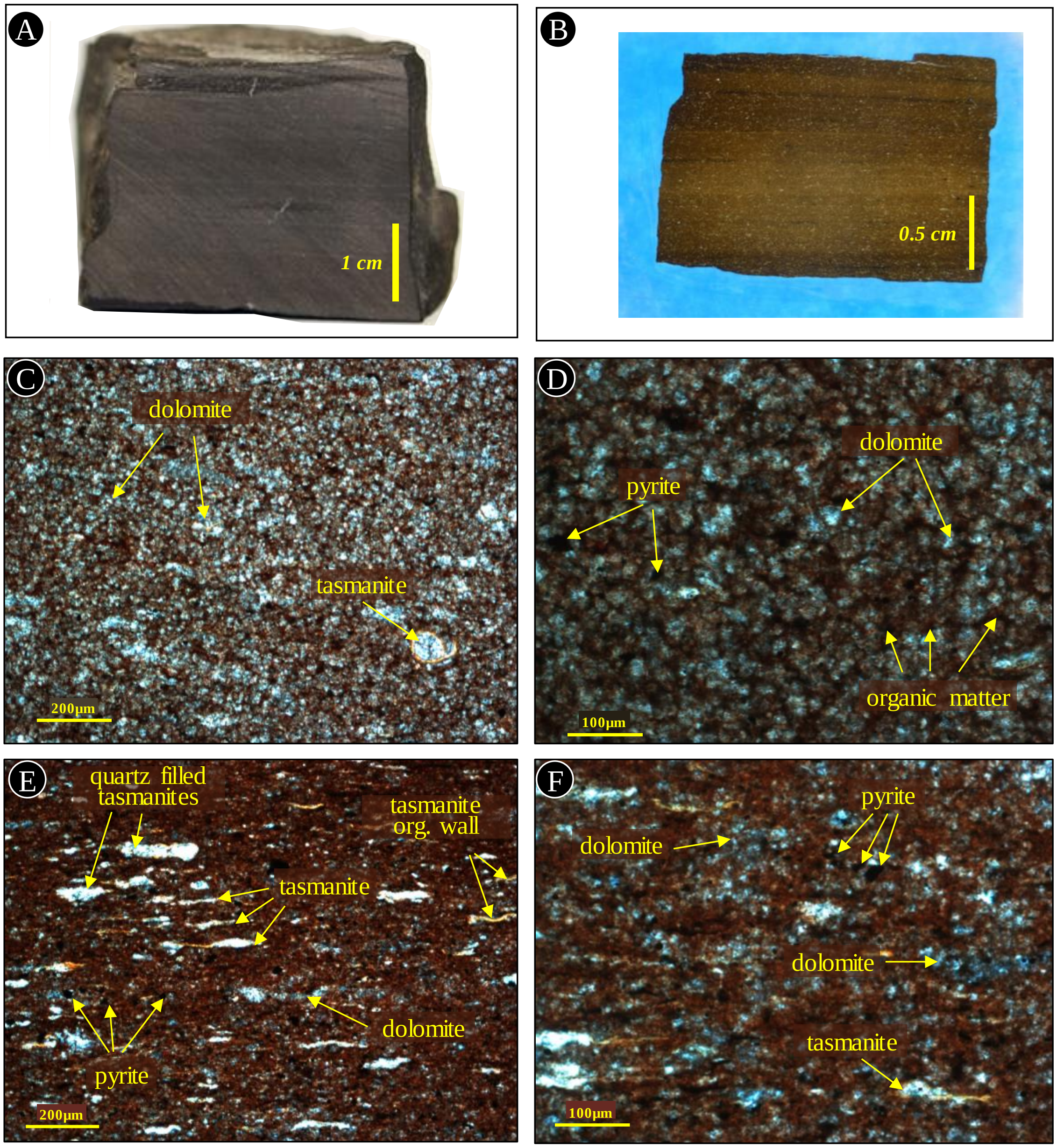

Figure 46. Petrographic characteristics of typical dolomitic mudstones. (**A**) (**B**) (**C**) and (**D**) photomicrographs correspond to a dolomitic mudstone sample which displays a 'high' degree of dolomitization where matrix is made of mosaics of dolomite; *tasmanites* and radiolarians are rare. Sample is 90% carbonates, 6% quartz and 4% clays; TOC 2 wt.%. (**E**) and (**F**) thin section photos correspond to a different sample also described as dolomitic mudstone, displaying a 'low' degree of dolomitization; the microfabric is recrystallized, with some remains of its primary depositional fabric. All thin sections photomicrographs were taken in plane-polarized light. Sample is 91% carbonates, 5% quartz and 3% clays; TOC is 3.5 wt.%.

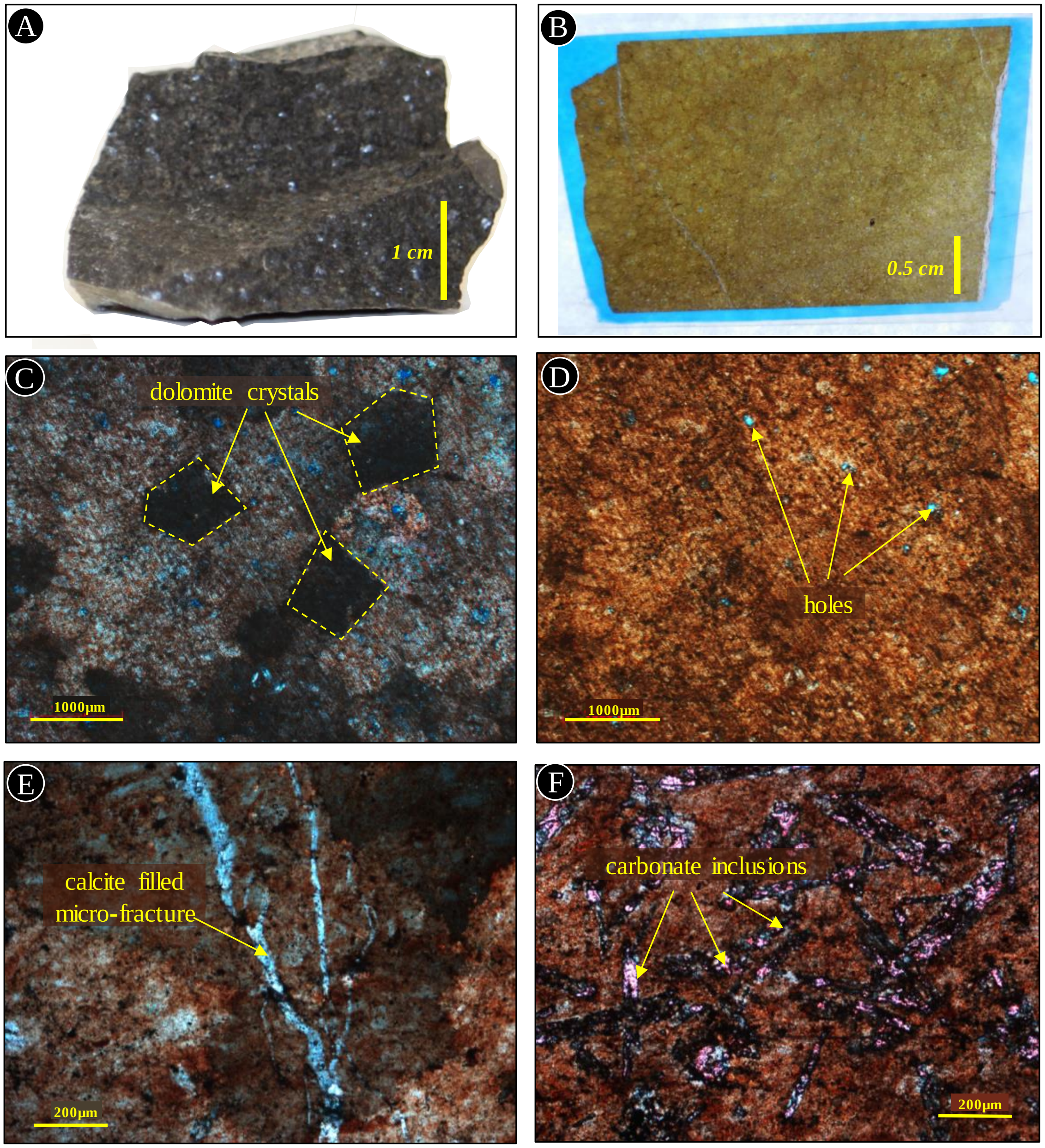

Figure 47. Petrographic characteristics of a coarse-grained dolomite sample. (**A**) Freshly fractured surface image. (**B**) Thin section photograph displaying a massive aspect (non-laminate at all). (**C**) and (**D**) are photomicrographs showing same field of view under cross-polarized light and plane-polarized light respectively; they show a massive rock with a matrix made of mosaics of subhedral crystals of dolomite. (**E**) Branched microfractures (no defined pattern) filled with calcite. (**F**) Dolomite crystals displaying inclusions of ferroan dolomite (ankerite). Sample is 87% carbonates and 6% quartz; TOC is 2 wt.%.

7. ORGANIC GEOCHEMISTRY

Results of Total Organic Carbon (TOC) and Rock-Eval pyrolysis were obtained from twenty outcrop samples and are presented in **Table 3**.

At first glance, results revealed a wide range of present-day TOC values from 0.45 to 15.7 wt.%, where higher TOC values are associated with soft lithologies (TOC ~14wt.%) and conversely lower TOC values are related to hard lithologies (TOC ~3wt.%) (**Figure 48A**). Other authors have also described a positive relationship between lithology and TOC content for the Woodford Shale (Comer & Hinch, 1987; Kirkland et al., 1992; Roberts & Mitterer 1992; Fishman et al., 2013; Galvis, 2017). In general, black shales are highly enriched in organic carbon (10 to 30wt%) whereas chert beds present lower TOC contents (3 to 9wt%).

When analyzed by lithofacies (**Figure 48B**), a direct relationship between mineralogical composition and TOC contents can be observed, where clay-rich siliceous shales yielded the highest TOC values ranging from 10 to 15.7 wt.% (mean= 13.7%) (**Figure 49**), whereas the quartz-rich Chert lithofacies presents lower TOC values between 0.45 and 6 wt.% (mean = 3.2%) (**Figure 49**). In the case of the dolomitic mudstone lithofacies, TOC contents range between 2.2 to 5.4 wt.% with an average of 3.3wt.%; though there is no clear relationship between TOC and carbonate contents (**Figure 49**), from petrographic analyses it was observed that the higher degree of dolomitization (i.e. more crystalline) the lower is the visible organic material within the matrix.

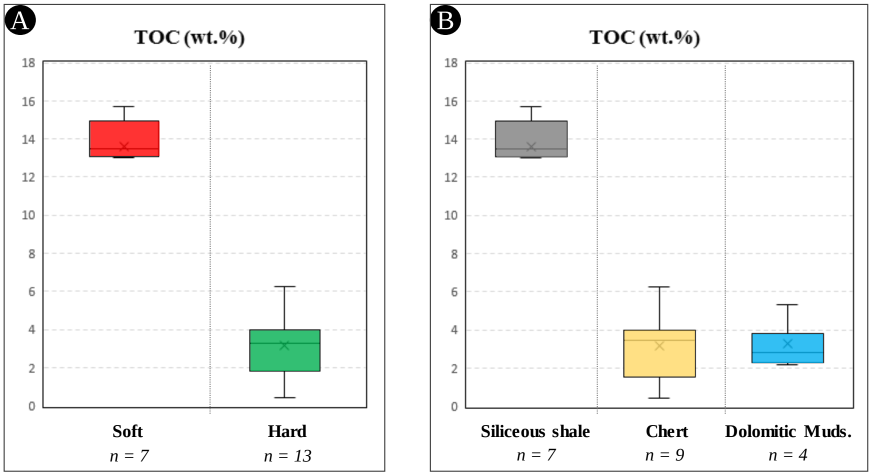

Figure 48. Boxes and whiskers plot showing distribution of TOC. **A**) differentiated by Soft and Hard lithologies. **B**) differentiated by the three main lithofacies identified: Siliceous Shale, Chert, and Dolomitic Mudstone. *n*= number of samples analyzed.

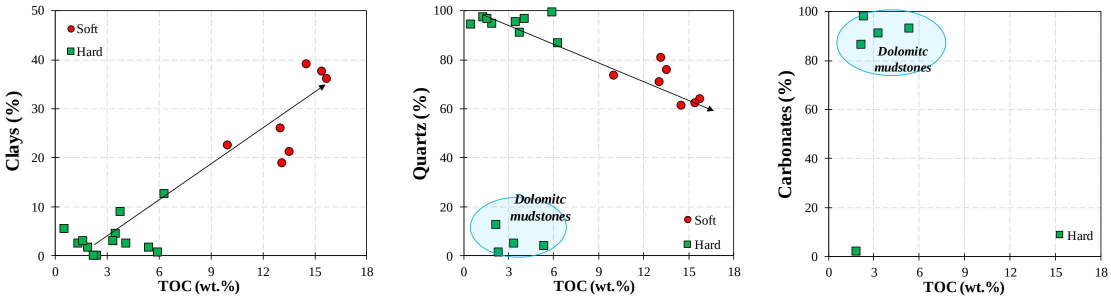

Figure 49. Scatter plots of clay, quartz and carbonate contents versus TOC differentiated by soft (red) and hard (green) lithologies.

When plotting TOC values stratigraphically, two main observations can be made (**Figure 50**). The first one is that regardless of stratigraphic position, soft lithologies (shales) contain elevated TOC values (>10 wt.%), and in the same way, hard lithologies present lower TOC values (<6 wt.%) (**Figure 50**).

The second observation is that there is no complete correlation between TOC values and the gamma ray curve. For example, soft samples from feet 26, 45 and 65 have almost identical TOC values of 13.0, 13.5 and 13.1 wt.% respectively, but markedly different gamma ray values of 479, 786 and 342 (cps) respectively (**Figure 50**).

So, to explain the lack of correlation of gamma ray and TOC values, we should recall that gamma ray readings are accounting for contributions of different beds contained within the diameter of investigation of the detector (Serra, 1984), which in this study was 1 foot (Scintrex user's manual). Then, considering that the Woodford Shale at the I-35 outcrop consists of rhythmically repeated soft and hard couplets, a direct relationship between TOC values and gamma ray readings would not be significant unless the entire foot was composed by the same gross lithology (e.g. 100% soft) which is sparse and rare in the middle and upper members of the Woodford Shale as reported by Galvis (2017).

On the other hand, owing to the typical cyclicity of soft (TOC ~14wt.%) and hard (TOC ~3wt.%) beds within the Woodford Shale, a very low or very high TOC value may or may not be representative of a whole interval depending on the proportion of soft and hard beds at a given interval. Indeed, Connock (2015) found high vertical variability of TOC values measured in Woodford Shale cores, where in some cases TOC oscillated between 10 to 5 wt.% in less than 1.5 feet, then highlighting the importance of conducting lithology-guided sampling methods rather than systematic ones at least for the Woodford Shale.

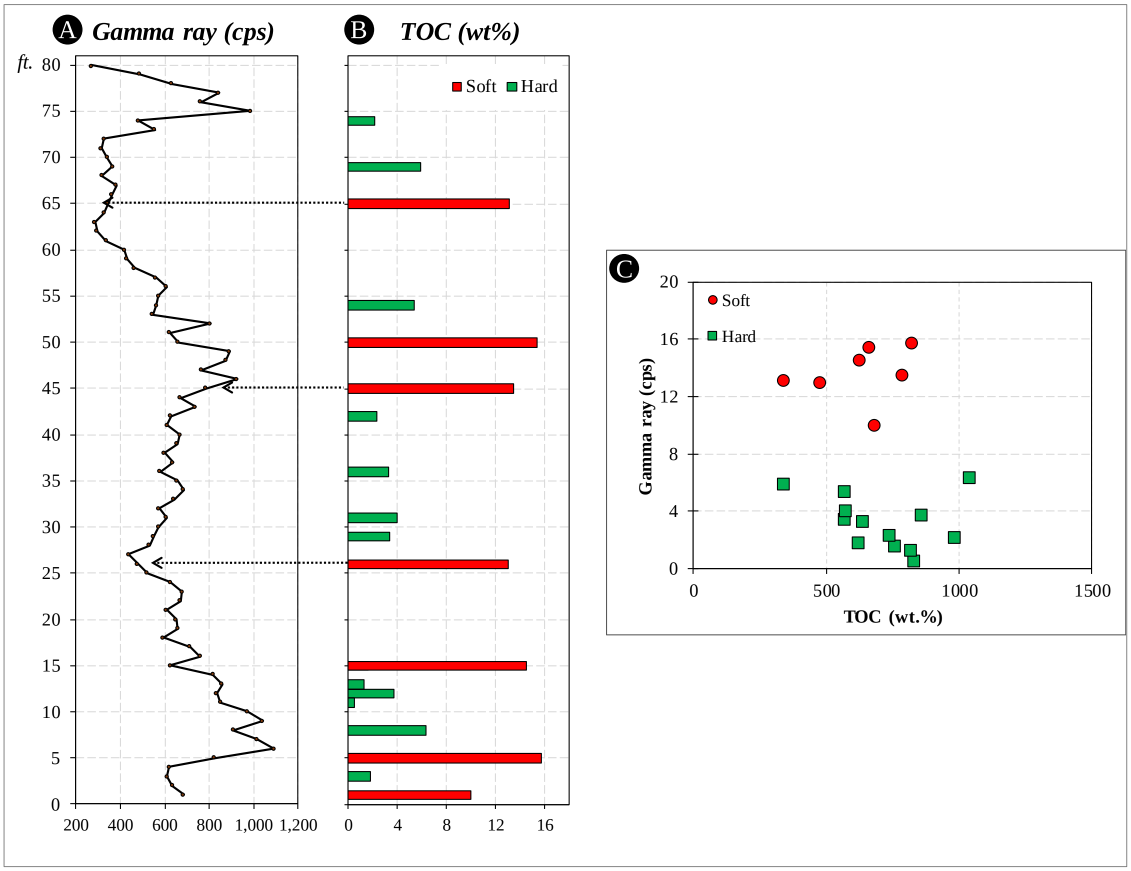

Figure 50. (**A**) Gamma-ray profile from I-35 outcrop, (**B**) Vertical plot showing TOC values colored by lithology (red: soft and green: hard). Notice how regardless of stratigraphic position and gamma-ray response, TOC values in soft lithologies are significantly higher than in hard lithologies. Dotted arrows are specific depths where TOC values are similar between them but gamma-ray readings are markedly different. (**C**) Scatter plot displaying no clear relationship between gamma-ray readings and TOC values.

Before starting with the interpretation of Rock-Eval pyrolysis data, cross-plotting S1 versus TOC helps to discriminate between the non-indigenous and indigenous nature of the hydrocarbons present in the samples (**Figure 51**) (Hunt, 1996); for this study the analyzed samples plotted in the indigenous region indicating the absence of migrated hydrocarbons (**Figure 51**).

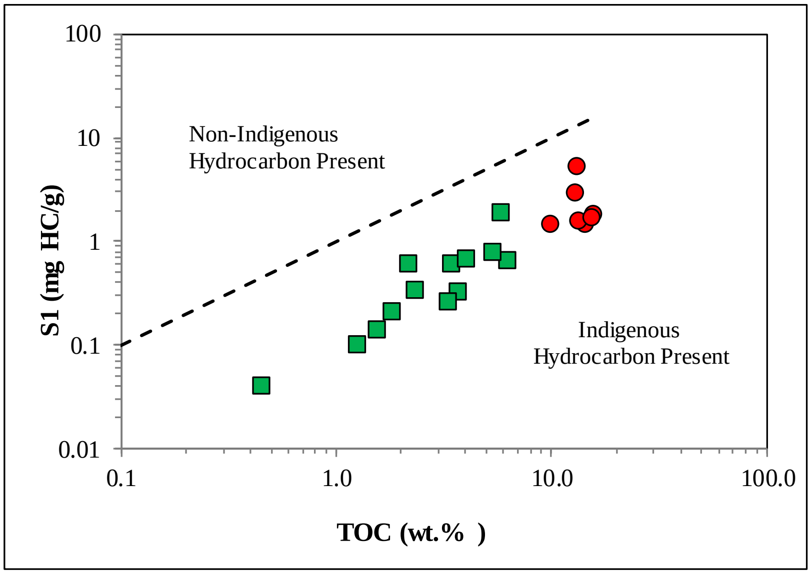

Figure 51. Plot of TOC versus S1 indicating the absence of migrated hydrocarbons for all samples analyzed (Hunt, 1996). Dashed gray line stands for S1/TOC= 1.5. Red dots are results of soft beds and green squares are hard bed results.

Similar to TOC values, Rock-Eval pyrolysis results are highly related to lithology (**Table 3**, **Figure 51**). For the Siliceous Shale lithofacies (soft beds) S1 values range from 1.5 to 5.4 mg HC/gm rock; whereas for Chert and Dolomitic Mudstone lithofacies (hard beds) S1 values are between 0.04 and 1.92 mg HC/gm rock. S2 peaks for siliceous shale lithofacies range from 48 to 78 mg HC/gm rock with an average of 77 mg HC/gm rock (**Table 3**, **Figure 52**) revealing an excellent source rock for all shale samples analyzed. S2 values for 'hard' lithologies shows a wider range with values from 0.3 to 37 mg HC/gm rock indicating poor to excellent generation potential for these rocks (**Figure 52**).

Overall, when plotting S2 versus TOC, a positive linear relationship is recognized regardless of lithology (i.e. soft-hard) (**Figure 52**), suggesting a uniform kerogen type of the organic matter occurring in soft and hard beds (Pepper & Corvi, 1995); similar results were obtained by Fishman et al., (2013) who used outcrop samples from south-central Oklahoma.

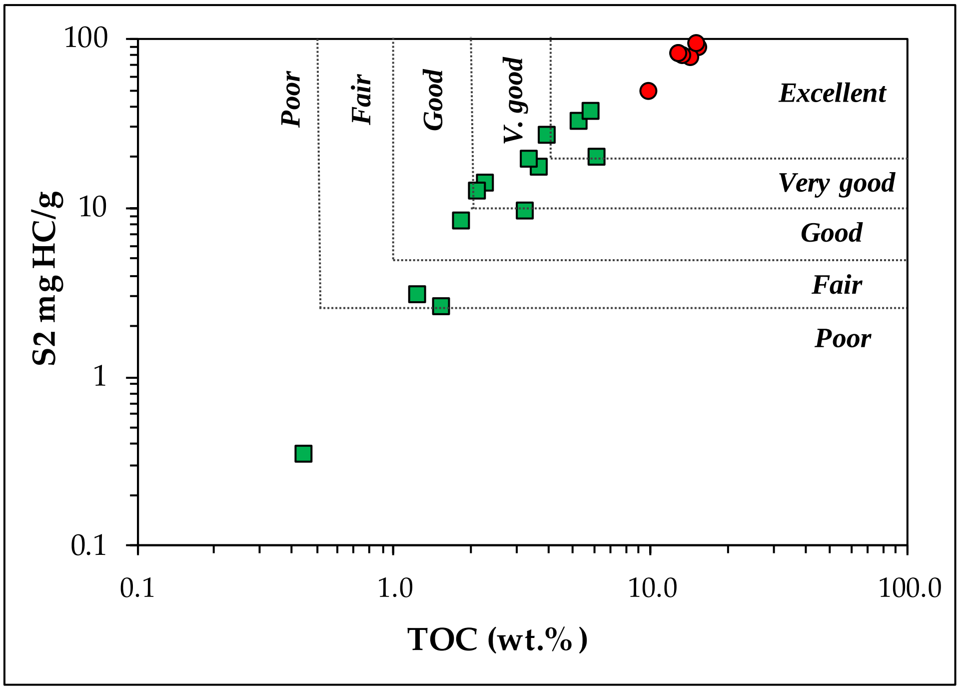

Figure 52. Plot of TOC S2 for studied samples showing excellent hydrocarbon generation potential for all soft samples (siliceous shale lithofacies), whereas generation potential for hard samples varies widely from poor to excellent. Red dots are results of soft beds and green squares are hard bed results. TOC and S2 reference values from Petters & Cassa (1994).

Regarding kerogen type, the most used parameters are the Hydrogen Index (HI) and Oxygen Index (OI) which are commonly plotted on a modified Van-Krevelen diagram developed by Tissot et al., (1974). In this study, most of the samples analyzed show high (HI) values from 473 mg HC/gm TOC to 657 mg HC/gm TOC, and moderate to high (OI) values from 9 to 95 mgCO2/gm TOC. Based on the modified Van-Krevelen diagram (**Figure 53A**), the majority of samples seem to be grouped close to the Type I pathway and some samples are dispersed across the plot. However, when the same samples are plotted on a S2 versus TOC diagram, most of them plot in the kerogen Type II region (**Figure 53A**).

Thus, I believe that a Type II kerogen (from S2 vs TOC plot) is more likely to occur in the I-35 outcrop rocks as reported by Lewan (1983) who petrographically characterized some samples from the same outcrop as being composed by a 90 v% of amorphous Type II kerogen, and the remainder of kerogen consisting of Type III kerogen and palyniferous Type I kerogen (i.e. *Tasmanites*). In addition, Jones (2017) conducted biomarkers investigations using several samples collected by this work, concluding a marine Type II kerogen for all samples analyzed.

A possible explanation for the Type I kerogen indicated by the modified van-krevelen diagram (HI vs. OI) (**Figure 53A**), could be the contrast in mineralogical composition and TOC contents for samples analyzed in this study which likely yielded highly varied HI and OI; this explanation was first introduced by Katz (1983). Additionally, Langford & Blanc-Valleron (1990) demonstrated uses of S2 versus TOC plots for generating more reliable results for determining kerogen type.

To summarize, results of kerogen quality of this work suggest a Type II kerogen for I-35 outcrop samples, coinciding with recent organic-geochemical works in the Woodford Shale in Oklahoma (Miceli-Romero, 2012, Serna-Bernal, 2013, Fishman et al., 2013; Conock, 2015; Wang 2016; Villalba, 2016; Galvis, 2017).

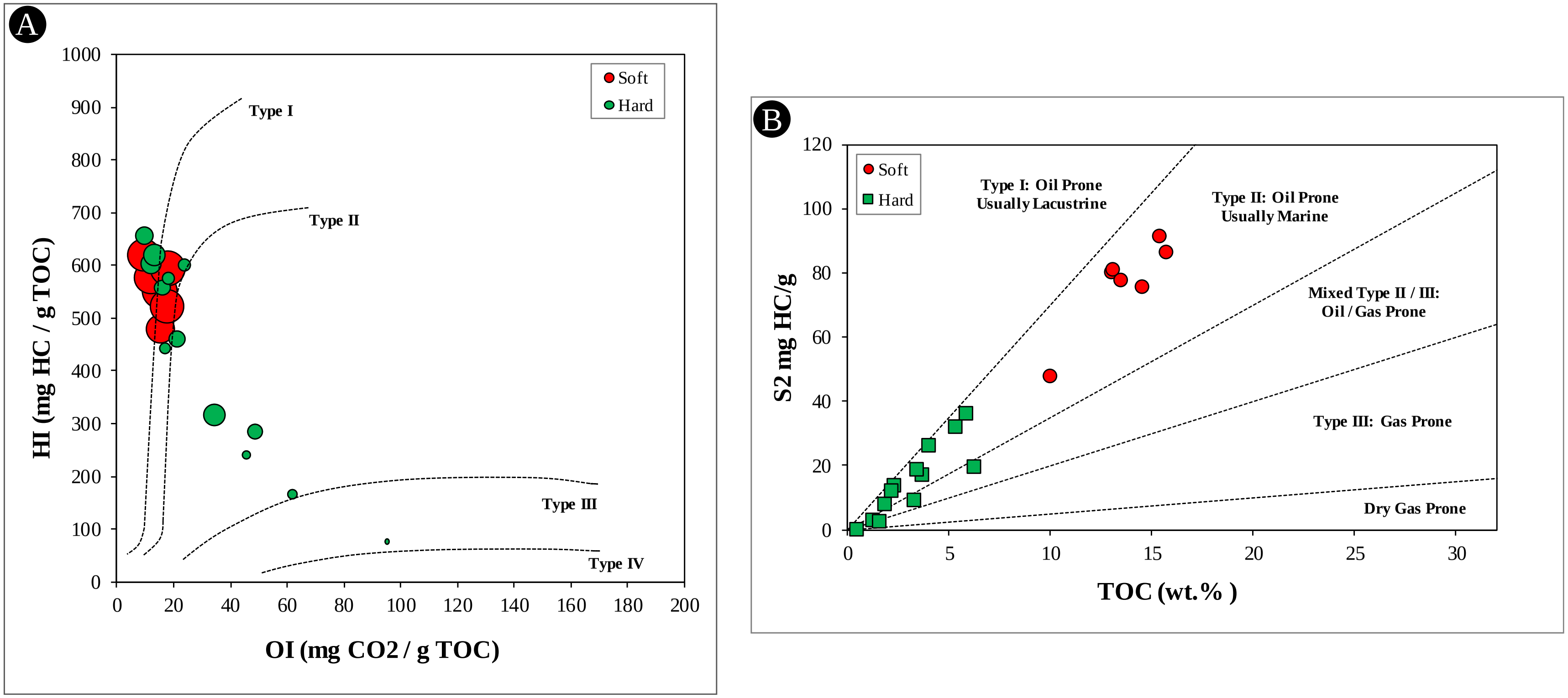

Figure 53. (**A**) HI versus OI values plotted on a modified Van-Krevelen diagram (Tissot et al., 1974). Size of the data points is proportional to TOC contents. (**B**) Plot of S2 versus TOC reveals Type II kerogen for analyzed samples.

As for thermal maturity, measured Tmax values ranging from 426 to 438 °C (~426°C), indicate immature rocks with respect to the oil window (Peters, 1986). Also, Tmax values can be converted into calculated vitrinite reflectance (%VR_o) by using the equation proposed by Jarvie et al., (2001). Calculated VR_o values range from 0.51 to 0.72% (mean= 0.6%), suggesting an immature to early mature source rock for most of the samples. These values are in accordance with the 0.50% R_o measured by Cardott & Chaplin, (1993) in the I-35 Woodford outcrop based on 79 measurements with 0.43 - 0.66% reflectance range.

The immature character of the Woodford samples at I-35 are attributed to the tectonic uplift of the Arbuckle mountains during the Pennsylvanian period (Ham et al., 1973); at greater burial depths, the Woodford Shale is mature enough to produce hydrocarbons (Cardott, 2014).

Foot	Sample No.	Lithofacies	Weathering Response	Leco TOC (wt.%)	S1 (mg HC/g rock)	S2 (mg HC/g rock)	S3 (mg CO2/g rock)	Tmax (°C)	Calculated %Ro	HI (mg HC/g TOC)	OI (mg CO2/g TOC)
1	2	Siliceous Shale	Soft	10.0	1.5	47.8	1.5	426	0.5	480	15
5	9	Siliceous Shale	Soft	15.7	1.9	86.5	2.4	429	0.6	551	15
15	27	Siliceous Shale	Soft	14.5	1.5	75.7	2.6	430	0.6	522	18
26	48	Siliceous Shale	Soft	13.0	2.9	80.4	1.3	431	0.6	618	10
45	86	Siliceous Shale	Soft	13.5	1.6	77.9	1.6	428	0.5	577	12
50	96	Siliceous Shale	Soft	15.4	1.7	91.6	2.8	431	0.6	595	18
65	126	Siliceous Shale	Soft	13.1	5.4	81.2	1.2	438	0.7	620	9
4	7	Chert	Hard	1.8	0.2	8.2	0.3	435	0.7	443	17
9	15	Chert	Hard	6.3	0.7	19.8	2.1	427	0.5	316	34
12	20	Chert	Hard	0.5	0.0	0.3	0.4	426	0.5	75	95
13	22	Chert	Hard	3.7	0.3	17.1	0.8	431	0.6	461	21
14	24	Chert	Hard	1.3	0.1	3.0	0.6	432	0.6	241	46
16	28	Chert	Hard	1.6	0.1	2.6	1.0	431	0.6	166	62
30	55	Chert	Hard	3.4	0.6	19.1	0.6	430	0.6	558	16
32	59	Chert	Hard	4.0	0.7	26.3	0.4	436	0.7	657	10
70	135	Chert	Hard	5.9	1.9	36.5	0.8	438	0.7	620	13
37	69	Dolomitic Mudstone	Hard	3.3	0.3	9.4	1.6	428	0.5	285	49
43	81	Dolomitic Mudstone	Hard	2.3	0.3	14.0	0.6	437	0.7	601	24
55	105	Dolomitic Mudstone	Hard	5.4	0.8	32.3	0.7	428	0.5	604	12
75	145	Dolomitic Mudstone	Hard	2.2	0.6	12.5	0.4	435	0.7	576	18

Table 3. Results of total organic carbon (TOC) and Rock-Eval analysis organized based on lithofacies.

8. ELEMENTAL CHEMOSTRATIGRAPHY

In chemostratigraphy, geochemical fingerprints of major and trace elements constitute the main input variables used to characterize sedimentary deposits; especially the combination of elemental signals (proxies) are useful to infer paleo-environmental conditions and consequently rock composition (Vine and Tourtelot,1970; Slatt, 1974; Pearce & Jarvis, 1992; Pearce et al., 1999; Sageman & Lyons, 2003; Tribovillard et al., 2006). Most recently, chemostratigraphy has been extensively used to characterize highly heterogeneous unconventional shales, which are usually difficult to describe by naked eye.

In this study, using X-ray fluorescence (XRF), the elemental composition was measured on 157 mudrock samples taken from the I-35 outcrop; their results are summarized in **Figure 54**. Twelve elements of interest for this study were: silicon (Si), aluminum (Al), potassium (K), titanium (Ti), zirconium (Zr), rubidium (Rb), calcium (Ca), magnesium (Mg), strontium (Sr), vanadium (V), molybdenum (Mo), and uranium (U). In addition, for consistency with previous results (Lithofacies, XRD, TOC), results of XRF were also differentiated by the two most distinctive lithologies in the Woodford Shale, soft and hard (**Figure 54**).

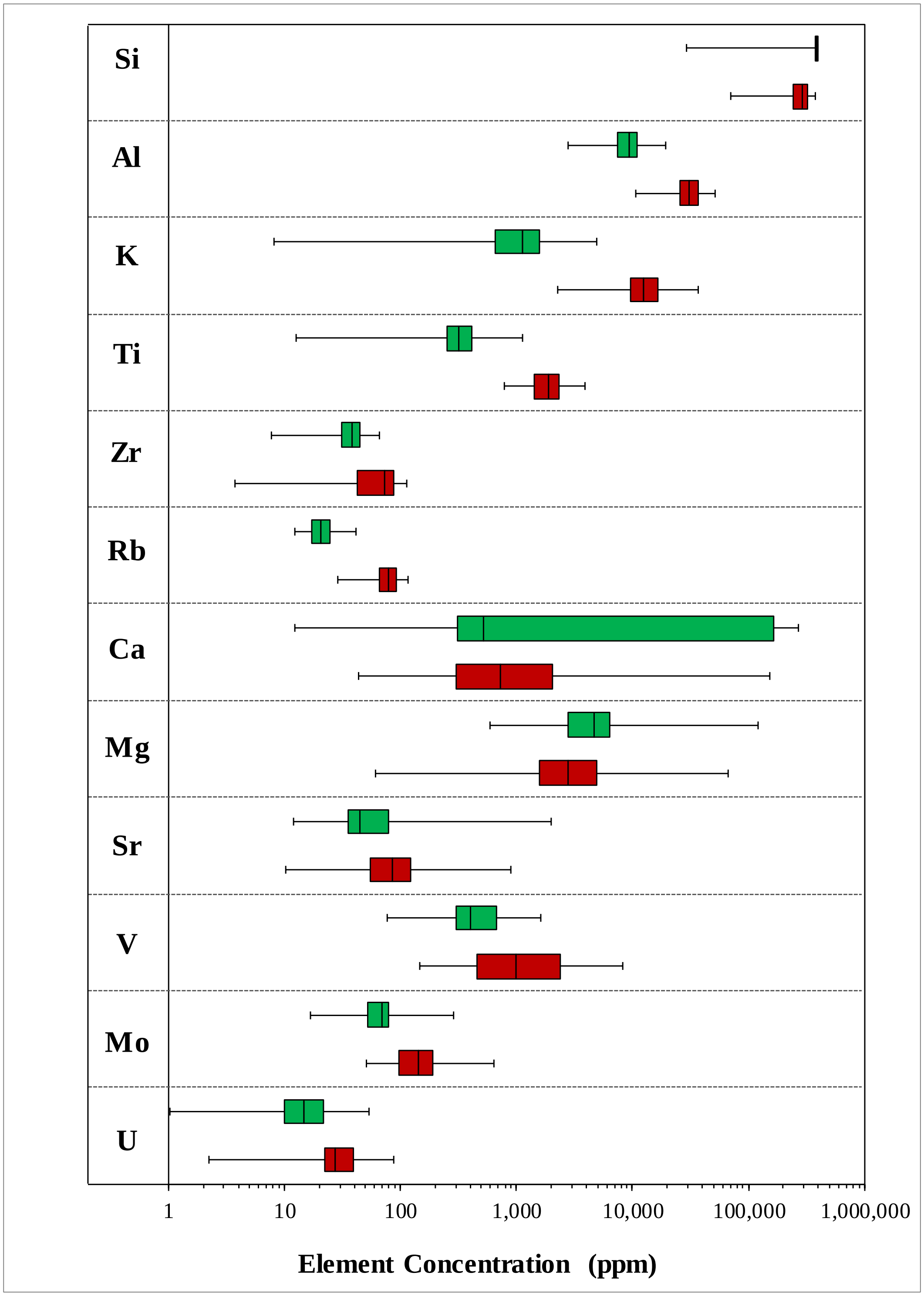

Figure 54. Compiled boxes and whiskers plot of concentrations of major and trace elements revised in this study. Hard lithologies (green boxes) and soft lithologies (red boxes). Soft samples n=80, hard samples n= 77. Concentrations of all elements reported in parts per million (ppm).

-Detrital elements

The major and trace elements traditionally regarded as detrital proxies include aluminum (Al), potassium (K), titanium (Ti), zirconium (Zr), rubidium (Rb) and silicon (Si).

In sedimentary deposits, Aluminum is the most reliable detrital proxy because of its general immobility during diagenesis (Calvert & Pedersen, 1993; Sageman & Lyons, 2003) and its relative scarcity in sea waters (Brumsack, 2006). Al is mainly associated with clay minerals (Sageman & Lyons, 2003), but also with K-feldspars (Pearce et al., 1999).

Potassium is usually associated with clay minerals, particularly illite unless sediments are enriched in K-feldspars (Weedon & Shackleton, 1997; Sageman & Lyons, 2003).

Titanium and zirconium are strongly associated with continentally derived sediments, and occur at relatively low abundances in sea-waters (Li, 1982; Bhatia & Crook, 1986; Sageman & Lyons, 2003,). Ti has a very high diagenetic stability under most environmental conditions, making it a very useful detrital proxy (Brookins, 1988).

Rubidium is a lithophile element that does not form any minerals on its own; however, it is present in several minerals in which it substitutes for K due to their similar ionic radius (Wedepohl, 1971). Rb is commonly associated with relatively fine-grained fractions including clay minerals (i.e. illite) and micas, and to a lesser extent to K-feldspar (Dypvik and Harris, 2001).

Silicon is commonly affiliated with a variety of minerals including quartz, clay minerals and feldspars (Pearce and Jarvis, 1992; Pearce et al., 1999, Brumsack, 2006). Because of this, it can be more useful to report it in the form of a silicon to aluminum ratio (Si/Al) to decrease the signal of the Si in clays and feldspars, and highlight signals where Si is actually associated with quartz (Turner, 2016). Consequently, excesses in Si/Al ratios may reflect biogenic input into the system (Davis et al., 1999, Sageman & Lyons, 2003; Rowe et al., 2008; Ross & Bustin, 2009).

When comparing concentrations of detrital proxies in soft and hard lithologies, a marked contrast is observed (**Figure 55**). It was found that Al, K, Ti, Zr and Rb are significantly higher in soft samples than in hard ones, which suggest comparatively higher concentrations of detrital-derived sediments in soft beds than in hard ones within the Woodford Shale. On the other hand, very high Si/Al ratios coupled with the very low values in continental proxies (Ti, Zr, Al, K) suggest that most of the Si present in the hard beds of the Woodford Shale is of a biogenic origin. These observations can be supported by the petrographic analysis where hard beds present elevated amounts of silicified radiolarians (i.e. biogenic quartz) (**Figure 40** and **Figure 41**) and soft beds contain detrital quartz grains (**Figure 44**).

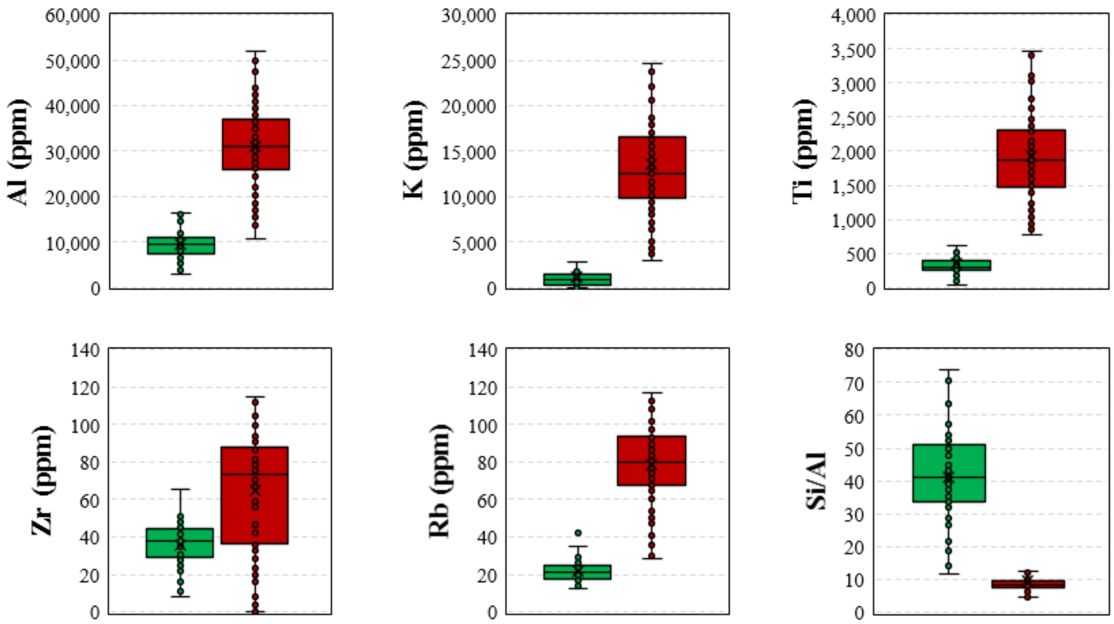

Figure 55. Individual box plots of main elements associated to detrital origin. Soft samples (red boxes) *n*= 80, hard samples (green boxes) *n*= 77. Notice higher abundances of detrital elements for soft beds. Si/Al contents are markedly higher for hard beds.

When cross-plotting Ti, K, Rb and Zr against Al (Figure 56), general linear trends with positive slopes were obtained suggesting that these elements are actually associated with the detrital and/or clay fraction within the Woodford Shale. The cross-plot of K versus Rb shows a high positive correlation indicating the substitution of K for Rb in clay minerals within the Woodford Shale (Figure 56). Si also exhibits a general positive relationship with Al in Figure 56; however, several data points plot off the Si-Al trend towards the upper left of the graph, indicating an excess of Si over Al which likely reflects a biogenic source. Additionally, data points in the lower left corner of the graph are associated with carbonate facies which possess low Si and Al contents (Figure 56).

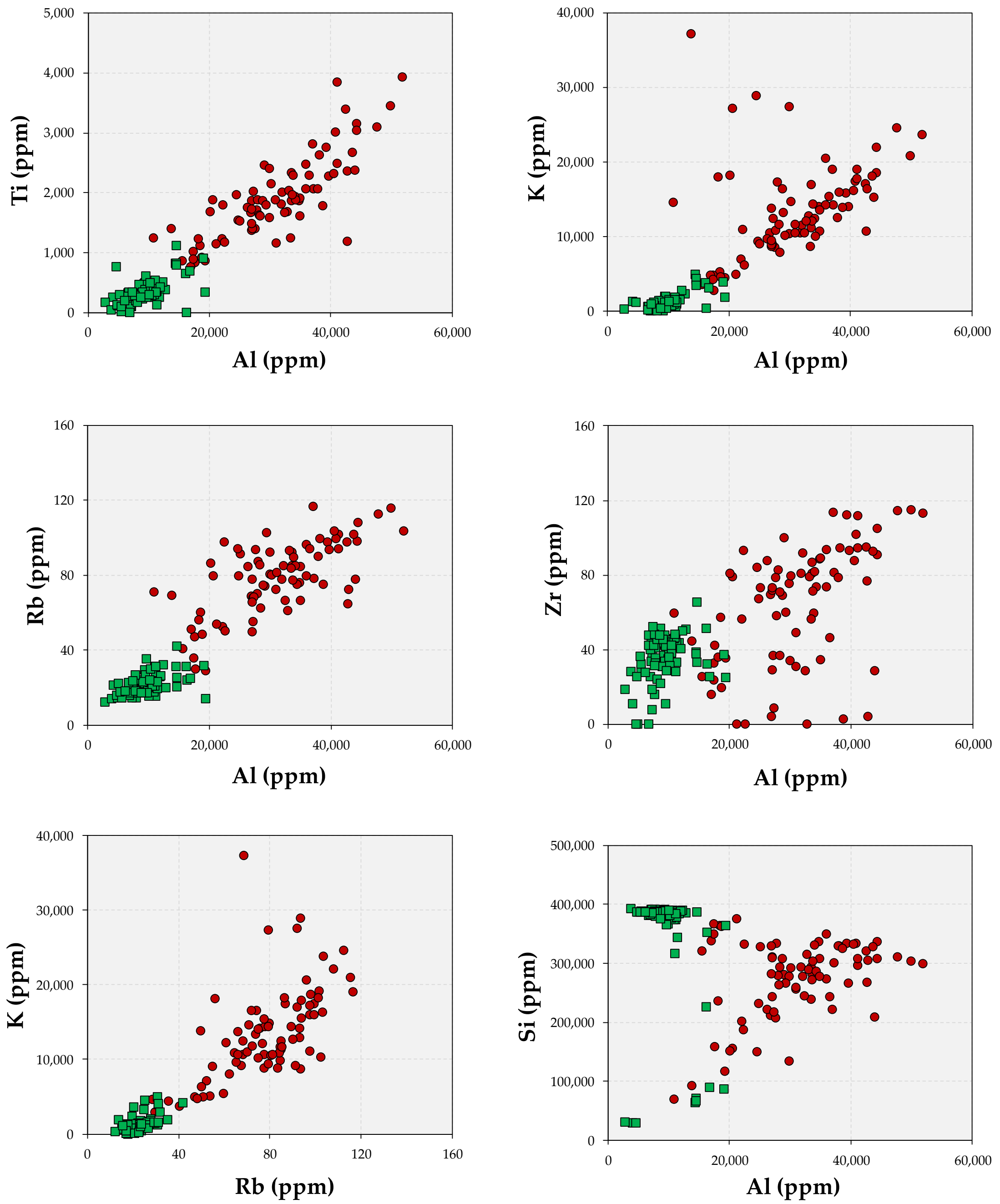

Figure 56. Cross plots between detrital elements differentiated by hard (green squares) and soft (red dots) lithologies. Ti, K, Rb, Zr show good positive covariance with Al suggesting a detrital origin for these elements. The K versus Rb plot shows strong positive covariance supporting the substitution of K by Rb. Si versus Al plot shows at least three populations, one showing a linear correlation with Al (red dots), t one in the upper left corner showing a silicon excess representing the chert beds and the outliers of the green squares in the lower left corner of the graph which represent the dolomitic lithofacies.

-Carbonate Elements

Elements like calcium (Ca), strontium (Sr) and magnesium (Mg) are commonly associated with the carbonate fraction of most black shale deposits (Vine & Tourtelot, 1970; Brumsack, 2006).

Calcium is present in several common minerals including calcite, dolomite, anhydrite and gypsum (McLennan and Taylor, 1995). Ca is also found in some feldspars, phosphates and clay minerals thus, illustrating the necessity of a multi-proxy approach (Turner, 2016).

Strontium is affiliated to a variety of rock forming minerals including calcite, dolomite, feldspars and gypsum (Salminen et al., 2005). In sedimentary environments, Sr substitutes extensively for Ca due to similarities in ionic ratios (Salminen et al, 2005). Moreover, Sr is highly associated to the secondary origin of dolomite (Weber, 1964; Wedepohl, 1971; Banner, 1995).

Magnesium is a major constituent of many mineral groups, including carbonates, silicates, sulphates, phosphates and borates (Salminen et al., 2005); in carbonate rocks, Mg is highly affiliated to dolomite formation (Wedepohl, 1971).

In this study, concentrations of Ca, Sr and Mg are extremely weak for most of the analyzed samples (**Figure 57**); in fact, only less than 10% of the samples showed significantly high values of Ca (>60,000 ppm), Sr (>450 ppm) and Mg (10,000 ppm). Regarding lithology (**Figure 57**), high concentrations of Ca, Sr and Mg in hard beds correlate with the previously defined dolomitic mudstones lithofacies. For the case of soft beds, moderate concentrations of Ca, Sr and Mg assisted in the definition of the Siliceous-Dolomitic Shale lithofacies.

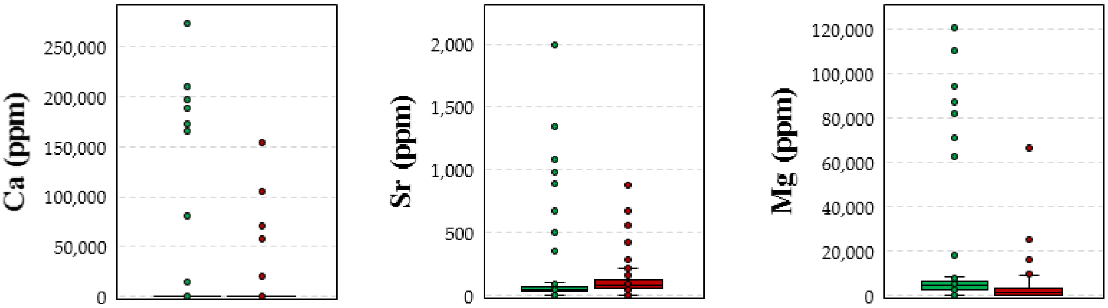

Figure 57. Individual box plot for the main major and trace elements related to carbonates. Soft samples (red boxes) *n*= 80, hard samples (green boxes) *n*= 77. Notice that most of the data points plot as outliers (i.e. outside boxes), confirming the low calcareous affinity for the majority of analyzed samples.

Cross-plotting Mg against Ca displays a positive linear trend (**Figure 58**), suggesting that within the Woodford Shale most of the carbonates are enriched in Mg, supporting the occurrence of dolomite. The plot of Sr versus Ca also shows a positive trend (**Figure 58**), thus proving the substitution of Ca by Sr in dolomite within Woodford samples (**Figure 58**). On the other hand, the negative covariance between Al and Ca, discards the detrital origin of carbonates within the Woodford Shale (**Figure 58**); indeed, petrographic observations suggested a diagenetic origin for dolomites evidenced by the presence of subhedral dolomite rhombs forming mosaics with some relicts of the precursor shale (**Figure 46**). Finally, Si against Ca displays a good negative relationship for the few samples (~15) that show elevated Ca concentrations (**Figure 58**), proving the scarcity of carbonate-siliceous mixed facies in the Woodford Shale.

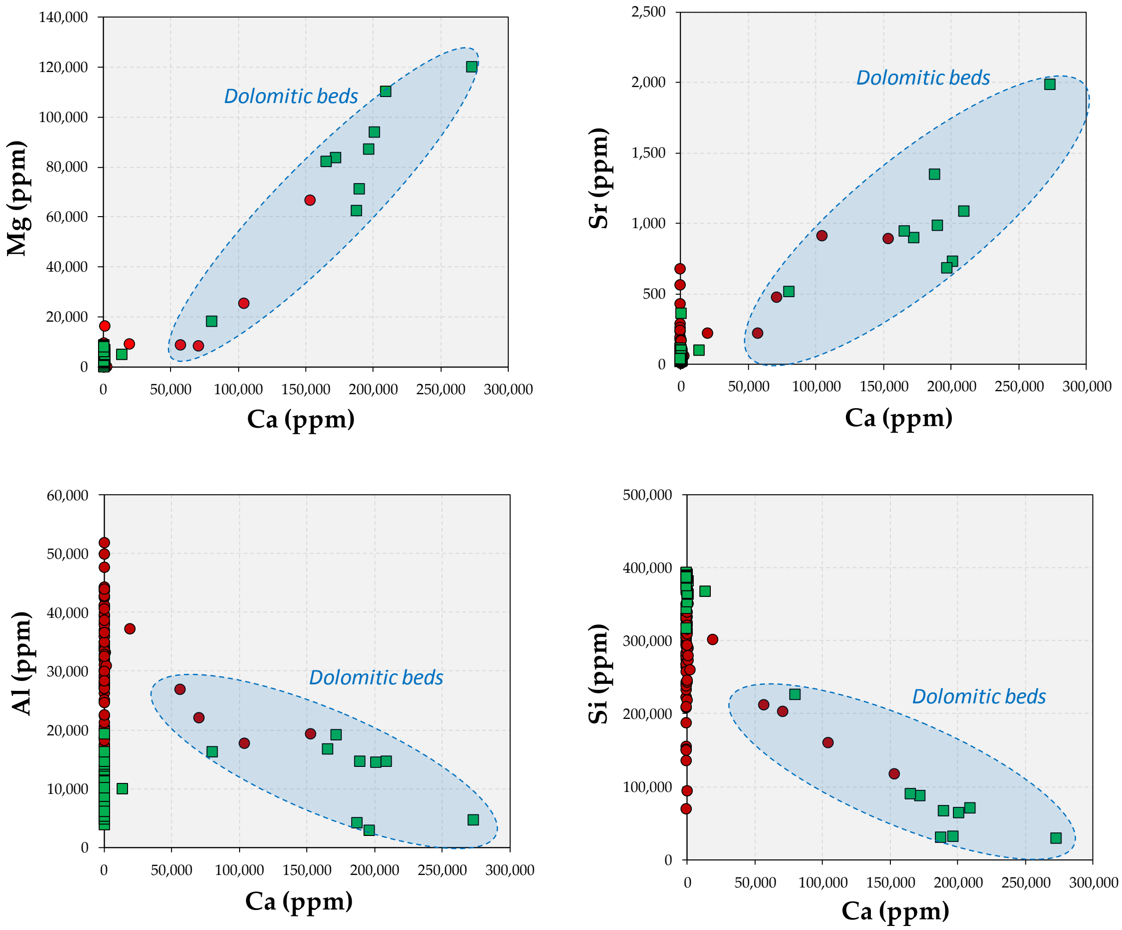

Figure 58. Carbonate proxies differentiated by Hard (green squares) and Soft (red dots) lithologies. Mg against Ca and Sr versus Ca depicting a positive a covariance supporting the presence of dolomite. Al against Ca and Si versus Ca show negative covariance suggesting that the Ca component is not related to quartz+clay rich facies. Notice that in the four graphs data points (157) are distributed into two main populations, one displaying Ca contents above 50, 000 ppm (i.e. dolomitic beds) the other one showing data points with almost zero Ca contents, thus demonstrating that about 90% of Woodford Shale samples from I-35 outcrop do not have a carbonate affinity.

-Redox-sensitive Elements

The most widely used redox-sensitive trace elements are molybdenum (Mo), vanadium (V) and uranium (U) (Vine and Tourtelot, 1970; Calvert & Pedersen, 1993; Algeo and Maynard, 2004; Tribovillard et al., 2006).

Molybdenum has emerged as the most useful proxy for paleo-redox conditions especially in black shales because it has a lack of chemical reactivity under oxic conditions (Calvert & Pedersen, 1993; Algeo and Lyons, 2006; Tribovillard et al., 2006; Sageman & Lyons, 2003). Mo is widely associated with organic matter and sedimentary sulphide minerals (Brumsack, 1989; Emerson & Huested, 1991; Calvert & Pedersen, 1993; Algeo & Maynard, 2004; Tribovillard, et al., 2006), in any case the fixation of Mo occurs within the sedimentary column close to the sediment/seawater interface (Brumsack, 1989). Additionally, according to Brumsack (1989) high concentrations of Mo in TOC-rich marine sediment indicate low sedimentation rates.

Vanadium has a redox chemistry comparable to Mo (Brumsack, 1998). V concentrations are associated with organic matter in anoxic sediments (Breit & Wanty, 1991; Emerdon & Huested, 1991; Calvert & Pedersen ,1993; Brumsack, 1998); however, because V is a highly mobile and unstable element (Brookins 1988), high concentrations of V reflect either an affinity of vanadium for organic matter or the favorability of conditions that preserve organic matter to partition dissolved vanadium into the sediment (Breit & Wanty, 1990). In addition, unlike Mo, V is not trapped in solid solution by Fe-sulfides making it a good indicator of anoxia, but not a reliable indicator of euxinia (Brumsack, 1989; Algeo and Maynard, 2004).

Uranium is well known for having a constant concentration in sea waters from all ocean basins (Swanson, 1961; Calvert & Pedersen, 1993). U is commonly fixed in the organic fraction, but also precipitates as sulfide minerals and may be present in phosphates generally in the form of nodules (Swanson, 1961). In anoxic basins, the enrichment of U is considered to occurs primarily within the sediment and not in the water column (Zheng et al., 2002; Algeo & Maynard, 2004; Tribovillard et al., 2006). In other words, a relationship can be established between U and organic matter but no correlation with bottom-water redox conditions (Zheng, et al, 2002). Additionally, U can be remobilized from sediments if oxygen penetrates to a depth where authigenic U has accumulated, resulting in the erasing of the uranium signal or in the vertical migration through the sediments (Tribovillard et al., 2006).

In this study, concentrations of redox-sensitive elements are highly related with lithology (**Figure 59**). Soft beds contain higher abundances of Mo, V and U than hard ones, which may imply that anoxic-euxinic conditions were stronger during deposition of soft beds (i.e. shales), resulting in significantly higher TOC contents for soft beds (~13 wt.%) compared to hard beds (~3 wt.%).

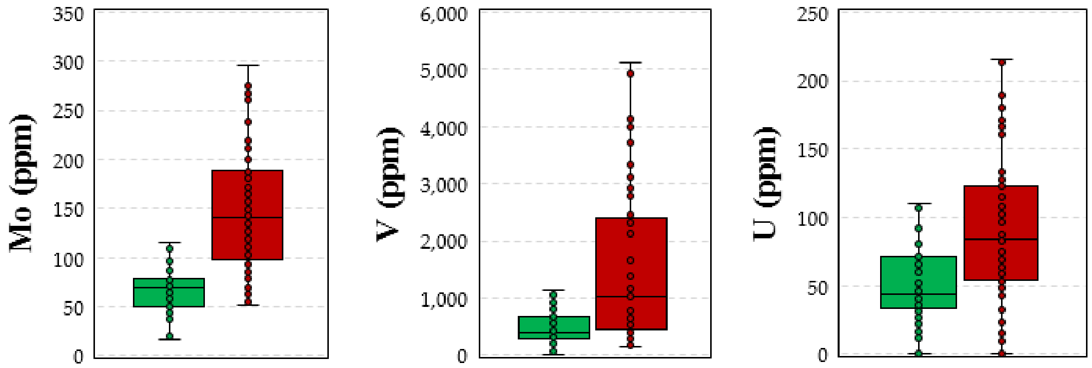

Figure 59. Individual box plots for the main redox-sensitive elements displaying higher abundances in soft beds (i.e. Siliceous Shales) than in hard ones (e.g. Cherts). Soft samples (red) *n*= 80, hard samples (green) *n*= 76.

A cross-plot of Mo versus TOC gives a good positive covariance (**Figure 60**), implying the affinity of Mo to the organic matter present within the analyzed samples, thus allowing further estimation of TOC contents by using Mo concentrations. Additionally, Mo displays a positive covariance with TOC and S, which suggests paleoenvironments of deposition under anoxic-euxinic conditions.

As for V and U, weak relationships are observed between V – TOC and V- Mo, whereas moderate positive relationships are observed for U - TOC and U – Mo (**Figure 60**), which might indicate the presence of V and U in other phases different than organic matter, probably in the form of authigenic phosphates, as evidenced by the synchronous increment of P with V (**Figure 61**).

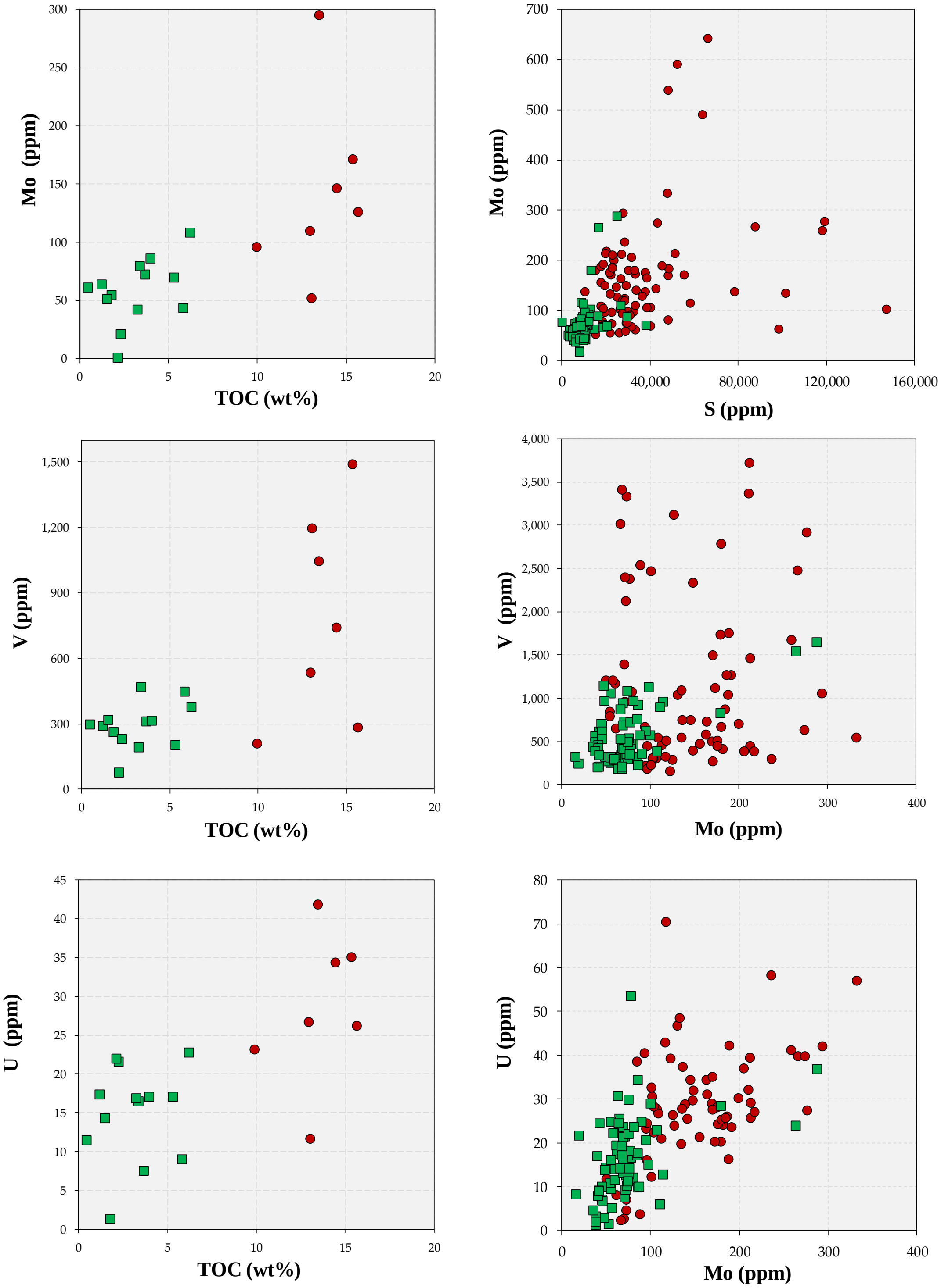

Figure 60. Cross plots between redox-sensitive elements differentiated by hard (green squares) and soft (red dots) lithologies. Overall, positive relationships of Mo-TOC and Mo-S which might indicate euxinic bottom waters.

8.1.Chemostratigraphic Variations with Depth

Vertical profiles of 12 elemental proxies are plotted in **Figure 61**, from which general trends, and spikes are qualitatively described. Graphical distinctions between 'hard' (green curve) and 'soft' (red curve) beds were implemented in order to better highlight the actual elemental contribution from each rock type (**Figure 61**).

At first glance, the dissimilar appearance between the two curves (i.e. red and green) is glaring (**Figure 61**). For most of the elemental proxies, regardless of their stratigraphic position, soft beds present higher concentrations than hard ones, with the exception being the Si/Al ratio and carbonate proxies (i.e. Ca, Sr, Mg) which show significantly higher concentrations within hard beds (**Figure 61**).

The Si/Al ratio curve for hard beds steadily displays high values throughout the section, reaching their highest values above foot 65 (**Figure 61**). Conversely, the very low Si/Al values for hard beds correlates with very high peaks of Ca, Sr and Mg, thus corroborating the position of dolomitic beds (**Figure 61**). Regarding Si/Al ratios of soft beds, these are extremely low and remains static throughout the section (**Figure 61**).

Throughout the section, concentrations of detrital and clay proxies (Ti, Zr, Al, K) are significantly higher in soft beds than in hard ones, displaying a decrement upsection followed by a subtle increment at the uppermost 10 feet, perhaps indicating more intense detrital pulses at the very end of the Woodford deposition at this section (**Figure 61**).

Carbonate proxies curves (Ca, Sr and Mg) are parallel throughout the section, remaining almost static and with low values (**Figure 61**), excepting a few discrete high peaks that also coincides with very low Si/Al ratios that correspond with the dolomitic beds.

Contrasting this interpretation, Turner (2016) reported the association of high Ca and Sr concentrations in the Upper Woodford Shale with phosphates. Although such association was not evident in this study, one can conclude that the presence of Ca and Sr within the Woodford Shale may be related to either phosphate (as found by Turner) or dolomites (this work).

For most of the section, redox-sensitive proxies (Mo, U and V) show lower concentrations in hard beds with respect to soft ones (**Figure 61**). Generally, V signal do not seem to be in phase with Mo and U, excepting *zone e* (75 - 81 feet) where Mo, U and V together depict a pronounced high peak for soft and hard beds, correlating with one of the highest gamma-ray readings (**Figure 61**). The V signal presents the lowest values for hard and soft beds at the *zone a* (0 - 25 feet) while Mo and U signals are higher across this zone. In the same way, Mo and U together reach their lowest values for soft and hard beds at *zone d* (60 – 70 feet), coinciding with the blocky trend in the gamma-ray (**Figure 61**), making this a potential important marker for chemostratigraphic correlations.

Through the description of individual vertical profiles, it was demonstrated that for most of the elemental proxies there is a large duality of signals between soft and hard lithologies even between adjacent samples, which could lead to biased interpretations if either solely hard beds or soft ones are accounted for interpretations. Then, since chemostratigraphic studies using outcrop samples cannot be done at high resolutions as done for well-cores (about 1 inch) and, taking into account that the Woodford Shale is characterized by interbedding of soft and hard lithologies, conducting lithology-guided sampling rather than systematic sampling is recommended.

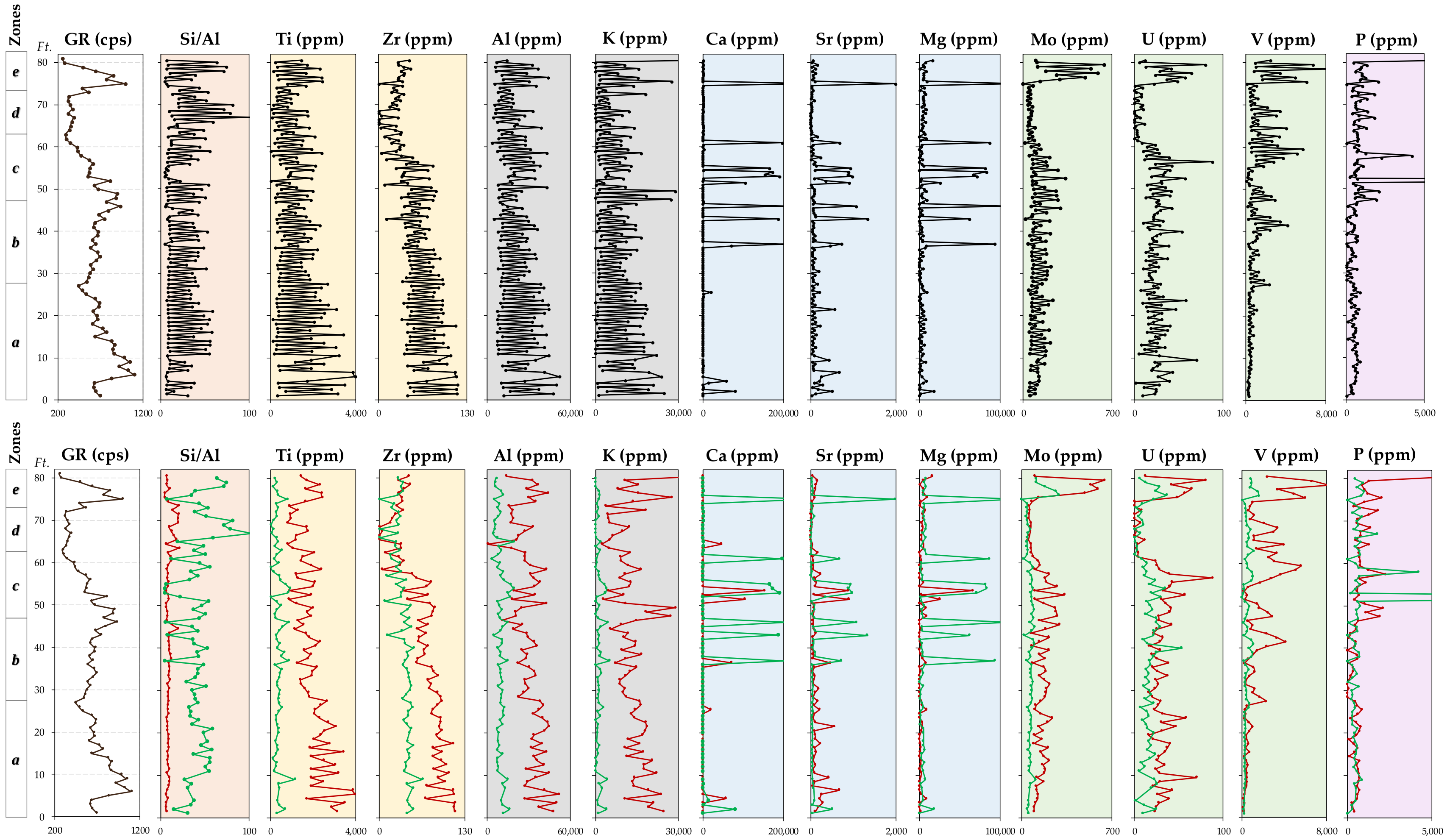

Figure 61. Chemostratigraphic profile of the I-35 Woodford section presenting the major and trace elements interpreted in this study along with outcrop gamma-ray profile. Upper graph represents stacked results for the 157 samples whereas lower graph separate elemental signals by sample lithology: soft samples (red curve) and hard samples (green curve).

8.2.Chemofacies Characterization

To analyze the variability of elemental proxies considering several of them simultaneously rather than describing individual trends, hierarchical cluster analysis (HCA) was performed using as input variables the previously revised major and trace elements including, Si/Al ratio, Al, K, Ti, Zr, Ca, Sr, Mg, Mo, U, V, and P. The usage of these elements has proved consistency across other previous chemostratigraphic studies of the Woodford Shale at different locations in Oklahoma (Trenton, 2014; Turner, 2016; Maynard, 2016; Zhang, 2016; Ekwunife, 2017; Galvis, 2017).

First, since major and trace elements are measured in different orders of magnitude (e.g. Al: 300,000 ppm and Mo:10 ppm), the standardization of variables is required to ensure that all elements will have the same influence on the results, otherwise the variables with larger values will dominate certain clusters (Templ et al, 2008); therefore, all 12 variables were standardized to mean 0 and variance 1.

The hierarchical cluster analysis was performed using Minitab software; we used Euclidean distance as a similarity measurement between variables and Ward's method for linkage, as suggested by (Güler et al., 2002; Templ et al., 2008; Turner, 2016). HCA results are graphically represented by a dendrogram (**Figure 62**). The optimal number of clusters needed to better represent the variability within the dataset was chosen by establishing a 'phenon line', which is a line that cuts the dendrogram at a level of Euclidian distance able to isolate meaningful clusters (**Figure 62**).

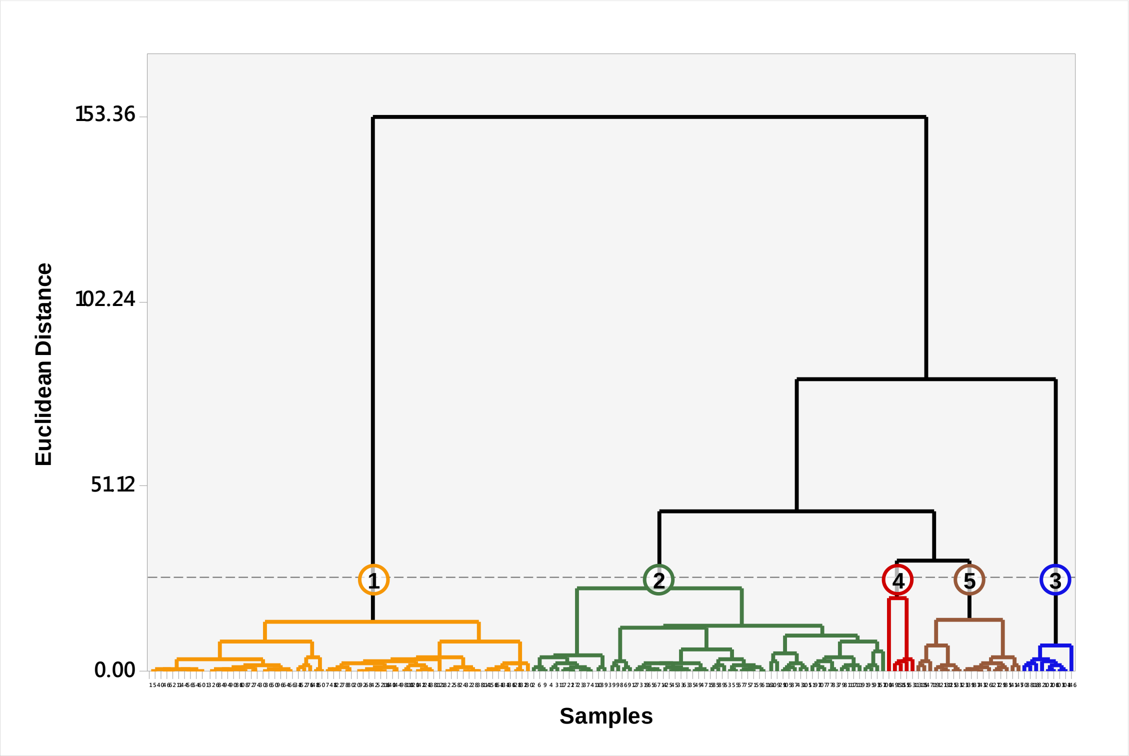

Figure 62. Dendrogram resulting from hierarchical clustering analysis showing how the 157 samples of the I-35 outcrop are distributed across the 5 clusters. Dashed line is ‘‘phenon line’’ chosen by analyst to select number of clusters. The y-axis represents the Euclidean distance between each cluster, the x-axis represents the samples number and the different clusters are numbered from 1 to 5. The clustering includes 12 standardized variables: Si/Al, Al, K, Ti, Zr, Ca, Sr, Mg, Mo, U, V and P.

In order to facilitate the geological interpretation of the five selected clusters, an enrichment ratio (ER) was calculated following equation (3) introduced by Phillips (1991). It is based on comparing average concentrations of an element in a given cluster, to the average concentration of that element in all the 157 samples (**Table 4**). The enrichment or depletion of certain elements in the clusters are then used for the characterization of the chemofacies (**Table 5**).

$$\boldsymbol{Enrichment\ Ratio\ (ER)} = \frac{\text{Avg. element X in cluster}}{\text{Avg. element X in all 157 samples}} \tag{3}$$

	Si/Al	Al (ppm)	K (ppm)	Ti (ppm)	Zr (ppm)	Ca (ppm)	Sr (ppm)	Mg (ppm)	Mo (ppm)	U (ppm)	V (ppm)	P (ppm)
Avg. 157 Samples	25	20444	7435	1154	50	13495	147	8197	120	22	1080	783
Avg. Cluster 1	47	8841	806	299	36	306	47	4030	76	15	559	578
Avg. Cluster 2	9	31813	14283	2036	80	5619	151	2790	163	31	1073	663
Avg. Cluster 3	6	12245	3057	683	26	194521	1056	86368	52	22	197	229
Avg. Cluster 4	10	31495	9963	1598	34	411	167	3383	468	55	4643	5258
Avg. Cluster 5	14	25475	10037	1417	18	492	37	3519	77	8	2437	956

Enrichment ratio	Si/Al	Al	K	Ti	Zr	Ca	Sr	Mg	Mo	U	V	P
Cluster 1	1.87	0.43	0.11	0.26	0.72	0.02	0.32	0.49	0.63	0.67	0.52	0.74
Cluster 2	0.36	1.56	1.92	1.76	1.59	0.42	1.03	0.34	1.35	1.43	0.99	0.85
Cluster 3	0.25	0.60	0.41	0.59	0.52	14.41	7.17	10.54	0.43	0.99	0.18	0.29
Cluster 4	0.41	1.54	1.34	1.38	0.69	0.03	1.13	0.41	3.89	2.48	4.30	6.72
Cluster 5	0.54	1.25	1.35	1.23	0.36	0.04	0.25	0.43	0.64	0.36	2.26	1.22

Table 4. Upper table presents averages of each of the 12 variables within the 5 different clusters. Lower table contains the results of enrichment ratio per cluster colored horizontally where higher values are in greenish and lower in reddish.

Chemofacies 1 is characterized by the highest Si/Al values within the section (avg. 47) indicating a very high biogenic input; very low concentrations of detrital proxies (Al, K, Ti and Zr) and low concentrations of carbonate proxies (Ca, Sr, Mg) are present. Redox proxies (Mo, U, V) are relatively low within the section (**Table 4**). Vertically, the presence of chemofacies 1 is ubiquitous across the entire section (**Figure 63**).

Chemofacies 2 contain the highest concentrations of detrital proxies (Al, K, Ti and Zr) among the section as well as very low Si/Al ratio (avg. 9) (i.e. low biogenic input); relatively high abundances of redox proxies (Mo, U and V) generally indicate organic rich beds. Chemofacies 2 are mostly observed in *zones a, b* and *c*, and almost absent in zones *d* and *e (***Figure 63***)*.

Chemofacies 3 is undoubtedly related to dolomitic beds, showing the highest concentrations of Ca, Sr and Mg accompanied by very low Si/Al ratios (avg. 6) and low detrital proxies (Al, K, Ti, Zr); redox proxies are very low (**Table 4**), especially Mo and V present the lowest concentrations compared to other chemofacies (**Table 4**). Vertically, chemofacies 3 is mainly clustered in the middle part of the section (*zones b* and *c*) (**Figure 63**).

Chemofacies 4 is enriched in P as well as in redox proxies (Mo, U and V), the latter having the highest concentrations in this chemofacies; detrital proxies (Al, K, and Ti) are high, whereas Si/Al ratios are moderate to low (avg. 10) compared to the rest of the population (**Table 4**). It is important to mention that in cases where samples contained phosphate nodules, the XRF measurements were not done over the phosphate nodule, meaning that the relatively high P values should be related to the surrounding rock matrix rather than nodules; just for context a typical concentration of P within phosphate nodules is above 500,000 ppm. The presence of Chemofacies 4 is restricted to the upper part of the section (*zone e*), where most of the phosphate nodules occur (**Figure 63**).

Finally, Chemofacies 5 is characterized by very high concentrations of V, and P; also, high concentrations of detrital proxies (Al, K, Ti) are observed accompanied by moderate values of Si/Al ratios (avg. 14) (**Table 4**). In contrast to Chemofacies 4, Chemofacies 5 presents very low concentrations of Mo and U. Vertically, Chemofacies 5 is limited to the uppermost part of the section (*zones c* and *d*) (**Figure 63**).

Cluster #	Chemofacies #	Samples in cluster	Elemental Responses	Interpretation
Cluster 1	**1**	65	Very High Si/Al Very Low Al, K, Ti, Zr Low Mo, U, V	High biogenic input, Low detrital input, Low organics
Cluster 2	**2**	60	Very High Al, K,Ti, Zr Low Si/Al Moderate Mo, U, V	High detrital input, Low biogenic input, Moderate organics
Cluster 3	**3**	9	Very High Ca, Sr, Mg Very Low Si/Al Very Low Al, K, Ti, Z Low Mo, U, V	High carbonates, Very low biogenic and detrital input, Low organics
Cluster 4	**4**	5	High Al, K, Ti Low Si/Al Very High Mo, U, V, P	High detrital input, Low biogenic input, High phosphates (upwelling?)
Cluster 5	**5**	18	High Al, K, Ti Moderate Si/ Al High V, P	High detrital input, Moderate biogenic input, High Phosphates (upwelling?)

Table 5. Summary table showing the characteristics of each cluster according to their elemental enrichments/depletions. Color code of clusters is the same for dendrogram and vertical profiles.

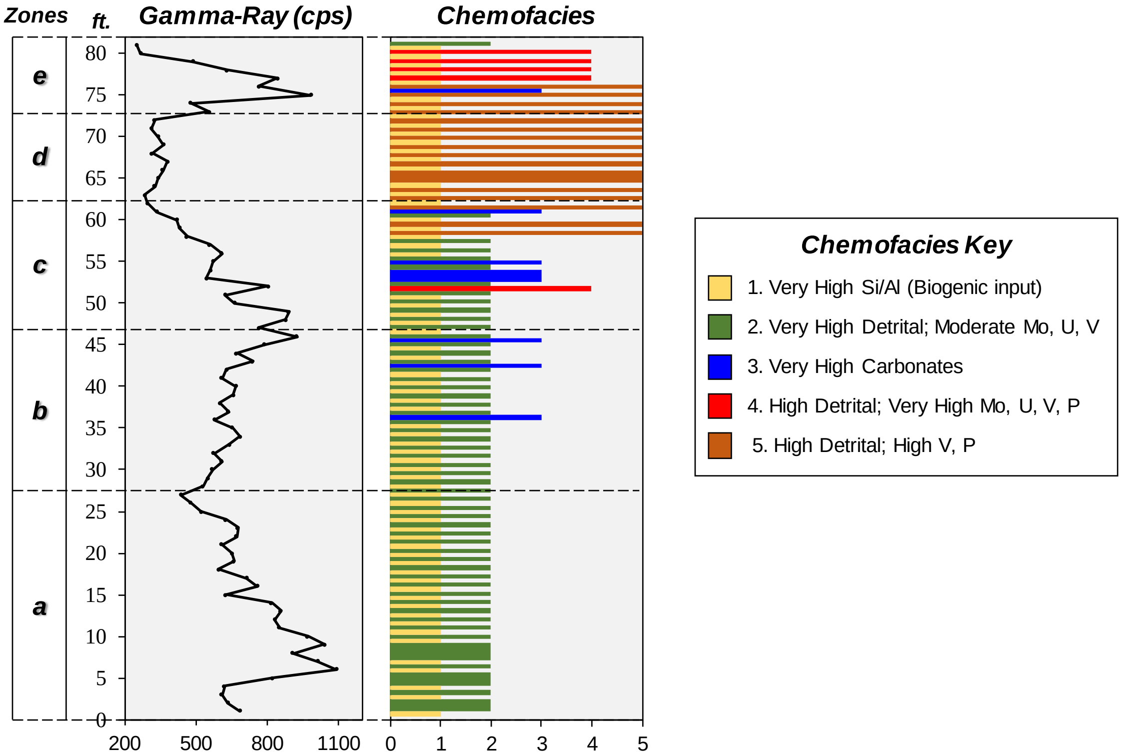

Figure 63. Vertical distribution of the five chemofacies identified by clustering analysis.

8.3.XRF and Lithofacies

In this study, elemental concentrations of specific elemental proxies were found closely related to lithofacies and perhaps to mineralogy (**Figure 64**). Si/Al ratios commonly used as a proxy for quartz content, is markedly higher in Cherts in comparison with the rest of the lithofacies (i.e. Siliceous Shales, Siliceous-Dolomitic Shale and Dolomitic Mudstone) (**Figure 64**).

Detrital proxies (Ti and Zr) and clay proxies (Al and K) display a parallel tendency within the four lithofacies (**Figure 64**). Siliceous Shale lithofacies presents the highest concentration of these elements; then in order of abundance are lithofacies of Siliceous-Dolomitic Shale, Dolomitic Mudstone and Chert in moderate to low concentrations (**Figure 64**). Carbonate proxies (Ca, Sr, and Mg) are highly restricted to the dolomitic lithofacies (Siliceous-Dolomitic Shale and Dolomitic Mudstone) (**Figure 64**). The concentration of these elements is minimum for the rest of the lithofacies (**Figure 64**). Also, the average concentration of the three revised carbonate proxies is higher in dolomitic mudstone lithofacies (hard beds) in comparison to Dolomitic Shales lithofacies (soft beds).

Redox-sensitive proxies (Mo, U and V) did not reveal consistent patterns across the four lithofacies as was reported in previous sections; in general, redox proxies concentrations are elevated in the siliceous shales (**Figure 64**).

To summarize, when grouped by lithofacies, elemental concentrations revealed the close relationships between elemental and mineralogical compositions, at least for the Woodford in I-35 outcrop; for that reason, I explored three different approaches to calculate mineralogical composition based on elemental data.

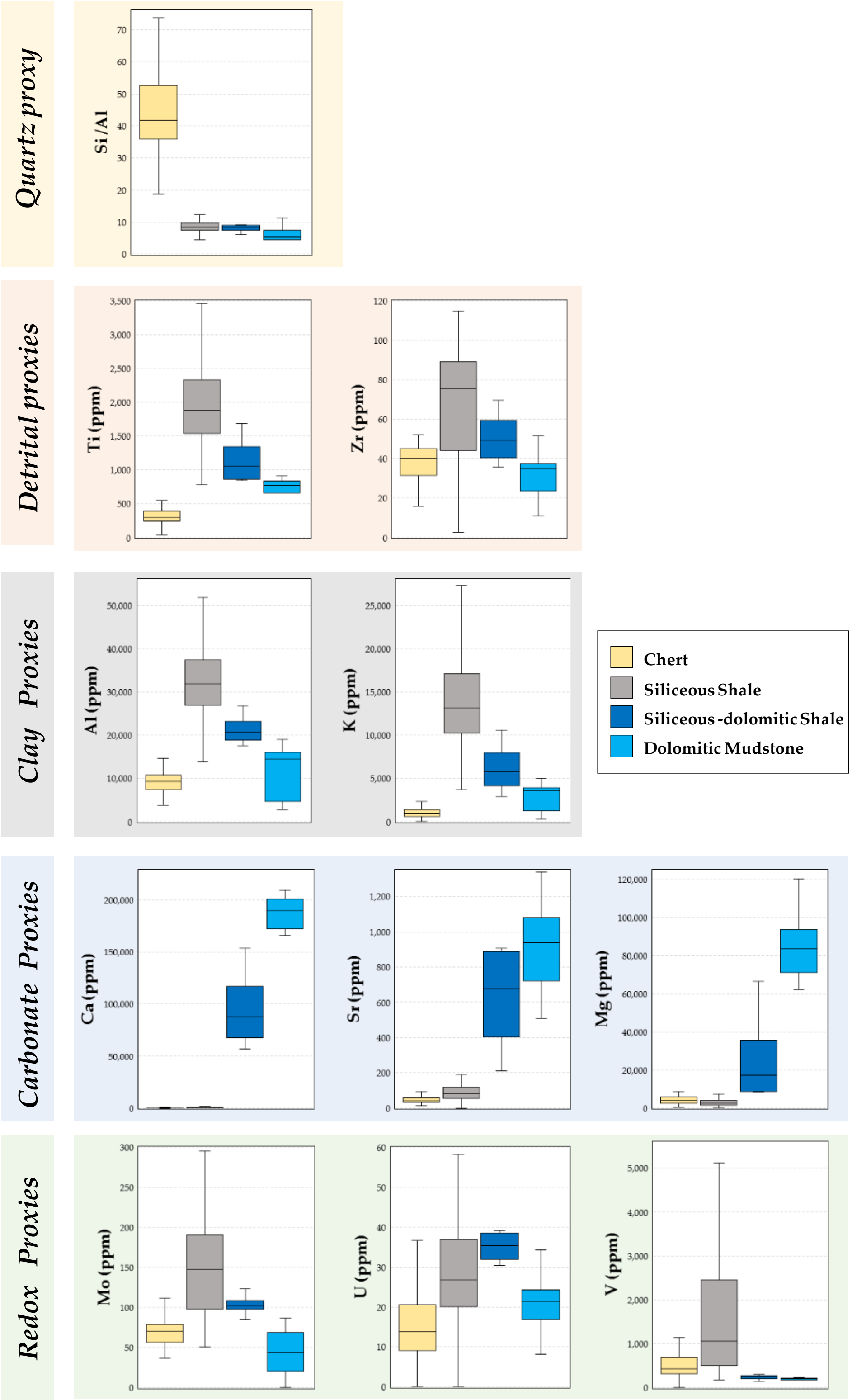

Figure 64. Elemental concentration across the lithofacies. Chert (n= 68); Siliceous Shale (n= 76); Siliceous-Dolomitic Shale (n= 4); Dolomitic Mudstone (n= 9).

8.4.Modeling Mineralogy Using Elemental Data

X-ray diffraction (XRD) is the most common technique used to identify and quantify mineral composition of rocks. However, owing to its relatively high-cost and length of time to analyze, usually only a few samples are tested with this technique. Consequently, over the last decade several authors have attempted to calculate mineral composition of mudrocks from X-ray fluorescence (XRF) elemental data, which is a relatively low-cost and rapid analytical technique (Ratcliffe, 2010; Wright et al., 2010; Stilwell et al., 2013; Thruston & Taylor, 2016; Ruppel et al., 2017). Most of these published methodologies that relate minerals from XRD to elements from XRF are based on empirically obtained linear regressions that are highly dependent on the mineral associations present in each formation.

As an alternative, by using our own XRF-XRD datasets, we explored three different approaches to estimate bulk mineralogy from elemental concentrations. Results from the better performing approach are later used to calculate the mineralogical brittleness index for comparisons with other mechanical properties.

XRD mineralogical composition from this study, as well as other published data for the Woodford Shale (O'Brien & Slatt, 1990; Kirkland et al., 1992; Fishman et al., 2013) reveals how simple the Woodford Shale mineralogy is, predominantly consisting of admixtures of quartz (54 - 99%) and clays (<50%), with few dolomite-rich beds, thus implying a facilitated capability for modeling mineralogy from XRF elemental concentrations. For this reason, hereinafter the Woodford mineralogy is simplified into quartz-clays-carbonates, and the significantly low proportions of other minerals (e.g. pyrite, gypsum) can be ignored for practical purposes.

8.4.1. Approach #1: Normalized Si – Al+K+Ti+Rb – Ca+Sr+M+Mn concentrations

Considering the correlation coefficient as a measure of the extent to which two variables vary together (Pearson, 1920), this approach is based upon the natural correlation coefficients obtained between elements (XRF) and minerals (XRD). First, a correlation matrix was built using as input variables the elemental and mineral concentrations obtained from 46 samples that were scanned by XRF and XRD (**Table 6**).

The matrix compared results of 30 elements with the simplified quartz, clays and carbonates mineralogy (**Table 6**). Then, the highest correlation coefficients (>0.80) were highlighted, statistically meaning that certain specific elements appear more related to a specific mineral. As shown in **Table 6**, silicon (Si) appears highly related with quartz. Aluminum (Al), potassium (K), titanium (Ti) and rubidium (Rb) are associated with clays. Calcium (Ca), strontium (Sr), magnesium (Mg) and manganese (Mn) are associated with carbonates. Remarkably, it is found that there is no overlap between sets of elements that represent each mineral, as is the case of Si exclusively with quartz, etc. Thus, according to this approach the calculated mineralogy will be the contribution of Si, Al, Ti, K, Rb, Ca, Sr, Mg, Mn, and each mineral group (i.e. quartz, clays and carbonates) is calculated in terms of their correlative elements, according to equations 4, 5, 6 and 7.

$$Total = Si + Al + Ti + K + Rb + Ca + Sr + Mg + Mn \quad (4)$$

$$Quartz\,\% = \frac{(Si) * 100}{Total} \quad (5)$$

$$Clays\,\% = \frac{(Al + K + Ti + Rb) * 100}{Total} \quad (6)$$

$$Carbonates\,\% = \frac{(Ca + Sr + Mg + Mn\,) * 100}{Total} \quad (7)$$

	Quartz	Clays	Carbonates
Si	0.91	0.06	-0.87
Al	-0.08	0.86	-0.31
K	-0.11	0.80	-0.25
Ti	-0.14	0.84	-0.25
Rb	-0.04	0.88	-0.35
Ca	-0.87	-0.38	0.98
Sr	-0.81	-0.26	0.87
Mg	-0.85	-0.39	0.96
Mn	-0.67	-0.43	0.82
Zr	0.08	0.60	-0.34
V	0.07	0.34	-0.22
Mo	0.10	0.48	-0.31
U	-0.13	0.46	-0.08
P	0.09	0.25	-0.20
Na	0.40	0.22	-0.47
S	-0.14	0.53	-0.11
Ba	-0.74	-0.14	0.75
Cr	0.78	-0.02	-0.71
Fe	-0.04	0.45	-0.16
Co	-0.22	0.43	0.01
Ni	-0.18	0.42	-0.03
Co	-0.20	0.25	0.08
Zn	-0.27	0.16	0.18
As	-0.24	0.47	0.01
Pb	0.02	0.69	-0.32
Th	-0.08	0.65	-0.22
Y	-0.28	-0.31	0.40
Nb	-0.19	0.28	0.06
Sn	-0.24	0.57	-0.03
Sb	-0.10	0.47	-0.12

Table 6. Pearson correlation coefficients calculated between 30 elements and 3 simplified mineralogy groups: quartz, clays and carbonates. Highlighted in green are the positive correlation coefficients >0.80.

8.4.2. Approach #2: SiO_2 – Al_2O_3*5 – CaO*2

This approach is based on a ternary diagram (SiO_2 – Al_2O_3*5 – CaO*2) developed by Brumsack (1989) to characterize major constituents of recent marine sediments. It is based on the fact that marine sediments may be regarded as mixtures of three main components: clays, quartz and carbonates. According to Brumsack (1989), the SiO_2 end-member represents contributions from silica and aluminosilicates, the Al_2O_3*5 represents the aluminosilicates, and the CaO*2 represents the carbonate component.

To calculate mineralogy using this approach, the first step is to convert concentrations of Si, Al and Ca to their oxide form (i.e. SiO_2, Al_2O_3 and CaO), which is obtained by multiplying the measured weight percent of each element (Si, Al and Ca) by the product of subdividing their corresponding oxide molecular mass by the element atomic mass, according to equations 8, 9, and 10.

Then, the mineral composition is calculated and normalized to 100 percent using equations 11, 12, 13, and 14.

$$SiO_2 = \frac{(\%Si) * 60.084}{28.086} \qquad (8)$$

$$Al_2O_3 = \frac{(\%Al) * 101.961}{26.892} \qquad (9)$$

$$CaO = \frac{(\%Ca) * 56.077}{40.078} \qquad (10)$$

$$Total = \; SiO_2 \; + (\,5 * Al_2O_3) + (2 * CaO) \quad (11)$$

$$Quartz\,\% = \frac{(SiO_2) * 100}{Total} \qquad (12)$$

$$Clays\,\% = \frac{(\,5 * Al_2O_3)\ *\ 100}{Total} \qquad (13)$$

$$Carbonates\,\% = \frac{(2 * CaO) *\ 100}{Total} \qquad (14)$$

8.4.3. Approach #3: MINLITH™

This approach uses the free-access computer algorithm MINLITH™, which calculates bulk rock composition of sedimentary rocks using information from chemical analysis (e.g. XRF) (Rosen et al., 2004). Input variables are entered in the form of oxides in wt.% and include a set of 18 elements and oxides listed in **Table 7**. Internally, the algorithm comprises a vast number of arithmetic operations designed to allocate oxides to normative minerals based on their standard chemical formulas (Rosen & Abbyasov, 2003). Although the MINLITH™ algorithm is capable of calculating up to 25 different minerals, in order to keep the Woodford Shale mineralogy simple, only quartz, clay and carbonates were normalized to 100 percent.

MINLITH Input Data

SiO_2	CaO	SO_3
TiO_2	Na_2O	F
Al_2O_3	K_2O	Cl
Fe_2O_3	P_2O_5	S
FeO	MnO	CO_2
MgO	C	SO

Table 7. List of oxides to input in MINLITH™ computer program. (Rosen et al., 2004)

Mineralogy was calculated using the three revised approaches, and results were plotted (**Figure 65**). It was generally observed that modeled quartz, clays and carbonate contents are comparable to the actual range obtained from XRD. However, looking closer in the case of quartz, Approaches #1 and #3 are good at predicting the higher quartz contents but seem to overestimate some of the lower contents (around 60 to 80wt.%) (**Figure 65**).

Approach #2 on the other hand, is better at resembling the actual range of data. With regard to the modeled clay contents an opposite behavior was observed (**Figure 65**), where Approaches #1 and #3 underestimate or do not predict accurately some high clay contents within the range of 20 to 40wt.%, whereas Approach #2 predicts most of the actual distribution of clays (**Figure 65**). As for the carbonate contents, none of the three approaches seem to model larger values (>85wt%), as accurately as for the very small-to-zero values (**Figure 65**), in other words the three approaches underestimate the actual high carbonate contents.

Despite this, considering that the composition of the Woodford Shale is largely made of quartz and clay admixtures, and that the carbonate contents are highly restricted to scattered and few dolomitic beds, moderate errors in the prediction of carbonate contents can be generally accepted, at least for the Woodford strata.

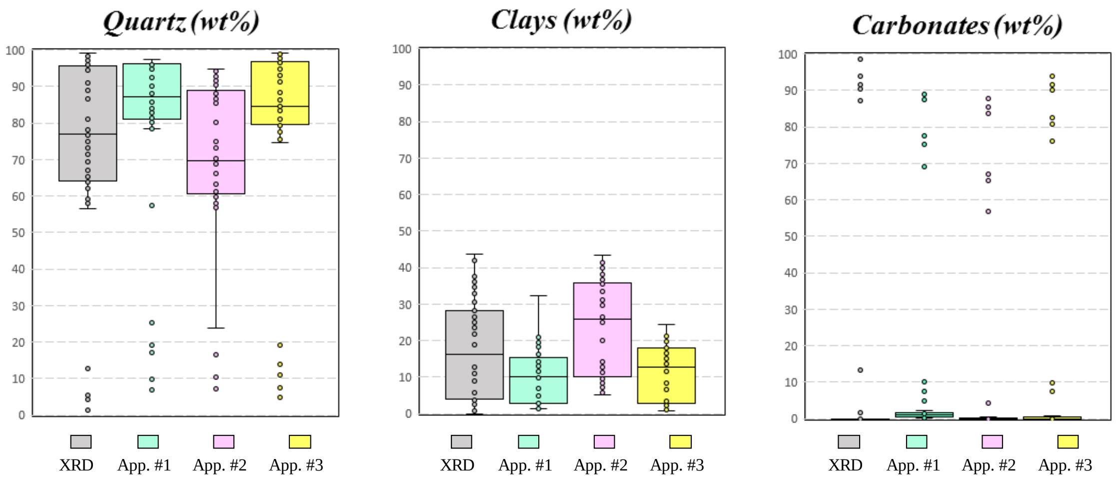

Figure 65. Boxes and whisker plots for quartz, clays and carbonate contents, comparing the actual mineralogy obtained by XRD (gray boxes) to the mineralogy obtained from the three approaches: Approach #1 (cyan box), Approach #2 (pink box) and Approach #3 (yellow box). Plots include samples that were scanned for XRD as well as XRF analyses (n=46).

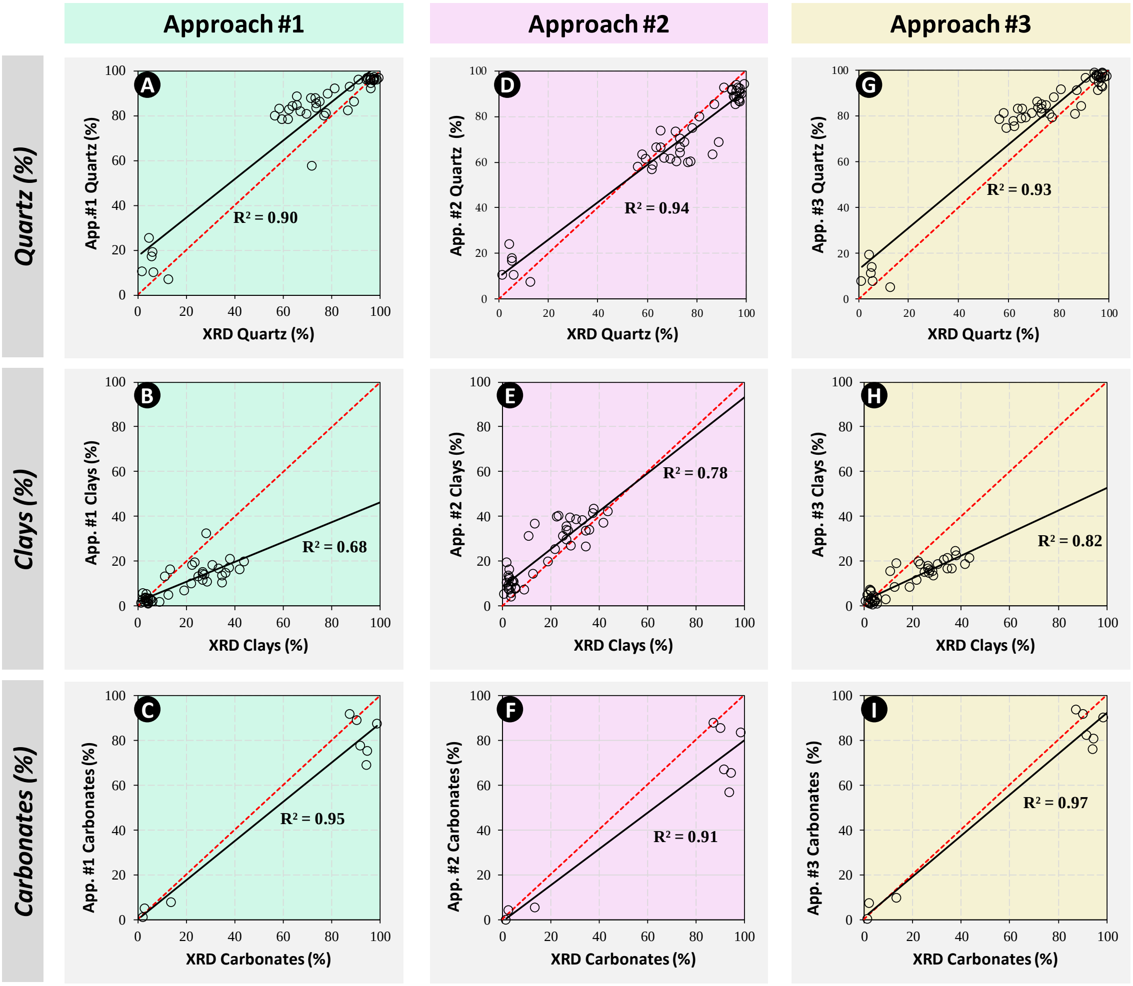

Figure 66. Cross-plots between the actual quartz, clay and carbonate contents measured by XRD analysis versus the results of calculated mineralogy by each of the three approaches: Approach #1 (cyan), Approach #2 (pink) and Approach #3 (yellow). The red line is an identity line (1:1 line).

Now, the simplest way to validate the accuracy of each approach is by regression analysis, which is a statistical process used to investigate the relationship between two variables (Miller, 1986); we analyzed the relationship between the 'predicted' mineralogy by each specific approach (e.g. Approach #1) with the actual mineralogy obtained from XRD (**Figure 66**).

The first observation has to do with the distribution of the data points; particularly in the case of quartz, results from the three approaches are clustered into two main groups (**Figure 66A**, **66D** and **66G**), one for high quartz contents (60 to 100%) and the other for very low quartz contents (<20%). This 'anomalous' clustering in the distribution of data points is not unanticipated and can be explained; since the Woodford Shale composition is mostly dominated by quartz, any clusters representing lower quartz contents can be directly related to the dolomite-rich beds within the Woodford Shale. Similarly, carbonate contents appear clustered into two groups (**Figure 66C**, **66F**, **66I**), the first one with elevated carbonate contents (>80%) related to the dolomitic beds, and the second group with minor amounts of carbonates (<15%) occurring within Siliceous Shales and Cherts.

Another key element to evaluate from regressions is the coefficient of determination denoted R^2, which indicates the proportion of the variance explained by the model (Nagelkerke, 1991). In other words, R^2 is a measure (from 0 to 1) of how close the predicted values are to the actual data, so the higher the R^2 the better the model fits the actual data. **Figure 66** shows that R^2 values are relatively high for all three mineral groups (i.e. quartz, clays and carbonates) predicted by the three approaches, they range from 0.68 to 0.97. Among the three approaches, quartz and carbonate contents persistently give elevated R^2 values (0.9-0.97) in comparison to clay content (0.68-0.82). Based merely on R^2 values, Approach #3 displays the highest R^2 numbers in predicting quartz (0.93), clays (0.82) and carbonates (0.97) (**Figure 66G**, **66H**, **66I**).

Despite the relatively high R^2 values obtained from the comparison between actual versus predicted mineralogy (quartz, clays and carbonates), it is noted that some of the approaches overestimates and/or underestimates some of the mineral groups, (e.g. clays) (**Figure 66B**, **66H**). To evaluate that, we considered an identity line (1:1 line) as reference reflecting y=x, or predicted=measured. Accordingly, we analyzed the contrast between the regression line (black line) and the identity line (red dashed line) for each approach, observing that clay contents predicted by Approach #1 and Approach#3 are markedly underestimated (**Figure 66B**, **66H**). Instead, the contrast is less marked for quartz and carbonate contents predicted by the three approaches (**Figure 66A**, **66D**, **66G**, **66C**, **66F**, **66I).** Overall, Approach #2 has data points closer to the identity line.

Finally, for an unbiased and more quantitative comparison of the efficiency of the three approaches, we used the root mean square error (RMSE). RMSE is a measurement of how accurately the model predicts the actual data (Barnston, 1992), so the smaller the RMSE value the better the model predicts the actual data. Additionally, RMSE values are reported in the same units as the response variable, which in this study is percent (%). The RMSE is calculated by the equation 15:

$$Root\ Mean\ Square\ Error = \sqrt{\frac{\sum_{i=1}^{n} (y_i - \hat{y}_i)^2}{n}} \qquad (15)$$

Where i is the variable in question (e.g. quartz percentage), y_i is the predicted variable (e.g. quartz percentage calculated by Approach #1), $\hat{y}_i$ is the measured variable (e.g. actual quartz percentage obtained by XRD), and n is the total number of samples (46) that had both XRF as well as XRD results.

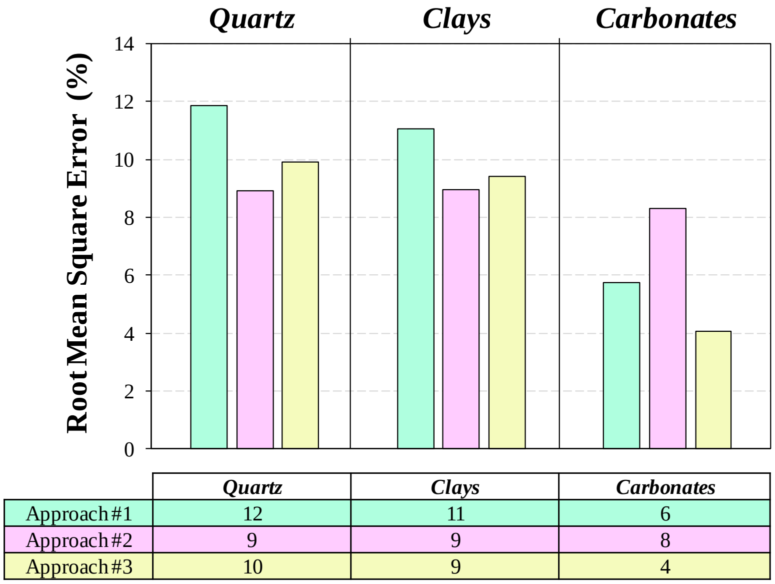

	Quartz	Clays	Carbonates
Approach #1	12	11	6
Approach #2	9	9	8
Approach #3	10	9	4

Figure 67. Comparison of the root mean square error (RMSE) for the three different approaches revisited in this study to estimate mineralogy using XRF data. Approach #1 (cyan), Approach #2 (pink) and Approach #3 (yellow).

Results of the root mean square error (RMSE) are displayed in **Figure 67**. Overall errors given by the three approaches are relatively low, ranging from 4 to 12% with higher errors for predicted quartz (6 - 12%) and clay contents (9 - 11%), and lower errors for carbonate contents (4 - 8%).

However, from the RMSE values across the approaches, Approach #2 better predicts actual quartz and clay contents. Even though it has the higher RMSE values for predicting carbonate contents (**Figure 67**), this can be accepted since within the Woodford Shale the presence of dolomitic beds is subordinate through the section. Thus, even with larger errors obtained by Approach #2 between the predicted and actual carbonate contents, it is still possible to associate the modeled carbonate contents to the actual dolomite-rich beds in the Woodford Shale.

Figure 68 graphically presents the summary of 46 samples that had both XRD (actual), and predicted mineralogy from XRF data, confirming that Approach #2 better resembles the actual data, and Approach #1 and #3 while similar between them, are further from fitting the actual data (**Figure 68**). Results of mineralogy calculated for the 157 samples using Approach #2 is presented in Figure 69, and its comparison with the measured mineralogy for 46 samples (XRD) clearly shows that the calculated mineralogy closely reflects the measured mineralogy.

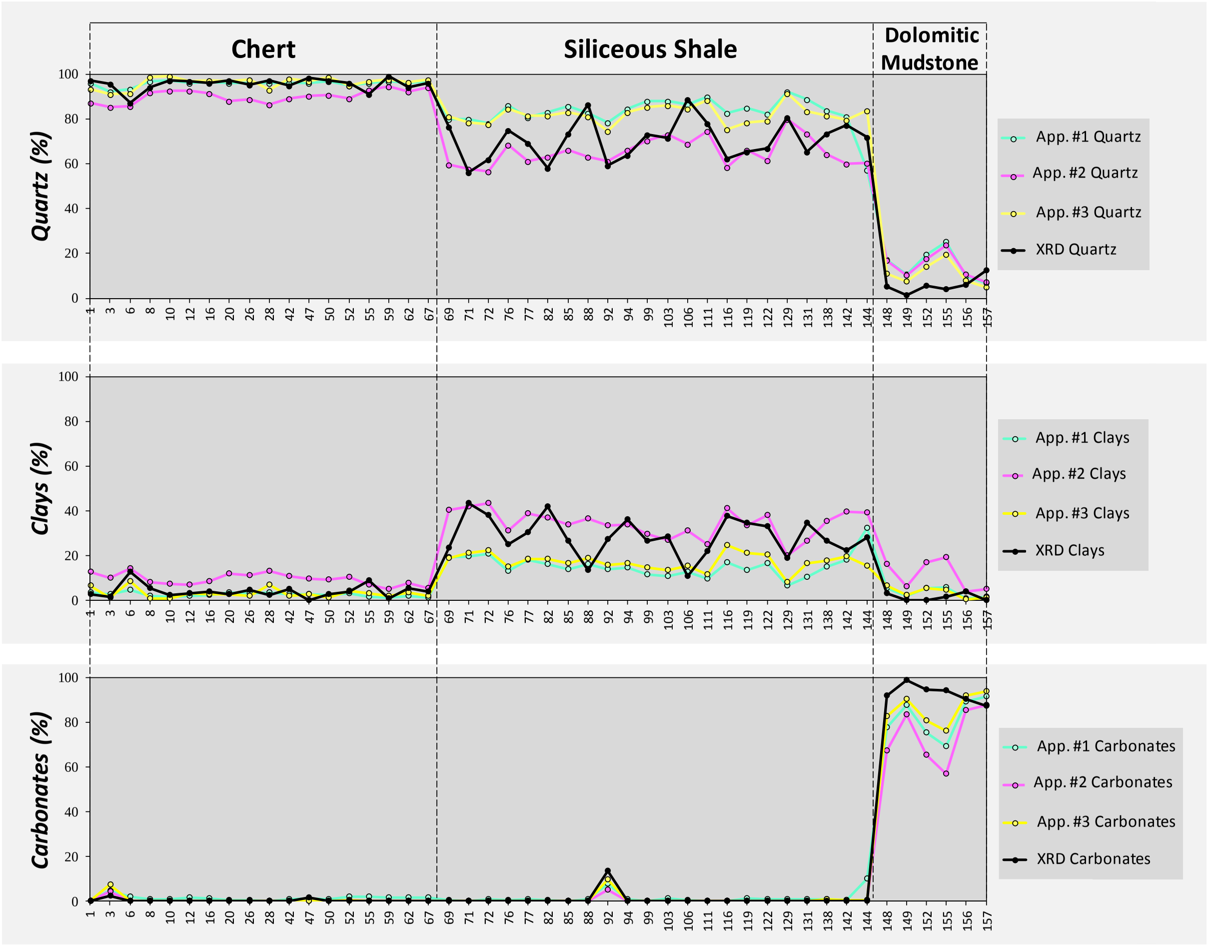

Figure 68. Scatter plot comparing the actual mineralogy obtained by XRD (black) to the mineralogy calculated by using the three approaches adopted in this study: Approach #1 (cyan), Approach #2 (pink) and Approach #3 (yellow). Data include samples that were scanned for XRD as well as XRF analyses (n= 46) however data points are not ordered by depth, instead they are arranged by lithofacies: Chert, Siliceous Shale and Dolomitic Mudstone.

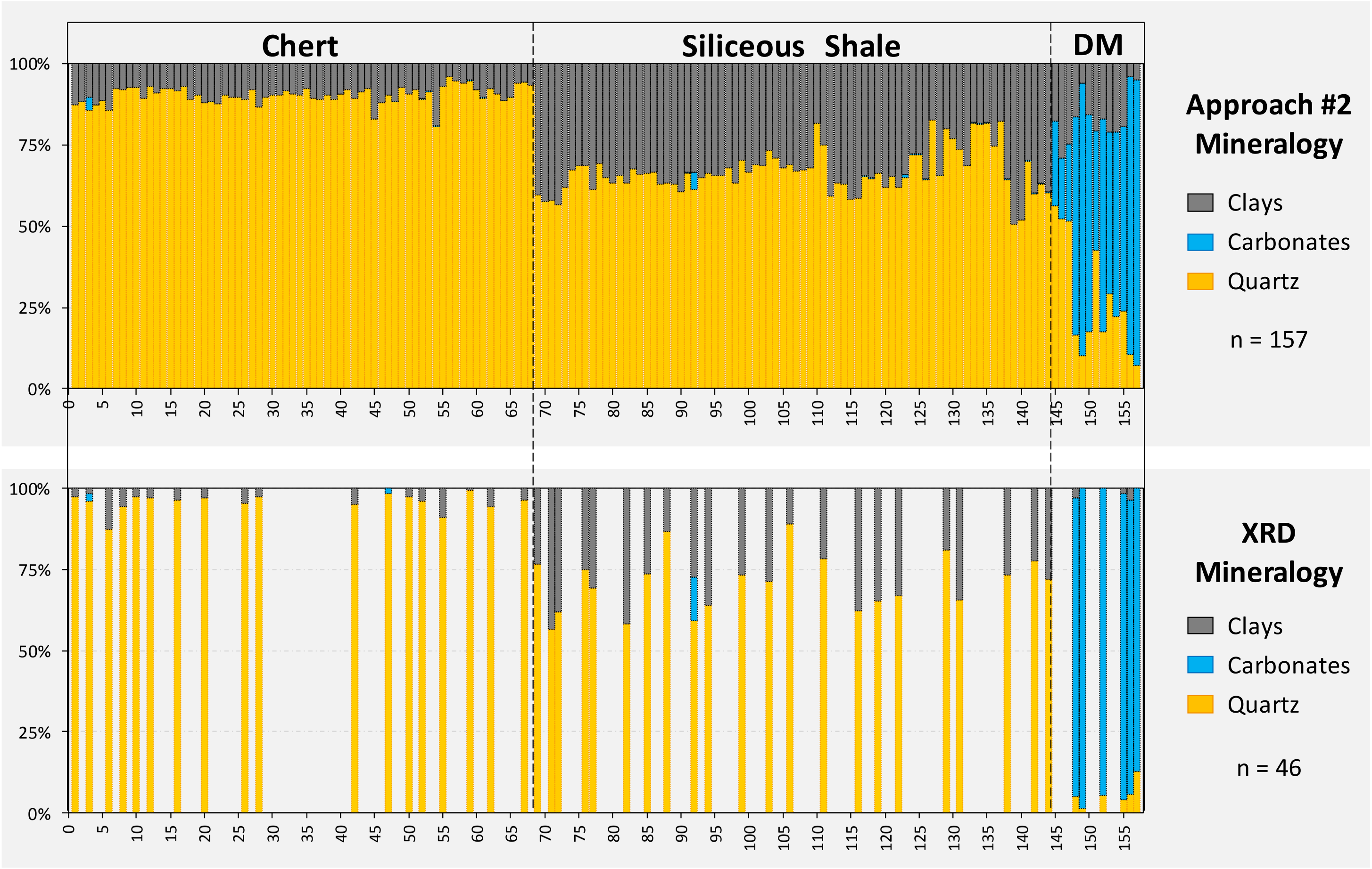

Figure 69. (**A**) Stacked-bar plot showing the simplified Woodford Shale mineralogical composition calculated using Approach #2 for 157 samples. Data points are not ordered by depth, instead they are arranged by lithofacies: Chert, Siliceous Shale and Dolomitic Mudstone (DM). (**B**) Stacked-bar plot showing the results of the XRD bulk analysis for 46 samples. Note the distinctive quartz and clay contents for Chert and siliceous shale lithofacies. Minerals are by weight percent (wt.%).

9. ROCK HARDNESS

Worldwide, the most used tests to measure mechanical properties of rocks are the uniaxial or triaxial tests. These tests are relatively pricey, highly destructive and somehow difficult to perform. An alternative method to indirectly estimate mechanical properties is the hand-held micro rebound hammer, which is relatively cheap, easy to operate and most importantly a non-destructive technique. Uses of the micro-rebound hammer to estimate mechanical properties of unconventional shales has been reliably proven by several researchers (e.g. Zahm & Enderlin, 2010; McClave 2014; Lee et al., 2014, 2016; Ritz et al., 2014; Dong et al., 2017).

In this study, to estimate rock hardness we used the hand-held micro rebound hammer (Piccolo 2). Hardness tests were performed on fresh cut surfaces of 157 samples from the I-35 outcrop. Hardness (LH) was measured parallel to the bedding plane, avoiding cracks, nodules or concretions and weathered beds (leached white).

At first glance, hardness results corroborate the soft - hard nature of Woodford Shale beds previously recognized at the field. As expected, soft beds present lower hardness values (avg. 540 LH), while hard beds present higher hardness values (avg. 800 LH) (**Figure 70**). Moreover, when hardness values are plotted by lithofacies, they revealed much narrower distributions (**Figure 70**), ordered from higher to lower hardness, Cherts are the hardest lithofacies (avg. 820 LH), followed by Dolomitic Mudstones (avg. 635 LH), Siliceous Shales (avg. 540 LH), and the least hard the Siliceous-Dolomitic Shales (avg. 499 LH).

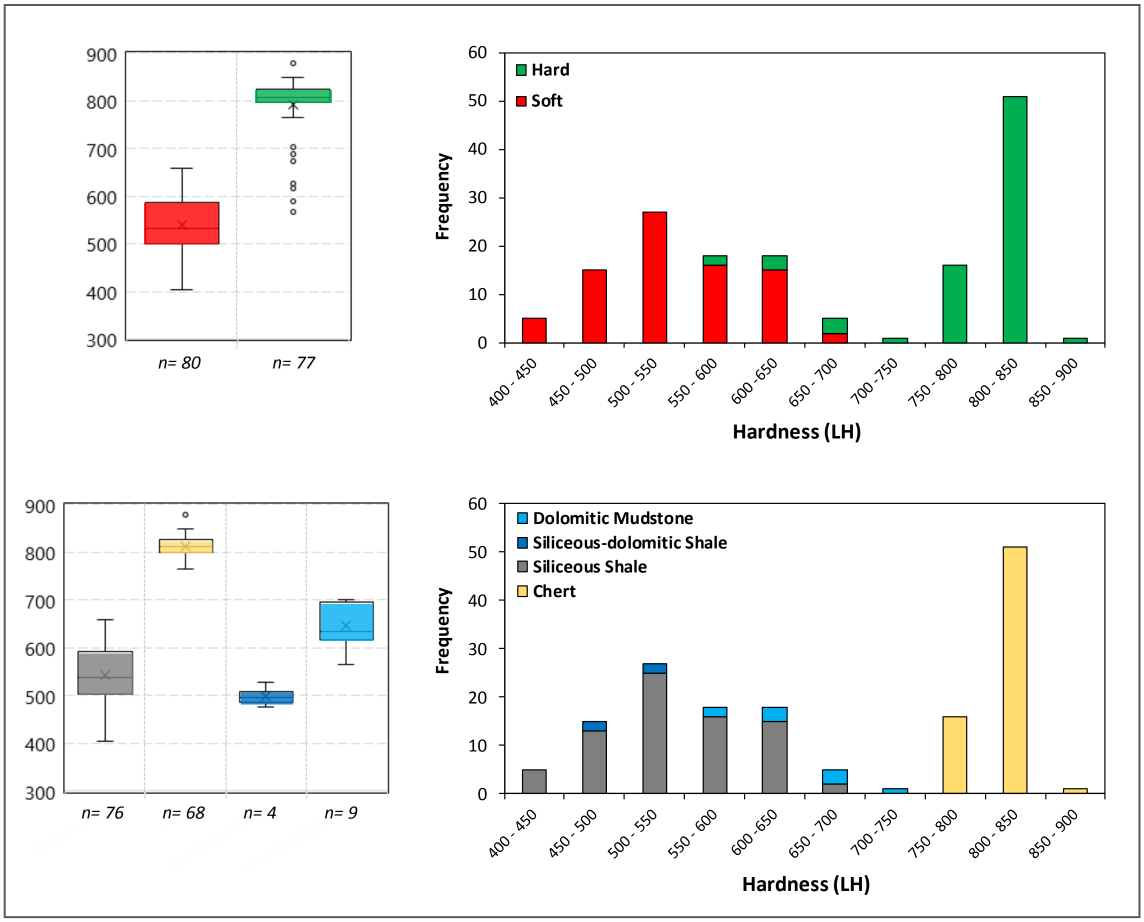

Figure 70. Boxes and whisker plots (left) and histograms (right) sowing distribution of hardness values for the 157 samples differentiated by weathering response (soft-hard) and by lithofacies. There is a number of hard beds that present hardness values similar to soft beds (upper graphs), these corresponds to dolomitic beds (lower graphs).

Preliminarily one might infer that the recognition of lithofacies coupled with hardness results can facilitate the prediction and understanding of variations on mechanical properties. One of the key objectives of this chapter is to determine the main factors influencing rock hardness; in this study, the elemental and mineralogical composition, TOC contents and rock fabric were evaluated.

First, a set of elemental proxies from XRF were plotted against hardness in order to evaluate relationships and trends (**Figure 71**). Silicon (Si) and Si/Al ratios which are the main proxies for quartz contents, show a positive covariance with hardness (at least for the Siliceous Shales and Cherts) (**Figure 71**).

Detrital/clay proxies such as Aluminum (Al), potassium (K) and titanium (Ti), negatively correlate with rock hardness, and illustrates that the more concentrated these elements are, the lower the rock hardness is (**Figure 71**).

Carbonate proxies, calcium (Ca), strontium (Sr) and magnesium (Mg) show positive correlations with hardness for the dolomitic lithofacies (Siliceous-Dolomitic Shale and Dolomitic Mudstones) (**Figure 71**).

Finally, organic-sensitive proxies such as vanadium (V), molybdenum (Mo) and uranium (U), do not reveal clear correlations with rock hardness (**Figure 71**), for this reason TOC content is no longer modeled using these elemental proxies.

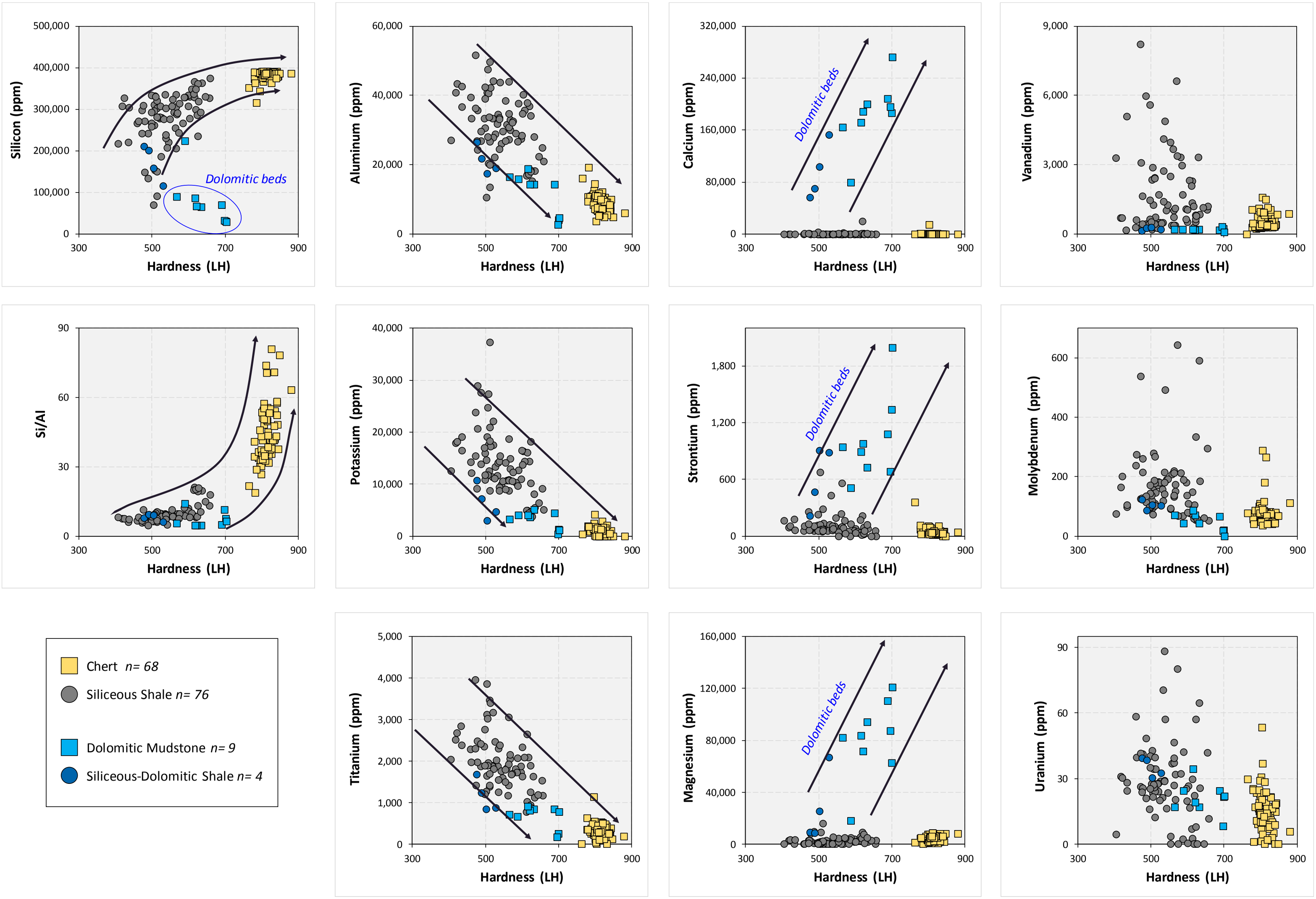

Figure 71. Relationships between elemental composition determined by XRF analysis with hardness.

To investigate mineralogy versus hardness, using the Approach #2 evaluated in the previous chapter of this work, we modeled quartz, clay and carbonate contents from XRF elements. Then, we were able to analyze relationships between hardness and mineralogy using 46 samples with XRD results (**Figure 72A**) but also using 111 samples with modeled mineralogy (**Figure 72B**); Interestingly obtained trends are pretty similar and attest to the reliability of our modeled mineralogy (**Figure 72**).

Based on **Figure 72**, rock hardness clearly increases as the content of quartz increases (**Figure 72**), and conversely, higher clay contents contribute to decrease the rock hardness (**Figure 72**). Also, it is noted that moderate to high carbonate contents (20 – 70%) contribute to increase the rock hardness (**Figure 72**); however, for very high carbonate contents (> 90%) the trend of hardness values is not clear; thus, indicating that other factors besides rock composition may be affecting hardness of the dolomitic beds (**Figure 72**).

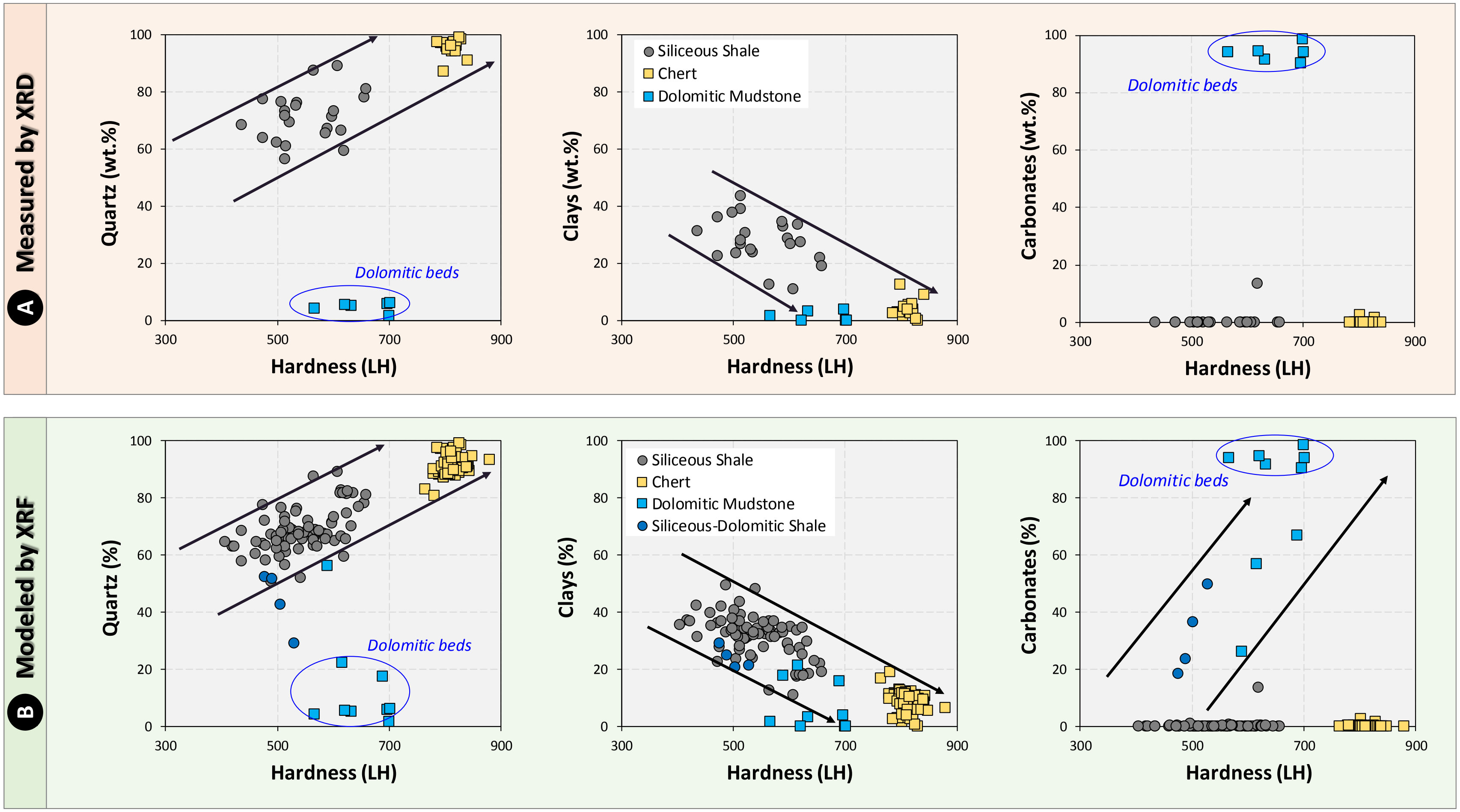

Figure 72. Relationships between mineralogy and hardness differentiated by lithofacies. (**A**) Contains XRD results for 46 samples. (**B**) Presents XRD results for the 46 samples and the modeled mineralogy (using Approach#2) for the remaining 111 samples.

When analyzing those samples that present very high carbonate contents (> 90%), a marked contrast in rock texture was observed, specifically in grain size (**Figure 73**). The higher hardness values (avg. 700 LH) were obtained in samples with the larger dolomite crystals (~1 mm) (**Figure 73**), while samples made of fine to very fine dolomite crystals (~0.02 mm) revealed lower hardness values (avg. 620 LH). In rock mechanics, it is proved that rock strength is inversely proportional to grain size, meaning that higher strengths are expected for finer-grained rocks (e.g. Brace, 1961; Olsson, 1974; Onodera & Kumara, 1980; Eberhardt et al., 1999).

To possibly explain the unexpected results of the hardness in fine-grained dolomitic beds, first we should recall that the tungsten ball in the hammer impacts around 0.5 mm of rock at a time (Proceq sales flyer 2015); which means that in the case of large crystal samples, the hammer is most likely impacting one single crystal (**Figure 73A**), whereas in the case of very fine crystals, the hammer perhaps impacts lots of dolomite crystals within the rock matrix which also contains some clays and organics (**Figure 73B**). For such reasons, under the same mineral composition, variabilities in rock hardness can be attributed to differences in texture, as is the case of the dolomite beds, where rock hardness is higher in coarsely crystalline dolomite beds and lower in fine grained dolomites.

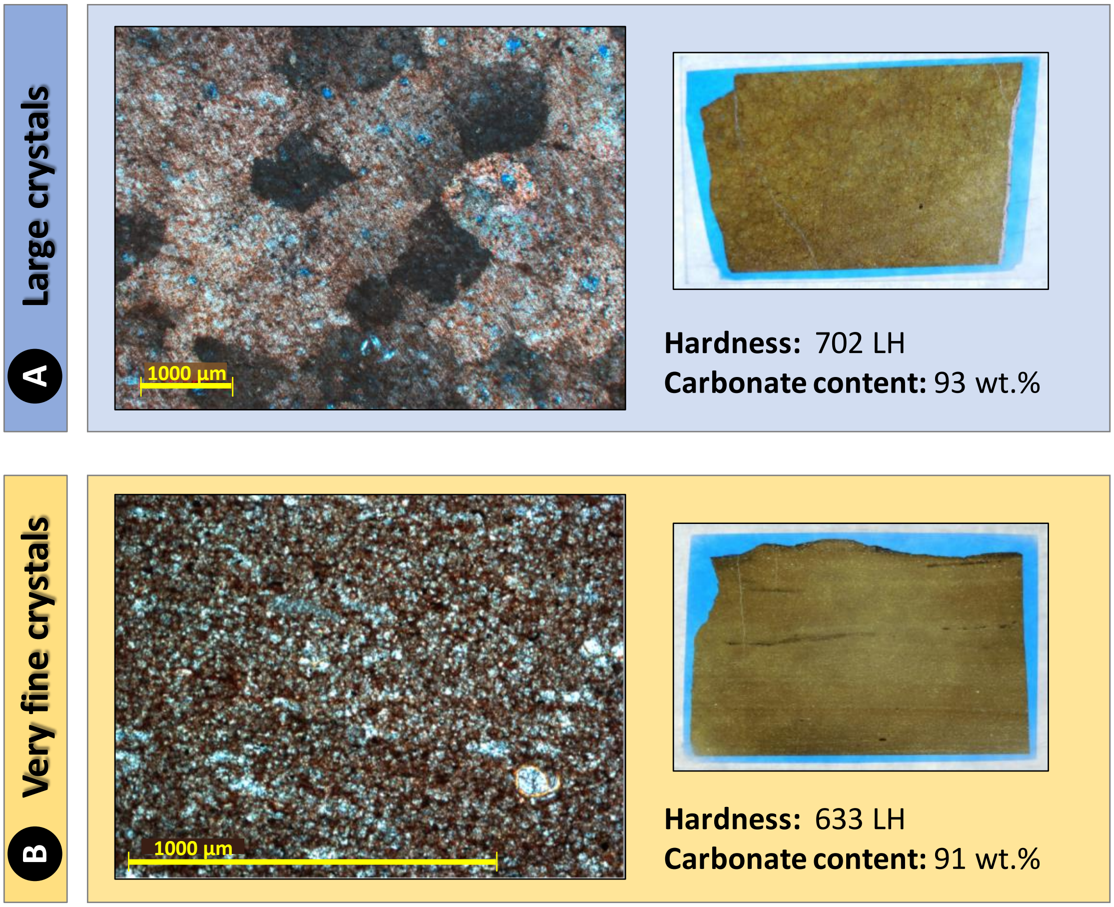

Figure 73. The effect of crystal size for dolomitic beds within the Woodford Shale. Rocks with similar carbonate contents (~90 %) yielded very different hardness values depending on the size of crystals. (**A**) Higher hardness (702 LH) for samples that present large crystals (~1 mm). (**B**) Lower hardness (633 LH) for samples that present very fine crystals (~0.02 mm).

With regards to the effect of TOC contents on rock hardness, overall they seem to be inversely proportional (**Figure 74**). Differentiated by lithofacies, the negative relationship is clear for Siliceous Shales and Dolomitic Mudstones (**Figure 74**). However, in Chert beds the effect of TOC on hardness appear to be insignificant. Indeed, TOC contents of Chert beds widely vary between 0.5 to 6%, but hardness values remain quite constant around 800 LH (**Figure 74**). So preliminarily, one may conclude that in Cherts hardness is more responsive to high quartz contents and its fabric assemblages rather than to variable TOC contents. Furthermore, for a more rigorous assessment of the impact of organic matter contents on the mechanical properties of the Woodford Shale, a much higher number of TOC data points is required.

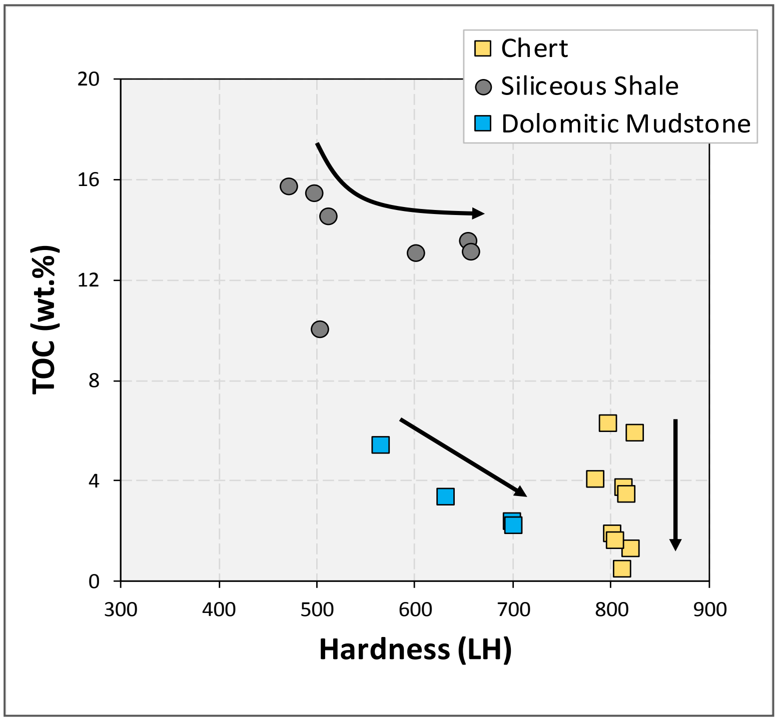

Figure 74. Relationships between TOC contents and hardness values for each of the lithofacies contained in the Woodford Shale at I-35. n=20

9.1.Mineralogical Brittleness Index

The evaluation of brittleness using mineralogical composition and TOC is based on the assumption that rock brittleness is a response of the abundance of "brittle minerals" compared to "ductile minerals" within the rock. In this study, by using equation (16) published by Wang & Gale (2009), mineralogical brittleness index (BI) was calculated with the main objective to validate whether hardness results can produce reliable insights on brittleness and UCS for the Woodford Shale rocks (*see next chapter*).

$$\boldsymbol{Miner.Brittleness\ Index} = \frac{Quartz + Carbonates}{Quartz + Carbonates + Clay + TOC} \qquad (16)$$

Even though TOC content has proved to contribute negatively to the brittleness of shale reservoirs (Walles, 2004; Wang & Gale, 2009), the very few number of TOC analyses (n=20) in comparison to mineralogical data (n=157) forced us to present two versions of brittleness index (including and excluding TOC) (**Figure 75**). When compared to rock hardness, almost identical trends were obtained for the two brittleness index equations (including and excluding TOC) (**Figure 76**), meaning that it is accepted to use the mineralogical brittleness index equation that excludes the TOC contents.

Additionally, up to date the mineralogical brittleness index remains as a relative measurement with range of values that varies from one formation to another; for instance, a 'high" brittleness index for the Eagle Ford may represent a "low" brittleness index in the Woodford Shale, which means there is no need to meet specific numbers.

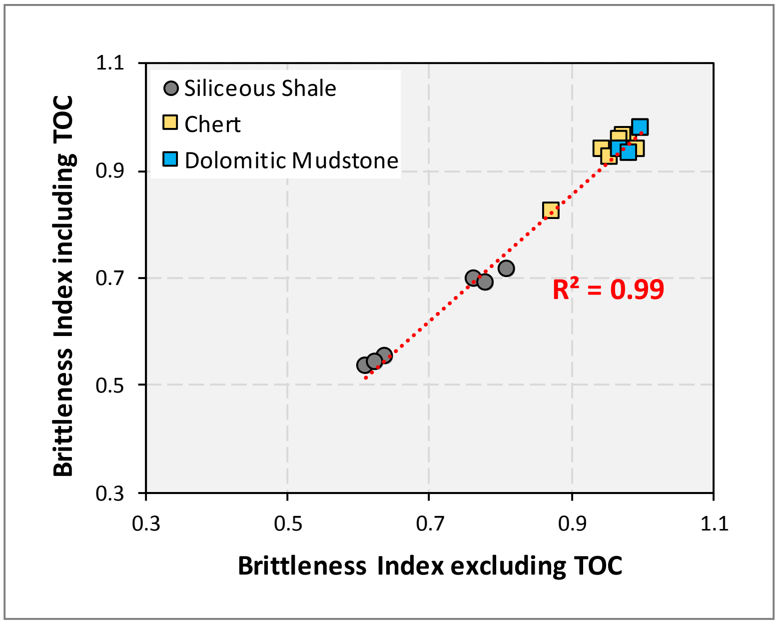

Figure 75. Cross-plot comparing results of including or not the TOC contents in the brittleness index equation.

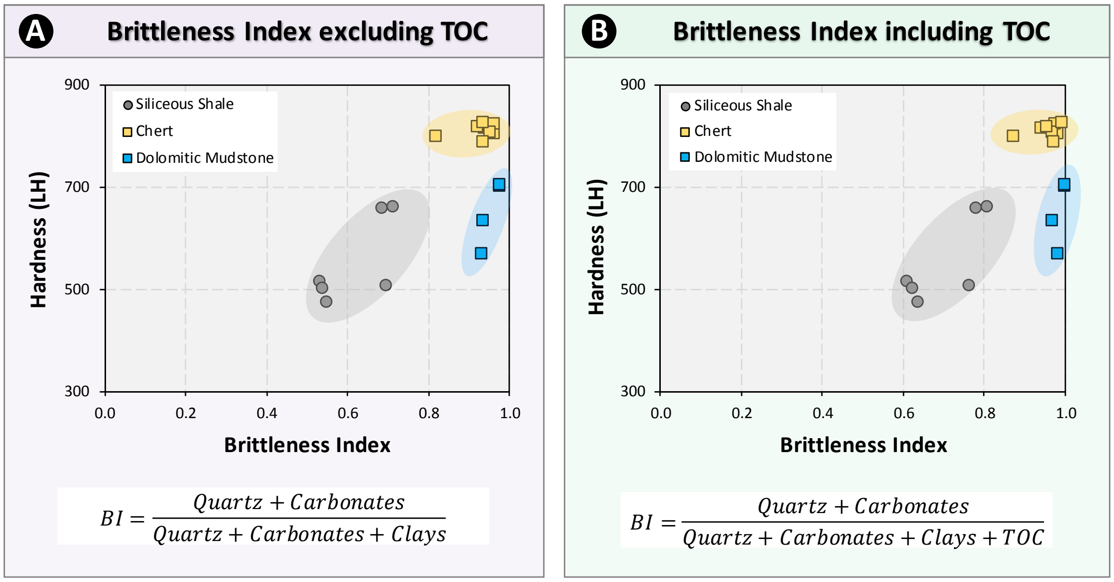

$$BI = \frac{Quartz + Carbonates}{Quartz + Carbonates + Clays}$$

$$BI = \frac{Quartz + Carbonates}{Quartz + Carbonates + Clays + TOC}$$

Figure 76. Comparison of results by including TOC contents or not in the brittleness index equation.

Cross-plots of rock hardness versus mineralogical brittleness index overall revealed a linear positive relationship (**Figure 77**). When grouped by lithofacies, mineralogical brittleness index values show well-clustered data points displaying little overlap (**Figure 77** and **Figure 78**). Lithofacies of Siliceous Shales present brittleness indices between 0.56 – 0.83 (avg. 0.69), whereas Chert samples present a much narrower range between 0.83 – 1.00 (avg. 0.92) (**Figure 78**). In the case of Siliceous-Dolomitic Shales, they present higher average brittleness index values (0.76) in comparison to Siliceous shales. Dolomitic Mudstones also present very high average brittleness index (0.94), with a similar range to Cherts (0.82 – 1.00) (**Figure 78**).

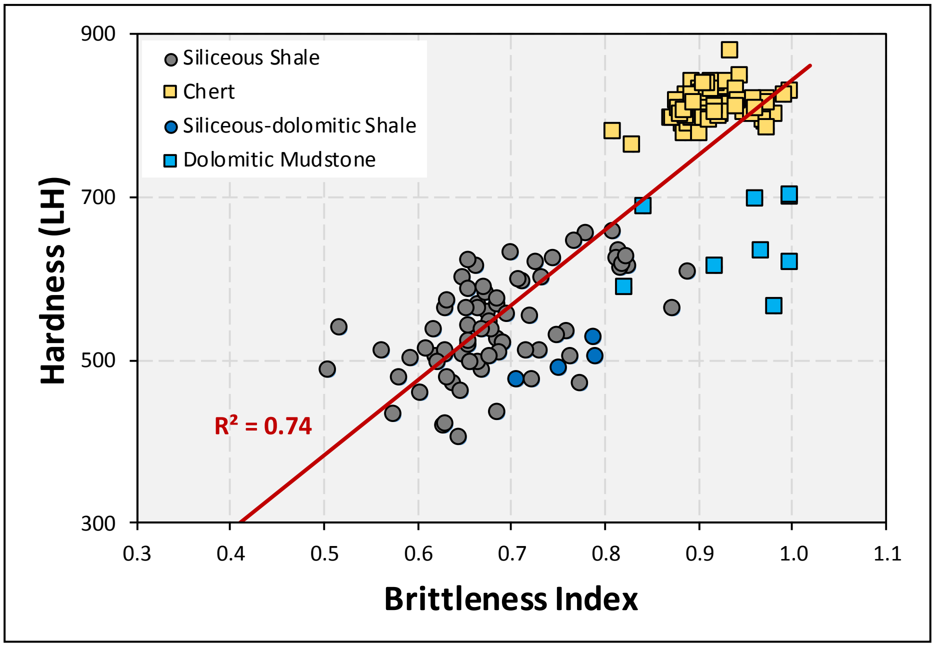

Figure 77. Cross-plot between rock hardness and brittleness index showing a good positive relationship between these two variables. Notice the well-defined clustering of Siliceous Shale and Chert lithofacies, while most dolomitic samples plot out of trend showing lower hardness values than Chert beds. n=157.

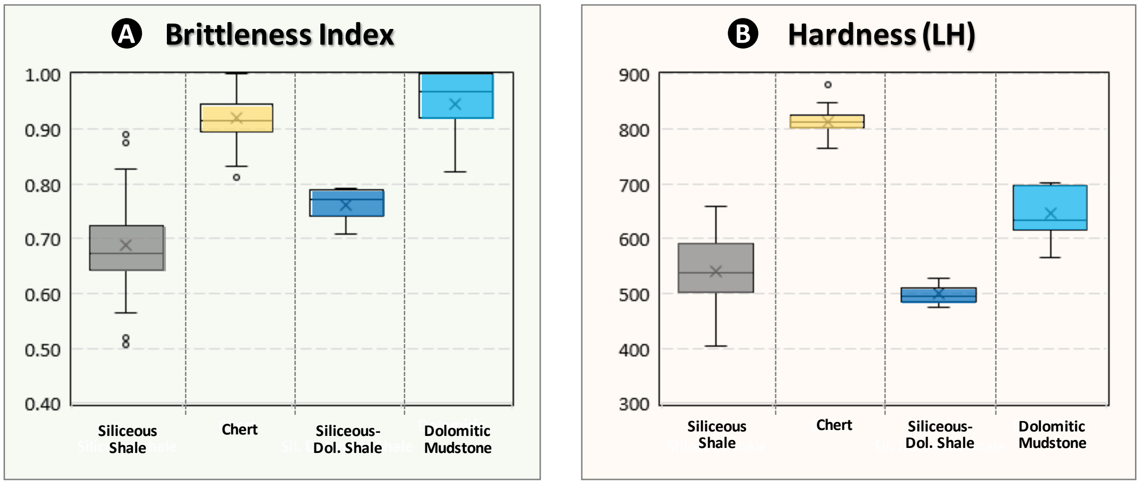

Figure 78. Boxes and whiskers plots of brittleness index values calculated using equation 16 (excluding TOC) and results of hardness tests. Notice the relatively low hardness of dolomitic mudstones which based on brittleness index should behave similarly to Chert beds. Siliceous Shale n= 76; Chert n= 68; Siliceous-Dolomitic Shale n= 4; Dolomitic Mudstone n=9.

When analyzing rock textures of Cherts and dolomitic mudstones, the dense matrix of Cherts is made up of interlocking micro-crystalline quartz (i.e. no visible grain contacts) (**Figure 79A**), whereas the microfabric of dolomitic mudstones is composed by mosaics of visible coarser dolomite crystals (**Figure 79B**), thus we infer that under same brittleness index, Chert beds are much more brittle than dolomite mudstones. Indeed, uniaxial compressive tests were performed on Cherts and dolomitic mudstones samples, resulting in higher young's modulus for Chert compared to the dolomitic mudstones (*see next chapter of this work*).

To summarize, the fact that a rock is mainly composed of brittle minerals (e.g. quartz, dolomite) does not directly indicate a very high rock strength, rather, the rock fabric (i.e. internal arrangement of those brittle minerals) plays a more important role in the understanding of rock mechanical properties.

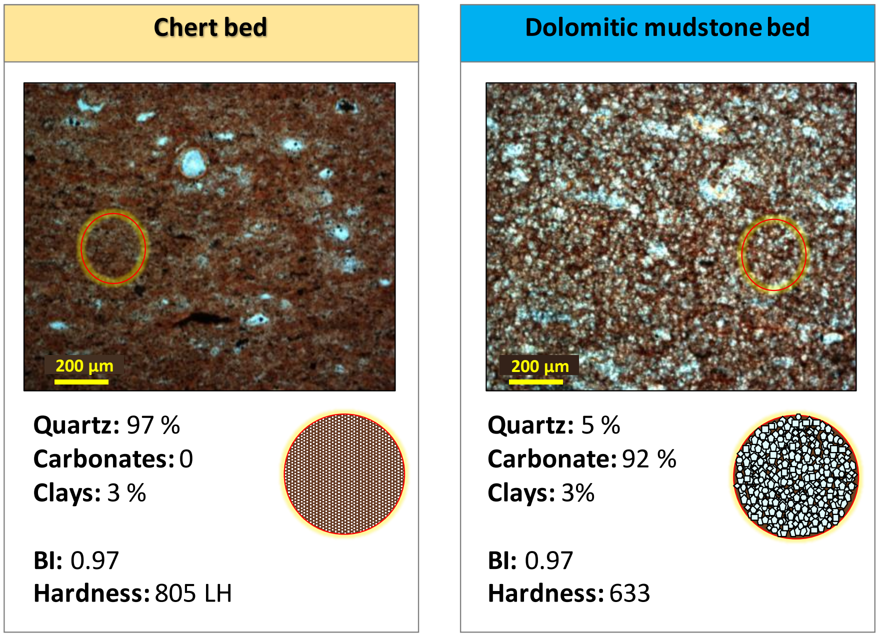

Figure 79. Thin sections of Chert and Dolomitic Mudstone beds showing identical brittleness indices (0.97), but contrasting rock hardness (805 and 633 LH). Notice invisible crystals in Chert beds while a visible interlocking of dolomite crystals in Dolomitic Mudstone bed.

9.2.Rock Hardness and Stratigraphy

When hardness results are plotted by depth, no significant trends can be observed (**Figure 81C**), indeed a very "spiky" curve is obtained representing small-scale cycles of high (around 800 LH) and low hardness (around 500 LH), which is somehow depicting the natural cyclicity of hard and soft beds within the Woodford Shale.

Then, when hardness results are separated by soft and hard beds (**Figure 81D**), it is observed that almost regardless of stratigraphic position, hardness of hard beds does not show significant vertical variations (mostly around 800 LH).

As opposed to the hard beds, hardness of soft beds exhibit more vertical variations (**Figure 81D**). For example, soft beds in the lower fourth of the section present the lowest hardness values along the section (avg. 500 LH), while the upper fourth of the section presents the highest hardness values of soft beds (avg. 600 LH) (**Figure 81D**).

Owing the typical soft-hard cyclicity of the Woodford Shale, the occurrence of a high-hardness bed neighbored by low-hardness beds is quite common (**Figure 81**), meaning that the hardness results (as well as other geomechanical analysis) would be highly influenced by the type of rock tested; in other words, if mostly hard samples are taken within an specific interval, the interpretation of a very indurated interval might not be true, for this reason throughout this study, we heavily emphasize on the distinction between rock types (hard and soft) while reporting results.

Thus, to make hardness results useful for comparison with other geomechanical properties computed using well-logs (e.g. UCS, brittleness, Young's modulus, Poisson's ratio), hardness data must be upscaled to the wireline log resolution (usually 1 foot). In this study, we propose an upscaling of properties based on a weighted average that uses the soft-to-hard ratios per foot (equation 17, **Figure 80**), so that the hardness value reported per each foot can reliably depict the contribution from hard and soft beds (**Figure 80**).

$$\textbf{Hardness per foot} = \frac{(\text{Avg. Hardness Soft beds} * \%\text{Soft}) + (\text{Avg. Hardness Hard beds} * \%\text{Hard})}{100} \qquad (17)$$

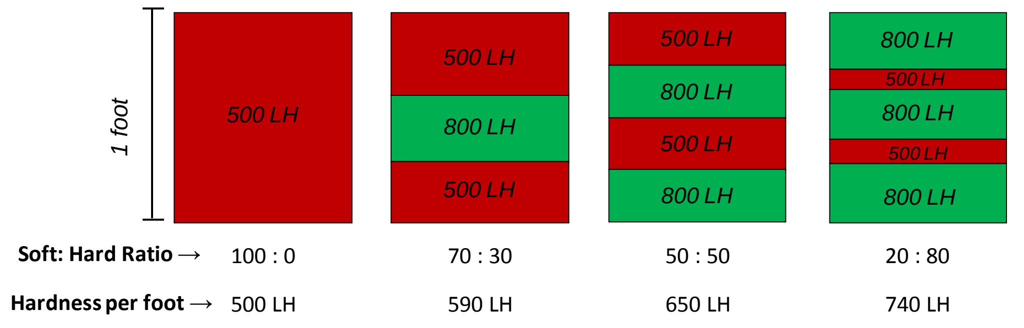

Figure 80. Schematics examples of the hardness per foot calculation (equation 17) for different accommodation of hard and soft beds within a foot. Single hardness values are representative of a foot only for cases when a foot is made up one lithology soft or hard (100:0 or 0:100 soft to hard ratios), which is extremely rare within the entire Woodford Shale as reported by Galvis (2017).

Once computed the weighted average on hardness values per foot (**Figure 81E**), a general upward increase in hardness is highlighted, which range from about 450 LH at the base to 750 LH at the top of the section. In more detailed observations, in the interval from 0 to 15 ft, the upscaled hardness is significantly lower (< 650 LH) than the rest of the section; yet with beds of very high hardness (800 LH), the proportions of soft over hard beds (80 : 20) suggest that the interval is predominately made of low-hardness beds, and the few hard beds should not account equally in the upscaled hardness per foot.

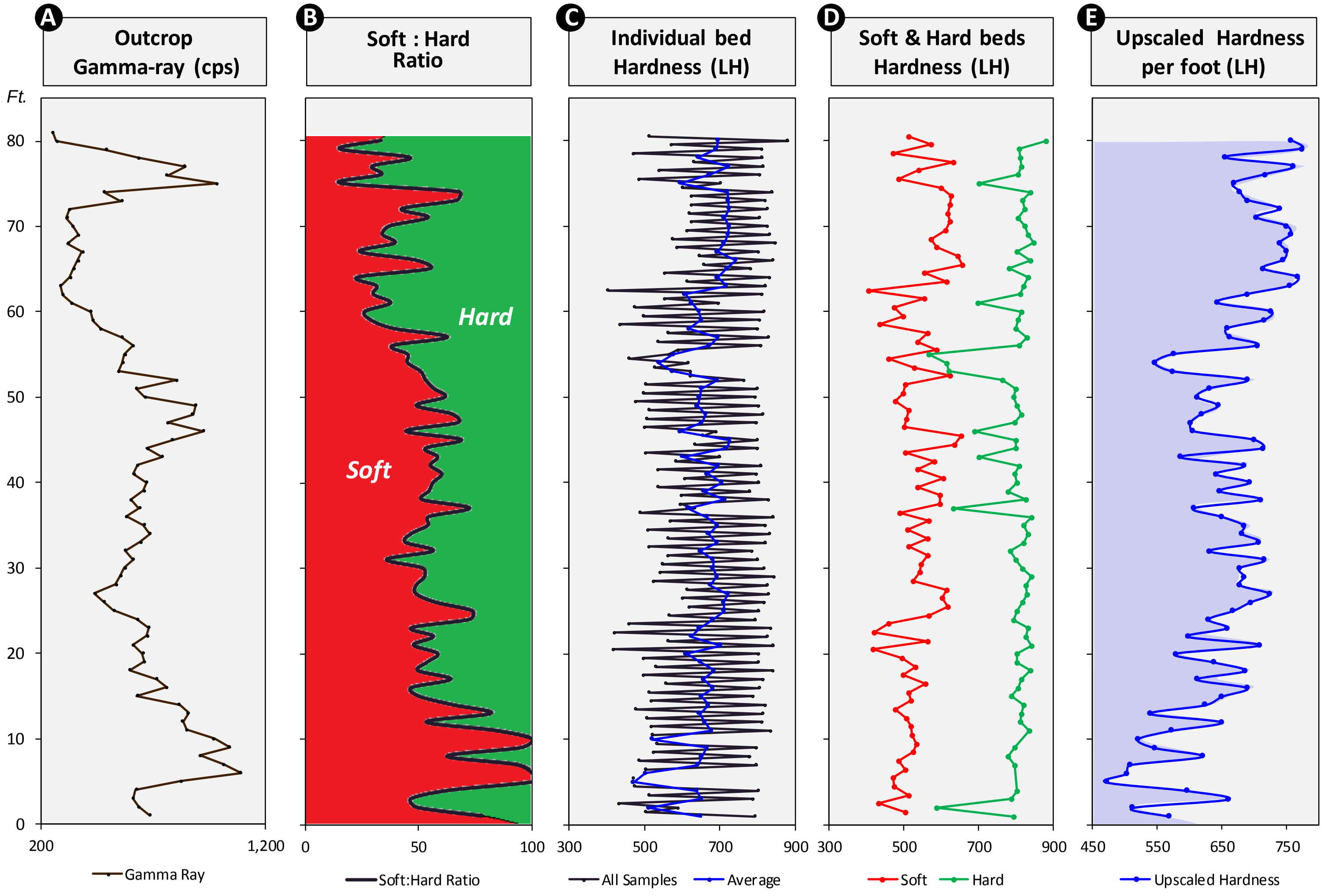

Figure 81. Vertical plots summarizing results of hardness tests conducted on 157 samples from the I-35 outcrop. Upscaled hardness per foot was calculated using equation (17).

Based on the upscaled hardness, the I-35 outcrop section can be subdivided into four main intervals (**Figure 82**): from bottom to top, the first interval (5 – 27 ft.) shows an increasing upward of hardness values from about 450 to 720 LH, coinciding with a decreasing upward of gamma-ray responses (**Figure 82**).

The second interval (27 – 45 ft.) is characterized for presenting moderately constant hardness values (avg. 700 LH), and is not matching with gamma-ray responses which increase upwards (**Figure 82**).

The third interval (45 – 63 ft.) shows an increasing upward of hardness values from about 600 to 760 LH, coinciding with the decreasing upward of gamma-ray responses similarly to the first interval (**Figure 82**). Also, the very low hardness values in this interval (around foot 53) corresponds to a zone where the highest number of dolomitic beds were described.

Finally, the fourth interval (63 – 81 ft.) is the hardest zone of the section, and consists of very high hardness values from about 750 to 780 LH (**Figure 82**). Gamma ray responses are blocky (no vertical change) along the 18-ft of this interval; at the outcrop this particular interval is the most indurated along the rest of the section (*see outcrop descriptions chapter).*

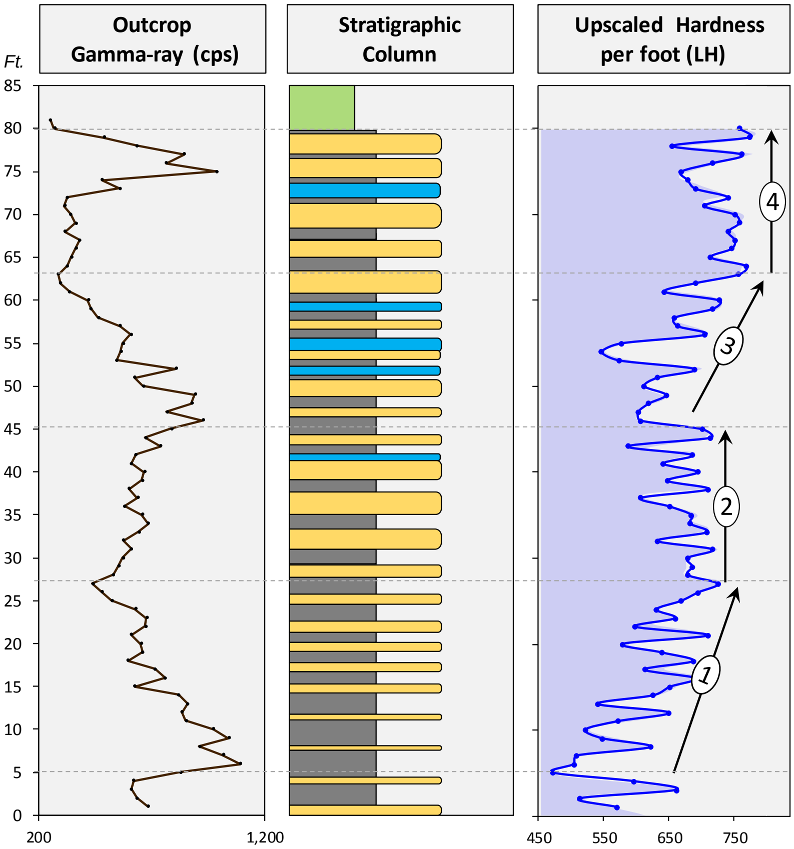

Figure 82. Upscaled hardness plot along with gamma ray and stratigraphic column of the Woodford section exposed at I-35.

10.UNCONFINED COMPRESSIVE TESTS

Since large samples were not possible to take at the I-35 outcrop, samples for uniaxial tests came from a nearby Woodford outcrop named Speake Ranch quarry (Galvis, 2017), located about 11 miles west of the I-35 outcrop. In this quarry, hardness tests were conducted on about 560 samples evenly distributed across the complete Woodford section (Becerra et al., 2017).

To constrain results from hardness tests with laboratory-based mechanical properties, uniaxial compressive tests were performed on 5 representative Woodford samples which comprise the 4 main lithofacies identified in this study (Chert; Siliceous Shale, Siliceous-Dolomitic Shale, and Dolomitic Mudstone). Thin sections and XRD mineralogy results were obtained for the five tested samples to corroborate the consistency between lithofacies characteristics identified at the I-35 outcrop and in the Speake Ranch quarry (**Figure 85**). In other words, since the same criteria was used to classify lithofacies in both outcrops, a Siliceous Shale bed found at I-35 shares similar characteristics as a Siliceous Shale bed at the Speake Ranch quarry.

The uniaxial compressive test is among the most used rock mechanic test to evaluate rock deformation, and from which several mechanical properties can be extracted using their resulting stress-strain curves (**Figure 83**).

First, the unconfined compressive strength (UCS) corresponds to the maximum stress that the specimen can sustain before failure (Hawkes & Mellor, 1970) (**Figure 83**); in this study failure was considered to occur when a sudden drop in applied load was observed.

Second, the Young's modulus (*E*) or modulus of elasticity is a measure of stiffness (Hawkes & Mellor, 1970). It is defined as the ratio of stress to strain and can be determined by computing the slope of a line that connects two points on the linear elastic portion at about 50% of the unconfined compressive strength (**Figure 83**). Accordingly, a stiffer material requires higher stress to be elastically deformed. The concept of stiffness should not be misinterpreted with rock strength (UCS), as strong materials require high stress to fail.

Third, the Poisson's ratio (υ) is a measure of the Poisson effect, which corresponds to the tendency of a material to expand or shrink in a direction perpendicular to the loading direction (Gercek, 2007). Poisson's ratio is defined as the ratio between radial strain and axial strain, and is commonly calculated at the 50% of the unconfined compressive strength (**Figure 83**); common values of Poisson's ratio for rocks range from 0 to 0.5, and generally, a rock with a high Poisson's ratio expands more perpendicularly when it is compressed in the axial direction (Gercek, 2007).

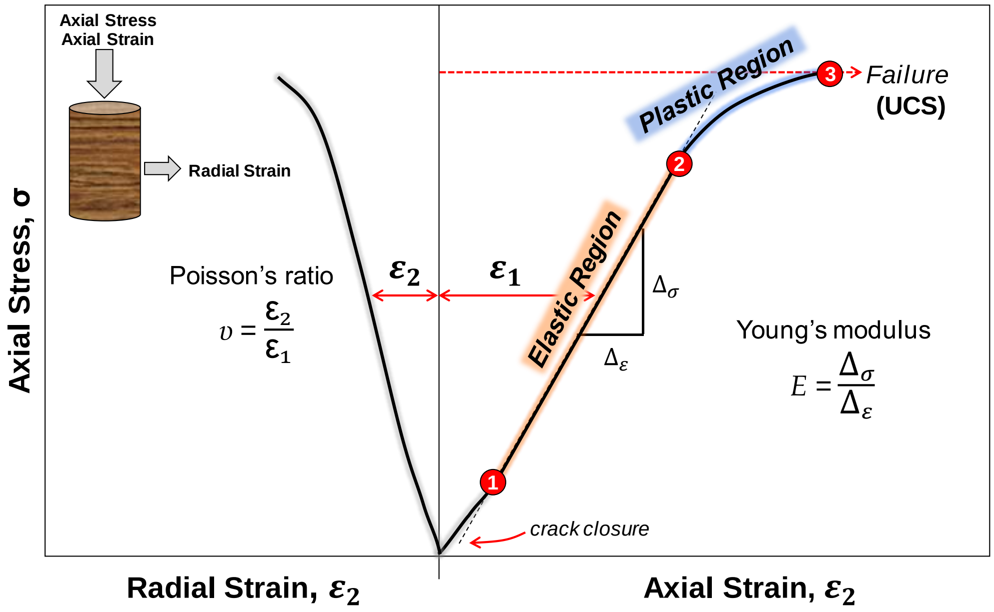

Figure 83. Schematic stress-strain curve derived from a uniaxial compressive test. The peak stress is the unconfined compressive strength. The slope of the elastic portion of the stress-strain curve corresponds to the Young's modulus (E). Poisson's ratio values are calculated at about 50% of the UCS.

Geomechanical properties derived from the uniaxial compressive tests are recorded in **Table 8**. And detailed stress-strain curves per each sample are presented in **Figure 84**.

Sample	Lithofacies	Hardness (LH)	UCS (MPa)	Young's Modulus (GPa)	Poisson's Ratio
A	Chert	892	151	31	0.14
B	Chert	905	155	24	0.22
C	Dolomitic Mudstone	693	139	19	0.17
D	Siliceous-Dolom. Shale	657	148	14	0.18
E	Siliceous shale	608	135	9	0.20

Table 8. Summary of mechanical properties extracted from uniaxial compressive tests of five Woodford Shale samples. Density is the result of weighting specimens and dividing it over their volume.

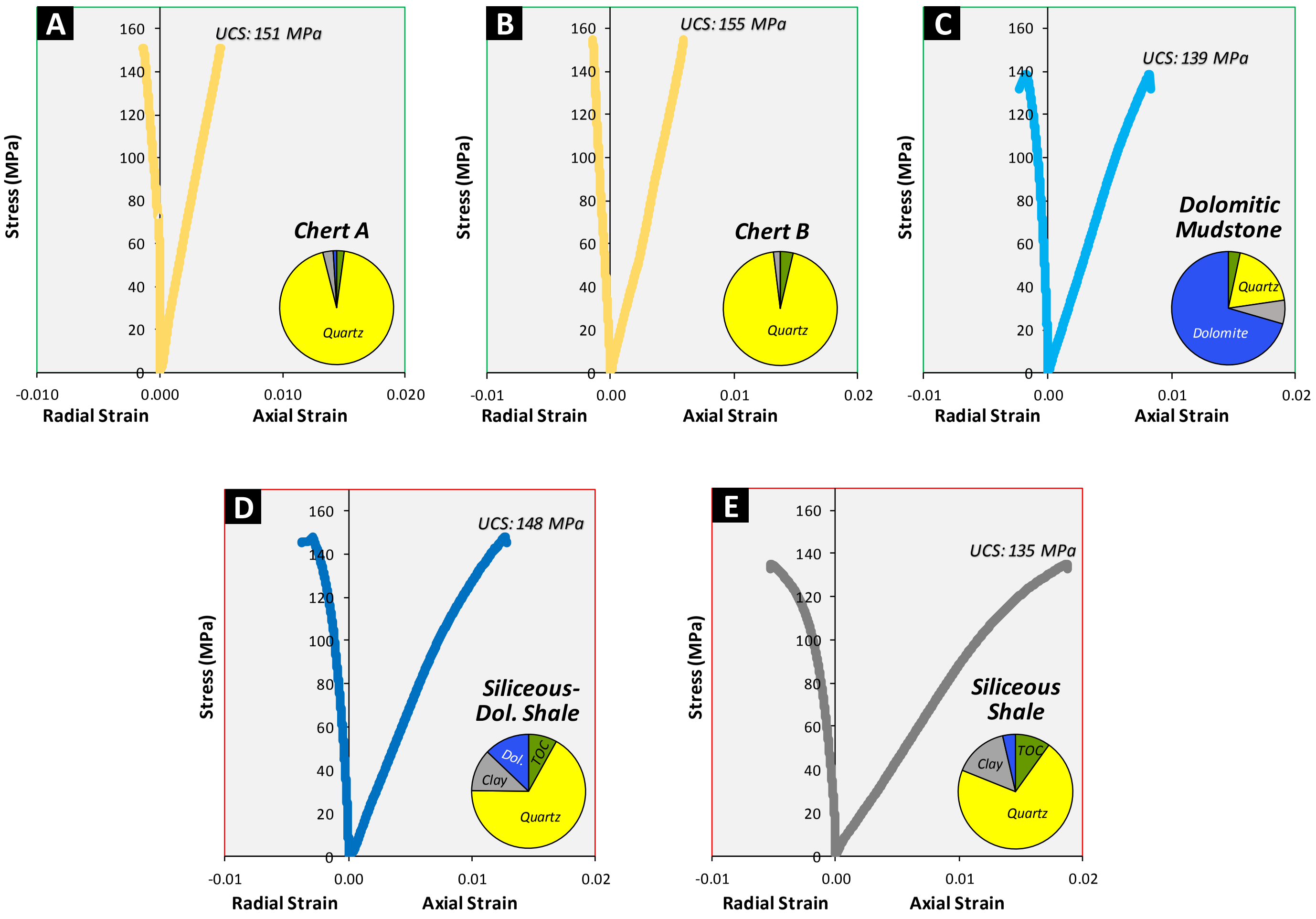

Figure 84. Stress – Strain curves resulting from uniaxial compressive tests on Woodford Shale samples from Speake Ranch (Carter County). Green (hard) and red borders (soft) mark the weathering response of samples in the field.

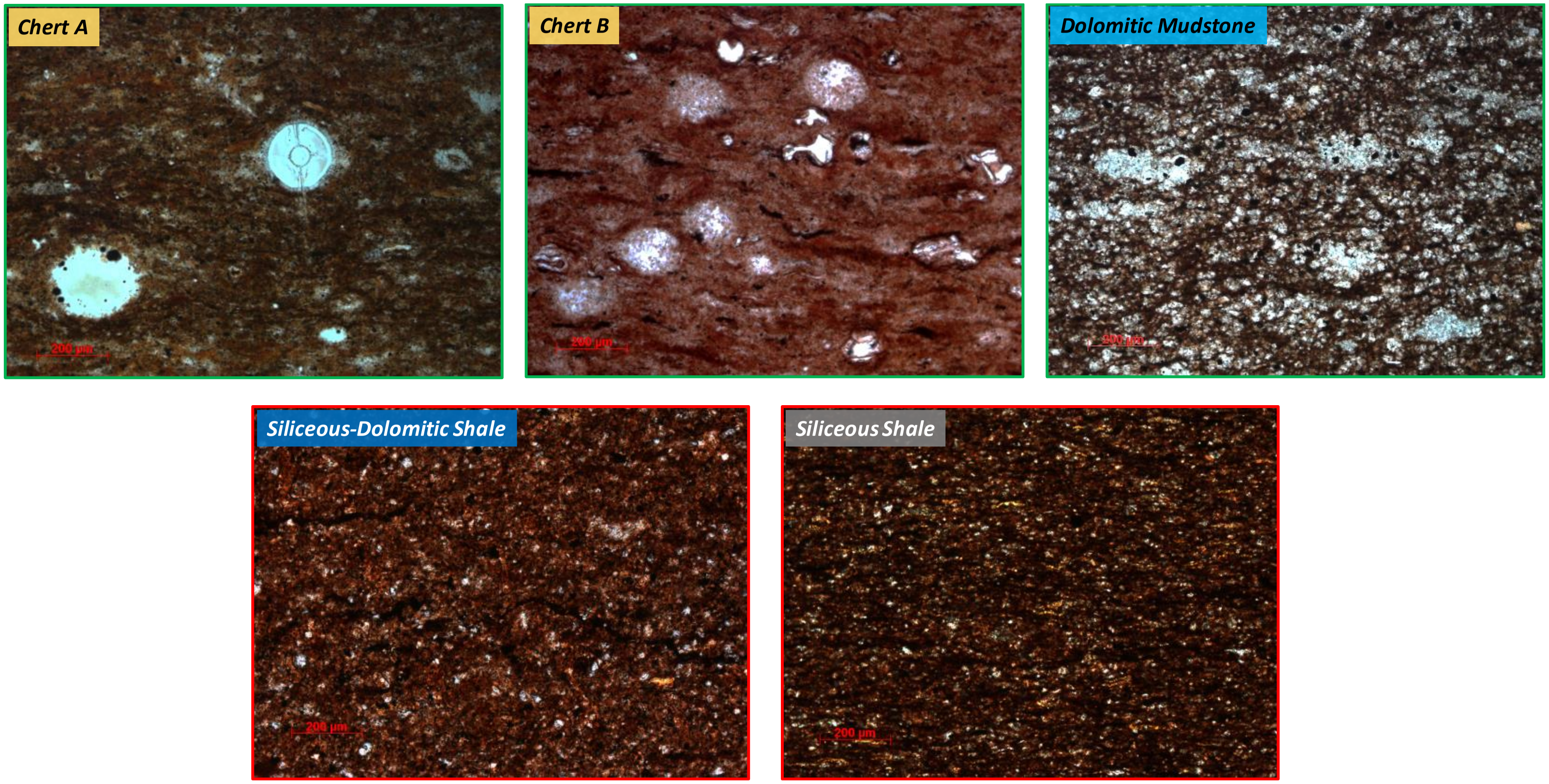

Figure 85. Photomicrographs of the actual five samples used for uniaxial tests in this study. All photomicrographs taken under cross-polarized light show same field of observation (200 µm scale).

At first glance, it is evident that UCS values for all five samples varies in a very narrow range between 135 to 155 MPa (**Figure 84** and **Figure 86**), and indicate they all are strong rocks (UCS > 100 MPa - Deer & Miller, 1966). This was unexpected considering the marked differences among tested lithofacies (i.e. mineralogy, TOC, microfabric, etc.). However, with relatively similar UCS values, the deformation behavior of the five samples is markedly different, displaying solely elastic deformation in Cherts and dolomitic mudstones (samples A, B and D **Figure 84**), whereas different amounts of plastic deformation sustained by the Siliceous-Dolomitic Shale and Siliceous Shale (samples D and E **Figure 84**).

Then, qualitatively from the stress-strain curves and based on the post-failure behavior, it can be concluded that among the tested lithofacies, Cherts and the Dolomitic Mudstones can be regarded as brittle rocks (**Figure 84**), while the Siliceous-Dolomitic Shale and the siliceous shale display can be regarded as ductile lithofacies (**Figure 84**).

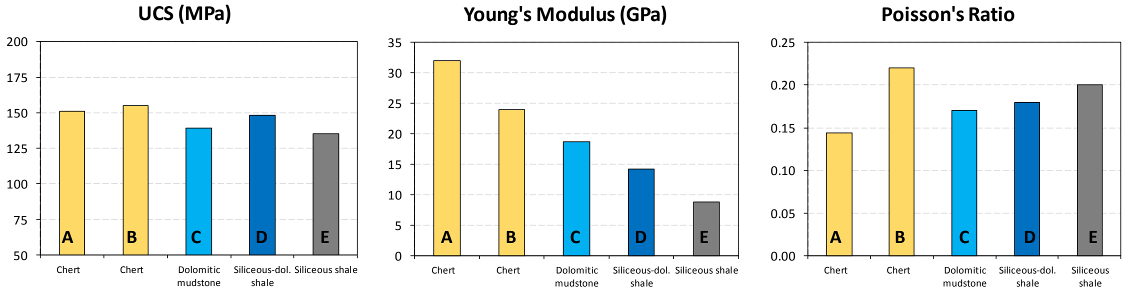

Figure 86. Bar graphs for UCS, Young modulus and Poisson's ratio parameters extracted from stress -strain curves.

Values of Young's modulus present a wide range, varying from 9 to 31 GPa. As higher Young's modulus defines stiffer materials; from stiffest to less stiff lithofacies are ordered: Chert > Dolomitic mudstone > Siliceous-Dolomitic Shale > Siliceous Shale (**Figure 86**).

The combined analyses of UCS and Young's modulus from this study provided an excellent opportunity to illustrate how rock strength differs from rock stiffness although sometimes they may covary. For example, Cherts and Siliceous-Dolomitic Shales (Samples A and D) present similar high UCS values (151 and 148 MPa respectively), however their Young's modulus are markedly different, 31 and 19 GPa respectively, thus implying that Cherts are strong (high UCS) and stiff (high E), and shales are still strong (high UCS) but not stiff (low E).

With regard to the Poisson's ratio, as its measure is highly dependent on the position on the stress and strain curve, its interpretation becomes more meaningful when it is coupled to Young's modulus. Indeed, the industry of unconventional resources have used this relationship with success to estimate rock brittleness, and it is well known that rocks with high Young's modulus and low Poisson's ratios are more brittle than rocks with low Young's modulus and high Poisson's ratios (Grieser & Bray., 2007; Rickman et al., 2008; Harris et al., 2011; Guo et al., 2013; Perez & Marfurt, 2014; Luan et al., 2014; Pei et al., 2016).

From this study, lithofacies of Siliceous Shales and Siliceous- Dolomitic Shales display the highest Poisson's ratios (0.2 and 0.18) with low Young's modulus (9 and 14 GPa) (**Figure 86**).

Whereas the Dolomitic Mudstone and Chert A sample present lower Poisson's ratios (0.14 and 0.17) with high Young's modulus (19 and 31 GPa) (**Figure 86**). Then, based on Young's modulus and Poisson's ratios, lithofacies are ordered from higher to lower brittleness: Chert > Dolomitic mudstone > Siliceous-Dolomitic shale > Siliceous Shale.

Among the tested Cherts, one sample (Chert B) yielded an anomalously high Poisson's ratio (**Figure 86**). A possible explanation can be attributed to the partially open vertical fractures in the specimen, which during axial loading could have led to higher radial displacement resulting in a higher Poisson's ratio (Walsh, 1965; Vachaparampil & Ghassemi, 2017) (**Figure 87B**). In fact, this issue is one of the limitations of the uniaxial or unconfined compressive tests versus the triaxial test, where confining pressure in the latter ensure the stability of natural fractures in the specimen.

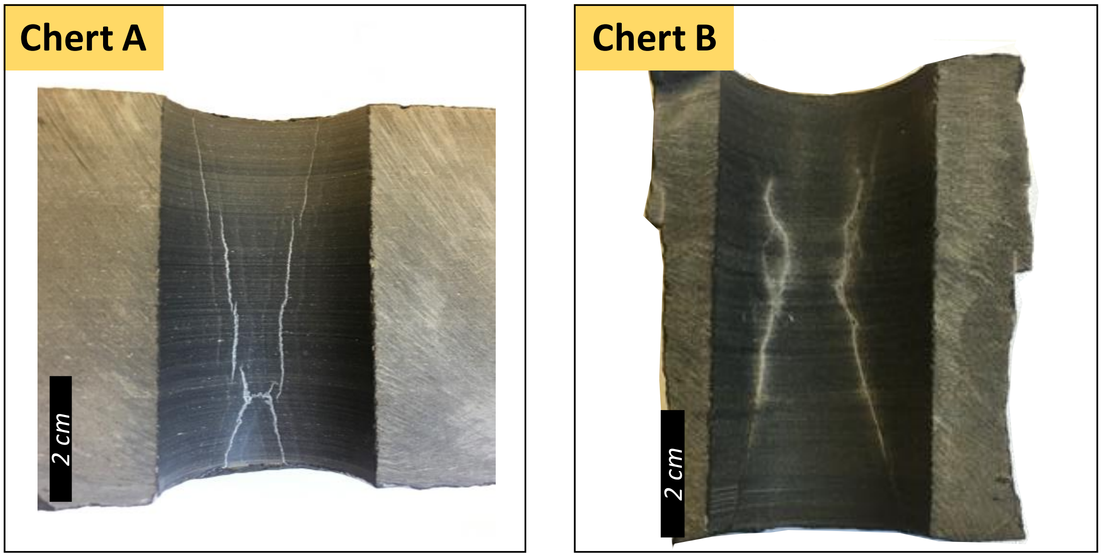

Figure 87. Photographs of the block were cylindrical specimens were taken showing natural fractures in both Chert samples. Vertical fractures in Chert A seems to be well cemented (quartz). Vertical fractures in Chert B are partially open, most likely due to weathering.

10.1. Quantification of Stress-Strain Brittleness

Brittleness plays an important role in the development of unconventional reservoirs as it implies the ability of a rock to fail and maintain open fractures during artificial fracturing. Although uncommon (due to sample availability), the assessment of brittleness by using stress-strain curves from rock-mechanics experiments are among the most straightforward and precise methods.

Based on the assumption that brittle rocks undergo little or no plastic deformation to fail, Hucka & Das (1974) developed an equation to quantitatively determine rock brittleness from stress-strain curves (**Figure 88**). Equation (18) illustrates the ratio of reversible strain (elastic strain) to total strain, where higher the ratio the more brittle the rock is (from a scale from 0.0 to 1.0).

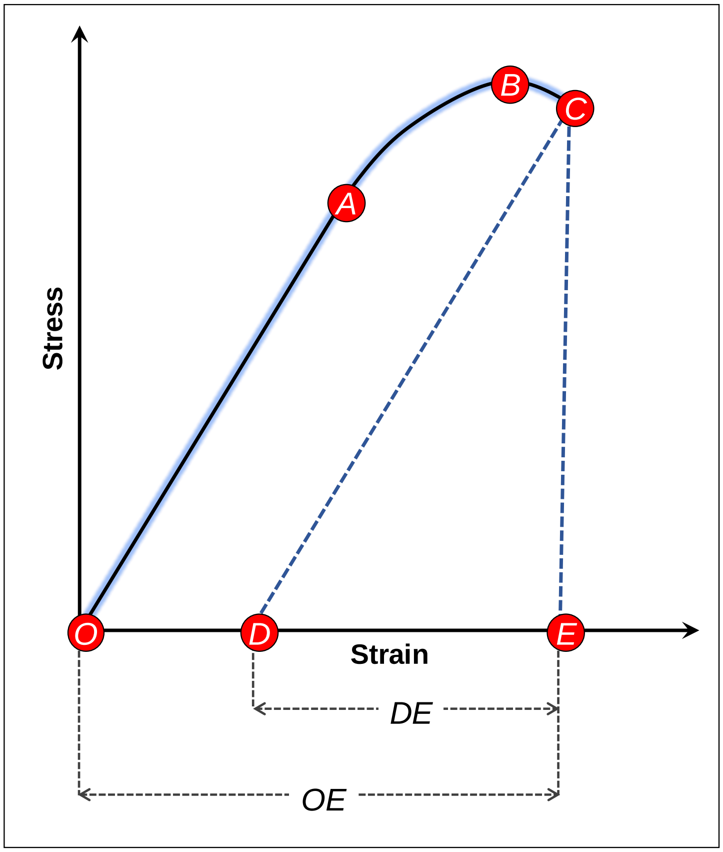

Figure 88. Brittleness as determined from a stress-strain curve. Segment **DE** represents the reversible elastic strain, and segment **OE** represents the total strain at failure. From Hucka & Das (1974).

$$\mathbf{Stress - Strain\ Brittleness} = \frac{Reversible\ Strain}{Total\ Strain} = \frac{DE}{OE} \qquad (18)$$

Results of brittleness using the stress-strain method yielded very high brittleness values for lithofacies of Cherts and Dolomitic Mudstone (1.0, 0.97 and 0.91) (**Figure 89**), and slightly lower values were obtained for siliceous-dolomitic shales and siliceous shales (0.83 and 0.82) (**Figure 89**). The relatively narrow range of brittleness (0.82 to 1.0) might give the idea that all tested samples were “brittle rocks” (which may be true compared with other shale reservoirs), however the detailed analysis of stress-strain curves do not suggest the interpretation of brittle rocks for the shale samples D and E (**Figure 89**).

Then, I can hypothesize that the brittle/ductile boundary for the main Woodford lithofacies is at approximately 0.85 (**Figure 89**). Rocks with brittleness greater than 0.85 are considered brittle and comprise the lithofacies of Cherts and Dolomitic Mudstones, which at the field were identified as "hard" beds. Conversely, rocks with brittleness <0.85 are considered ductile and comprise the lithofacies of Siliceous Shales and Siliceous-Dolomitic Shales, and are identified at the field scale as "soft" beds.

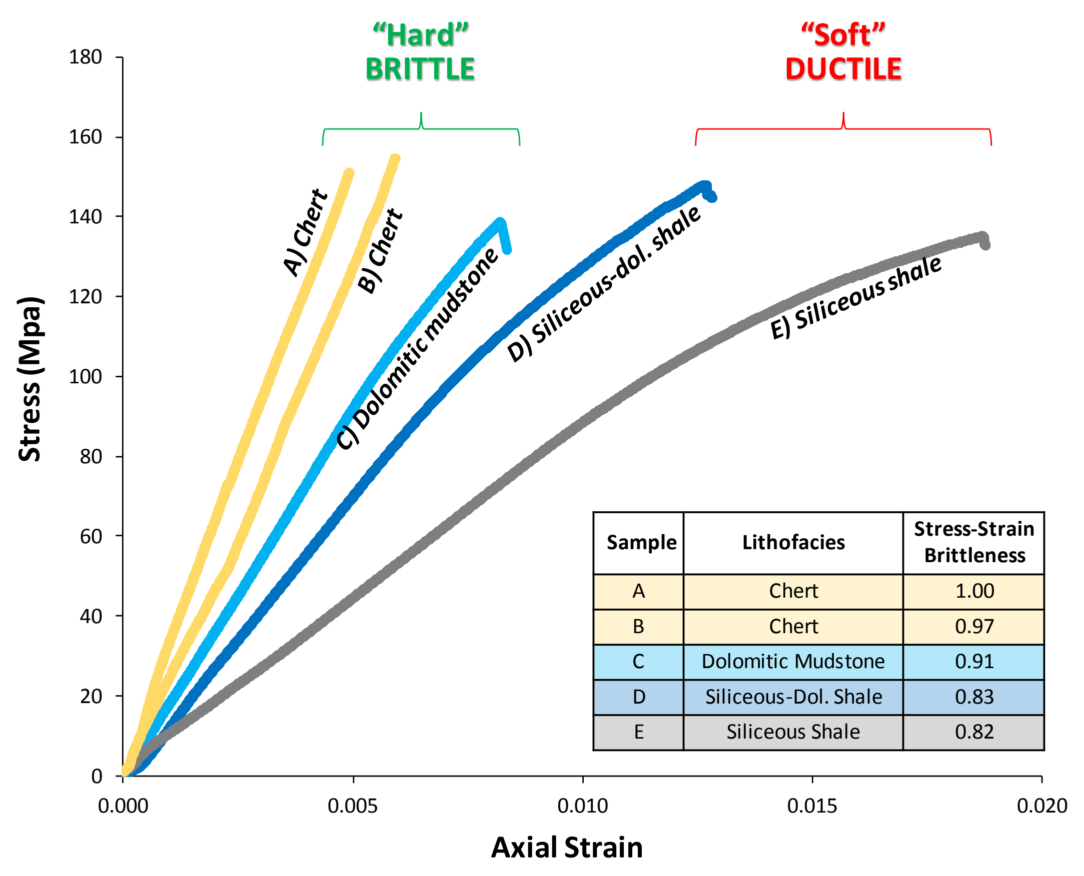

Sample	Lithofacies	Stress-Strain Brittleness
A	Chert	1.00
B	Chert	0.97
C	Dolomitic Mudstone	0.91
D	Siliceous-Dol. Shale	0.83
E	Siliceous Shale	0.82

Figure 89. Summary of stress-strain curves for the five tested Woodford Shale samples. Notice the similarity in UCS values (135 – 155 MPa) but highly contrasting deformation paths. Samples A, B and C are brittle and samples D and E are ductile.

Another and perhaps more common method to estimate brittleness is via mineralogical composition as proposed by Wang and Gale (2009). Values of mineralogical brittleness index computed for the five lab-tested samples reveal a very good positive relationship when compared to the stress-strain rock brittleness (**Figure 90** and **Table 9**).

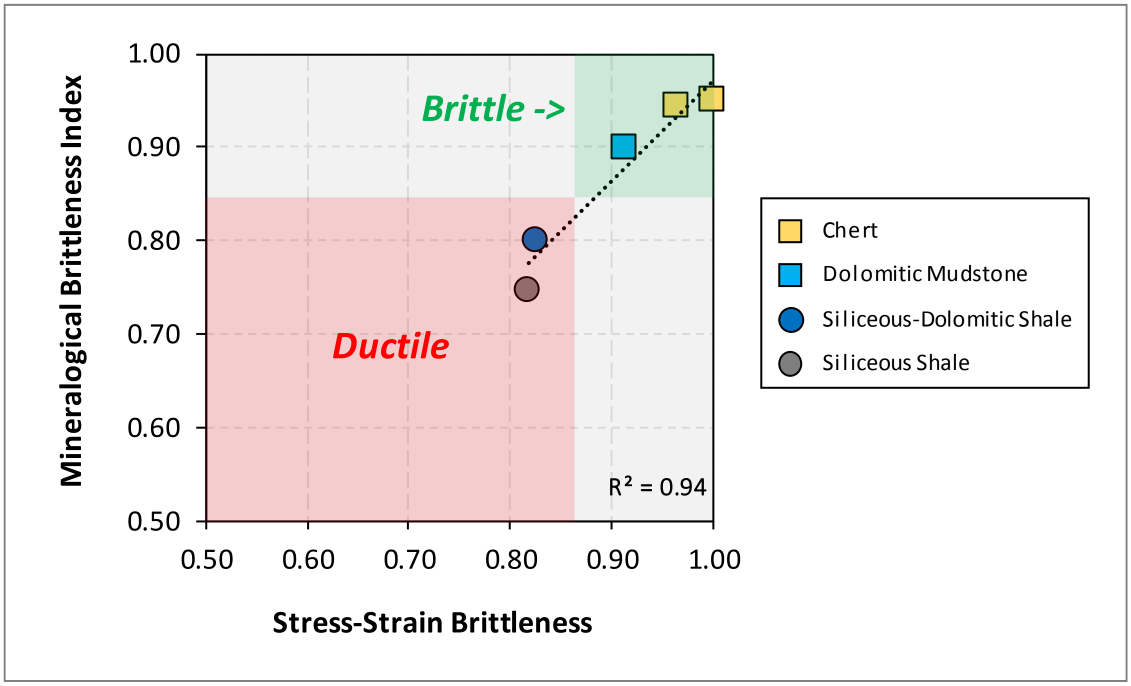

Figure 90. Cross plot comparing mineralogical brittleness index calculated using Wang & Gale equation (2009) versus the stress-strain brittleness calculated from uniaxial test curves. Note the proposed brittle-ductile boundary at 0.85 brittleness.

Sample	Lithofacies	TOC (wt%)	Quartz (wt%)	Clays (wt%)	Carbonates (wt%)	Stress-Strain Brittleness	Mineralogical Brittleness Index
A	Chert	2	96	3	1	1.00	0.95
B	Chert	4	98	2	0	0.97	0.94
C	Dolomitic mudstone	4	20	7	73	0.91	0.90
D	Siliceous-dolom. shale	9	73	13	14	0.83	0.80
E	Siliceous shale	11	79	17	4	0.82	0.75

Table 9. Results of stress-strain brittleness and mineralogical brittleness index for the five tested samples. Mineralogy was measured by XRD analysis.

In addition to the good correlation between the stress-strain and mineralogical brittleness, the previously observed brittle/ductile boundary of 0.85, is still working to differentiate between brittle and ductile rocks using the mineralogical brittleness index (**Figure 90**). Though establishing a cut-off based on 5 samples might be ambiguous, the 0.85 boundary between brittle (hard) and ductile (soft) rocks was validated with mineralogical brittleness indices calculations from the 157 samples of the I-35 outcrop, resulting in that hard beds present brittleness greater than 0.85 and soft ones less than that (**Figure 91**). Thus, it can be concluded that the mineralogical brittleness index is a good indicator of the actual brittleness of the Woodford Shale rocks as determined by stress-strain curves.

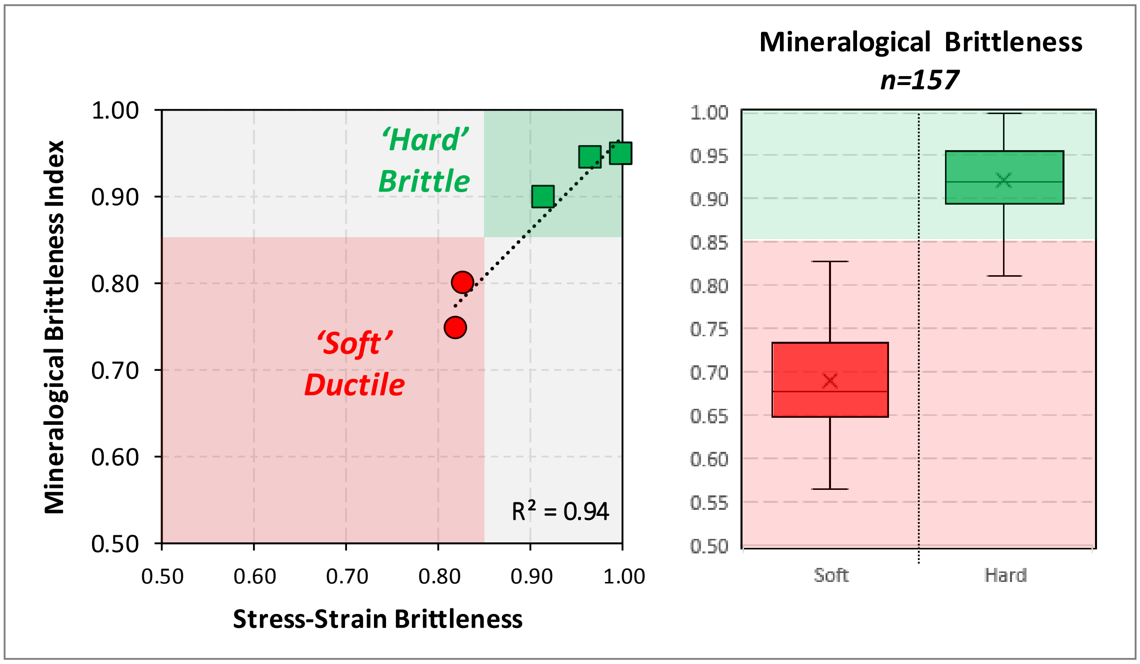

Figure 91. Letf: Cross plot comparing mineralogical brittleness index versus stress-strain brittleness for the five samples tested for UCS tests. Right: Box plot showing results of mineralogical brittleness index calculated on the 157 samples taken at I-35 outcrop differentiated by soft and hard samples. Note that the proposed brittle-ductile boundary at 0.85 brittleness seems to work for the entire set of samples taken at the outcrop.

10.2. Hardness and Mechanical Properties Correlations

In recent years, rock hardness is being measured using the micro-rebound hammer (Equotip™) and it has been extensively used to construct empirical equations and predict UCS (unconfined compressive strength) (e.g. Hack, 1993; Verwal & Mulder, 1993; Aoki & Matsukura, 2008; Daniels et al., 2012; Lee et al., 2014, 2016; Murray, 2015).

Accordingly, we measured rock hardness on the same five UCS-tested samples (**Figure 92**). Generally, a good positive relationship is obtained between UCS and hardness ($R^2 = 0.71$), however when analyzed in detail, samples with higher hardness do not necessarily present higher UCS values (**Figure 92**). For example, hardness of the dolomitic mudstone (sample C) is higher than the siliceous-dolomitic mudstone (sample D), however, the opposite was obtained from UCS values of these two lithofacies (**Figure 92**).

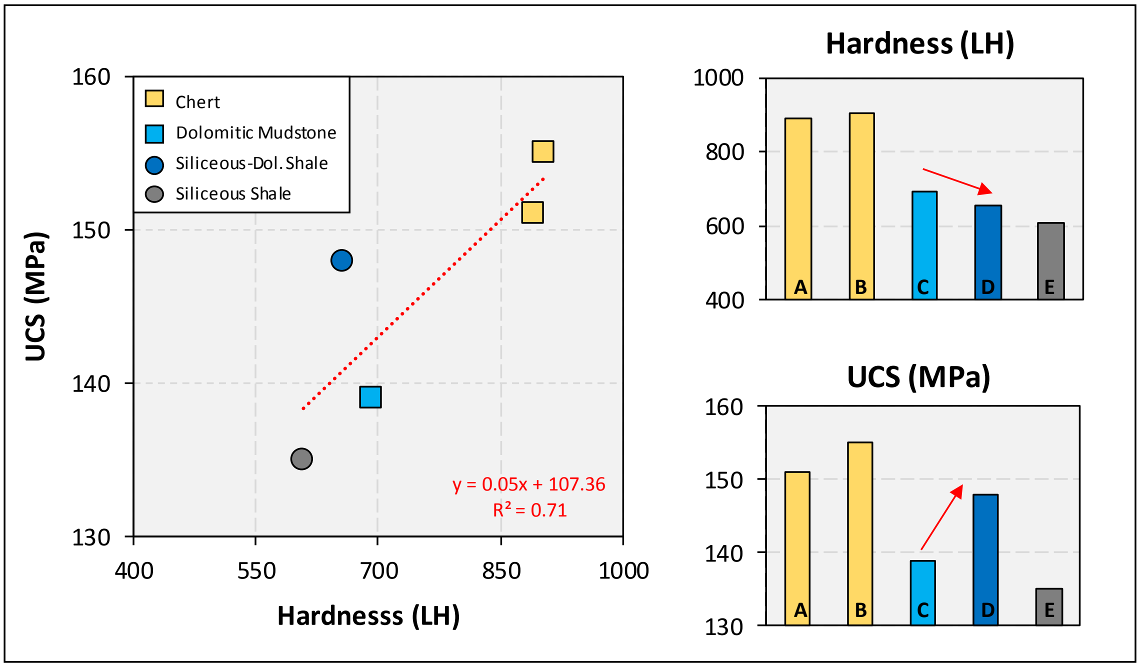

Figure 92. Relationships between hardness measured using a micro-rebound hammer and laboratory-based UCS.

Since developing an empirical equation using only five samples is not quite reliable, an extensive compilation of the published data relating UCS and hardness (Equotip impact device type D) was conducted; in total 246 data points were compiled from 11 different studies which tested different rock types, including sedimentary, igneous, and metamorphic rocks (**Figure 93**).

Generally, from **Figure 93A** a very poor positive relation can be seen between hardness and UCS. Indeed most of the data sets do not show a good relationship among them (**Figure 93B**); and particularly the Woodford samples are completely out of this weak trend (**Figure 93A**). Then, since data points came from different rock types, in **Figure 93B** data points were grouped by lithology, resulting in weak exponential relationships. Our Woodford Shale samples seem unrelated to these groups, not even the shale group where most of the data points are from the Eagle ford and Niobrara unconventional plays (**Figure 93B**). This observation suggests the necessity to generate specific equations for the Woodford strata.

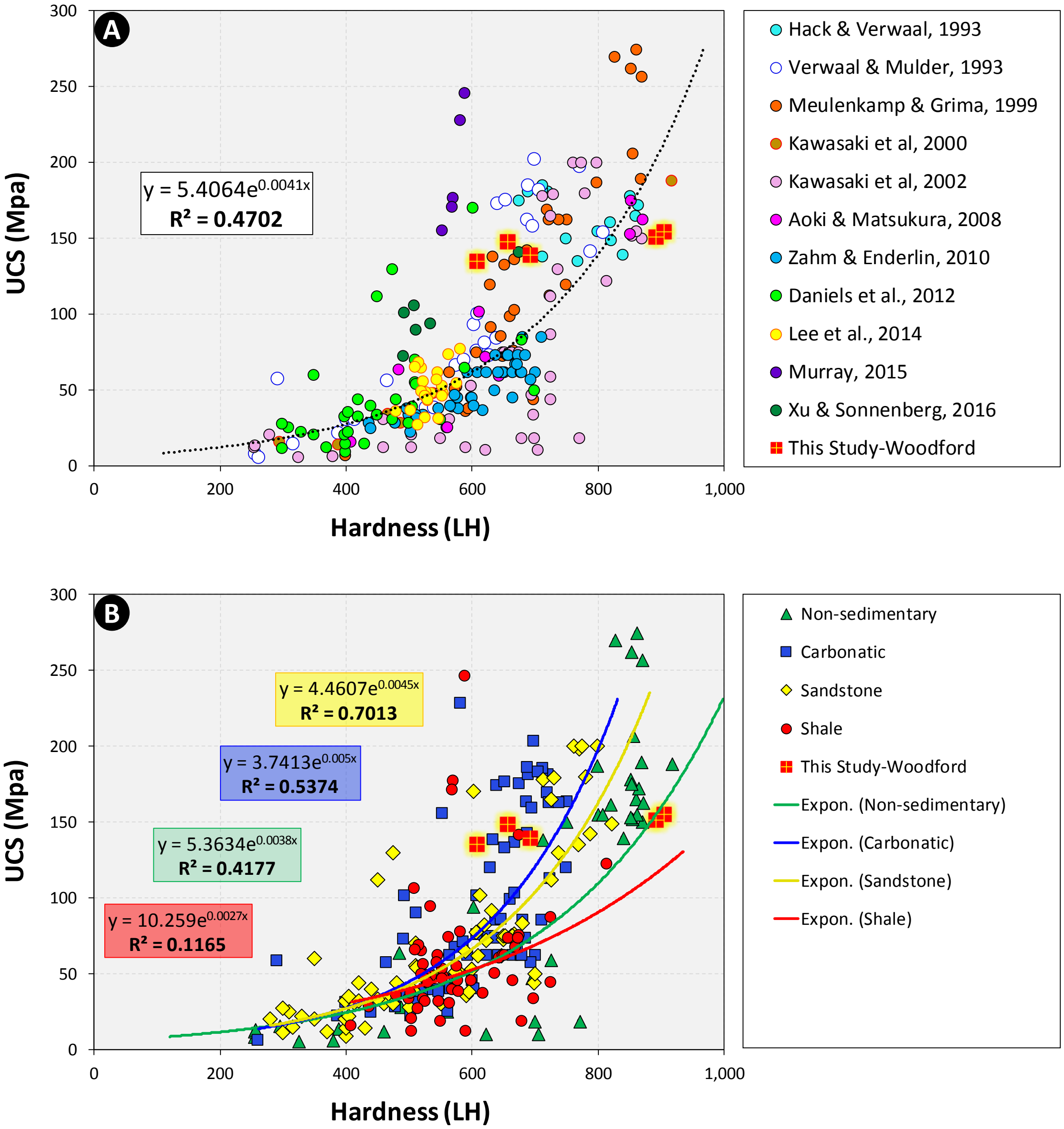

Figure 93. Literature compilation of hardness tied to UCS values. All of the above studies used the Equotip probe D (that was used in this study). (**A**) Size and color of the data points indicates the source of the data. (**B**) Data points are separated by rock type: Non-sedimentary, carbonates, sandstones and shales. Red diamonds highlight the results of this study.

In order to provide a possible explanation to the apparent weak relationship between hardness and UCS values, first, one should recall that the hardness tester (Equotip hammer) has a minimum impact energy (11 Nmm) and is intended to record deformation of a material elastically and plastically without failure (Leeb, 1979); meaning that hardness values are dependent on the elastic and plastic characteristics of the material (i.e. brittleness). On the other hand, considering the definition of rock strength (UCS) as the maximum stress that can be sustained by a rock before it fails, UCS values may or may not be related to the elastic and plastic characteristics of a material, and basically the case of the same UCS values for a ductile and a brittle rock is totally possible (**Figure 94**).

Although, for specifics types of rocks UCS and hardness values might be related, technically rock hardness and UCS measure different properties. Indeed, the Equotip developer (Leeb, 1979), illustrated the case of two different materials which present equal strength (UCS) but different elastic properties (Young's modulus) (**Figure 94**). And conclude that materials with lower Young's modulus release more energy when the hammer's impact body rebounds, and results in higher hardness values. Thus, Hardness and UCS should be used with caution as not always high hardness means high UCS, but instead should be more related to elastic property (Young's modulus).

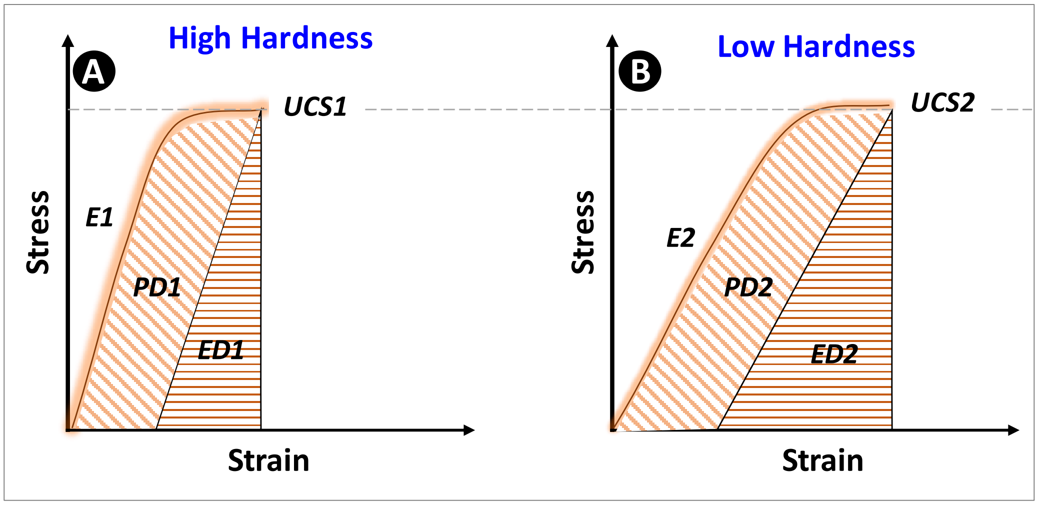

Figure 94. Simplified stress – strain curves for two materials of equal UCS but of different Young's modulus. **E**: Youngs' modulus. **PD**: Plastic deformation. **ED**: Elastic deformation. Redrawn from Leeb (1979).

A cross-plot of hardness versus Young's modulus for this study reveals a good positive correlation, which follows the expected hardness trend: Chert > Dolomitic mudstone > Siliceous-dolomitic shale > Siliceous shale (**Figure 95**). Then, since the Young's modulus in this study showed a relation with brittleness, the latter was cross-plotted with hardness evidencing a very good positive correlation (**Figure 95**); which also depicts the expected brittleness trend: Chert> Dolomitic mudstone > Siliceous-dolomitic shale > Siliceous shale.

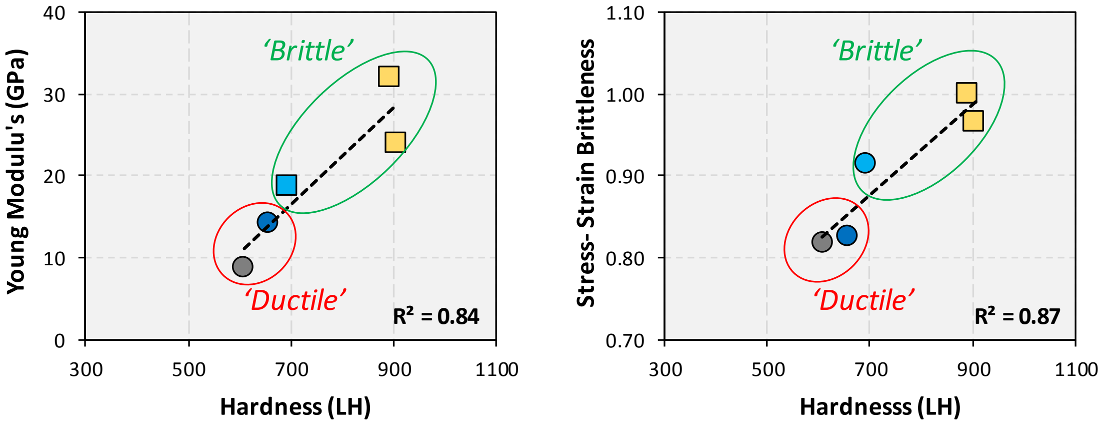

Figure 95. Cross-plots showing good positive relationships between Young's modulus and brittleness versus hardness.

In summary, it can be concluded that hardness measurements can be used as a good indicator of rock stiffness and rock brittleness **Figure 95.** For mechanical properties, it can be arguable that only one tested sample may not be representative of an entire lithofacies group, however when plotting the range of hardness values taken on 157 samples from I-35 outcrop (uppermost Woodford) and 415 samples from Speake Ranch (complete Woodford) (**Figure 96**), the observed trend of Chert > Dolomitic mudstone > Siliceous-dolomitic shale > Siliceous Shale seems to be pervasive across the entire Woodford Shale.

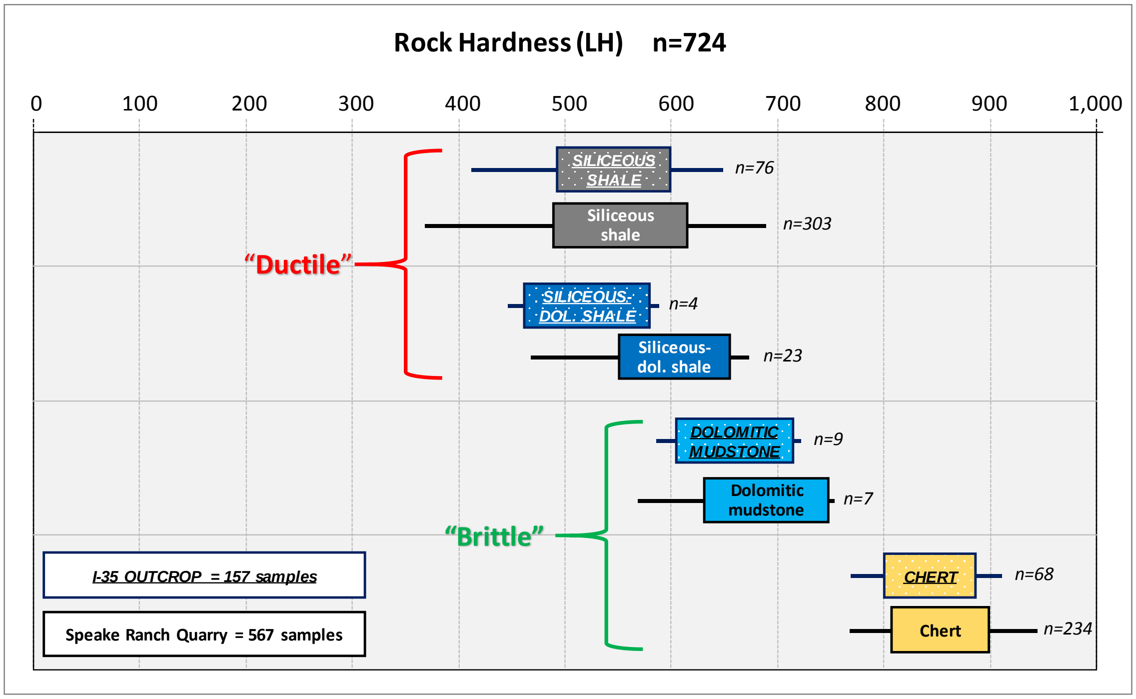

Figure 96. Comparison between hardness results gathered from I-35 outcrop samples and samples from Speake Ranch quarry.

11.NATURAL FRACTURES

The presence of natural fractures is crucial for the development of artificial hydro-fractures. Quantifying fractures from borehole or cores is not straightforward due to the limited lateral extent (diameter), so the study of natural fractures in outcrops offers much more resolution helping to understand fracture patterns in the subsurface.

The I-35 outcrop (roadcut) presents a clear exposure to investigate fractures and mechanical stratigraphic relations. At this location fracture intensities were measured along bed-parallel scanlines of 3 feet long over approximately 600 beds. For each bed, the weathering response (“soft” or “hard”) was recorded, as well as their bed thickness, which in this study coincides with fracture height as only bed-bounded fractures were counted. Fracture planes orientations were measured when perfectly evident.

Bedding orientation of the Woodford strata in this outcrop is N65°E dipping 48° SW. Two well-defined and conjugate fracture sets were recognized, set I and set II usually intersect each other at an angle of approximately 65 degrees (**Figure 97**). The mean orientation of Set I fractures is N13°W dipping 59° NE. And Set II fractures mean orientation is N52°W, dipping 64°NW. Both fracture sets are obliquely oriented to the strike of the bedding planes (**Figure 97**).

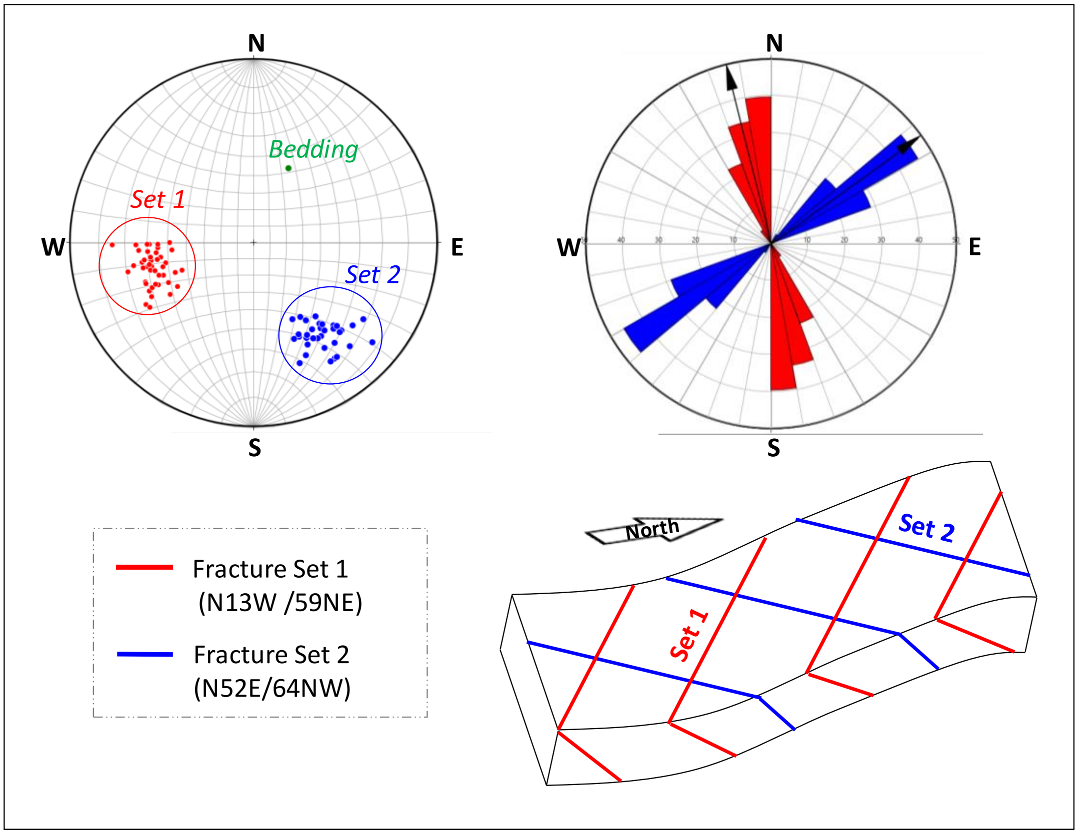

Figure 97. Orientation of the two main fractures sets identified at the I-35 outcrop. Fractures set I and set II are conjugate sets and intersect each other at an angle of 65°. Fracture sets are oblique to the bedding strike.

Generally, fractures patterns are better developed within ‘hard’ beds (**Figure 98**), they are nearly perpendicular to the bedding planes and systematically spaced across the beds (**Figure 98**). ‘Soft’ beds present a smaller amount of fractures, these are discontinuous and barely perfectly bed-bounded (**Figure 98**). Many fractures die-out within the interface with ‘soft’ beds, however a few fractures may cut both ‘hard’ and ‘soft’ beds (**Figure 98**).

Figure 98. Picture taken around foot 20 at the I-35 outcrop, showing abundant and well developed vertical fractures in hard beds (green lines) which generally terminate against soft beds (red lines).

Investigations of fracture densitiesnsities versus bed thickness evidence that overall ‘hard’ beds contain more fractures than soft beds for any given bed thickness (**Figure 99**); average fracture intensity of hard beds is about 3 times higher compared to the fracture intensities of soft beds. **Figure 99** shows that the greater population of fractures are contained within thin beds of 0.5 to 2 inches. This observation coincides with results of Ghosh (2015, 2016) who conducted several fracture studies on different Woodford Shale outcrops in Southern Oklahoma.

Additionally, prior fracture studies on cores conducted by Gale et al., (2014), reported that fractures in the Woodford are mostly contained in thin beds (< 6 cm) compared with other unconventional resources shales (e.g. Barnett, Marcellus, New Albany, etc.), the Woodford Shale is the one presenting the least of natural fractures height.

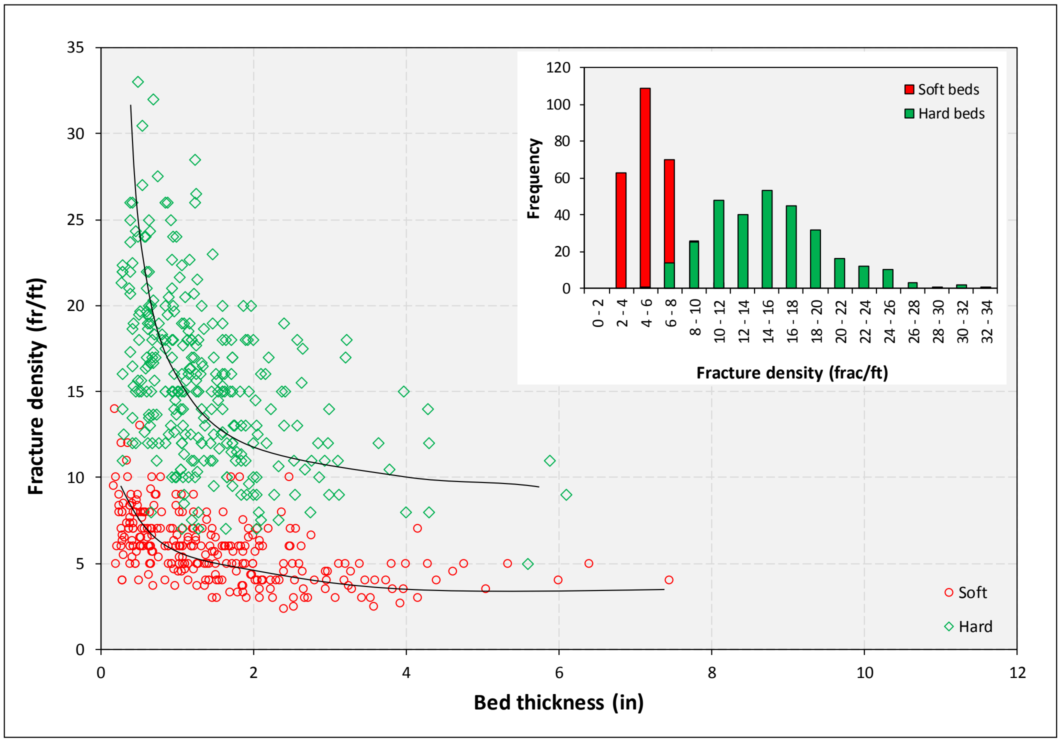

Figure 99. Cross-plot of fracture density and bed thickness. Histogram displaying fracture density measured along scan-lines. Note the greater amount of fractures within hard beds n= 576.

Figure 99 also reveals data points broadly scattered and does not appear to be a simple linear relationship between bed thickness and fracture density (**Figure 99**), which implies there must be another factor(s) accounting for variations in fracture density at variable bed thicknesses. In this work, when fracture density and bed thickness are separated by soft-to-hard ratios, different slopes and better correlation factors were obtained for bed thickness and fracture density (**Figure 100**).

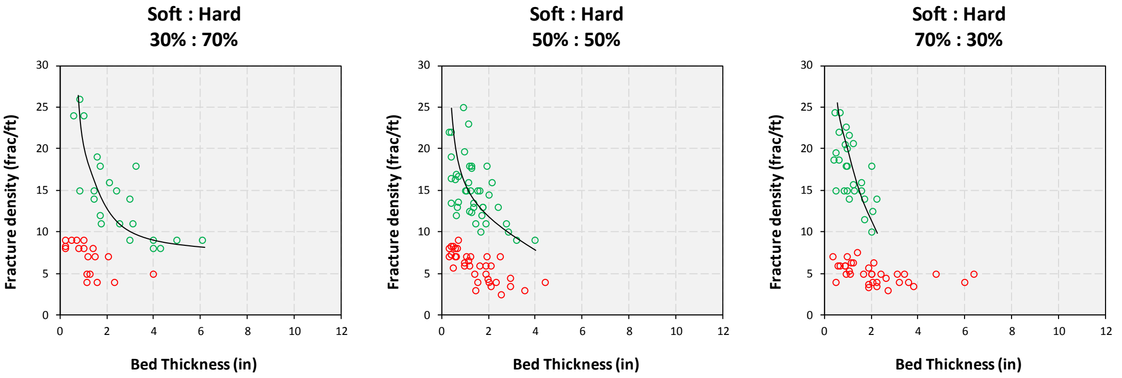

Figure 100. Cross-plots of fracture density versus bed thickness for three cases of soft-to-hard ratios. Note in the 30:70 case, fracture density seems to be more sensitive to variations of bed thickness when hard beds dominate. In cases where there is too much soft beds (70:30) bed thicknesses of hard beds seem not to correlate with fractures densities.

Intervals where the percentage of hard beds is greater with respect to soft beds (30:70), a gentler negative slope is observed for hard beds (green dots) showing that fracturing of thin beds is more intense whereas thick beds present a lower amount of fractures (**Figure 100**). In contrast, for intervals of about 70 percent of soft beds, the fracture intensity of hard beds seems to vary independently of bed thickness, where beds below 2 inches present different degree of fracturing, varying from 10 fractures up to 25 fractures per lateral foot (**Figure 100**).

Thus, it can be inferred that hard beds present higher fracture densities when contained within intervals with higher amounts of shale beds (higher soft-to-hard ratios), whereas lower densities are observed when hard beds are contained in intervals predominantly made of hard beds (lower soft-to-hard ratios) (**Figure 100**). In other words, a thin hard bed may present different amounts of fracture whether it is neighbored by lower or greater amount of soft beds.

This tendency is also observed when vertically plotting fracture densities per individual beds, where the zones that present higher soft-to-hard ratios display higher fracture densities (**Figure 101**). Also, it was demonstrated that at any given stratigraphic position, hard beds present greater fracture densities compared to soft beds (**Figure 101**).

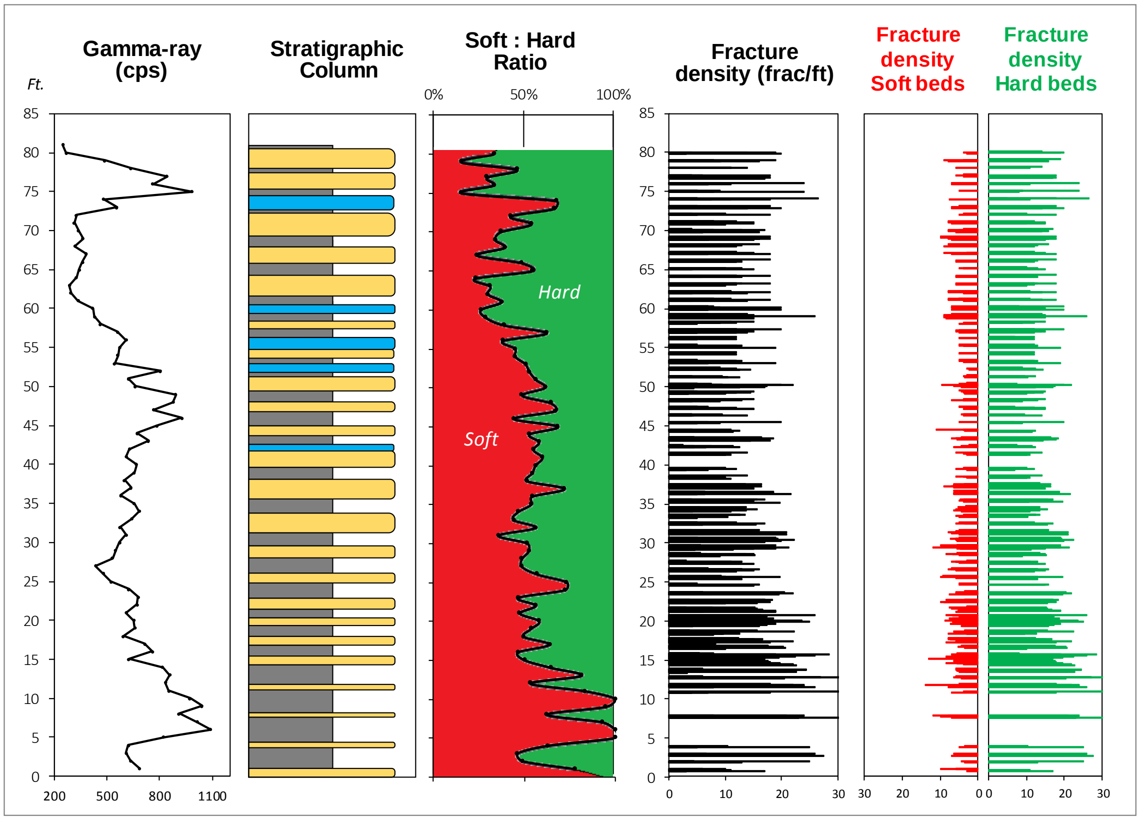

Figure 101. Vertical plot showing fracture density across the Woodford section exposed at I-35. Note the higher fracture densities coinciding with zones that present higher soft-to-hard ratios.

12. SYNTHESIS OF SOFT AND HARD BEDS CHARACTERISTICS

Rock types of the Woodford Shale at the I-35 outcrop can be grouped into two main groups, ‘soft’ lithofacies and ‘hard’ lithofacies. Across the different laboratory results, we demonstrated that these two rock types are not only contrasting in weathering responses (as initially identified), but also by their mineral/elemental composition, rock fabric and mechanical properties. Siliceous shales are the main lithofacies within the ‘Soft’ group and Cherts are the main lithofacies within the ‘Hard’ group. Dolomitic lithofacies occur in minor proportions (< 8%) and because of that are not considered within this summary of rock characteristics of soft and hard beds.

Rock composition

Based on XRF results, eight elemental proxies were found to be key to differentiate between hard and soft beds; Si/Al, Al, K, Ti, Zr, U, Mo and V. Si/Al was found as the main proxy for quartz type (biogenic/authigenic), yielding significantly higher values for hard beds (Si/Al avg. 45) in comparison to soft beds (Si/Al avg. 10) (**Figure 102**). On the other hand, the abundance of detrital/clay proxies Al, K, Ti, Zr is greater in soft beds, which usually reach average values between 3 to 14 times more than in hard beds (**Figure 102**); thus, indicating a relatively higher detrital affinity for soft beds than for hard ones.

Redox-sensitive proxies such us U, Mo, and V are present in greater proportions within soft beds, with average values twice or three times higher in soft beds (**Figure 102**), suggesting higher organic contents in these beds.

With regards to XRD mineralogy, even though both soft and hard beds are largely composed by quartz and minor clays and carbonate contents, quartz contents in hard beds are markedly higher (>85 wt.%) than in soft beds (avg. 70 wt.%) (**Figure 102**). In the same way, clay contents are notably lower in hard beds (avg. 4%) compared to soft ones (avg. 28 wt.%). Additionally, Leco TOC values were about 5 times higher in soft beds when compared to the hard beds (**Figure 102**).

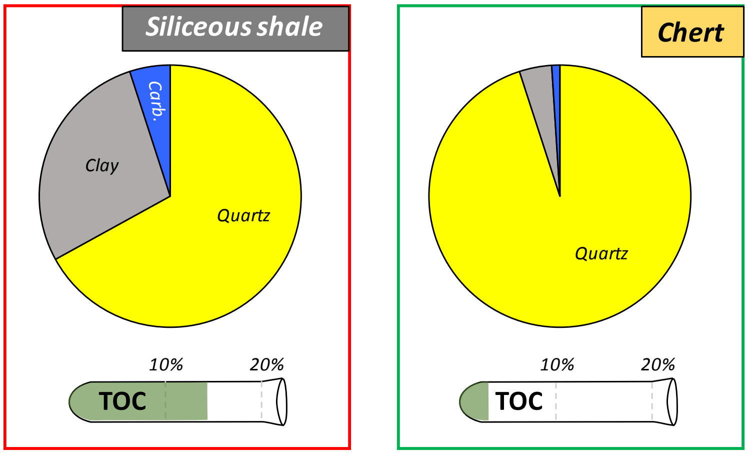

Weathering Response	Lithofacies	Quartz (%)	Clays (%)	Carbonates (%)	TOC (wt.%)
Soft	Siliceous Shale	67	28	5	14
Hard	Chert	95	4	1	3

Weathering Response	Lithofacies	Si/Al	Al (ppm)	K (ppm)	Ti (ppm)	Zr (ppm)	U (ppm)	Mo (ppm)	V (ppm)
Soft	Siliceous Shale	10	30,000	14,000	2,000	70	30	180	1,700
Hard	Chert	45	9,000	1,000	315	35	16	76	500

Figure 102. Summary of rock composition for Soft and Hard beds of the Woodford shale at I-35 outcrop, including elemental composition (from XRF), mineralogical composition (from XRD), and organic richness (from TOC).

Rock Fabric

During field work, rock fabric (represented via weathering responses) was the first criterion to differentiate soft and hard beds. Interestingly most of these rock characteristics are pervasive across different scales, from centimeter scale in hand scale down to micron scale in thin sections and SEM images (**Figure 103**)

Soft beds are commonly dark-gray to black. Lamination is the most distinctive feature; however, it is important to mention that lamination is more visible in outcrops as this feature is enhanced by modern weathering. Microscopically, the dark matrix of soft beds is composed by authigenic quartz, parallel-oriented clay minerals and amorphous organic matter (**Figure 103**). Coarser particles consist of flattened *Tasmanites cysts* which follow the parallel lamination (**Figure 103**); other coarser particles in very minor proportions are detrital silt-sized quartz and pyrite crystals.

Hard beds are similar in color to the soft beds (dark-gray to black). Hard beds appear massive and blocky at the field scale and are not fissile. Thin sections and SEM images of hard beds exhibit a very tight matrix composed mainly by micro-crystalline quartz aggregates (authigenic/biogenic), where grain-to-grain contacts are 'welded' (**Figure 103**). Coarser particles within hard beds are recrystallized radiolarians and *Tasmanites* cysts which are dispersed throughout; both fossils generally occur well preserved and rounded (**Figure 103**), filled by different materials (e.g. quartz, pyrite, bitumen, etc.). Vertical fractures in hard beds are commonly observed in hand specimen as well as in thin sections, most of them are filled with bitumen, and in minor amounts filled by chalcedony quartz.

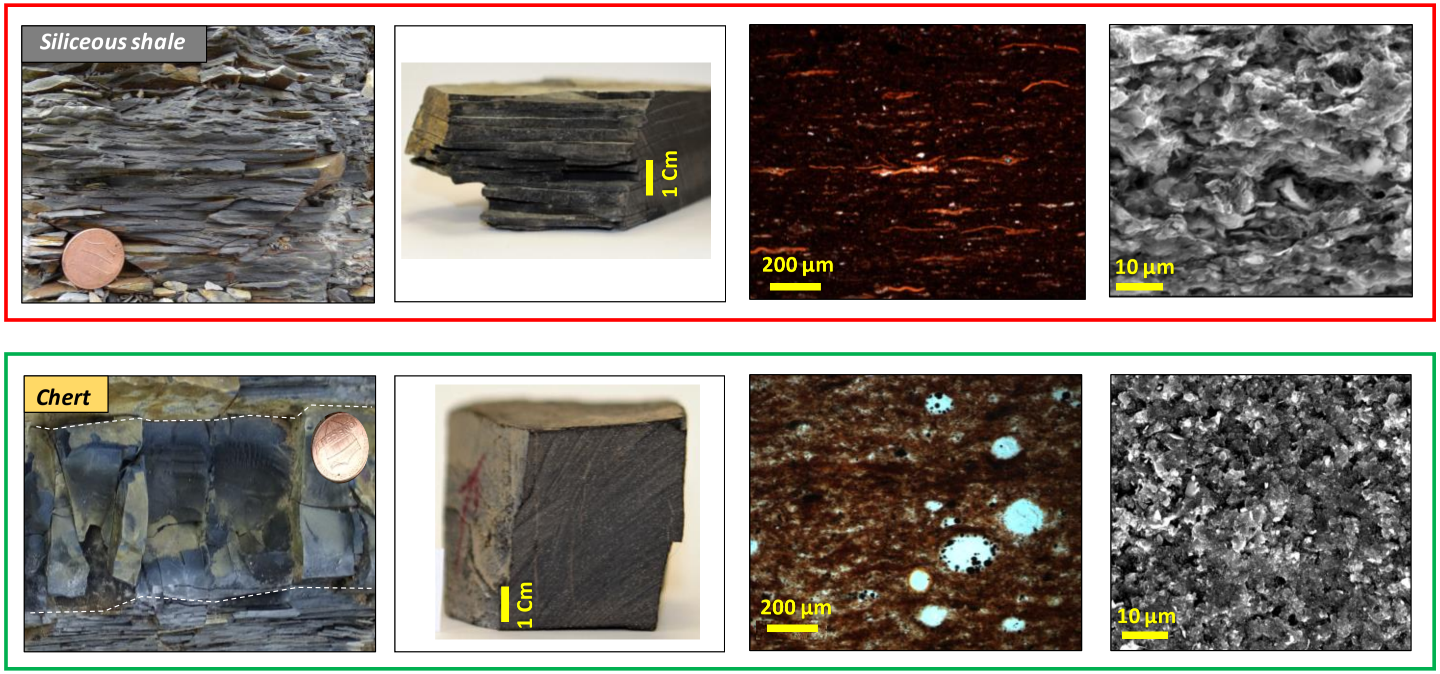

Weathering Response	Lithofacies	Physical Appearance	Microfabric	Fossils
Soft	**Siliceous Shales**	Fissile, Laminated	Subtle preferred parallel orientation	Flattened *tasmanites*
Hard	**Chert**	Hard, massive	Random oriented microcrystalline aggregates	Well-preserved, rounded silicified radiolarians and *tasmanites*

Figure 103. Summary of rock fabric characteristics for soft and hard beds from field scale down to the micrometer scale.

Mechanical properties

Hard and soft beds were expected to present very contrasting mechanical properties since the field work activities; soft beds were easier to break with the hammer than hard beds, which suggested marked differences in rock strength between these two rock types.

Based on stress-strain curves obtained by uniaxial tests, soft beds presented ductile failure while hard beds failed as brittle (Figure 104). Similarly, brittleness indices were calculated using mineralogy and stress-strain curves, revealing higher brittleness values for hard beds in comparison to the soft beds.

Other mechanical properties as UCS and Young's modulus were found to be higher in hard beds compared to soft ones, making hard beds much stronger and stiffer than soft beds (Figure 104). Additionally, hardness measured using the micro-rebound hammer yielded highly contrasting values, hard beds (avg. 815 LH) are harder than soft ones (avg. 540 LH) (**Figure 104**).

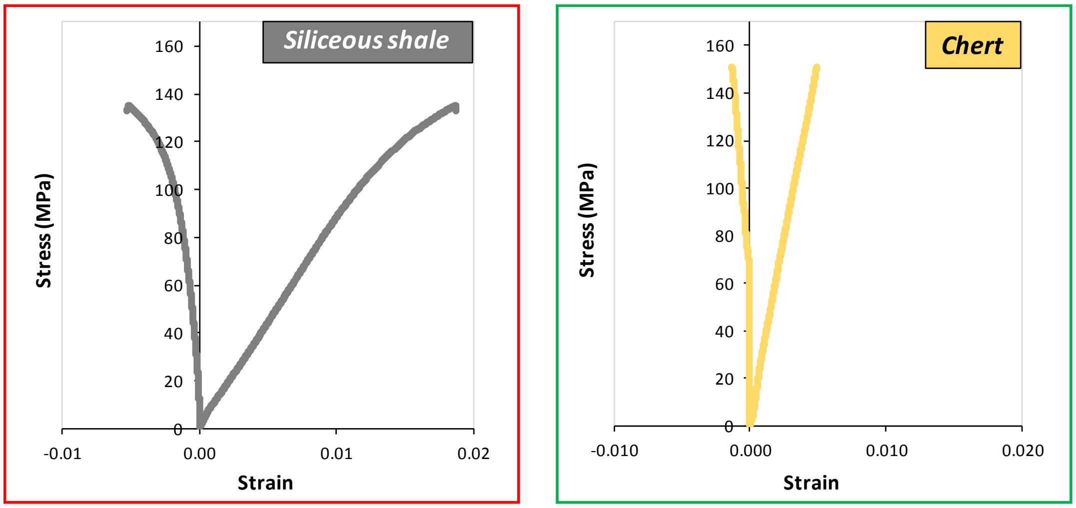

Weathering Response	Lithofacies	UCS (Mpa)	Young's Modulus (GPa)	Poisson's Ratio	Hardness (LH)	Mineralogical Brittleness Index	Stress-Strain Brittleness
Soft	**Siliceous Shales**	135	9	0.2	540	0.69	0.82
Hard	**Chert**	153	27	0.14	815	0.92	0.98

Figure 104. Summary of mechanical properties of soft and hard beds of the Woodford Shale at I-35 outcrop.

13.CONCLUSIONS

- The measured exposure (81 ft) of Woodford Shale at the I-35 outcrop comprises parts of the middle and upper informal Woodford members. The complete lower and most of the middle members are covered by vegetation. The overlying and underlying formational contacts with the Sycamore Limestone and Hunton group, respectively, are present at this location and were documented in detail with Gamma ray profiles.

- Four main lithofacies were identified: Siliceous Shale, Chert, Dolomitic Mudstone and Siliceous-Dolomitic Shale. About 90% of these mudrocks corresponds to Siliceous Shales and Cherts. These two lithofacies contain similar mineral phases: quartz, clays and minor amounts of dolomite, pyrite and feldspars. Regardless of stratigraphic position, Siliceous Shales show significantly higher clay contents (10 to 30 wt.%) than Chert lithofacies (<10 wt.%). Siliceous-Dolomitic Shales are a variety of Siliceous Shales, but with greater amounts of dolomite (<50 wt.%). Dolomitic Mudstone lithofacies contain elevated amounts of dolomite/ankerite (>80 wt.%) and minor amounts of quartz and clays.

- Chert beds are largely made of microcrystalline quartz aggregates (authigenic/biogenic), amorphous organic matter and traces of clay flakes. Radiolarians and *Tasmanites* are common and well-preserved in Cherts, these fossils usually occur silicified and rounded. *Tasmanites* are less abundant than radiolarians. Additionally, vertical to sub-vertical microfractures are more common in Cherts than in others lithofacies, these are usually filled with chalcedony quartz, bitumen or calcite.

By contrast, Siliceous Shales are typically laminated and composed of microcrystalline quartz (predominantly authigenic) mixed with clay minerals (mainly illite) and organic matter. The presence of flattened *Tasmanites* without quartz infillings is pervasive within Siliceous Shales.

- In terms of organic matter quality as determined by Rock-Eval Pyrolysis, Type II kerogen was identified for both Cherts and Siliceous Shales. However, Siliceous Shales preserve greater amounts of organic matter (avg. TOC 13 wt.%) in comparison to Cherts (avg. TOC 3 wt.%). Lower TOC values of Cherts can be attributed to poor preservation and/or dilution of organic matter by the biosiliceous particles.

- Several elemental proxies were found useful for paleo-environmental conditions and rock composition of the Woodford Shale: Detrital proxies (Al, K, Ti and Zr), carbonate proxies (Ca, Sr and Mg) and redox-sensitive proxies (Mo and U). Generally, Siliceous Shales contain higher concentrations of detrital proxies than Chert beds, which in turn present elevated Si/Al ratios and supports a greater contribution from biogenic/authigenic supply within this lithofacies. Dolomitic lithofacies were distinguished by very high concentrations of Ca, Sr and Mg. Correlations of redox-sensitive proxy versus TOC showed Mo as the most reliable proxy for organic contents in the Woodford strata. Generally, Siliceous Shales contain greater concentrations of Mo and correlate with the higher TOC contents among the Woodford lithofacies.

- Three different approaches were tested to model a simplified Woodford shale mineralogy (quartz, clays and carbonates) from XRF data. The approach that better depicted the actual Woodford Shale mineralogy uses the normalized concentrations of SiO_2, Al_2O_3*5 and CaO*2, which represented the silica, aluminosilicate, and carbonate component of the Woodford strata. Although this method ignores the contribution from other elements in other mineral phases (e.g. pyrite, feldspars), it proved to be useful for obtaining estimates of the bulk clay, quartz and carbonates variability within the Woodford Shale and helped to populate vertical profiles of mineralogical brittleness index.

- Owing to the super high-resolution data sets that are commonly gathered from XRF analyses, the implementation of quick and reliable approaches that model mineralogy from elemental concentrations can be beneficial in several aspects: 1) providing a continuous and decent approximation of the mineral composition; 2) calculation of mineralogical brittleness index; 3) decreasing the number of expensive XRD analyses; 4) guiding further and more complex laboratory analysis (e.g. porosity-permeability, geomechanical tests); 5) improving petrophysical models; 6) defining lithofacies.

- Rock hardness was measured using a micro-rebound hammer (piccolo 2^{TM}) and provided insights on mechanical properties of lithofacies in the Woodford Shale. Cherts are the hardest lithofacies (avg. 820 LH), and Siliceous Shales showed lower hardness values (avg. 540 LH).

- After mineral composition, the rock fabric (e.g. massive or laminated) was encountered as an important factor affecting the hardness of the Woodford Shale strata at the bed scale, more lamination results in lower hardness, and conversely fewer laminations give higher hardness. Other controls on rock hardness were related to organic contents and crystal size (in the case of dolomitic beds).

- Based on uniaxial compressive tests, the two main rock types described as hard and soft at the field scale were proved to correspond to brittle and ductile rocks respectively. Cherts are the strongest (highest UCS), stiffest (highest Young's modulus) and more brittle lithofacies (absent of plastic deformation). Siliceous Shales are the most ductile among the four lithofacies, sustaining the greatest amount of plastic deformation before failure accompanied by the lowest UCS and Young's modulus values.

- Rock brittleness was assessed using the mineralogical brittleness index and the stress-strain curves from the uniaxial tests. In general, a brittle/ductile boundary for the main Woodford lithofacies was identified at approximately 0.85. Rocks with brittleness >0.85 are considered brittle and comprise the lithofacies of Cherts and Dolomitic Mudstones, which in the outcrop were identified as "hard" beds. Conversely, rocks with brittleness <0.85 were considered ductile and comprise the lithofacies of Siliceous Shales and Siliceous-Dolomitic Shales, and were identified at the field scale as "soft" beds.

- Although rock hardness from the micro-rebound hammer has been extensively used to construct empirical equations and predict UCS values, this association was not clearly observed for the Woodford Shale rocks of this study. Indeed, it was demonstrated that the published empirical equations that may work in other formations with other rock types, do not work to reliably predict UCS values from hardness in the Woodford Shale mudrocks. This observation suggests the necessity of conducting more mechanical tests to evaluate empirical relationships between hardness and UCS for the Woodford Shale strata.

- Good correlations were found between rock hardness, Young's modulus and rock brittleness (mineralogical and stress-strain brittleness). Thus, hardness measurements can be used as a good indicator of rock stiffness and rock brittleness.

- The study of natural fractures in the outcrop revealed that overall, hard beds contain more fractures than soft beds for any given bed thickness; average fracture frequency in hard beds is about 3 times higher compared to the fracture frequencies in soft beds. Additionally, it was observed that when hard beds are contained within intervals with higher amounts of shale beds (higher soft-to-hard ratios), these have higher fracture densities than in intervals predominantly made of hard beds. In other words, a thin hard bed may present different amounts of fractures whether it is neighbored by lower or greater amounts of soft beds.

- Perhaps the most important conclusion of this study is that the Woodford Shale is composed by two main rock types: ‘hard-brittle’ and ‘soft-ductile’ beds, which presented highly contrasting characteristics (*see synthesis*). So, it is very important to mention that the distinction of soft and hard beds is not only a visual descriptor based on weathering responses, but also across numerous samples and several laboratory techniques conducted in this work (XRD, XRF, TOC, SEM, Hardness and UCS), from which the distinction between soft and hard beds was glaring. Additionally, it was demonstrated that regardless of their stratigraphic position, hard and soft beds maintain their unique properties.

14.LIMITATIONS AND RECOMMENDATIONS

Laboratory results throughout this thesis have demonstrated that, depending on the rock type (soft or hard), results can be highly contrasting even at adjacent beds, and allows to suggest that interpretations could be ambiguous as they are dependent on the type of rock sampled. It has also been demonstrated that almost regardless of stratigraphic position a soft bed or hard bed maintain their lithological properties; for those reasons laboratory results from Woodford Shale strata must be addressed with caution and making more emphasis on how representative is a sample in a given interval.

Traditionally in the oil industry, rock sampling for the different laboratory analyses is conducted systematically (at equally-spaced intervals), which may be useful in vertically homogeneous formations or in formations where vertical heterogeneities are highly predictable or easier to detect on well-cores or logs. For example, when heterogeneities are of low frequency or stacked in thick packages (>1 ft.) (e.g. Eagle Ford, Wolfcamp), a 1-ft separated systematic rock sampling can be enough to fully capture all the lithologic and stratigraphic heterogeneities. However, in the case of high-frequency interbedded formations as is the Woodford Shale, several factors may pose disadvantages for the traditional systematic rock sampling:

- First, on well cores, the physical appearance of soft and hard beds looks similar as they both are dark black (**Figure 105**), thus making difficult to pick lithological differences based on rock color. As opposed to other formations where differences in color are more evident, they may suggest lithological changes and facilitates the recognition of lithology heterogeneities. For example, in the Eagle Ford or Wolfcamp formations limestone beds highlight from the shale beds just by their lighter colors on well cores. Thus, if a geoscientist approaches for the first time a Woodford Shale core for sampling, the rock color most possibly does not work for differentiating rock types, and other proxies must be used (e.g. hardness, XRF).

- Second, because of rock fabric and mineral composition, hard beds are usually better preserved as they are more resistant to weathering than the soft ones. Thus, hard beds usually are the easiest to retrieve with a core plug or collect at the field. And sometimes, the rock collector might discard the soft ones because these are difficult to collect as core disking is common. For example, for geomechanical tests, meeting specific sample dimensions and rock integrity is important, and usually the tested rocks are the ones better preserved owing to the lack of disking (as the hard beds). In my opinion, several of the published literature on the Woodford shale is limited by specimen integrity, and not all the spectrum of rock types is tested; indeed, usually the most clay-rich lithofacies remain untested because of their poor preservation.

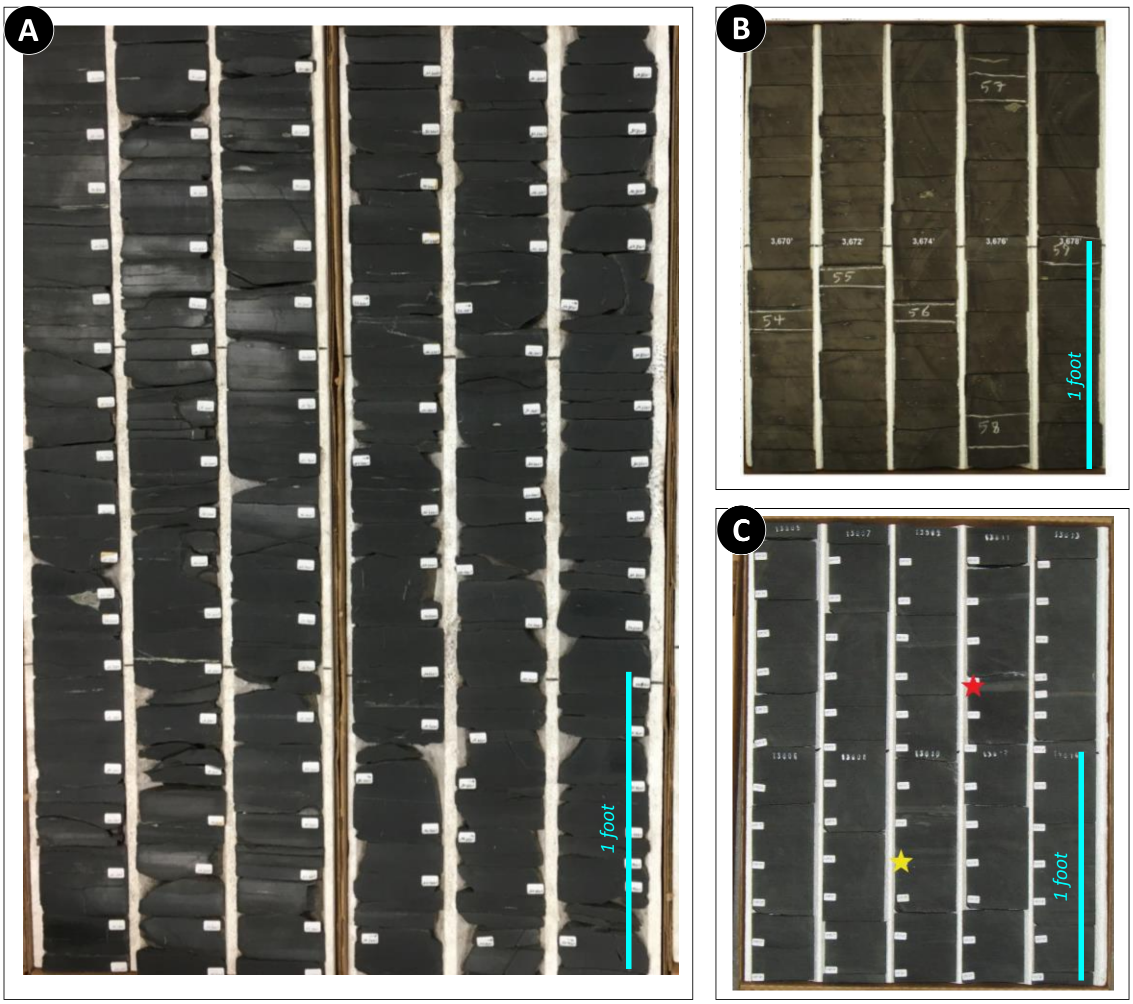

Figure 105. Example of three different Woodford Shale cores displaying several feet of black rocks which show minimal variation. (**A**) Courtesy of Richard Brito. (**B**) Watson, 2008. (**C**) Turner, 2016.

- Third, and most importantly, thicknesses and frequency of hard-soft cycles may vary drastically vertically across the Woodford Shale. For instance, there are some intervals consisting of thicker soft beds and thinner hard beds (**Figure 106A**), and intervals made of thicker hard beds than soft beds (**Figure 106C**). Additionally, there are more complex intervals where vertical changes in thickness and frequency of soft-hard beds can occur within a few feet (**Figure 106B**).

For example, the lower half of the interval **B** (**Figure 106B**) (12 – 14 ft.) presents thicker soft beds with thin hard beds but the upper half of the interval (14 – 16 ft.) displays a higher frequency of thinner soft and hard beds.

Figure 106 presents three actual examples from the I-35 outcrop of different stacking patterns (of 5-ft thick each) in which bed thicknesses and soft-to-hard ratios varies from case to case. These examples illustrate how variable would be the laboratory results if six samples were to be collected systematically at every foot (yellow diamonds in **Figure 106**). For example, the case of interval **A**, too many hard beds would be collected (4 out of 6) although the interval is made up mostly of soft beds) (**Figure 106A**). Similarly, even though interval **C** mostly consists of hard beds, the majority of samples would fall within soft beds (**Figure 106C**). In such two cases, samples would not be representative of the dominant lithology at the given 5-ft intervals. In other words, given the high frequency interbedding of the Woodford Shale strata, a systematic sampling would present many uncertainties depending on where the sample point falls. In contrast, a lithology-guided sampling is recommended either aided by XRF or hardness measurements, which are relatively quick and cheap techniques to conduct at very high resolutions.

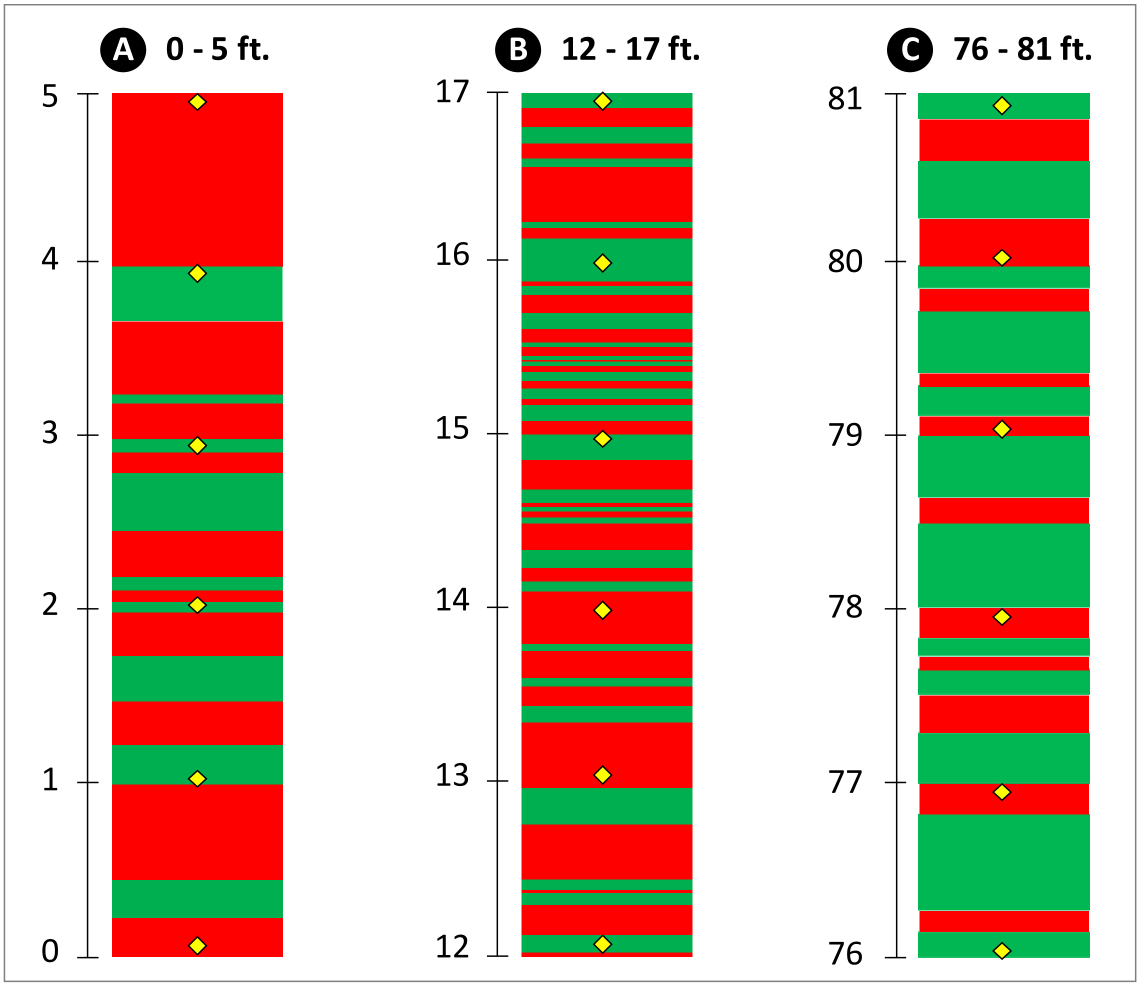

Figure 106. Examples of 5-ft intervals from the I-35 Woodford outcrop. Notice the differences on frequency between hard and soft beds in the three cases. (**A**) abundant thick soft beds predominate in respect to hard ones. (**B**) The lower and upper third of the interval present thicker and abundant soft beds while the middle part presents similar thicknesses and amounts of hard and soft beds. (**C**) thicker and abundant hard beds dominate in reference to the hard beds. Yellow diamonds indicate the location of samples at a given 1-ft systematic sampling. Bed thicknesses were directly measured from the outcrop.

Further, in order to illustrate how contrasting would be the TOC results depending on the rock type chosen by different sampling methods, **Figure 106**, presents the example of a 5-ft interval using three different hypothetic methods for sampling: a) systematic, b) random, and c) lithology-guided (**Figure 107**).

In the example of systematic sampling of **Figure 107**, organic richness is over-estimated (TOC >10 wt.%) across the entire 5-ft interval, which is not true as the interval is mainly made of hard beds with TOC's lower than 3%. In the second example, samples are randomly distributed, and almost completely different interpretations of organic richness can be made from the prior example (**Figure 107b** and **Figure 107c)**.

Therefore, for a more accurate representation of the organic richness of the interval, my recommendation would be to equally cover with samples the soft and hard beds, and then upscale the results (TOC in this case) to a log scale (1-ft) by using the weighted average equation proposed in this work (equations 19 to 21). This equation basically works by averaging the TOC values of the soft samples separately from the hard samples, and then by using the soft to hard ratio per foot the 'Upscaled TOC' per foot is re-calculated (**Figure 107**); in this way, measured TOC values would be more comparable to log-derived TOC curves.

The same approach can be applied for different laboratory results as mechanical properties (UCS, Young's modulus and Poisson's ratio), brittleness indices and mineralogy.

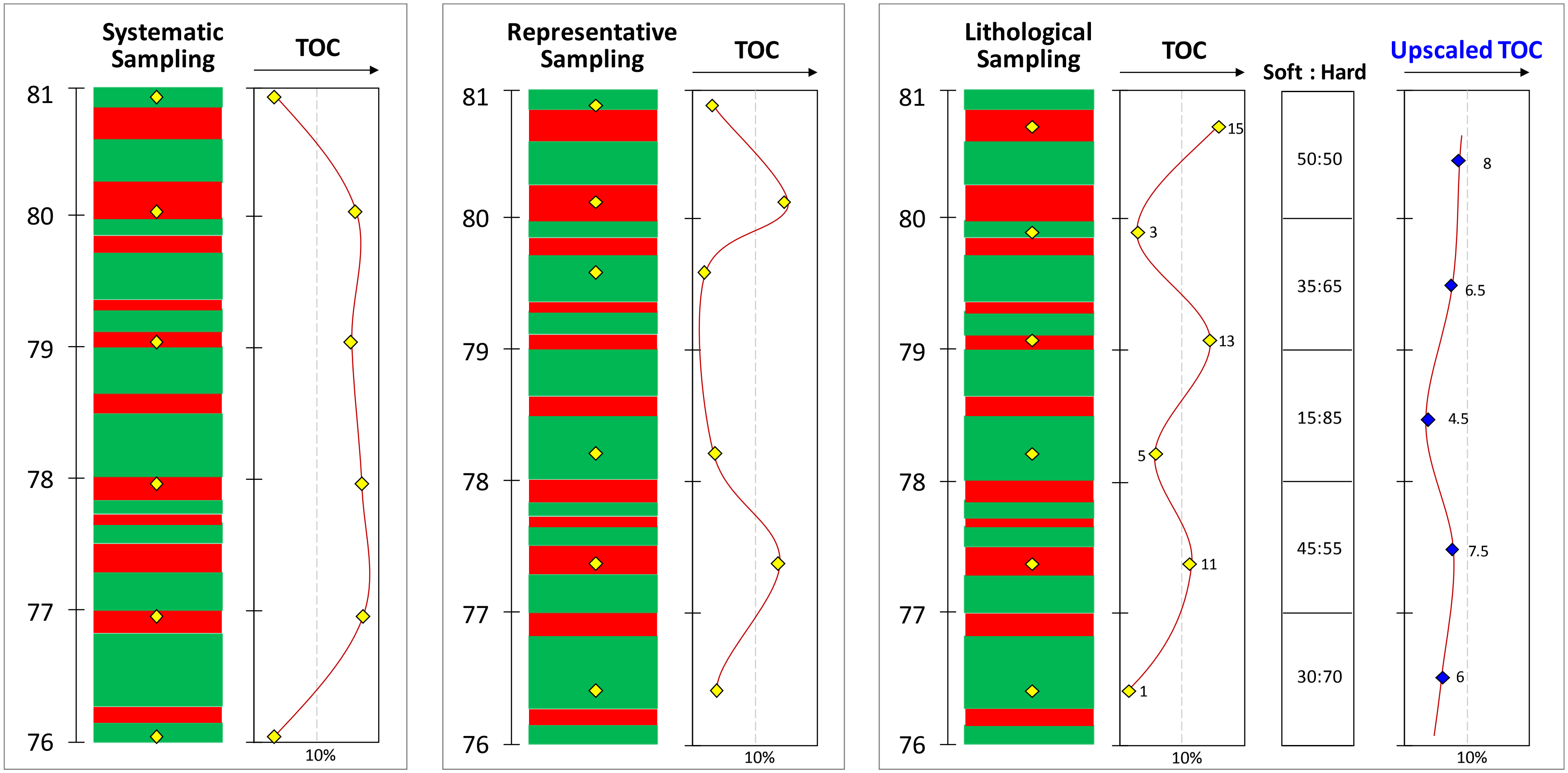

Figure 107. Examples of possible TOC curves for different sampling methods on a given 5-ft interval (Interval C in Figure 106). Yellow diamonds indicate the location of samples. (**a**) Systematic sampling showing overestimation of TOC values because mostly soft beds were sampled. (**b**) Random sampling showing a different TOC curve than (a), since most of the samples were taken on hard beds. (**c**) Lithological sampling properly depicting the vertical variability between hard and soft beds within the interval. Upscaled TOC (blue diamonds) calculated using equations 19 to 21 shows a more accurate curve of TOC, which consider the proportions of soft and hard beds per foot.

$$Upscaled\ TOC = \frac{(Avg.TOC\ Soft\ beds * \%Soft) + (Avg.TOC\ hard\ beds * \%Hard)}{100} \quad (19)$$

$$Upscaled\ TOC\ (76 - 77\ ft) = \frac{(13 * 30) + (3 * 70)}{100} \quad (20)$$

$$Upscaled\ TOC\ (76 - 77\ ft) = 6\ wt\% \quad (21)$$

As a final recommendation regarding rock sampling in the Woodford Shale, sample sets for different laboratory analyses should be preferably taken at the same depth. Given the thin-bedded nature of the Woodford Shale, even results from two adjacent beds might present very different values of TOC and mineralogy, for that reason it is highly recommended not to merge results from near depths. In the Woodford Shale strata, samples from just a few inches of separation most likely correspond to different facies.

Lastly, in order to distinguish between soft and hard beds in cores, subtle changes can be seen on the back side of the core, where soft beds appear smoothed in comparison to the irregular surfaces in hard beds which are much more resistant to the coring bit (**Figure 108**). However, a more straightforward and reliable way would be to use a micro-rebound hammer, where hardness values above ~800 LH can be related with hard beds and lower values with soft beds (**Figure 70**).

Figure 108. Examples of subtle changes in the back side of a Woodford Shale core that can help to distinguish soft and hard beds. Courtesy of Richard Brito.

REFERENCES

Algeo, T., & Maynard, J., 2004, Trace-element behavior and redox facies in core shales of Upper Pennsylvanian Kansas-type cyclothems. Chemical Geology, v. 206, p. 289-318.

Algeo, T. J., & Lyons, T. W., 2006, Mo-total organic carbon covariation in modern anoxic marine environments: Implications for analysis of paleoredox and paleohydrographic conditions. Paleoceanography, 21(1).

Algeo, T.J., Lyons, T.W., Blakey, R.C., and Over, D.J., 2007, Hydrographic conditions of the Devono-Carboniferous North American Seaway inferred from sedimentary Mo-TOC relationships: Palaeogeography Palaeoclimatology Palaeoecology, v. 256, p. 204-230.

Aoki, H., & Matsukura, Y., 2008, Estimating the unconfined compressive strength of intact rocks from Equotip hardness. Bulletin of Engineering Geology and the Environment, 67(1), 23-29.

ASTM, D., 1992. 2938, Standard Test Method for Unconfined Compressive Strength of Intact Rock Core Specimens. ASTM International, West Conshohocken, PA.

Ataman, O., 2008. Natural Fracture Systems in the Woodford Shale, Arbuckle Mountains, Oklahoma. Oklahoma State University, MS thesis, 185p.

Aufill, M., 2007, High resolution magnetic susceptibility of the Oklahoma Woodford Shale and relationship to variations in outcrop spectral-gamma response: Stillwater, OK, Oklahoma State University, unpublished M.S. thesis, 210 p.

Badra, H., 2011. Field characterization and analog modeling of natural fractures in the Woodford Shale, southeast Oklahoma. University of Oklahoma, MS thesis, 156p.

Banner, J.L., 1995. Application of the trace element and isotope geochemistry of strontium to studies of carbonate diagenesis. Sedimentology, 42(5), pp.805-824.

Barnston, A.G., 1992. Correspondence among the correlation, RMSE, and Heidke forecast verification measures; refinement of the Heidke score. Weather and Forecasting, 7(4), pp.699-709.

Barrick, J. E. and Klapper, G., 1990, STOP 2 - Henryhouse and Haragan Formations (Late SilurianEarly Devonian) and Woodford Shale (Late Devonian-Early Mississippian), p. 11-13, in Ritter, S. M., (ed.), Early to Middle Paleozoic conodont biostratigraphy of the Arbuckle Mountains, southern Oklahoma. Oklahoma Geological Survey Guidebook 27.

Bhatia, M.R. & Crook, K.A.W. 1986. Trace element characteristics of graywackes and tectonic setting discrimination of sedimentary basins. Contributions to Mineralogy and Petrology, 92, 181-193.

Boardman, 2009. Preliminary analysis of phosphate nodules in the Woodford Shale, Late Devonian-Early Mississippian, southern Oklahoma, Oklahoma State University, MS thesis, 77p.

Bontempi, C.P., 2015, High resolution stratigraphy of thin bedded shales radiolarites, Woodford Shale, Arbuckle wilderness area, Oklahoma. MS thesis, University of Oklahoma, 81p.

Brace, W.F., 1961, January. Dependence of fracture strength of rocks on grain size. In The 4th US Symposium on Rock Mechanics (USRMS). American Rock Mechanics Association.

Bramlette, M.N., 1946. The Monterey Formation of California and the origin of its siliceous rocks (Vol. 212). US Government Printing Office.

Breit, G.N. and Wanty, R.B., 1991. Vanadium accumulation in carbonaceous rocks: a review of geochemical controls during deposition and diagenesis. Chemical Geology, 91(2), pp.83-97.

Brookins, D. G., 1988, Eh-pH diagrams for geochemistry: in Kesler, S. E., Geochimica et Cosmochimica Acta vol. 53(3), Springer-Verlag, New York p. 763.

Brumsack, H. J., 1989, Geochemistry of recent TOC-rich sediments from the Gulf of California and the Black Sea. Geologische Rundschau, v. 78, p. 851-882.

Brumsack, H. J., 2006, The trace metal content of recent organic carbon-rich sediments: implications for Cretaceous black shale formation. Palaeogeography, Palaeoclimatology, Palaeoecology, 232(2), 344-361.

Calvert, S.E. and Pedersen, T.F., 1993. Geochemistry of recent oxic and anoxic marine sediments: implications for the geological record. Marine geology, v. 113(1-2), p. 67-88.

Cardott, B.J. and Lambert, M.W., 1985. Thermal maturation by vitrinite reflectance of Woodford Shale, Anadarko basin, Oklahoma. AAPG Bulletin,69(11), pp.1982-1998.

Cardott, B.J. and Chaplin, J.R., 1993. Guidebook for selected stops in the western Arbuckle Mountains, southern Oklahoma (No. 3). Oklahoma Geological Survey.

Cardott, B.J., 2005. Overview of unconventional energy resources of Oklahoma. In: Cardott, B.J. (Ed.), Unconventional Energy Resources in the Southern Midcontinent, 2004 Symposium: Oklahoma Geological Survey Circular, 110, pp. 7–18.

Cardott, B.J. 2012. Thermal maturity of Woodford Shale gas and oil plays, Oklahoma, USA. Journal of Coal Geology, 103, 109-119.

Cardott, B.J., 2014, Woodford Shale play update: Expanded extent in the oil window: AAPG Search and Discovery Article #80409, 51 slides.

Comer, J.B., and Hinch, H.H., 1987, Recognizing and quantifying expulsion of oil from the Woodford Formation and age-equivalent rocks in Oklahoma and Arkansas: AAPG Bulletin, v. 71, p. 844-858.

Connock, G.T., 2015, Paleoenvironmental interpretation of the Woodford Shale, Wyche Farm shale pit, Pontotoc County, Arkoma Basin, Oklahoma with primary focus on water column structure. M.S. thesis, University of Oklahoma, 253 p.

Daniels, G., Mcphee, C., Sorrentino, Y., & McCurdy, P. 2012. Non-Destructive Strength Index Testing Applications for Sand Failure Evaluation. Proceedings of SPE Asia Pacific Oil and Gas Conference and Exhibition, (L), 1–12.

Davis, C., Pratt, L., Sliter, W., Mompart, L., and Murat, B., 1999, Factors influencing organic carbon and trace metal accumulation in the Upper Cretaceous La Luna Formation of the western Maracaibo Basin, Venezuela, in Barrera, E., and Johnson, C. C., eds., Evolution of the Cretaceous Ocean-Climate System: Boulder, Colorado, Geological Society of America Special Paper 332.

Deere, D.U. and Miller, R.P., 1966. Engineering classification and index properties for intact rock. Illinois Univ At Urbana Dept Of Civil Engineering.

Dong, T., Harris, N.B., Ayranci, K. and Yang, S., 2017. The impact of rock composition on geomechanical properties of a shale formation: Middle and Upper Devonian Horn River Group shale, Northeast British Columbia, Canada. AAPG Bulletin, 101(2), pp.177-204.

Donovan, R.N., 2001, Field study of the Sycamore Formation on Interstate Highway 35 in the Arbuckle Mountains, Oklahoma, in K.S. Johnson, ed., Silurian, Devonian, and Mississippian geology and petroleum in the southern Midcontinent, 1999 symposium: OGS Circular 105, p. 139-149.

Dypvik, H. and Harris, N.B., 2001. Geochemical facies analysis of fine-grained siliciclastics using Th/U, Zr/Rb and (Zr+ Rb)/Sr ratios. Chemical Geology, 181(1), pp.131-146.

Eberhardt, E., Stimpson, B. and Stead, D., 1999. Effects of grain size on the initiation and propagation thresholds of stress-induced brittle fractures. Rock Mechanics and Rock Engineering, 32(2), pp.81-99.

Ekwunife, I.C., 2017, High-Resolution Chemostratigraphy of The Woodford Shale in the McAlister Quarry, Ardmore Basin, Oklahoma. M.S. thesis, University of Oklahoma. In progress.

Ellis, R.M.T., 2013. Analysis of the Cyclostratigraphy at the Devonian–Carboniferous Boundary in South-Central Oklahoma. M.S. thesis, University Of Oklahoma, 51p.

Emerson, S.R. and Huested, S.S., 1991. Ocean anoxia and the concentrations of molybdenum and vanadium in seawater. Marine Chemistry, 34(3-4), pp.177-196.

Ettensohn, F.R., Fulton, L.P. and Kepferle, R.C., 1979. Use of scintillometer and gamma-ray logs for correlation and stratigraphy in homogeneous black shales: Summary. Geological Society of America Bulletin, 90(5), pp.421-423.

Fay, R.O., 1989, Geology of the Arbuckle Mountains along Interstate 35, Carter and Murray Counties, Oklahoma: OGS Guidebook 26, 50 p.

Fishman, N.S., G.S. Ellis, A.R. Boehlke, S.T. Paxton, and S.O. Egenhoff, 2013, Gas storage in the Upper Devonian–Lower Mississippian Woodford Shale, Arbuckle Mountains, Oklahoma: How much of a role do chert beds play?, in J.Y. Chatellier and D.M. Jarvie, eds., Critical assessment of shale resource plays: AAPG Memoir 103, p. 81-107.

Franklin, K.E., 2002, The Depositional History of the Sycamore Limestone. M.S. thesis, Oklahoma State University, 98 p.

Gale, J.F., Laubach, S.E., Olson, J.E., Eichhubl, P. and Fall, A., 2014. Natural fractures in shale: A review and new observations. AAPG bulletin, 98(11), pp.2165-2216.

Galvis, H.A., 2017. Detailed Lithostratigraphic Characterization and Sequence Stratigraphy of a complete Woodford Shale Outcrop Section in Southern Oklahoma. M.S. thesis, University of Oklahoma, 169 p.

Gaswirth, S.B. and Higley, D.K., 2014. Geologic assessment of undiscovered oil and gas resources in the Cambrian–Devonian stratigraphy of the Anadarko Basin, Oklahoma, Kansas, Texas, and Colorado. U.S. Geological Survey Digital Data Series DDS–69–EE, 42p.

Gercek, H., 2007. Poisson's ratio values for rocks. International Journal of Rock Mechanics and Mining Sciences, 44(1), pp.1-13.

Ghosh, S. and Slatt, R.M. 2015. Woodford shale fracture distribution from outcrop and core studies. Poster presentation at: AAPG Woodford Forum May.

Ghosh, S., Bontempi, C.P. and Slatt, R.M. 2016. Woodford Shale Fracture Distribution from Arbuckle Wilderness and Us-77d Outcrops. Poster presentation at: Applied Geoscience Conference, Houston, March.

Gilbert, M.C., 1982. Geologic setting of the eastern Wichita Mountains with a brief discussion of unresolved problems, in Geology of the eastern Wichita Mountains: Oklahoma Geological Survey Guidebook 21, p. 1-30

Gilbert, M.C., 1987. Petrographic and structural evidence from the igneous suite in the Wichita Mountains bearing on the Cambrian tectonic style of the Southern Oklahoma aulacogen: Geological Society of America Abstracts with Programs, v. 19, no. 3, p. 152

Granath, J.W., 1989. Structural evolution of the Ardmore basin, Oklahoma: progressive deformation in the foreland of the Ouachita collision. Tectonics,8(5), pp.1015-1036.

Grieser, W.V. and Bray, J.M., 2007, January. Identification of production potential in unconventional reservoirs. In Production and Operations Symposium. Society of Petroleum Engineers.

Güler, C., Thyne, G.D., McCray, J.E. and Turner, K.A., 2002. Evaluation of graphical and multivariate statistical methods for classification of water chemistry data. Hydrogeology journal, 10(4), pp.455-474.

Guo, T.K., Zhang, S.C. and Ge, H.K., 2013. A new method for evaluating ability of forming fracture network in shale reservoir. Rock and Soil Mechanics, 34(4), pp.947-954.

Hack, R, Hingira, J & Verwaal, W. 1993. Determination of Discontinuity Wall Strength by Equotip and Ball Rebound Tests, International Journal of Rock Mechanics, Mineral Science and Geomechanics, vol. 30, no. 2, pp. 151-5.

Hallam, A., 1967. The depth significance of shales with bituminous laminae.Marine Geology, 5 (5-6), pp.481-493.

Ham, W.E., R.E. Denison, and C.A. Merritt, 1964. Basement rocks and structural evolution of southern Oklahoma: OGS Bulletin 95, 302 p.

Ham, W.E., and others, 1973, Regional geology of the Arbuckle Mountains, Oklahoma: OGS Special Publication 73-3, 61 p.

Hardie, W.E., 1990. Subsurface structural study of the buried Ouachita thrust front, southeastern Oklahoma: Oklahoma City Geological Society, Shale Shaker, v. 41, p. 32-55.

Harris, N.B., Miskimins, J.L. and Mnich, C.A., 2011. Mechanical anisotropy in the Woodford Shale, Permian Basin: Origin, magnitude, and scale. The Leading Edge, 30(3), pp.284-291.

Hass, W.H., and J.W. Huddle, 1965, Late Devonian and Early Mississippian age of the Woodford Shale in Oklahoma as determined by conodonts, in Geological Survey research: U.S. Geological Survey Professional Paper 525-D, p. 125-132.

Hawkes, I. and Mellor, M., 1970. Uniaxial testing in rock mechanics laboratories. Engineering Geology, 4(3), pp.179-285.

Hesse, R., 1988. Diagenesis# 13. Origin of chert: Diagenesis of biogenic siliceous sediments. Geoscience Canada, 15(3).

Hester, T.C., H.L. Sahl, and J.W. Schmoker, 1988, Cross sections based on gamma-ray, density, and resistivity logs showing stratigraphic units of the Woodford Shale, Anadarko basin, Oklahoma: U.S. Geological Survey Miscellaneous Field Studies Map MF-2054, 2 sheets.

Hester, T.C., J.W. Schmoker, and H.L. Sahl, 1990, Log-derived regional source-rock characteristics of the Woodford Shale, Anadarko basin, Oklahoma: U.S. Geological Survey Bulletin 1866-D, 38p.

Hatcher Jr, R.D., 1989. Tectonic synthesis of the US Appalachians. The Appalachian-Ouachita orogen in the United States: Boulder, Colorado, Geological Society of America, Geology of North America, 2, pp.511-535.

Hoffman, P., J.F. Dewey, and K. Burke, 1974, Aulacogens and their genetic relation to geosynclines, with a Proterozoic example from Great Slave Lake, Canada, in Modern and ancient geosynclinal sedimentation: SEPM Special Publication v. 19, p. 38-55.

Hucka, V. and Das, B., 1974, October. Brittleness determination of rocks by different methods. In International Journal of Rock Mechanics and Mining Sciences & Geomechanics Abstracts (Vol. 11, No. 10, pp. 389-392). Pergamon.

Hunt, J.M., 1996. Petroleum geochemistry and geology. 743p.

Ingram, R.L., 1953, Fissility of mudrocks: Geological Society of America, Bulletin, v. 64, p. 869-878.

Irwin, M. L., 1965. General theory of epeiric clear water sedimentation: American Association of Petroleum Geologists Bulletin, v. 49, p. 445-459.

Jarvie, D.M., Claxton, B.L. Henk, F. and Breyer, J.T., 2001, Oil and shale gas from the Barnett Shale, Fort Worth Basin, Texas (abs.): AAPG Annual Meeting Abstracts, p. A100.

Jarvie, D.M., Hill, R.J., Ruble, T.E. and Pollastro, R.M., 2007, Unconventional shale-gas systems: The Mississippian Barnett Shale of north-central Texas as one model for thermogenic shale-gas assessment: American Association of Petroleum Geologists Bulletin 91, 475-499.

Johnson, K.S., and B.J. Cardott, 1992, Geologic framework and hydrocarbon source rocks of Oklahoma, in K.S. Johnson and B.J. Cardott, eds., Source rocks in the southern Midcontinent, 1990 symposium: OGS Circular 93, p. 21-37.

Johnson, K.S., 2008. Geologic history of Oklahoma. Earth sciences and mineral resources of Oklahoma: Oklahoma Geological Survey Educational Publication, 9, pp.3-5.

Jones, D.L. and Murchey, B., 1986. Geologic significance of Paleozoic and Mesozoic radiolarian Chert. Annual Review of Earth and Planetary Sciences, 14(1), pp.455-492.

Jones, L.C., 2017. An Integrated Analysis of Sequence Stratigraphy, Petroleum Geochemistry, and the Hangenberg Crisis in the Woodford Shale, Oklahoma. M.S. thesis, University of Oklahoma. In progress.

Katz, A., Sass, E., Holland, H.D., and Starinsky, A., 1972, Strontium behavior in the aragonite-calcite transformation: An experiment study at 40-98oC, Geochemica et Cosmochemica Acta, vol. 36, no. 4.

Kawasaki, S., Yoshida, M., Tanimoto, C., Masuya, T. 2000. The Development of Property Evaluation Method for Rock Materials Based on the Simple Rebound Hardness Test: Investigations on the Effects of Test Conditions and Fundamental Properties. Journal of Japan Society of Engineering Geology Vol.41, no.4, pp.230-241 (in Japanese with English abstract).

Kawasaki S, Tanimoto C, Koizumi K, Ishikawa M. 2002. An attempt to estimate mechanical properties of rocks using the Equotip Hardness tester. Journal of Japan Society of Engineering Geology 43: 244– 248 (in Japanese with English abstract).

Keith, B.D., 2014. Mississippian Carbonates in Indiana and beyond. Indiana Geological Survey. 28 slides.

Keller, G.R., Lidiak, E.G., Hinze, W.J. and Braile, L.W., 1983. The role of rifting in the tectonic development of the midcontinent, USA.Tectonophysics, 94(1), pp.391-412.

Kirkland, D.W., Denison, R.E., Summers, D.M., & Gormly, J.R. 1992. Geology and organic geochemistry of the Woodford Shale in the Criner Hills and western Arbuckle Mountains, Oklahoma. In: Johnson, K.S. & Cardott, B.J. (eds.) Source rocks in the southern mid-continent: 1990 Symposium: OGS Circular, 93, 38-69.

Krystyniak, A.M., 2005, Outcrop-based gamma-ray characterization of the Woodford Shale of south-central Oklahoma. M.S. thesis, Oklahoma State University, 145p.

Lambert, M.W., 1993, Internal stratigraphy and organic facies of the Devonian-Mississippian Chattanooga (Woodford) Shale in Oklahoma and Kansas, in B.J. Katz and L.M. Pratt, eds., Source rocks in a sequence stratigraphic framework: AAPG Studies in Geology 37, p. 163-176.

Langford, F.F. and Blanc-Valleron, M.M., 1990, Interpreting Rock-Eval pyrolysis data using graphs of pyrolyzable hydrocarbons vs. total organic carbon. American Association of Petroleum Geologist, Bulletin 74, p.799-804.

LaPointe, P. R., and J. A. Hudson, 1985. Characterization and interpretation of rock mass joint patterns: Geological Society of America Special Paper 199, 37 p.

Lee, J. S., Smallwood, L., & Morgan, E. 2014. New Application of Rebound Hardness Numbers to Generate Logging of Unconfined Compressive Strength in Laminated Shale Formations. In 48th US Rock Mechanics/Geomechanics Symposium. American Rock Mechanics Association.

Lee, J.S., Kieschnick, J., Geyer, C., Brumley, J. and DeSpain, L., 2016, June. Comparison of Different Methods to Estimate Uniaxial Compressive Strength in a Barnett Shale. In 50th US Rock Mechanics/Geomechanics Symposium. American Rock Mechanics Association.

Leeb, D., 1979. Dynamic hardness testing of metallic materials. NDT International, 12(6), pp.274-278.

Lewan, M.D., 1983, Effects of thermal maturation on stable organic carbon isotopes as determined by hydrous pyrolysis of Woodford Shale: Geochimica et Cosmochimica Acta, v. 47, p. 1471-1479.

Lewan, M.D., 1985, Evaluation of petroleum generation by hydrous pyrolysis experimentation: Philosophical Transactions of the Royal Society of London, series A, v. 315, p. 123-134.

Li, Y. 1982. A brief discussion on the mean oceanic residence time of elements. Geochimica et Cosmochimica Acta. V. 46; 2671-2675.

Luan, X., B. Di, J. Wei, X. Li, K. Qian, J. Xie, P. Ding. 2014. Laboratory Measurements of brittleness anisotropy in synthetic shale with different cementation. In: Proceedings of the 2014 SEG Annual Meeting. Denver, Society of Exploration Geophysicists. pp.3005–3009.

Lundegard, P.D. and Samuels, N.D., 1980. Field classification of fine-grained sedimentary rocks. Journal of Sedimentary Research, 50(3).

Maynard, S., 2016, Correlation of Bioturbated Facies, Chemostratigraphy,Total Organic Carbon, and Sequence Stratigraphyin The Woodford Shale of South Central Oklahoma. M.S. thesis, University of Oklahoma, 133 p.

McClave, G.A., 2014. Correlation of Rebound-Hammer Rock Strength With Core and Sonic-log Derived Mechanical Rock Properties in Cretaceous Niobrara and Frontier Formation Cores, Piceance Basin, Colorado. Unconventional Resources Technology Conference (URTEC).

McLennan, S. M., Taylor, S. R., 1995, The geochemical evolution of the continental crust, Reviews of Geophysics, v. 33, p. 241-265.

Meulenkamp, F & Grima, M. 1999. Application of neural networks for the prediction of the unconfined compressive strength (UCS) from Equotip hardness, International Journal of Rock Mechanics and Mining Sciences, vol. 30, pp. 29-39.

Miceli-Romero, A., and R.P. Philp, 2012, Organic geochemistry of the Woodford Shale, southeastern Oklahoma: How variable can shales be?: AAPG Bulletin, v. 96, p. 493-517.

Molinares Blanco, C.E., 2013, Stratigraphy and palynomorphs composition of the Woodford Shale in the Wyche Farm Shale Pit, Pontotoc County, Oklahoma: Norman, University of Oklahoma, unpublished M.S. thesis, 90 p.

Moore, D.M. & Reynolds, R.C. 1997 X-ray Diffraction and the Identification and Analysis of Clay Minerals. Oxford University Press, Oxford, New York, USA.

Murray, C.D., 2015. Mechanical stratigraphy and sonic log relationships using the Proceq Bambino in the Niobrara Formation, Denver Basin. M.S thesis, Colorado School of Mine, 101 p.

Nagelkerke, N.J., 1991. A note on a general definition of the coefficient of determination. Biometrika, 78(3), pp.691-692.

Nowaczewski, V., 2011, Biomarker and paleontological investigations of the Late Devonian extinctions, Woodford Shale, southern Oklahoma. M.S. thesis, University of Kansas, 96p.

O'Brien, N.R., And Slatt, R.M., 1990, Argillaceous Rock Atlas: New York, Springer-Verlag ed., 141 p.

Olsson, W.A., 1974. Grain size dependence of yield stress in marble. Journal of Geophysical Research, 79(32), pp.4859-4862.

Onodera, T.F. and Asoka Kumara, H.M., 1980. Relation between texture and mechanical properties of crystalline rocks. Bull Int Assoc Eng Geol, 22, pp.173-177.

Over, D.J. 1992. Conodonts and the Devonian-Carboniferous boundary in the Upper Woodford Shale, Arbuckle Mountains, south-central Oklahoma. Journal of Paleontology, 66, 293-311.

Paxton, S.T., Olsen, T., Price, C., Gross, E., and Allison, S. 2015. Spectral Gamma-Ray Profile of Woodford Shale - OHMEGCO Locality, Oklahoma. PowerPoint presentation prepared for Ardmore Geological Society, January. 108 slides.

Pearce, T.J. & Jarvis, I. 1992, Applications of geochemical data to modelling sediment dispersal patterns in distal turbidites: Late Quaternary of the Madeira Abyssal Plain. Journal of Sedimentary Petrology, v. 62, p. 1112-1129.

Pearce, T.J., Besly, B.M., Wray, D.S., & Wright, D.K. 1999, Chemostratigraphy: a method to improve interwell correlation in barren sequences – a case study using onshore Duckmantian/Stephanian sequences (West Midlands, U.K.). Sedimentary Geology, 124, 197-220.

Pearson, K., 1920. Notes on the history of correlation. Biometrika, 13(1), pp.25-45.

Pei, P., Ling, K., Hou, X., Nordeng, S. and Johnson, S., 2016. Brittleness investigation of producing units in Three Forks and bakken formations, williston basin. Journal of Natural Gas Science and Engineering, 32, pp.512-520.

Pepper, A.S. and Corvi, P.J., 1995, Simple kinetic models of petroleum formation. Part I: oil and gas generation from kerogen: Marine and Petroleum Geology, v. 12, p. 291-319.

Perez Altamar, R. and Marfurt, K., 2014. Mineralogy-based brittleness prediction from surface seismic data: Application to the Barnett Shale. Interpretation, 2(4), pp.T255-T271.

Perry Jr, W.J., 1989. Tectonic evolution of the Anadarko Basin region, Oklahoma. U.S. Geological Survey Bulletin 1866-A.

Peters, K.E., 1986. Guidelines for evaluating petroleum source rock using programmed pyrolysis. AAPG bulletin, 70(3), pp.318-329.

Peters, K.E., and Cassa, M.R., 1994, Applied source rock geochemistry, in Magoon, L.B., and Dow, W.G., eds., The petroleum system—From source to trap: Tulsa, Okla., American Association of Petroleum Geologists Memoir 60, p. 93-117.

Phillips, N.D., 1991, Refined Subsidence Analyses as a Means to Constrain Late Cenozoic Fault Movement, Ventura Basin, California. MS Thesis, University of Texas at Austin, 545p.

Potter, P.E., Maynard, J.B., and Pryor, W.A., 1980. Sedimentology of Shale. New York: Springer-Verlag, 303p.

Potter, P.E., Maynard, J.B., And Depetris, P.J., 2005, Mud and Mudstones: Introduction and Overview: Berlin, Springer ed., 297 p.

Priest, S. D. and Hudson, J. A. 1981. Estimation of discontinuity spacing and trace length using scanline surveys. International Journal of Rock Mechanics and Mining Sciences and Geomechanics Abstracts, 18, 183-97.

Priest, S.D., 1993. Discontinuity analysis for rock engineering. Springer Science & Business Media. 473p

Puckette, J., D.R. Boardman, and W.L. Watney, 2013, Woodford Shale: Correlating rock properties in outcrop and core with wireline log characteristics: AAPG Search and Discovery Article #50885, 46 p.

Ratcliffe, K.T., Wright, A.M., Montgomery, P., Palfrey, A., Vonk, A., Vermeulen, J. and Barrett, M., 2010. Application of chemostratigraphy to the Mungaroo Formation, the Gorgon field, offshore northwest Australia. Australian Petroleum Production and Exploration Association Journal, 50, pp.371-385.

Rickman, R., Mullen, M.J., Petre, J.E., Grieser, W.V. and Kundert, D., 2008, January. A practical use of shale petrophysics for stimulation design optimization: All shale plays are not clones of the Barnett Shale. In SPE Annual Technical Conference and Exhibition. Society of Petroleum Engineers.

Ritz, E., Honarpour, M., Dula, W.F. and Dvorkin, J.P., 2014. Core Hardness Testing and Data Integration for Unconventionals. Unconventional Resources Technology Conference (URTEC).

Roberts, C.T., and R.M. Mitterer, 1992, Laminated black shale-bedded chert cyclicity in the Woodford Formation, southern Oklahoma, in K.S. Johnson and B.J. Cardott, eds., Source rocks in the southern Midcontinent, 1990 symposium: OGS Circular 93, p. 330-336.

Rosen, O.M. and Abbyasov, A.A., 2003. The quantitative mineral composition of sedimentary rocks: calculation from chemical analyses and assessment of adequacy (MINLITH computer program). Lithology and Mineral Resources, 38(3), pp.252-264.

Rosen, O.M., Abbyasov, A.A. and Tipper, J.C., 2004. MINLITH—an experience-based algorithm for estimating the likely mineralogical compositions of sedimentary rocks from bulk chemical analyses. Computers & geosciences, 30(6), pp.647-661.

Ross, D.J.K., Bustin, R.M., 2009. Investigating the use of sedimentary geochemical proxies for paleoenvironment interpretation of thermally mature organic-rich strata: examples from the Devonian–Mississippian shales, Western Canadian Sedimentary Basin. Chemical Geology 260, 1–19 p.

Rowe, H. D., R. G. Loucks, S. C. Ruppel, and S. M. Rimmer, 2008, Mississippian Barnett formation, Fort Worth Basin, Texas: Bulk geochemical constraints on the severity of hydrographic restriction and the biogeochemical cycling and fate of iron: Chemical Geology, v. 257, p. 16-25.

Rowe, H., Hughes, N., & Robinson, K. 2012. The quantification and application of handheld energy-dispersive x-ray fluorescence (ED-XRF) in mudrock chemostratigraphy and geochemistry. Chemical Geology, 324-325, 122-131.

Ruppel, S.C., Rowe, H., Milliken, K., Gao, C. and Wan, Y., 2017. Facies, rock attributes, stratigraphy, and depositional environments: Yanchang Formation, Central Ordos Basin, China. Interpretation.

Sageman, B.B. & Lyons, T.W. 2003, Geochemistry of fine-grained sediments and sedimentary rocks. In: Mackenzie, F. (ed.) Sediments, Diagenesis, and Sedimentary Rock. Treatise on Geochemistyr, 7, 115-158.

Salminen R., Batista, M.J., Bidovec, M., Demetriades, A., DeVivo, B., DeVos, W., Duris, M., Gilucis, A., Gregorauskiene, V., Halamic, J., Heitzmann, P., Lima, A., Jordan, G., Klaver, G., Klein, P., Lis, J., Locutura, J., Marsina, K., Mazreku, A., O'Connor, P.J., Olsson, S.A., Ottesen, R.T., Petersell, V., Plant, J.A., Reeder, S., 2005, Geochemical Atlas of Europe, Part 1: Background Information, Methodology and Maps. Geological Survey of Finland, 526 p. Available online at: http://www.gtk.fi/publ/foregsatlas/ [Accessed February 2017].

Saxon, C.P., 1998. Structural style of the Wichita and Arbuckle orogenies, southern Oklahoma: Norman, University of Oklahoma, unpublished PhD dissertation, 248 p.

Schwartzapfel, J.A., 1990, Biostratigraphic investigations of late Paleozoic (Upper Devonian to Mississippian) Radiolaria within the Arbuckle Mountains and Ardmore basin of south-central Oklahoma: Dallas, University of Texas, Ph.D. dissertation, 475 p.

Schwartzapfel, J.A. and Holdswort, B.K. 1996, Upper Devonian and Mississippian Radiolarian Zonation and Biostratigraphy of the Woodford, Sycamore, Caney and Goddard Formations, Oklahoma, Cushman Foundation for Foraminiferal Research, Special Publication No. 33.

Serna-Bernal, A., 2013, Geological Characterization of the Woodford Shale McAlister Cemetery Quarry, Criner Hills, Ardmore Basin, Oklahoma: M.S. thesis, University of Oklahoma, 141 p.

Serra, O., 1984. Fundamentals of Well-log Interpretation: The acquisition of logging data, 684 p.

Shaw, A. B., 1964. Time in stratigraphy: McGraw-Hill, New York, 365 pp.

Sierra, R., Tran, M.H., Abousleiman, Y.N. and Slatt, R.M., 2010, January. Woodford shale mechanical properties and the impacts of lithofacies. In 44th US rock mechanics symposium and 5th US-Canada rock mechanics symposium. American Rock Mechanics Association.

Siy, S.E., 1988, Geochemical and petrographic study of phosphate nodules of the Woodford Shale (Upper Devonian-Lower Mississippian) of southern Oklahoma. M.S. thesis Texas Tech University, 172 p.

Slatt, R.M., 1974. Geochemistry of bottom sediments, Conception Bay, southeastern Newfoundland. Canadian Journal of Earth Sciences, 11(6), pp.768-784.

Slatt, R.M., Jordan, D.W., D'Agostino, A.E. and Gillespie, R.H., 1992. Outcrop gamma-ray logging to improve understanding of subsurface well log correlations. Geological Society, London, Special Publications, 65(1), pp.3-19.

Slatt, R.M., N. Buckner, Y. Abousleiman, R. Sierra, P. Philp, A. Micelli-Romero, R. Portas, N. O'Brien, M. Tran, R. Davis, and T. Wawrzyniec, 2012, Outcrop-behind outcrop (quarry): multiscale characterization of the Woodford gas shale, Oklahoma, in J. Breyer, ed., Shale reservoirs—Giant resources for the 21st century: AAPG Memoir 97, p. 382-402.

Stanley, T.M. and Chang, J.M., 2012. Geologic Map of the Ardmore 30′ X 60′ Quadrangle and the Oklahoma Part of the Gainesville 30′ X 60′ Quadrangle, Carter, Jefferson, Love, Murray, and Stephens Counties, Oklahoma. Oklahoma Geological Survey.

Stilwell, H., Martinez, N., Hildred, G. and Zaitlin, B., 2013. Forensic Chemostratigraphy in Geosteering Multilateral Wells: An Example from Devonian to Carboniferous-Aged Sequences in Southern Alberta. Unconventional Resources Technology Conference (URTEC).

Sullivan, K.L., 1985, Organic facies variation of the Woodford Shale in western Oklahoma: Shale Shaker, v. 35, p. 76-89.

Suneson, N., 1996. The geology of the Ardmore Basin in the Lake Murray Stake Park Area, Oklahoma, prepared for the spring field meeting of the Oklahoma Academy of Science, 44 p.

Swanson, V.E., 1961, Geology and geochemistry of uranium in marine black shales, a review: U.S.G.S. Professional Paper 356-C, p. 67-112.

Templ, M., Filzmoser, P. and Reimann, C., 2008. Cluster analysis applied to regional geochemical data: problems and possibilities. Applied Geochemistry, 23(8), pp.2198-2213.

Thurston, D. and Taylor, J., 2016, June. Logging for Free-The Use of XRF on Cuttings Data in Unconventional Oil and Gas Exploration and Reservoir Characterization. In SPWLA 57th Annual Logging Symposium. Society of Petrophysicists and Well-Log Analysts.

Tissot, B., Durand, B., Espitalie, J. and Combaz, A., 1974. Influence of nature and diagenesis of organic matter in formation of petroleum. AAPG Bulletin, 58(3), pp.499-506.

Tourtelot, H.A., 1960. Origin and use of the word “shale”. American Journal of Science, 258, pp.335-343.

Treanton, J.A. 2014. Outcrop-derived chemostratigraphy of the Woodford Shale, Murray County, Oklahoma. M.S. thesis, The University of Okl ahoma. 83p.

Tribovillard, N., Algeo, T.J., Lyons, T., & Riboulleau, A. 2006. Trace metals as paleoredox and paleoproductivity proxies: an update. Chemical Geology, 232, 12-32.

Turner, B. J., 2016, Utilization Of Chemostratigraphic Proxies For Generating And Refining Sequence Stratigraphic Frameworks In Mudrocks And Shales, Ph.D dissertation, University of Oklahoma, 135 p.

Vachaparampil, A., Hu, L., Zhou, X., Ghassemi, A., Gill, I., Chitrala, Y., 2016. Geomechanical Anisotropy of Utica Shale from Static and Dynamic Measurements. Paper presented at the 48th US Rock Mechanics / Geomechanics Symposium held in Houston, TX, USA, 23-26 June. American Rock Mechanics Association.

Vachaparampil, A. and Ghassemi, A., 2017. Strength Criteria for Shale under True-Triaxial Stresses. Paper presented at the 51st US Rock Mechanics / Geomechanics Symposium held in San Francisco, California, USA, 25-28 June. American Rock Mechanics Association.

Van Hise, C. R., 1904. A treatise on metamorphism: U. S. Geol. Survey Monograph 47, pp. 562-655.

Verwaal, W & Mulder, A. 1993. Estimating Rock Strength with the Equotip Hardness Tester', International Journal of Rock Mechanics, Mineral Science and Geomechanics, vol. 30, no. 6, pp. 659-62.

Villalba, D.M., 2016, Organic Geochemistry of The Woodford Shale, Cherokee Platform, OK and its Role in a Complex Petroleum System. M.S. Thesis, University of Oklahoma, 126 p.

Vine, J.D. and Tourtelot, E.B., 1970. Geochemistry of black shale deposits-A summary report. Econ. Geol., v.65, p. 253-272.

Von Almen, W.F., 1970, Palynomorphs of the Woodford Shale of south-central Oklahoma with observations on their significance in zonation and paleoecology: Michigan State University, unpublished Ph.D. dissertation, 179 p.

Walles, F., 2004. A New Method to Help Identify Unconventional Targets for Exploration and Development Through Integrative Analysis of Clastic Rock Property Fields.

Walsh, J.B., 1965. The effect of cracks in rocks on Poisson's ratio. Journal of Geophysical Research, 70(20), pp.5249-5257.

Wang, F.P. and Gale, J.F., 2009. Screening criteria for shale-gas systems. The Gulf Coast Association of Geological Societies. 15p.

Wang, T., 2016, An Organic Geochemical Study of Woodford Shale and Woodford-Mississippian Tight Oil from Central Oklahoma. Ph.D. dissertation, University of Oklahoma 299 p.

Watson, B.P., 2008. Internal Stratigraphy, Composition, and Depositional Setting of the Woodford Shale in Southern Seminole County, Oklahoma. M.S thesis, Oklahoma State University, 152 p.

Weber, J.N., 1964. Trace element composition of dolostones and dolomites and its bearing on the dolomite problem. Geochimica et Cosmochimica Acta, 28(10-11), pp.1817IN271833-18321868.

Wedepohl, K.H., 1971. Environmental influences on the chemical composition of shales and clays. In: Ahrens, L.H., Press, F., Runcorn, S.K., Urey, H.C. (Eds.), Physics and Chemistry of the Earth. Pergamon, Oxford, pp. 305–333.

Weedon, G.P., & Shackleton, N.J., 1997. Inorganic geochemical composition of Oligocene to Miocene sediments and productivity variations in the Western equatorial Atlantic: results from sites 926 and 929. Proc. Ocean Drill. Program Sci. Results 154, 507 – 526.

Wright, A.M., K.T. Ratcliffe, and D.R. Spain, 2010. Application of inorganic whole rock geochemistry to shale resource plays. In Canadian Unconventional Resources and International Petroleum Conference. Society of Petroleum Engineers.

Xu, J. and Sonnenberg, S., 2016. Brittleness and Rock Strength of the Bakken Formation, Williston Basin, North Dakota. Unconventional Resources Technology Conference (URTEC).

Zahm CK, & Enderlin M., 2010, Characterization of rock strength in Cretaceous strata along the Stuart City Trend. Texas: Gulf Coast Association of Geological Societies Transactions v. 60. p. 693–702.

Zhang, J., 2016. Comprehensive Reservoir Characterization of the Woodford Shale in Parts of Garfield and Kingfisher Counties, Oklahoma. M.S. thesis, University of Oklahoma 165 p.

Zheng, Y., Anderson, R.F., van Geen, A. and Fleisher, M.Q., 2002. Remobilization of authigenic uranium in marine sediments by bioturbation. Geochimica et Cosmochimica Acta, 66(10), pp.1759-1772.